HIERARCHICAL FINITE ELEMENT METHOD FOR THE PROGNOSTIC ANALYSIS OF STRUCTURAL HEALTH MONITORING

A Thesis
Presented to
The Academic Faculty

By

Youngchul Park

In Partial Fulfillment
of the Requirements for the Degree
Doctor of Philosophy in the
School of Computational Science and Engineeing
School of Aerospace Engineering

Georgia Institute of Technology

August 2017

HIERARCHICAL FINITE ELEMENT METHOD FOR THE PROGNOSTIC ANALYSIS OF STRUCTURAL HEALTH MONITORING

Approved by:

Professor Dimitri N. Mavris, Advisor
School of Aerospace Engineering
Georgia Institute of Technology

Professor George A. Kardomateas
School of Aerospace Engineering
Georgia Institute of Technology

Dr. Neil Weston
School of Aerospace Engineering
Georgia Institute of Technology

Professor Polo Chau
School of Computational Science & Engineering
Georgia Institute of Technology

Professor Le Song
School of Computational Science & Engineering
Georgia Institute of Technology

Date Approved: March 2, 2017

ACKNOWLEDGEMENTS

The beginning of my journey to my doctorate degree started when I met my mentor, Dr. Mavris. Without his endless faith and encouragement, I would never have succeeded on this journey. So, I would like to heartily thank my advisor Professor Dimitri Mavris. I'd like to extend special thanks to Dr. Neil Weston for his effort and advice during my life at ASDL. I would like to extend my thanks to my committee, Professor George Kardomateas, Professor Polo Chau, and Professor Le Song, for their time and effort. I have valued their advice and mentoring. I also want to sincerely thank Dr. Woongje Sung, Dr. Jongkig Moon, Dr. Dongwook Lim, and Dr. Byungho Ahn at ASDL. I'd also like to acknowledge the support of my friends at ASDL: Youngjin Kim, Hyungu Choi, Sanggyu Min, Syan Ghosh, David Rancort, Jason Corman, and Mario Lee.

Above all, I sincerely thank my family. Without the endless love and support of my parents, Dongho Park and Joonyub Kim, I would not have accomplished this work. To my lovely wife, Seoeun, I truly thank you for being by my side with unwavering support and steadfast belief in me. Siwan, my son, I could not have overcome the many difficulties I have faced without seeing your smile-the most beautiful and joyful smile in the world. I love you!

TABLE OF CONTENTS

LIST OF TABLES

LIST OF FIGURES

SUMMARY

The structural design of vehicles has become lighter but stronger because of new materials and more precise analysis of structural safety. But, the future generation of aircraft will suffer more severe load conditions and service conditions due to their more extreme mission. Current methodologies for aircraft certification, and maintenance scheduling are based on statistical distributions, and a heuristic understanding that assumed the future aircraft can be operated in similar environments and maneuvers, which is an assumption that may be highly uncertain. To overcome the shortcomings of conventional methodologies, we need a paradigm shift, the digital twin. However, the 'detail' is not always sufficient for the philosophy of damage tolerance design to simulate a crack propagation. Therefore, this study suggests a new digital twin method for the purpose of damage tolerant safety and develops a framework for its application.

In aerospace applications for novel lightweight structures, manufacturers design their aircraft to ensure design safety based on regulations for damage tolerance design, which assumes the existence of cracks and the ability to sustain defects until periodic maintenance. However, design regulations guide only the possibility of cracks based on standard history operation regardless of the current condition for individual aircraft. Since each individual aircraft has a unique condition of operation, the study of structural health monitoring suggests identifying any defects as early as possible and taking corrective action early to minimize the operation cost and the maintenance cost. The structural health monitoring examines the current state of individual aircraft and simulates the propagation of cracks under various conditions through a computational model referred to as the digital twin, which represents the actual aircraft and plays a key role in a reliable simulation of crack propagation in structural health monitoring. Since defects or crack sizes are minuscule, the finite element of digital twin requires an extremely fine mesh, which requires enormous computation time, making a general finite element method unsuitable for analyzing the behavior of micro cracks. Therefore, this study proposes a new methodology, the hierarchical finite element

method (HFEM), to solve the problem of adaptable mesh size and computation time. The HFEM transfers external loads from global-level to base-level model as grid forces, which is the result of global-level of FE analysis.

In the pre-processing stage of the HFEM, classes of a finite element model are categorized into three levels: a micro-level, a base-level, and a global-level model. The global-level model is an entire system of a structure with an appropriate element size. The HFEM first partitions the various shape and size of the component elements in the global-level model into k clusters using a K-means clustering algorithm. Each cluster center is a candidate for the base-level model, which conducts the crack simulation with fine meshes. Each candidate of the base-level model has a stress distribution map generated by six components of unit loads. In the case of composite materials, the stress map contains additional information, amplification factors, from the micro-level model by applying six components of unit loads on the candidate unit cells, which depend on fiber array types.

Post-processing is the simulation of the prognosis for the digital twin with actual aerodynamic loads to predict the remaining life based on the crack propagation analysis. The constituent element in the base-level model behaves individually with cellular automata rules, an effective way of simulating complex systems without central control. The simulation emerges to a stable or unstable point according to simple local operating rules and neighboring effects. This study investigates local rules and neighboring effects for the crack propagation to employ it in the crack simulation in the HFEM. Crack simulation advances the analysis by regarding an element as a dead cell if the residual strength, calculated based on the fracture mechanics, reaches a critical factor. A mathematical crack-closure model determines critical factors with a size of influence region and the effect of neighboring elements, the former of which determines its life cycle.

This study will create a virtual simulation environment to analyze the life cycle of aircraft based on the proposed HFEM by assuming that installed fiber optic sensors are on the wing. Like a real application, embedded sensors at certain locations provide the strain information along the

span of the wing. Strains, acting as aerodynamic loads, need to transfer at the independent node of multi-point constraints. Independent nodes deliver loads to their dependent nodes, which are surrounding nodes of the independent node, to represent a pressure effect. This study proposes a K-means clustering method to classify all elements into clusters to represent a center of the cluster as an independent node and members of the cluster as dependent nodes. Then, cluster centers deliver aerodynamic forces as an appropriate way to the digital twin.

In the virtual simulation, the digital twin, adopting the cyclic load from virtual sensors, will analyze the remaining life of the aircraft. However, the remaining life is not able to be predicted with currently acquired cyclic loads because it requires future cyclic loads. Therefore, this study proposes an inverse transport wing standard (TWIST) method to forecast the future time-series of cyclic loads based on current loads. TWIST is a spectrum generating method developed to standardize a stress spectrum of transport aircraft by using historical data of fatigue life. In this study, as following the method of TWIST, acquired data from sensors can be samples of standard spectrum to generate a predicted historical data. Thus, the digital twin with the stress spectrum of predicted historical data enables the prognosis of remaining life based on accumulated data.

The affordability of the HFEM for the prediction of remaining life will be a turning point from inspections based on schedules to inspections based on demand approach. Further, the HFEM enables us to evaluate complex decision making for a damaged aircraft component with reliable information of the current condition.

CHAPTER 1
INTRODUCTION

1.1 Background

World War I and World War II witnessed the rapid development of structural design technology in aerospace engineering. After World War II, engineers began to apply the concept of safety to structural design technology. Studying the limits of stress and the elastic zone, structural engineers used the safety factor to prevent the failure of a structure by examining uncertainty in the design of aircraft with applied loads. Despite the introduction of these safety factors, some aviation accidents occurred in the 1950s. In 1954, an accident involving a Comet airplane, Figure 1.1, was found to result from fatigue failure without exceeding the allowable load [1]. This accident led to the introduction of a safe-life design method based on fatigue life, which has evolved into a safe-life design concept that guarantees structural safety within a design life.

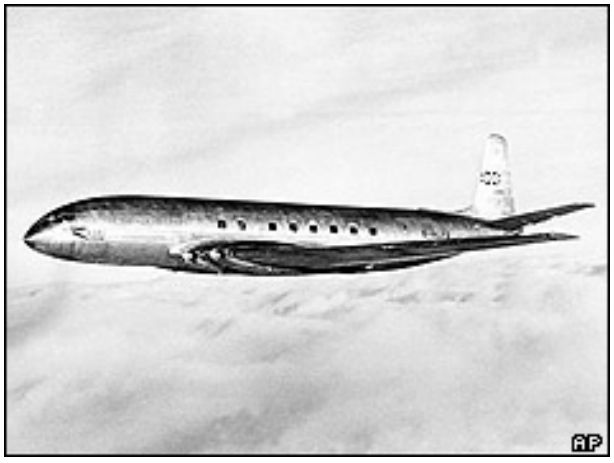

Figure 1.1: BBC News in 1954, “Metal fatigue” caused the Comet crash [1]

Despite the efforts of structural design engineers to prevent structural failures, the B707, illustrated in Figure 1.2, was involved in an accident that occurred in 1977. The National Transportation

Safety Board(NTSB), an independent U.S. government investigative agency responsible for civil transportation accident investigation, determined that the accident may have resulted from potential cracks and fatigue cracks inside the aircraft that led to an additional examination of structural failure [2]. Thus, aerospace engineers examined approaches to detect cracks that can lead to a catastrophic failure in an aircraft and overcoming potential deficiencies. The result of such efforts led to the development of the fail-safe design concept applied to aircraft.

Figure 1.2: A Dan-Air Boeing 707 similar to the crash aircraft [2]

The fail-safe design does not apply to all parts of the aircraft, only to critical parts such as the primary structure of an aircraft. Even though an aircraft may have some cracks or potential defects in its most critical parts, the design concept ensures the safety of a structure until the next inspection cycle. In other words, the aircraft structure is designed to ensure safety against crack propagation until the next inspection cycle under the assumption that the structure contains potential defects or cracks . This method is referred to as damage tolerance design. Any civil aircraft needs to meet criteria from FAA certification process which is related to damage tolerance philosophy in satisfying the FAA damage tolerance requirements. Swif T. described the latest FAA certification steps to be taken in the damage tolerance analysis by itemized it and included details of required certification testing in Ref. [3].

During operation, an aircraft designed using damage tolerance certification allows cracked structures to withstand all design loads until inspectors can detect and determine the critical size of crack inside the structure, or damage, or excessive deformation of the entire structure. Damage tolerance design, which generally combines the existing safe-life and fail-safe concepts, must guarantee that the design is able to withstand simultaneous cracks and also predict their propagation. When the damage tolerance design is analyzed with the simultaneous presence of cracks at multiple locations, this design method is referred as widespread fatigue damage (WFD). WFD is raised to consider multiple site damage and multiple element damage cracks that are typically too small to initially be reliably detected with normal inspection methods. As an aircraft ages, these cracks will grow, and eventually imperil the structural integrity of the aircraft. WFD specifications are included in a FAA rule announced on Jan. 2011 and all aircraft manufacturers are now required to prove the compliance of the criteria of WFD [4]. The WFD is not only required for the manufacturer, but also airline companies who must adjust maintenance schedule to comply with WFD criteria.

From historical lessons, all recently and currently manufactured aircraft structures must meet the design requirements specified in regulations such as those listed in Federal Aviation Regulations (FARs) for civil aircraft and those for US Military Standards and Specifications for military aircraft. Specifically, civil aircraft needs to follow criteria that is provided by FAA within AC (advisory circular). For example, the fatigue and damage tolerance design for transport aircraft is written in AC 23-13A and all manufactures must comply criteria in AC23-13A [5]. Design requirements are typically validated through finite element analysis and experiments with actual structures. However, because of their cost and time, experiments are usually used only as a means of validating the results of design through finite element analysis. Thus, at the design stage of an aircraft, finite element analysis is a critical step that must follow proper methods and procedures according to regulations. In finite element analysis, design engineers perform stress and a margin of safety analysis to evaluate the safety of an aircraft under the static loading conditions of a

structure. Static loads are usually considered in two forms, limit load and ultimate loads according to the airworthiness regulations. Static stress analysis typically uses the ultimate load, which is the limit load multiplied by a safety factor of 1.5. The results of an analysis under an ultimate load allows for local breakage and buckling, while ensuring the overall safety of a structure. Once design engineers evaluate safety under the ultimate load, they conduct a fatigue analysis under the condition of a limit load based on stress information, which is the result of the static analysis.

To demonstrate safety within the fatigue life of an aircraft structure, a fatigue analysis for dynamic loads should be conducted. The dynamic loads are obtained from either a flight record of a similar aircraft when no actual flight data are available, or by a standardized load spectrum. Typical standard load spectra are the transport wing standard spectrum (TWIST) for civil aircraft, FELIX for a helicopter with a fixed or articulated rotor system, HELIX for a helicopter with a hinged or articulated rotor system, and a fighter aircraft loading standard for fatigue evaluation (FALSTAFF) of a fighter aircraft [6].

The dynamic loads are then utilized to analyze both the safe-life and fail-safe design requirements which also advocated as fatigue analysis and damage tolerance analysis. First, the safe-life requirement calculates the fatigue life corresponding to the stress through the $S-N$ or $\varepsilon-N$ curve, applies Miner's rule that accumulates the damage, and compiles the stress cycle . Miner's rule is a standard cumulative damage method presented in the FAA Advisory Circular for calculating damage at various amplitude loadings by assuming that fatigue failure occurs when the accumulated damage reaches value 1 [7].

Based on the result of the fatigue life analysis, fatigue critical locations are recognized, and the critical locations are assumed as locations where cracks can initially occur. Thus, the critical location needs to prove its future safety by the damage tolerance analysis. The damage tolerance design method, based on the LEFM theory, assumes that the stress intensity factor is calculated from partial damage, or that a latent crack progresses when the stress intensity factor reaches a critical stress intensity factor. Thus, this method calculates fatigue life by estimating the propaga-

tion cycles of a crack during the length of the propagation of an initial crack to the final length of the fracture crack .

1.2 Problems with current structural design concepts

1.2.1 Inherent risks for uncommon operation

Design requirements and concepts that ensure the structural safety of aircraft were discussed in the previous section. The newest design concept, WFD, requires the certification of a damage tolerant structure for simultaneous cracks, a critical requirement for all newly designed aircraft. According to FAA regulations, to ensure the safety of operation against flaws, a damage tolerance analysis that includes inspection schedules must be discussed for structural endurance of a structure or a part until the next scheduled inspection to repair the flaw that inherently existed, accidentally occurred, or periodically accumulated. The maintenance schedule, inspections, or even the method of damage tolerance analysis is based on historical experience. In other words, these design requirements are based on an empirical database and entail the evaluation of safety using guesswork and then estimating the load and repetition of events that an aircraft will experience.

All aircraft in a fleet share a manual of scheduling and maintenance, both of which are determined from the results of the damage tolerance analysis at the design stage. We refer to this task as design-based maintenance scheduling, which is a means of overcoming the limitations of the current aircraft design concept. However, recent studies have pointed out problems of uncertainties that need to be accounted for maintenance, an approach that would not have been addressed or even possible with design-based, maintenance scheduling for future aircraft. For example, E. H. Glaessgen and D.S. Stargel[8] argued that existing methodologies for vehicle certification, fleet management, and sustainment based on a heuristic understanding of structural behavior are not suitable for future generations of NASA and U.S. Air Force vehicles, which must be lighter, while being subjected to extreme service conditions. They also claimed that, for future generation air-

craft, we need to shift from design-based maintenance to demand-based maintenance scheduling that decides the maintenance requirement based on the current structural health.

The problem of design-based maintenance scheduling is not only an issue for future aircraft, but also some of current aircraft groups that have irregular flight patterns. For example, suppose that aircraft A and aircraft B are the same aircraft, and they start operating at the same time. Aircraft A frequently flies over short distances in areas with heavy wind and heavy maneuvers. Aircraft B is relatively easy to maneuver and mainly flies long distances. It is clear that the durability of the landing gear system or other structures of aircraft A will be lower than that of aircraft B. However, since they are the same aircraft type, the two aircraft are under the same maintenance cycle. An explanation of this risk was reported in testimony by the FAA in March 2010 [9]. Representatives of the FAA explained that on-demand operators like aircraft B in the example, which have an irregular history for short-range flights, have more takeoffs and landings that entail the most critical loads. Therefore, they also claimed that on-demand operators encounter inherent risks that cannot be predicted by a general damage tolerance concept.

Motivating Question 1

How should the inherent risk for operational uncertainties be covered for future generation aircraft or an on-demand operator?

The simplest and only way of detecting a possible crack or defect as early as possible is regulatory inspection and maintenance. However, the development of IT (Information Technology) and sensor technologies should soon usher in a new era of aircraft operating systems. A more detailed description of the framework introduced in this study appears in the following chapters. In summary, however, we reiterate that design-based maintenance scheduling must shift to demand-based scheduling to adapt to the future generation of aircraft with a structural health monitoring system.

1.2.2 Cost burden for design-based maintenance

The current structural design has been secured by maintenance or inspection for an inherent problem such as exist or newly developed damage which were not expected at design stage. The maintenance replaces a TCI (time change item) periodically to block any catastrophic failure from the certain part. The other hand, inspection finds any damage, crack, or fatigue weariness to confirm that the certain part has enough residual strength by generally NDI (non-destructive inspection) method. NDI determines the existence of cracks on the basis of test results based on separate determination criteria after non-destructive testing, which is generally conducted by observation or special tools. When inspection equipment or inspectors detect a defect in a product by NDI, they determine whether the product can be used as is or not. Thus, inspectors must be well trained in the various methods of NDI, listed in Table 1.1.

Table 1.1: The relative uses and merits of various NDI methods [10]

	Test method				
	Ultrasonics	X-ray	Eddy current	Magnetic particle	Liquid penetrant
Capital cost	Medium to high	High	Low to medium	Medium	Low
Consumable cost	Very low	High	Low	Medium	Medium
Time of results	Immediate	Delayed	Immediate	Short delay	Short delay
Effect of geometry	Important	Important	Important	Not too important	Not too important
Access problems	Important	Important	Important	Important	Important
Type of defect	Internal	Most	External	External	Surface breaking
Relative sensitivity	High	Medium	High	Low	Low
Formal record	Expensive	Standard	Expensive	Unusual	Unusual
Operator skill	High	High	Medium	Low	Low
Operator training	Important	Important	Important	Important	Important
Training needs	High	High	Medium	Low	Low
Portability of equipment	High	Low	High to medium	High to medium	High
Dependent on material composition	Very	Quite	Very	Magnetic only	Little
Ability to automate	Good	Fair	Good	Fair	Fair
Capabilities	Thinkness gauging; some composition testing	Thinkness gauging	Thinkness gauging; grade sorting	Defects only	Defects only

In the case of current systems of aircraft operation, inspections and maintenance follow guidelines in a manual that includes inspection location, periods, methods, and other information and they are determined at the design stage. As the decision applies to all of the same models regardless of their operational environments or current conditions, for some individual aircraft, an extra unnecessary inspection must be conducted, which incurs additional costs of parts and labor. As aircraft inspections and maintenance require considerable time and labor, the cost is prohibitive. For example, every six years, an airline must perform one inspection that requires 50,000 man-hours and 20 months to complete. While performing the inspection, inspectors have to replace TCIs in batches without evaluating their current conditions. We can avoid incurring the cost of inspections and maintenance if TCIs take operation type into consideration. For example, if an aircraft operates primarily short range, TCIs should relate more to the landing gear section. Like the TCI example, maintenance and replacement in aerospace operations are inefficient because of their ineffectiveness and demand for high safety, both of which are prohibitively expensive. The reason for the inefficiency of maintenance is strongly related to the airtight safety demand that covers significant uncertainty of an entire fleet, not only individual aircraft. Figure 1.3a and 1.3b show the difference between the failure uncertainty of an individual aircraft and that of a fleet of ten aircraft.

Each of the ten aircraft shown in Figure 1.3b has its own uncertainty of structural failure that is determined by operating conditions, and each failure uncertainty has a unique mean and variance for its uncertainty distribution. Therefore, the uncertainty becomes much larger, so inspection and maintenance must cover the increased area.

As the aircraft fleet ages, uncertainty to be covered by inspections and maintenance increases. Thus, the required cost increases as the aircraft undergo a greater workload. Since the design of aircraft is similar and their materials have identical deterioration properties, the characteristic for the cost requirement of maintenance of all fleets is generally unique. Pyles[11] examined the relationship between the ages of estimates of USAF aircraft fleets and maintenance and modification

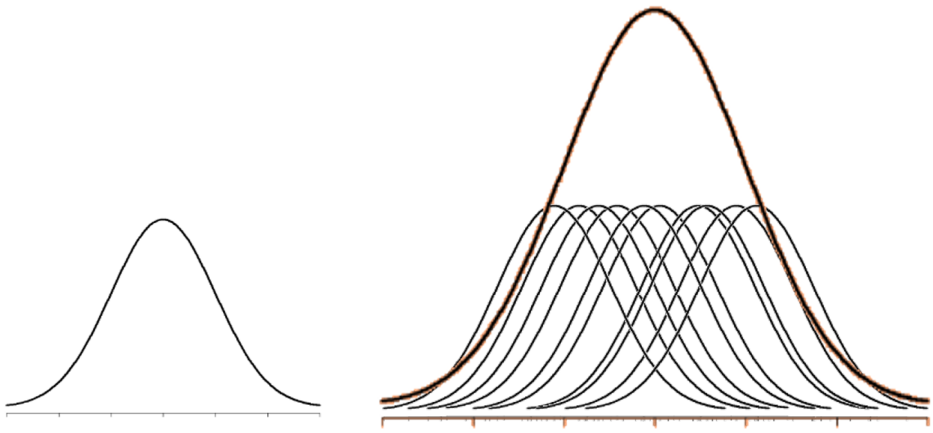

(a) Uncertainty of one aircraft (b) Uncertainty of ten aircraft

Figure 1.3: Uncertainty of a structural failure comparisons for one aircraft vs. ten aircraft

workloads and material consumption. The author provided a foundation for the future effects of maintenance-resource requirements, aircraft availability, and annual operating costs. Figure 1.4 illustrates his two workload growth models. The linear equation assumes that the annual workload increases a fixed amount each year as if the growth were a fixed percentage of the initial workload. In contrast, the compound equation assumes that the annual workload increases at a fixed percentage of the accumulated workload of the previous years. For a typical aircraft fleet, he claimed that both equations provided acceptably accurate estimates of life cycle workloads or costs.

Many global airlines have focused on maintenance costs and methods for reducing them. According to the 2015 IATA benchmark analysis[12], in 2014, the airlines spent $62.1 billion, excluding overhead, on global maintenance, repair, and overhaul (MRO). MRO, which consists of requirements that guarantee the safety of both passengers and crew members, represents around 9% of total operating costs. With a 3.8% increase annually, the cost of MRO is expected to reach $90 billion in 2024. The ICF International Forecast in 2014[13] reported that the strongest drivers of MRO market growth were engine and component markets, shown in Figure 1.5, with engine parts the largest portion spent on MRO. Not surprisingly, most engine manufacturing companies

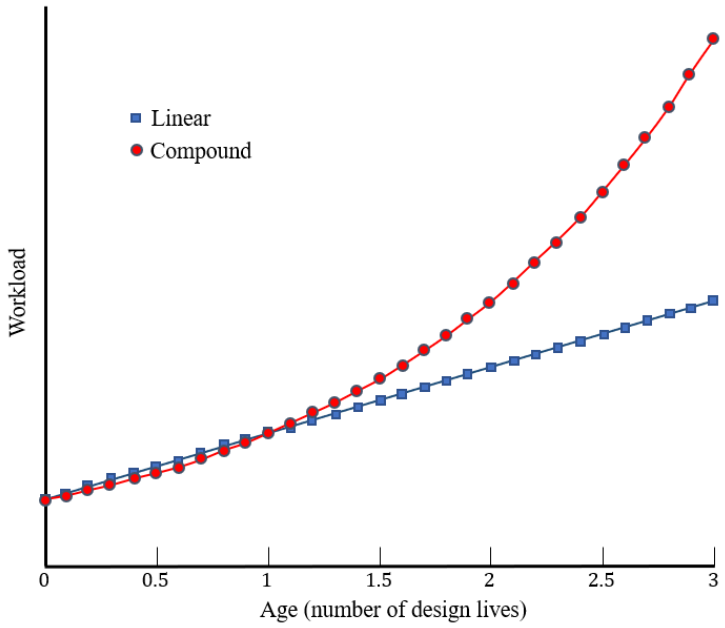

Figure 1.4: Predictions of linear and compound growth equations [11]

are devoting more and more attention to their maintenance capabilities. For example, General Electric Aviation, one of the biggest manufacturers of aircraft engines, adopted a new maintenance system that replaced its traditional design-based system. The company is currently selling not only aircraft engines, but also maintenance service that can monitor the structural health of engines in real time.

Another engine company, Rolls Royce, using onboard sensors and live satellite feeds, established an Engine Health Management (EHM) system to track the health of thousands of its engines operating worldwide. The company has dramatically reduced the maintenance costs of its customers, such as Boeing and Airbus. According to Johann Bordais[14], vice president of service and support for Embraer Commercial Aviation, "By replacing traditional inspection procedures such as general and detailed visual inspections and non-destructive inspections such as X-rays, eddy currents and dye penetrantless time would be needed to perform time-consuming disassemblies to gain access to inspection areas. The inspection times would come down to minutes instead of hours in some cases" (*Aug 12, 2016, online Aviation Week*)

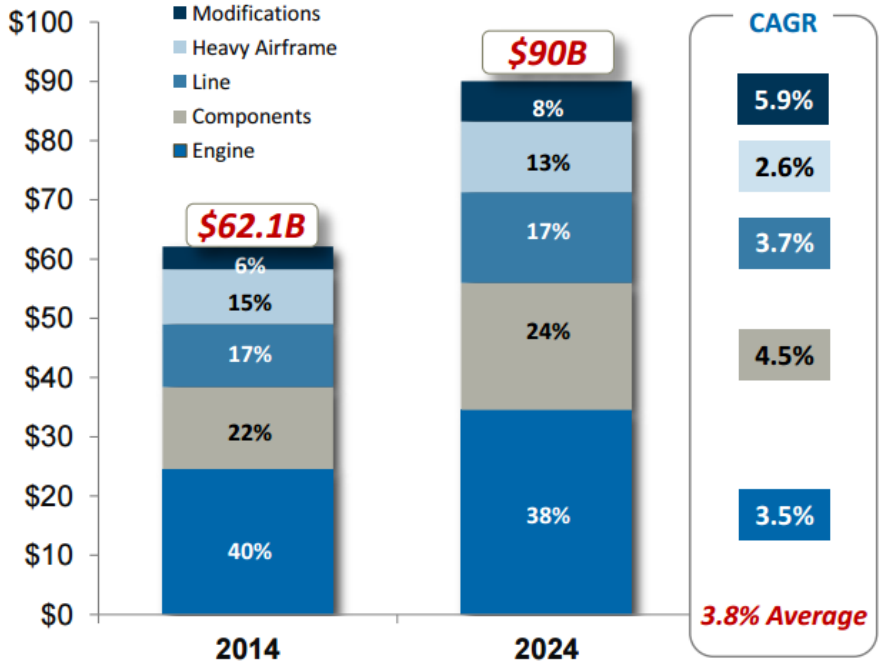

Figure 1.5: Global MRO Expenditures in 2014 and 2024 predictions (in $B) [13]

Other strong drivers of MRO, in addition to engines, are scheduling maintenance for components, predicted to be 24% of MRO expenditures in 2024, and heavy airframes, 13% of expenditures related to inspections that detect defects that potentially lead to structural failure. The two parts, maintenance for components and heavy airframes, are both related to structural maintenance and inspection scheduling. Thus, we can assume that 37% of MRO expenditures go to structural maintenance and inspection scheduling. SHM can impact this high potential MRO market reducing labor intensity of the schedule.

Motivating Question 2

To cover the uncertainty of a fleet, not an individual aircraft, design-based maintenance requires unnecessary expenditures. How can we reduce unnecessary expenditures on ensuring structural safety for aircraft operation?

This study has asserted that design-based scheduling needs to shift to demand-based scheduling for future generations of aircraft. The prohibitive cost also underscores the necessity of a paradigm shift. We could minimize the cost burden of unnecessary inspection and maintenance if we were able to control inspection and maintenance scheduling while recognizing the current condition of an aircraft.

1.2.3 Unacceptability of design-based maintenance for drones

In the near future, a large number of delivery or surveillance systems will consist of a vast number of autonomous drones that conduct aerial routine cycles from a smart warehouse to customers homes. During the cyclic routine, drones are exposed to cyclic loads caused directly by rotating propellers, or indirectly by forcing aerodynamic loads. Cyclic loads lead to the accumulation of damage from fatigue, which could cause catastrophic structural failure of the drones.

Motivating Question 3

Drones also require numerous checks and inspections that mitigate the weaknesses of current design problems. In light of the explosive growth and supply of drones, how can we control the safety of drone airworthiness?

Since drones fly above populated cities, the catastrophic failure of drones could cause an unexpected concatenation of incidents. To prevent the worse-case scenario, an intelligent algorithm of drones must monitor their health during operation. The algorithm should have a smart way to detect damage from fatigue and to estimate the remaining life of a part after it is damaged. As described in Figure 1.6, based on the analysis of the remaining life, a decision algorithm orders a drone to fly to a repair station after the drone aborts a current mission.

Figure 1.6: Health decision requirement for drones

1.3 Structural Health Monitoring

Aircraft manufacturers have expended a great deal of effort to meeting requirements by airline and government regulators (e.g., FAA, EASA) relating to low maintenance costs, high operational efficiency, and eco-friendliness. However, as aircraft structures always incur high maintenance costs, which ensure high operational efficiency and eco-friendliness, airlines have sought ways to control and maintain high efficiency and friendly aircraft; as a result, they have applied state-of-the-art sensor and IT technology to develop a system capable of instantly assessing defects in an aircraft structure. The largest aircraft manufacturing companies, Boeing and Airbus, are currently working on a road map for an SHM (structural health monitoring) system that will be installed on their aircraft in 2018 and 2020, respectively. Figure 1.7 shows the road map of the Airbus.

The SHM systems can shift the maintenance paradigm from design-based maintenance cycle to a demand-based maintenance cycle by monitoring and preventing the possibility of structural defects in aircraft. In some cases involving fighter aircraft, the time required for inspection decreases by up to 44%, as shown in Table 1.2. Major research programmers in this area suspect that up to 20% of current maintenance and inspection costs of civil and military transportation can be saved [16].

The development of SHM systems affects not only maintenance costs but also design and

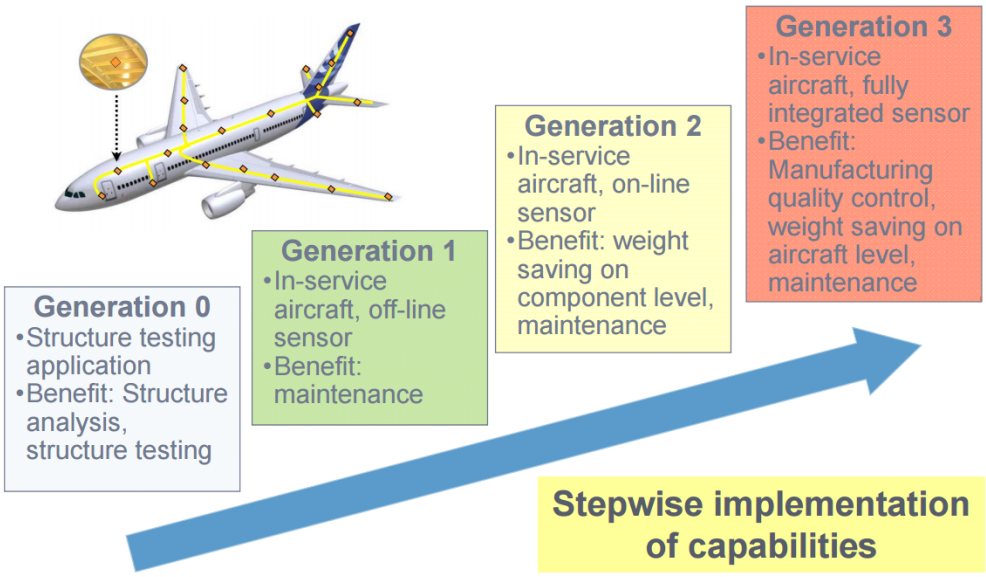

Figure 1.7: SHM Development and Application Roadmap for Airbus [15]

fabrication. If safety is ensured in the long-term operation in SHM-embedded aircraft fleet, the paradigm of structural design will be able to shift from a high-demand safety factor to a design with less-demand safety factor. After all, sensors in the SHM system can inform us about unexpected structural failure while the aircraft is in operation, leaving little uncertainty that must be dealt with during the design stage. While operating, however, an SHM system must ensure design safety that complies with airworthiness regulations, which demand static, fatigue, and damage tolerance analysis. To satisfy the safety requirements of an aircraft structure, the SHM should use an FEM that can represent the aircraft appropriately applying load conditions that the aircraft undergoes to determines sufficient fatigue life and damage tolerance capabilities. When the FEM can mirror and predict aircraft performance over the life of its corresponding physical twin in a simulation, we refer to the FEM as a digital twin," the key parameter of SHM.

1.4 Roles of Digital Twin in SHM

A digital twin is a virtual representation of an aircraft used in health monitoring to predict its remaining life or to diagnose the current status of its health. GE, the one of the leaders in the use of

Table 1.2: Expectation of inspection time effort for a modern fighter aircraft [16]

Inspection type	Current inspection time (% of total)	Estimated pontential for smart systems	Time saved (%of total)
Flight line	16	0.40	6.4
Scheduled	31	0.45	14.0
Unscheduled	16	0.10	1.6
Service instructions	37	0.60	22.2
	100		44.0

the digital twin for the purpose of monitoring service, defined it as "a living model of the physical asset or system, which will continually adapt to changes in the environment or operations and deliver the best business outcome" [17]. This definition is the one most commonly used in various fields. NASA and the U.S. Air Force predicts that the digital twin will become more essential technique for the future generation of aircraft.

According to a paper from E.H. Glaessgen and D.S. Stargel [8], the majority of future aircraft will become increasing lighter while being subjected to higher loads and more extreme service conditions than the current generation of aircraft. Thus, current approaches for certification, fleet management, and sustainment will be unable to address the more extreme requirements of future vehicles because they are largely based on statistical distributions of material properties, heuristic design philosophies, physical testing, and an assumed similarity between testing and operational conditions. Therefore, the historically based design approach might not be suitable for future aircraft, which calls for a new approach that assures the design safety of future aircraft. The approach must be capable of capturing unexpected loading during operation and evaluating it instantly for stress and fatigue failure (crack initiation) and crack propagation. With such capabilities, the SHM framework with the digital twin, an on-board integrated vehicle health management system, will be essential for future generations of vehicles.

1.5 Challenge of current digital twin method

In the on-board framework, the digital twin needs to use a finite element model with which we can verify the safety of airworthiness by stress evaluation, fatigue analysis, damage tolerance analysis, and so on. One big problem is that an airworthiness analysis that checks structural safety requires different fidelities of finite element models. Stress and fatigue analyses for a global aircraft requires a coarse mesh. A damage tolerance analysis, however, should have a very fine element model that demonstrates the phenomenon of crack propagation. Thus, to have the functionality of damage tolerance design, the digital twin should be a finite element model that is meshed with remarkably fine element. For example, while the typical wing span of an aircraft is 60 m, a standard surface flaw size is 3.175 mm. To simulate crack propagation in a wing, the element size needs to be 1/100th the flaw size; the element number in the wing would then be in the millions, which is not suitable for our purposes of the on-board framework structural health monitoring.

A contradiction of the digital twin:

- Diagnosis requires a coarse mesh for determining the status of the each element in the global size of the system.
- Prognosis requires a fine mesh for analyzing the severity of the crack regarding the fracture mechanics for a particular area with a crack.

1.5.1 Previous studies for the contradiction of digital twin

In a technical report, Scott C. Forth[18] proposed a hybrid numerical analysis method for structural health monitoring. The report developed a new hybrid surface-integral-finite-element numerical scheme that entails modeling a three-dimensional crack propagating through a thin, multi-layered coating. The new hybrid method enables the analysis of the incremental growth of three-dimensional non-planar cracks. This method uses a fine mesh at the surface, where the appearance

of cracks is highly likely, and a coarse mesh at the plane of symmetry, where the likelihood of reducing computation time is quite low. That is, this method still requires a large amount of computation time because it involves monitoring the global size of an aircraft. Although Forth used 3-D mesh to represent crack propagation, which is good to observe more detail phenomenon, the 2-D mesh is more desirable in the aerospace field because we generally use it for the global aircraft FE model that consists of thin skins.

In another study, S. Gopalakrishnan and his co-authors[19] proposed a spectral FE method that originally solved a wave propagation problem. Since the sizes of the elements should be of the same order as the wavelengths of the signals, the detection and diagnosis of an initial crack requires a reasonably fine mesh that is smaller than the wavefront length. This approach uses an integral transform method to solve FEM in a different way. Using wave propagation, it is highly accurate for crack detection and propagation analysis. Also, computational time is shorter than that of the conventional FEM. However, this method is more suitable as it uses active control SHM; that is, it more likely requires an embedded active actuator to generate a wavefront signal. This method also transforms a dynamic load in a time series to a frequency domain, so its application for a conventional FEM tool is difficult. Moreover, in the case of modeling complex geometry, this method has less flexibility than conventional FEM.

1.6 Problem Formulation

1.6.1 Research Objective

Although the development of the digital twin was prompted by the need for a method of diagnosing the current system or the state of the physical object and preventing failure from crack propagation, the use of the digital twin has become more widespread since machine-learning based techniques were introduced. Using a machine-learning algorithm and advanced mechanical engineering theory, this study seeks a solution to address the size problem of the digital twin for crack propagation.

To achieve this goal, this study introduces and validates a new digital twin method that manages all safety criteria. To understand the purpose and the role of the digital twin, we must study the process of design safety validation. The details of this process will be described in Chapter 2, but not before discussing the main flow of the process during the development of aircraft. The process for safety validation during the development is shown in Figure 1.8. The process has been the standard for more than 50 years.

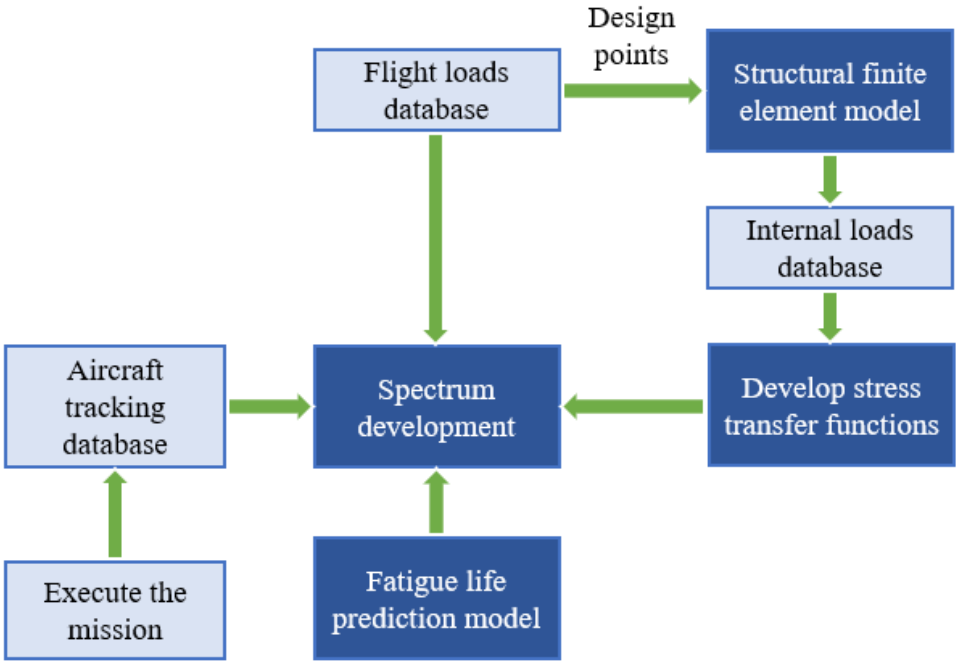

Figure 1.8: Schematic of the current life prediction process [20]

The process begins with the development of the external loads on an aircraft, which are placed in a database that is based on a mission analysis. A stress evaluation group applies the loads to the structural finite element model that represents a global model of the entire aircraft. They analyze the ultimate stress criteria and calculate the margin of safety for the static load. At the same time, the load group develops the internal loads in the airframe for each design load case and develops a dynamic spectrum from the database. The fatigue analysis and damage tolerance experts utilize these internal load cases and relate them to the external loads for local stresses with details such as

fastener holes, cutouts, and fillets. Such a model sometimes resembles a very fine element model for a detailed analysis or a simple mathematical model for a non-complex case. For the dynamic load generation that is needed by the fatigue analysis, they apply stress that is from static analysis to the loads in the flight load database to develop a stress spectrum at each point of the critical design part of the airframe [20].

This whole process is quite complicated and requires the collaboration of many teams and their members. Generally, the safety evaluation of a small business jet could require more than 100 specialized engineers over the course of several years. This study attempts to simplify such a complicated process with a new digital twin method and create it in a framework that can be mounted on an aircraft.

Research Objective

Develop an on-board intelligent framework that can determine the requirements of inspection or maintenance by analyzing airworthiness criteria with a new digital twin method while monitoring the current structural health condition.

To develop this framework, we need to implement the same series of processes used in the design stage for aircraft in operation with actual loads in a digital twin, which is a finite element model as the representative model of the aircraft. It is necessary that we build a system that can derive variable results by performing basic stress analysis, advanced fatigue analysis, and damage tolerance analysis for each independent aircraft in a given unique environment. This system must not only predict the fatigue life in the current state by acquiring and learning the loads experienced by the actual aircraft, but also enable the prediction of the future state by estimating the future load spectrum based on the learned history. Then the intelligent framework can determine the requirements of inspection, or maintenance, based on the prognosis of the remaining life of

its parts, while monitoring structural health through embedded sensors. Development of such a complex framework requires a comprehensive system that can be connected and interactive after the accomplishment of the following sub-objectives.

- To develop a new digital twin method that can be used for multidisciplinary purposes to identify and validate structural safety based on airworthiness certification criteria
- To establish an on-board diagnostic method for identifying a critical location vulnerable to the initiation of a crack based on the stress analysis for static loads and the fatigue analysis for dynamic loads.
- To retrieve crack propagation theories for an on-board prognosis method that are capable of scheduling inspection and maintenance based on the current conditions of an aircraft.
- To improve the algorithm of load spectrum generation for forecasting a future load spectrum.

To focus on the development of a framework and its sub-algorithms, this study presents a simplified example. It makes the following environmental assumptions to demonstrate the functionality of the on-board framework and then tests and validates the framework under the following assumptions for NASA CRM (common research model), a hypothetical virtual aircraft:

- The aircraft is a conventional transport aircraft that demonstrates the framework. For this purpose, the NASA CRM represents the base model of an imaginary aircraft.
- The imaginary aircraft has sensors embedded on its wings. The purpose of the sensors is not for active SHM that can detect an actual crack. Instead, they are measurement tools such as a strain gauge or fiber optic sensors.
- Sensors transfer accurate load data to the framework from external computation that converts strain to external loads.

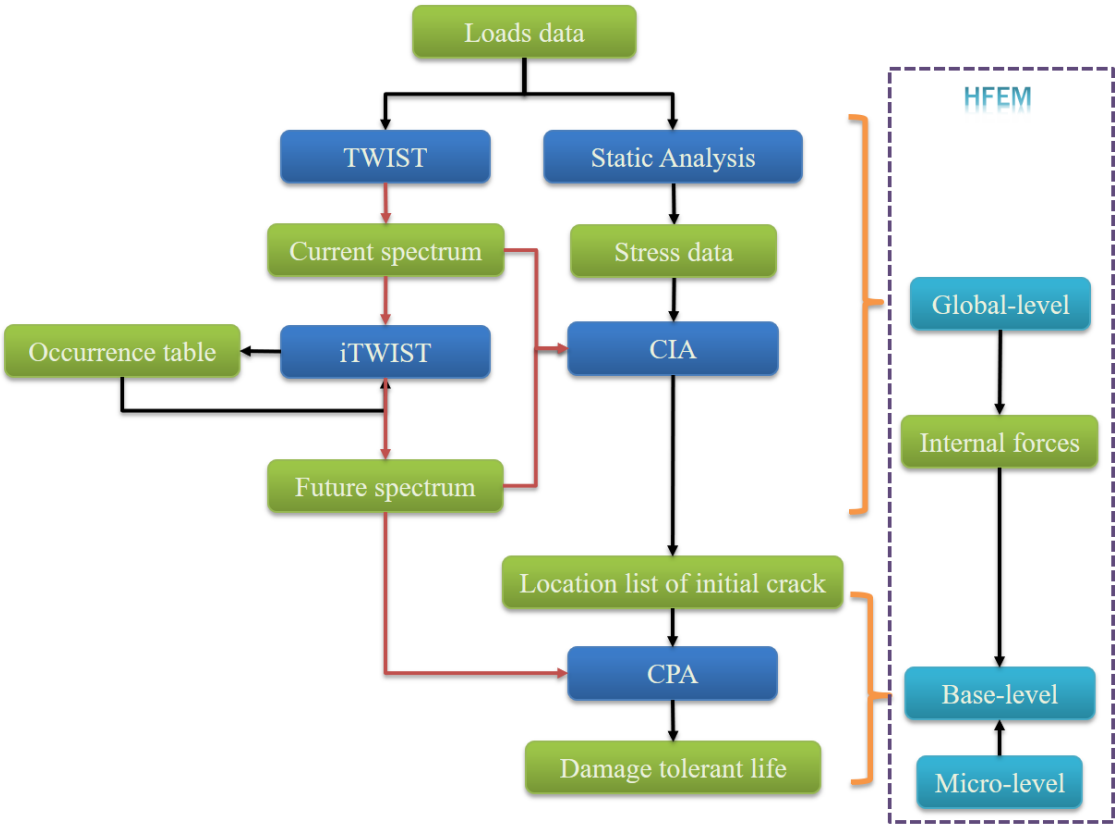

Figure 1.9: The main flow diagram of the on-board framework with the HFEM application

- This study uses aerodynamic loads calculated from GT-QHL [21], a simple load-generating program that assigns an acceptable load condition for a common aircraft in the absence of external loads for real load cases of a particular aircraft.

Based on the research objective and assumptions, Figure 1.9 shows the computational flow for fulfilling the research objective for the entire framework with sub-objectives. In the flow chart, the green boxes represent the datasets of inputs and outputs, the blue boxes represent sub-programs and methods, the light-blue boxes in the HFEM(Hierarchical Finite Element Model) section are the digital twin level that will be discussed in the next chapter, the black arrow indicates the flow of the ASCII data, and the red arrows indicate the flow of the dynamic loads.

At the traditional design stage, checks of airworthiness primarily entail the use of two FE models: the global finite element and local detail finite element models. Since the SHM has to

evaluate airworthiness as a process in the traditional design stage, the SHM framework with digital twin requires that a simultaneous global and locale finite element analysis. A full FE model with very fine meshes with a detailed design that represents all components of the airframe could be an option for a simultaneous analysis in digital twin. However, the full FEM with fine meshes requires considerable computing power, which is not even possible at the design stage because of considering the thousands of load cases. Thus, this study proposes an integrated FE model, a new digital twin method in the SHM system. Although Chapter 1.5.1 introduced representative approaches such as the hybrid mesh method and spectral FE, which could solve the problem, neither is suitable for this study.

To solve the contradiction of the digital twin that requires multi-fidelity finite element models, we could apply hierarchical finite element models separately, depending on their purposes, to achieve an adaptable mesh size and computation time. For example, Figure 1.10 depicts the stress analysis for aerodynamic loads and crack initiation analysis performed using a global-level model and the simulation of crack propagation for a specific area performed using a base-level model. In addition, in the case of anisotropic material, we might want to observe microscopic behavior. Therefore, the hierarchical models require additional micro-models that can represent the lamina, or fiber, and the matrix.

1.6.2 Research question 1

In the scenario of the design stage of an airworthiness check, we recognize that the process requires several FE models. For example, the load conditions are first checked in global FE model to learn about stress distribution. Then, from the fatigue analysis, we select the critical locations. For crack prorogation, we need fine mesh FE models to calculate stress intensity factors.

Likewise, this framework requires different mesh types of FE models such as global-, base-, and micro-levels inside of the dotted box in Figure 1.9. For the independent FE models, let us assume that a comprehensive method successfully interconnects the FE models, thus acting like

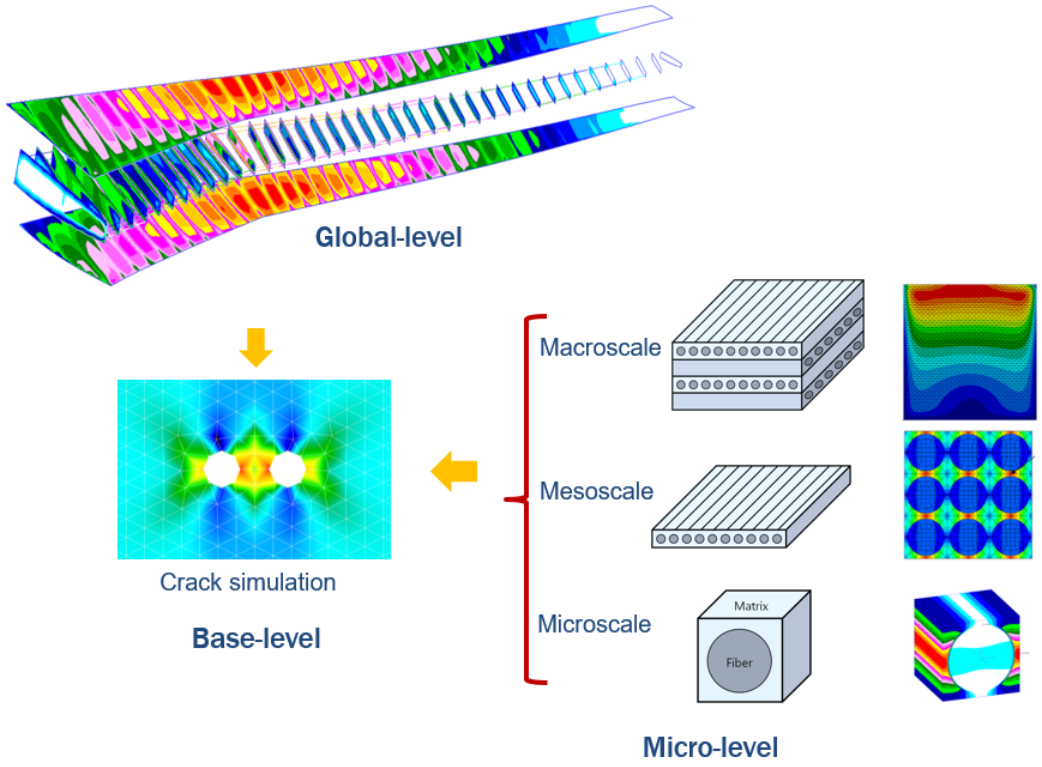

Figure 1.10: The basic idea of a new digital twin method

one FE model, then we can use the comprehensive method as a new digital twin. As we have discussed in the previous chapter, for the comprehensive method, the hierarchical finite element method (HFEM) is proposed as a new digital twin method with two FE models that are connected for an isotropic material or three FE models connected for an anisotropic material.

To act as a digital twin, the hierarchical FE models, which must be connected, are needed to transfer data such as loads or stress. For example, the static stress analysis needs to be conducted in global-level FE models. Then the stress information must be incorporated into the CIA (crack initiation analysis) and the CPA (crack propagation analysis) models. The CIA and CPA modules should able to increase or decrease the intensity of load spectrum from iTWIST(inverse transport wing standard spectrum) by the ratio of stress to match up the intensity of stress on the location of elements. Therefore, in the on-board framework, the modules are required to work together seamlessly.

Research Question 1

How can independent FE models with various fidelities interconnect and transfer load data acting as one interacted FE model?

Integrating all FE models, which have variable fidelity, into one FE model is a complicated problem, as FE models also have variable dimensionality. External loads, which would be subject to the global FE, should be distributed to the local FE with appropriate methodology. Thus, to integrate FE models in HFEM, research Question 1 raises the following technical questions.

Technical Questions about RQ 1

- External loads need to be applied to the aircraft wing. Information from the sensors are point loads, but the wing is subjected by pressure force. How should the external loads be applied to the aircraft wing in global-level FE?

  - The point forces can be expressed as pressure force with MPC(multi-points constraints) element in global-level FE. Detail techniques will be discussed in the load transfer method section.

- External loads are introduced into the global-level model with coarse mesh, but the crack propagation analysis must be conducted on a base-level model meshed with a fine element. How can the external loads be transferred from the global- to base-level model?

  - From the result of global-level FE, we will have internal forces that caused by the external forces. The base-level FE will use the internal forces for the crack propagation analysis. The transferring solution will be discussed in the interconnection method.

- To use composite material in one representative FEM, we must account for both macromechanical failure, which can result from the delamination or static failure of a layer or layers, and micromechanical failure, which can result from the delamination or static failure of the matrix or fiber. However, Analyzing micromechanical failure in a macro mechanical FEM is not possible because the models are all independent with varying dimensionality, raising the following question: What is an efficient way of viewing micromechanical attributes in an HFEM(one representative FEM) that is a macromechanical model?

  - This study will use a scale factor introduced by SIFT(strain invariant failure theory) to represent the micromechanical behavior of composite material for a global model with macromechanical behavior. The following section, Composite Mechanical Property, will introduce the theory and scale factor, is an amplification factor.

Summary of RQ 1

If an HFEM that incorporates all levels of the FE model is obtained by the methods described above, we must determine if this HFEM works properly. For verification, the HFEM needs to prove the functionality of the digital twin; that is, prove that the digital twin represents a system or a part with the same results as if there is only one FE. The following lists the factors from HFEM required for each module in the framework.

- CIA: material properties for fatigue analysis, stress results for the global-level model
- CPA: material properties for crack growth, stress results for the base-level model, CIA results

Since the CIA and CPA use only stress data from a finite element model, the stress that comes out from the result of HFEM can be an indicator for the validation of its functionality.

Hypothesis for RQ 1

If the hierarchical finite element method (HFEM) can derive integrated results by connecting independent finite element models, it will calculate an identical stress value as that of a general finite element method that uses one model.

By answering the technical questions, we have seen how HFEM can overcome the dimensionality problem of the FE level. We also know that CIA and CPA modules that use HFEM require only stress data. Therefore, an indicator of whether HFEM is working properly is stress, which needs to be verified with the results of a reliable source such as a conventional FE tool. For the validation of HFEM, Chapter 3.5 presents a flat plate problem that can be depicted as a simplified aircraft wing. The chapter will present not only the validation, but also the actual application method of the integrated algorithm between global- and base-level models, such as the technical method for finding an element, its corresponding nodes, and corresponding forces around the nodes from the large quantity of ASCII data in the FE results file.

1.6.3 Research Question 2

We have assumed that load cases are imported from an external analysis correlated with embedded sensors. The series of static loads need to be multiplied with a non-dimensional standardized spectrum that constitutes accumulated historical data for a specific aircraft. The historical data for the spectrum are mainly about the response of 1g load and exceedance gust or maneuver. A representative historical spectrum is TWIST (Transport WIng Standard specTrum), widely used when the historical data for the aircraft is not available. We will present a detailed background and methodology for the TWIST in Chapter 6, Future Load Spectrum Generation. Briefly, the TWIST generates a spectrum based on the accumulated history from ten conventional transport aircraft. However, for the purpose of this study, aircraft safety should not be examined from fleet-based

data that involve high variance. Instead, this study requires an investigation of unique load conditions that an aircraft will most likely experience.

Research Question 2

How can we use currently accumulated load data to generate a future load spectrum that can represent unique load conditions that an aircraft will experience?

The TWIST is a random load-generation algorithm based on a study of ten historical transport aircraft. Recorded historical information is stored in a table format that serves as a basis for random selection of the intensity of cyclic loads for the generation of a load spectrum. Thus, the random collection of cyclic load points and their frequencies depends on the data collected from the ten aircraft listed in the table. Then the series of loads generated from the table are applied to the new conventional transport aircraft under the assumption that it will exhibit similar flight behavior. For our framework, we also utilize the method of TWIST, but not the table from the ten aircraft. Instead, we use a table that will be created by a specific loading from an aircraft in which the framework will be installed. Since the load data will be collected from only this aircraft, the load occurrence table will be unique for this aircraft. Therefore, the load spectrum generated from the occurrence table eventually becomes a very suitable load spectrum unique to that aircraft. Chapter 6 will expand on this research question with a more detailed algorithm for this method and its application.

Hypothesis for RQ 2

The TWIST has widely used an algorithm to generate a standard fatigue spectrum based on the historical gust occurrence data. If the gust occurrence data is replaced with the exceedance data from embedded sensors in a specific aircraft, the unique spectrum will be generated for a specific aircraft by the TWIST algorithm.

1.6.4 Research Question 3

The CIA (crack initiation analysis) must first exploit the load spectrum generated from iTWIST to estimate the critical locations. For compliance with the airworthiness criteria, the selection of critical locations must be decided by a fatigue analysis, which is generally depends on the characteristics of the ductility of a material. High ductility material usually has a high cycle fatigue life. In this case, a suitable option is the S-N approach. In other words, the ε-N approach is generally low ductility material that exhibits a low cycle fatigue life. We will discuss details of the $S - N$ and the $\varepsilon - N$ theories in Chapter 4. These methods, which have been used for over 100 years in the aerospace field, are well established. Based on conventional methods, we prefer to create a simple program that can estimate critical locations while an aircraft is in operation or on the ground. Moreover, in the framework, the CIA must operate within the new digital twin method, the HFEM introduced earlier. Since the new digital twin uses several FE models, the module of the CIA requires cooperation within a complex environment. Eventually, the CIA has to reliably estimate and select critical locations that will be required to do a damage tolerance analysis.

Research Question 3

To estimate critical locations, what method should be used and how will it work with the new digital twin method?

The CIA module calculates the remaining life of the aircraft and its parts by the $S - N$ or the $\varepsilon - N$ approach. The former, the stress-life approach, is generally used on a material with a high-cycle fatigue life, such as the aluminum alloy. In the case of a low fatigue life of generally less than 1,000 cycles, the latter, strain-life approach, is a suitable option. This study examines both approaches, but focuses more on the high cycle fatigue analysis for the aluminum alloy. Thus, the development of the CIA module is based on one of the fatigue analyses that depends on the type of material for on-board purposes while working within HFEM. The purpose of the developed program is to identify critical locations, an approach that differs from conventional fatigue analysis tools developed for design safety. Theoretically, however, they share the same objective which is to calculate fatigue life cycles, so the outcome of the CIA module should be similar to conventional software for estimating the remaining life.

Hypothesis for RQ 3

Since the CIA module has been developed for on-board purposes operating with HFEM and conventional fatigue analysis tools theoretically share the method for complying with airworthiness, the CIA and the tools will show similar fatigue life results under the same conditions.

To validate the Hypothesis for RQ3, Chapter 4.6 will propose a simple example and explore the results of validation. In the chapter, we will validate the CIA module by comparing the calculated fatigue life with the results from a commercial fatigue analysis tool. In the HFEM, for the selection

of theories that depends on the fatigue characteristic of material, crack initiation can be analyzed by either the stress-life or the strain-life approach, both of which are generally used for analyzing fatigue life during the design stage of an aircraft. Although many aircraft manufacturers have their own tools for this analysis, some commercial tools are available for the purpose of design validation. One tool, MSC.Fatigue, can calculate the fatigue life of a system or its parts. Since MSC.Fatigue is widely used in many industrial fields, it can be a benchmark solution for the module developed in this research.

Unlike the conventional analysis tool at the design stage, on-board crack initiation tools need to be targeted to a specific purpose. Further, the process of analysis needs to be automatic, that is, without any human interaction. Because of this special functionality, the CIA in this study is designed to calculate fatigue life without any input from a human. The required data such as spectrum, static stress, and etc. will automatically feed into CIA module for each element. And, once fatigue life is automatically calculated after a flight or a certain period of time, it will incorporate with the global-level of the HFEM to decide which element will be initiated for crack propagation.

1.6.5 Research Question 4

The CPA module must be capable of analyzing crack propagation in the base-level model by accounting for the phenomena of crack closure and opening. Calculating crack propagation requires a complex analysis because it must account for several variables such as stress, the shape of a crack, the size of a crack, the direction of loading, the opening mode of a crack, and properties of materials. Without the consideration of various variables, the analysis of crack propagation with a simple da of dN curve generates an inaccurate estimate of life cycles and often too conservative results. Thus, the CPA module should provide a detailed analysis that is able to account for the characteristics of a crack.

Research Question 4

How can on-board CPA analyze crack propagation by compiling advanced theories about the phenomenon of crack growth, closure, and openness to guarantee the fidelity of airworthiness

Even in the early design stages, a crack propagation analysis is a complex task. Therefore, this study constructs an algorithm under several assumptions:

- A crack opening is a mode I case
- The tip stress concentration does not vary
- The material property is ductile isotropic

Although under these assumptions, we slightly simplify the analysis, we must still account for a number of phenomena that we cannot ignore. The most important phenomenon for crack propagation is the crack closure and opening because of the plastic region that sometimes forms at the crack tip. Chapter 5 of this thesis analyzes a simple example for the crack propagation with a crack closure and without crack closure.

The CPA module also requires validation, which will show that it calculates reasonable cycles of crack propagation. Generally considered a standard tool for aircraft manufacturers at the design stage, the NASGRO, developed by NASA, is the benchmark used in this study.

Hypothesis for RQ 4

The results of crack propagation from the CPA that is developed for on-board purposes by integrating with the HFEM will be similar to the results of the analysis tool for the proof of airworthiness in the design stage.

Chapter 5.4 will present the results of validation in a comparison of the results of the CPA module to those from NASGRO. In the chapter, we will discuss about how the crack closure phenomenon affects the crack propagation cycles and how an advanced theory can be applied in a real example. The simple algorithm of crack calculation for the crack growth with closure effect is also provided in the Appendix B.

CHAPTER 2

FUNDAMENTAL BACKGROUND THEORIES

2.1 Airworthiness for Structural Safety

Figure 2.1: Structural design requirements of aircraft

To explain the roles of the digital twin and the on-board SHM framework, this chapter introduces structural design for airworthiness with Figure 2.1. The digital twin requires a finite element model with which we can analyze the static strength, fatigue, and damage tolerance for the SHM framework to fulfill airworthiness requirements. The structure of civil aircraft designs must comply with the Federal Aviation Regulations (FAR) and that of military aircraft must meet Military Specifications, Mil-spec. Examples of FAR categories for commercial aircraft are listed below, but this study focuses on FAR Part 25.

- Federal aviation regulation (FAR), VOL. III, PART23 AIRWORTHINESS STANDARDS:

NORMAL, UTILITY, AND AEROBATIC CATEGORY AIRPLANE

- Federal aviation regulation (FAR), VOL. III, PART25 AIRWORTHINESS STANDARDS: TRANSPORT CATEGORY AIRPLANE
- Federal aviation regulation (FAR), VOL. III, PART27 AIRWORTHINESS STANDARDS: NORMAL CATEGORY ROTORCRAFT
- Federal aviation regulation (FAR), VOL. III, PART29 AIRWORTHINESS STANDARDS: TRANSPORT CATEGORY ROTORCRAFT
- JAR(Joint Airworthiness Requirements)- EUROPEAN COUNTRIES

With regard to the standard design of aircraft that meet airworthiness requirements, FAR suggests methods for both design and analysis as well as design criteria, indicating that that the digital twin and the FE model must undergo analyses of static and ultimate strength, fatigue, and damage tolerance to satisfy the requirements of FAR. Fatigue analysis, which identifies initial critical locations of possible cracks, typically advances to damage tolerance analysis.

2.2 Aerodynamic loads

To verify the safety of a design, aerospace engineers use the results of static stress analysis under an ultimate load which is the limit load multiplies by a safety factor of 1.5. Static stress analysis requires mainly three input categories: geometry, material properties, and aerodynamic load (static load). Geometry is constructed from CAD modeling such as CATIA and Unigraphics, and its format is usually Parasolid or IGES. The geometry can be meshed with an appropriate size or shape of an element, both of which depend on their purpose. The meshed geometry, the finite element model, acts as a digital twin in the SHM during the process of airworthiness analyses. During the analysis, the digital twin is subjected to aerodynamic loads defined by a limit load for dynamic analysis or an ultimate load for static analysis. The loads in the design stage are generated

by an aerodynamic group for a number of flight conditions based on V-n diagram, Figure 2.2. In the case of the digital twin, loads are actual loads calculated by sensor information. The actual loads, however, fall with the categories of the design loads described below.

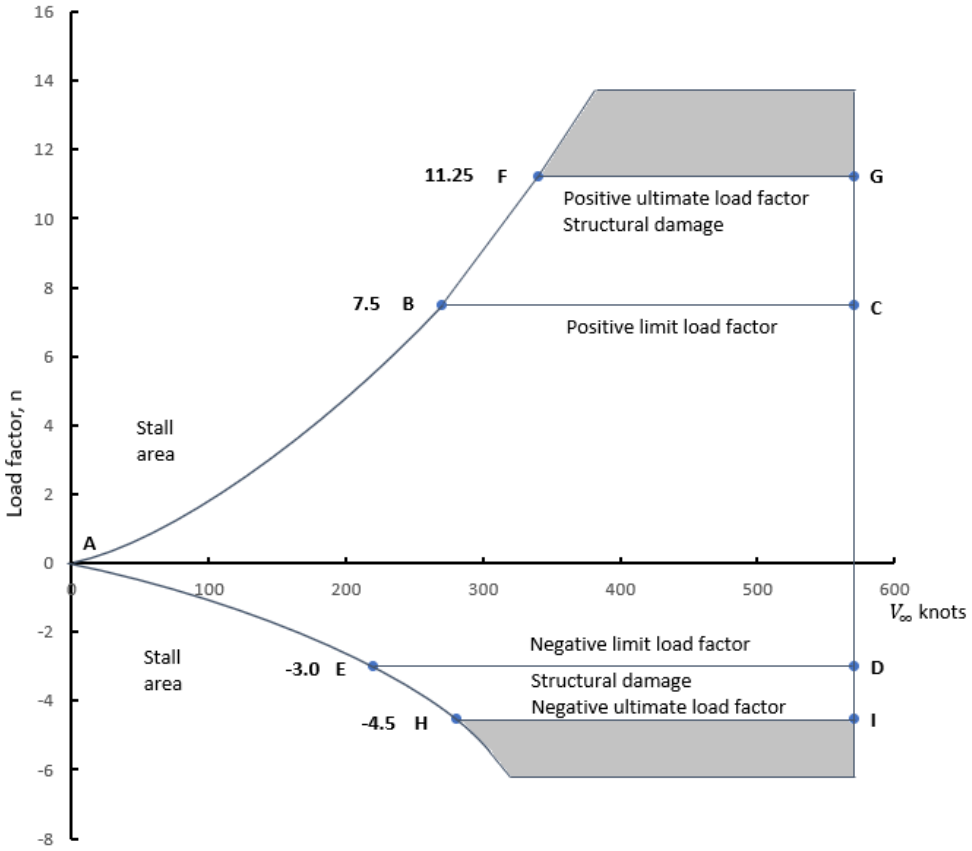

Figure 2.2: V-n diagram for a typical jet trainer aircraft [22]

Loading conditions from the envelop described in Figure 2.2 are all 1g conditions that corresponds to mean stress in stress spectrum. Gust or maneuver conditions are considered as shifted curve of the V-n diagram which corresponds to amplitude stress in stress spectrum

- Limit loads: maximum loads expected in service. FAR Part 25 (and most other regulations) specifies that there be no permanent deformation of the structure at limit load.
- Ultimate loads: limit loads times the safety factor, which Part 25 specifies as 1.5. For military aircraft, researchers may set the safety factor to as low as 1.20 while composite sailplane

manufacturers may use 1.75. The structure must be able to withstand the ultimate load for at least three seconds without failure.

During operation, aerodynamic loads are changed by maneuver or gust condition, but must stay in the envelope described in Figure 2.2. In other words, the aircraft designed by the envelope will be experienced any combination of load condition in the envelop, but the critical condition might be appeared on the line of envelope. Thus, to ensure the structural safety, various loading conditions, specially conditions on the envelope, must be accounted by following the type of aircraft operation. To simplify the environment for the analysis of the framework, however, this study will use one loading condition by assuming that it is the most critical loading condition for fatigue standpoint for a study purpose. The aerodynamic loads and constraints are described with six degrees of freedom, three translations, and three moments for the finite element model that is utilized in this study.

2.3 Stress

This section will provide a detailed background of theories of stress, its corresponding strain, and constitutive laws for various types of material properties. For the analysis of stress by mathematical approaches, we generally assume that material is elastic, isotropic, homogeneous, and infinitely divisible without changes in properties. By adding an external force to an object made of a material, we can cause deformation by exerting an internal force through the inside of the object that is distributed across the exposed surface. For example, the Figure 2.3 illustrates a general loaded solid body. To determine the state of stress at point Q in the object (a), we expose an isolated section. In (b), the arbitrary selected section that is oriented by surface normal x establishes the yz plane. Both external and internal forces remain across the isolated section. In the general case, internal forces are not uniform, but we assume that the distribution at a point in the section will have components in the normal and tangential directions in which the units of the internal

force distribution are the force per unit area. The force distribution for the normal direction is referred to as normal stress, σ, and that for the tangential direction is referred to as tangential stress, (c). Normal stress is also regarded as tensile stress when it is forced outside of the surface and compressive stress when it is forced onto the surface [23].

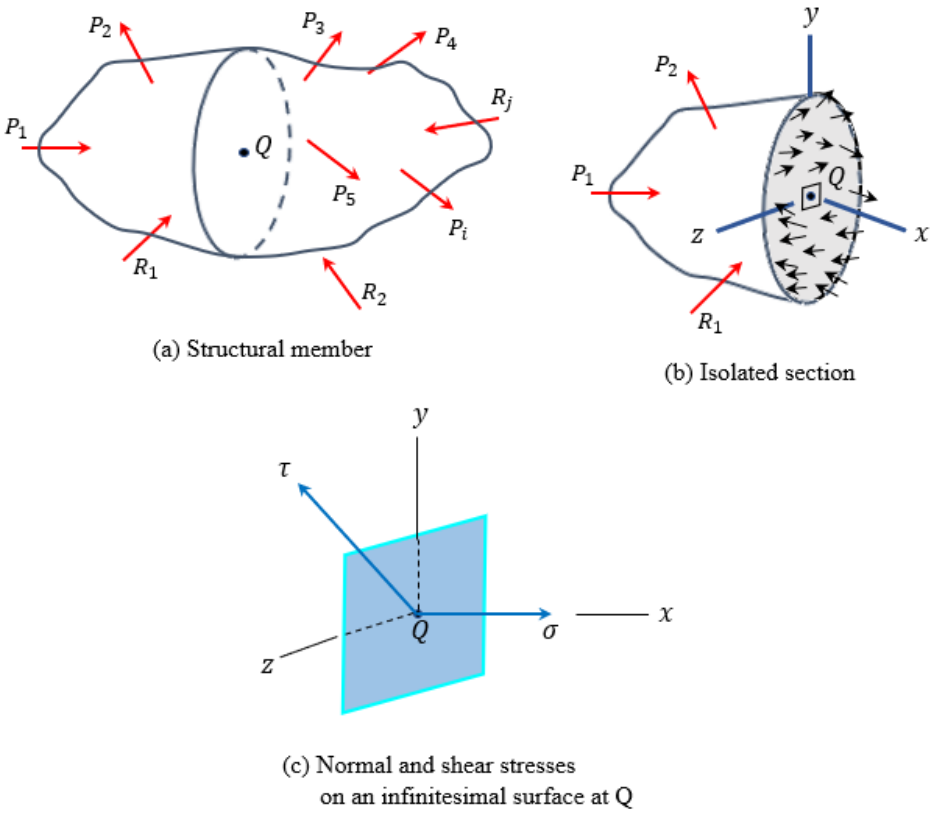

Figure 2.3: General loaded solid body [23]

In the previous example, the normal stress is expressed as an internal force distribution per unit area; thus, we can obtain Eq. (2.1) for the magnitude of stress.

$$\sigma = \frac{P}{A}, \tag{2.1}$$

where A is the cross section and P is the applied axial load. The equation is derived under a certain condition that stress is uniformly distributed over the cross section. The case of non-

uniformly distributed forces (e.g., a case in which the load does not act as the centroid of an object) requires a more complicated analysis. Sometimes, even the axial load at the centroid does not form uniformly distributed forces because of non-uniform geometry such as holes and tapers. In this case, the load is transmitted through the non-uniform geometry while producing high localized stress, referred to as stress concentration. The stress concentration is a very important factor for fatigue analysis and it is highly correlated with geometrical shape. Young [24] listed various examples of stress concentrations and stress formulas based on a study in a book by Raymond Roark [24], *Roarks Formulas for Stress and Strain*, a reference commonly cited in many studies and software packages for structural analysis.

We have discussed normal stress established for the normal direction to the plane of an isolated section. For Cartesian components, normal stress can be established for the x, y, and z directions. Then, net shear stress is also resolved into components. Therefore, in general, a complete state of stress is defined by nine stress components: $\sigma_x, \sigma_y, \sigma_z, \tau_{xy}, \tau_{xz}, \tau_{yx}, \tau_{yz}, \tau_{zx}$, and τ_{zy}. Figure 2.4 shows the states of stress at a point described by three mutually perpendicular surfaces for the nine stress components. In the diagram, the 1, 2, and 3 coordinate systems correspond to the x, y, z coordinates, but here after, we will refer to the $1, 2, 3$ systems.

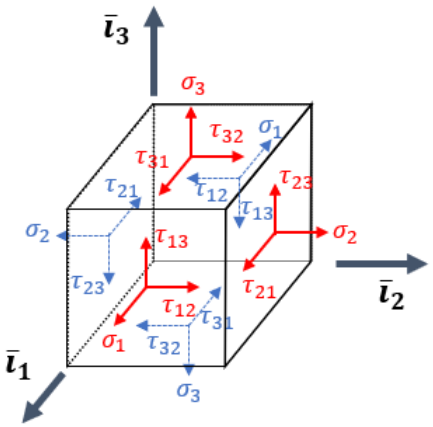

Figure 2.4: Stress components acting on a differential volume element [25]

The nine stress components can be reduced by force and moment equilibria. To show the

reduced stress components, Bauchau and Craig [25] explain the equilibrium equations in their first chapter. The results produce the following equations.

$$\tau_{23} = \tau_{32}, \qquad \tau_{13} = \tau_{31}, \qquad \tau_{12} = \tau_{21}. \tag{2.2}$$

These equations correspond to

$$\tau_{yz} = \tau_{zy}, \qquad \tau_{xz} = \tau_{zx}, \qquad \tau_{xy} = \tau_{yx}. \tag{2.3}$$

The reduced stress components for three-dimensional states are now six components: σ_1, σ_2, σ_3, τ_{12}, τ_{23}, and τ_{31}. The six independent stress values are often arranged in a 3×3 matrix for practical purposes as follows:

$$\begin{bmatrix} \sigma_1 & \tau_{12} & \tau_{31} \\ \tau_{12} & \sigma_2 & \tau_{23} \\ \tau_{31} & \tau_{23} & \sigma_3 \end{bmatrix} \tag{2.4}$$

So far, the principal requirements of normal stress are that geometry remain uniform throughout its volume, that loads be exerted through the centroids of the cross sections, and that the material be homogeneous. As previously mentioned, if the geometry is not uniform, we need a special factor such as the stress concentration factor. In addition, if the load does not act on the centroid of the cross section, axial stress should be combined with other stress contributors such as bending stress. The framework of this study will use finite element models that calculate equivalent stress, which is the combined representative stress for these factors. Very often, however, stress for a specific part is calculated separately in the global finite element and then analyzed in detailed

stress surveys. This is because the global FEM is often not able to capture a phenomenon such as stress concentration for a complex geometry of detail part.

2.4 Strain

Strain is the amount of deformation under tensile or compressive loading and is measured by a static test. For the test, an ASTM standard tension specimen with a diameter of 0.505 inch is generally used. As the specimen is slowly stretched by a test equipment such as MTS, the axial load is measured and recorded by a gauge attached to the specimen. The deflection, elongation, or extension of the length of the gauge is obtained by $L - L_0$, in which L is the length of the gauge measured when the load is forced and L_0 is the initial length of specimen. Then we can calculate strain by

$$\varepsilon = \frac{L - L_0}{L_0}. \tag{2.5}$$

A uni-axial state of strain is characterized by the simplified form of Hooke's law,

$$\sigma = E\varepsilon, \tag{2.6}$$

where ε is the unit strain in the direction of unit stress σ, and E is a constant of proportionality called the modulus of elasticity, or Young's modulus, for the material. The modulus of elasticity, a measure of the stiffness of a material, is the slope of the stress-strain curve that can be obtained by the specimen test. Figure 2.5 presents the stress-strain diagram obtained from the standard tensile test.

The first region of stress-strain diagram, which begins at origin O and extends to A, is a linear region with proportional deformation. The slope of this line, O to A, is the modulus of elasticity, which has the same units as stress because the slope has units of stress divided by strain. With an increase in stress beyond A, materials generally reach a point where strain begins to increase

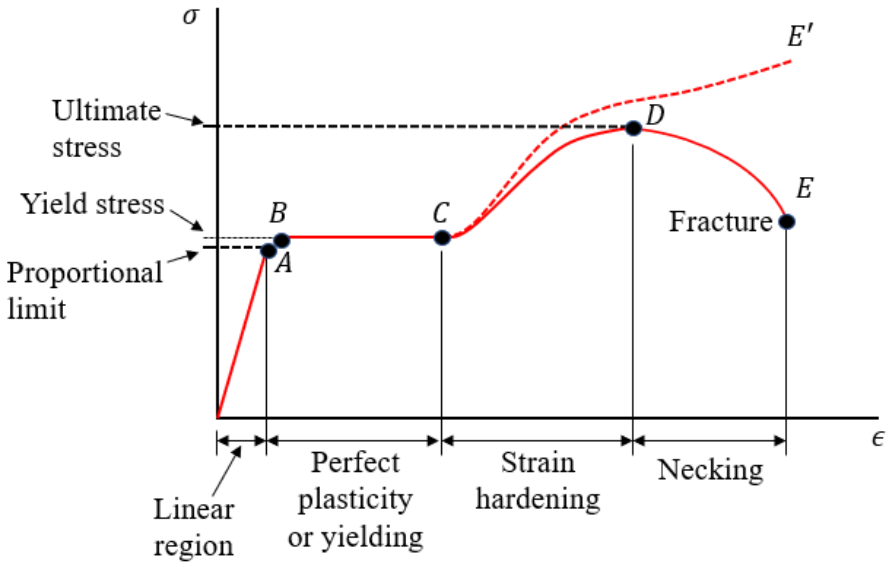

Figure 2.5: Stress-strain diagram for typical structural steel under tension [26]

rapidly without a corresponding increase in stress. The point is referred to as the yield point, and the stress at the point is referred to as the yield stress. Any additional load beyond the yield point causes permanent deformation. Although an aircraft is designed to withstand ultimate stress, which is point D, when an aircraft in flight engages in a maneuver that causes stress beyond the yield point, it must be examined carefully immediately after the flight.

From historical lessons, we have recognized failure in the linear region, OA, which is the safety region. The failure occurs because of recursive loading in the region while forming cycles of stress. The cyclic stress develops plastic deformation even though the stress is under the linear region. We call this failure "fatigue failure," which we will discuss it great detail in the following sections.

2.5 Constitutive laws for materials

Simplified Hooke's law, introduced in Eq. (2.6), shows the linear relationship between applied loads and resulting elongations. This equation, the simplified Hooke's law, however, is strongly limited by its application since it shows only longitudinal stress and strain by uniaxial load. The

modulus property also assumes isotropic material that has an identical property in every direction. To express a general version of Hooke's law, Eq. (2.6) can be expressed as Eq. (2.7)

$$\sigma_{ij} = C_{ijkl}\varepsilon_{kl}, \tag{2.7}$$

where σ_{ij} is a second-order tensor form with the nine components of stress, ε_{kl} is the corresponding strain for the stress, and C_{ijkl} is a fourth-order tensor with $81(3^4)$.

Invoking the symmetry of the stress tensor develops $C_{ijkl} = C_{jikl}$,and the symmetry of the strain tensor develops $C_{ijkl} = C_{ijlk}$. Therefore, the number of independent constants decreases from 81 to 36 for the symmetry relationship of the stress and strain. For a reduced number of constants, Eq. (2.7), generalized Hooke's law, can be described as Eq. (2.8).

$$\sigma_i = C_{ij}\varepsilon_j (i, j = 1, 2, ..., 6), \tag{2.8}$$

where the reduced notation for stress and strain is defined by the following equivalences.

$$\begin{aligned}
\sigma_1 &= \sigma_{11} & \varepsilon_1 &= \varepsilon_{11} \\
\sigma_2 &= \sigma_{22} & \varepsilon_2 &= \varepsilon_{22} \\
\sigma_3 &= \sigma_{33} & \varepsilon_3 &= \varepsilon_{33} \\
\sigma_4 &= \sigma_{23} & \varepsilon_4 &= 2\varepsilon_{23} \\
\sigma_5 &= \sigma_{31} & \varepsilon_5 &= 2\varepsilon_{31} \\
\sigma_6 &= \sigma_{12} & \varepsilon_6 &= 2\varepsilon_{12}
\end{aligned} \tag{2.9}$$

The C_{ij} are referred to as "elastic constants, moduli and stiffness coefficients." The six components of stress strain can be stored in an array, $\bar{\sigma}$ and $\bar{\varepsilon}$. Then, the strain energy, A, stored in a

differential element of the material, can be expressed as Eq. (2.10):

$$A = \frac{1}{2}\bar{\varepsilon}^T\bar{\sigma} = \frac{1}{2}\bar{\varepsilon}^T\bar{C}\bar{\varepsilon}, \tag{2.10}$$

where $\bar{\sigma} = \bar{C}\bar{\varepsilon}$ from Hooke's law. Conversely, Hooke's law can be expressed in the form of ε.

$$\varepsilon_i = S_{ij}\sigma_j, \tag{2.11}$$

which is also expressed as a matrix form with six components,

$$\bar{\varepsilon} = \bar{S}\bar{\sigma}. \tag{2.12}$$

Here, note that

$$\bar{S} = \bar{C}^{-1}. \tag{2.13}$$

Also, Eq. (2.10) can be extended as,

$$A = \frac{1}{2}\bar{\varepsilon}^T\bar{\sigma} = \frac{1}{2}\bar{\varepsilon}^T\bar{C}\bar{\varepsilon} = \frac{1}{2}\bar{\sigma}^T\bar{S}\bar{\sigma}. \tag{2.14}$$

The stored strain energy is a positive quantity for any deformation or stress state the material is subjected to, indicating that both stiffness and compliance matrices are symmetric and definitely positive. Then, the 36 components are reduced to 21 independent coefficients, which can be written

in the following matrix:

$$\begin{bmatrix} \sigma_1 \\ \sigma_2 \\ \sigma_3 \\ \tau_{23} \\ \tau_{13} \\ \tau_{12} \end{bmatrix} = \begin{bmatrix} C_{11} & C_{12} & C_{13} & C_{14} & C_{15} & C_{16} \\ & C_{22} & C_{23} & C_{24} & C_{25} & C_{26} \\ & & C_{33} & C_{34} & C_{35} & C_{36} \\ & & & C_{44} & C_{45} & C_{46} \\ & & & & C_{55} & C_{56} \\ \textit{sym} & & & & & C_{66} \end{bmatrix} \times \begin{bmatrix} \varepsilon_1 \\ \varepsilon_2 \\ \varepsilon_3 \\ \varepsilon_{23} \\ \varepsilon_{13} \\ \varepsilon_{12} \end{bmatrix} \tag{2.15}$$

The components of the matrix in Eq. (2.15) are 21 constants, and C_{ij} characterizes the behavior of the material. The matrix in Eq. (2.15) represents an anisotropic material. We obtain these constants only from experiments, but experiments cannot be conducted for some constants. In the case of such experiments, we use theoretical equations.

Many cases of materials show a characteristic symmetry about a plane. In this case, the stress-strain relationship is reduced, as shown in Eq. (2.16).

$$\begin{bmatrix} \sigma_1 \\ \sigma_2 \\ \sigma_3 \\ \tau_{23} \\ \tau_{13} \\ \tau_{12} \end{bmatrix} = \begin{bmatrix} C_{11} & C_{12} & C_{13} & 0 & 0 & C_{16} \\ & C_{22} & C_{23} & 0 & 0 & C_{26} \\ & & C_{33} & 0 & 0 & C_{36} \\ & & & C_{44} & C_{45} & 0 \\ & & & & C_{55} & 0 \\ \textit{sym} & & & & & C_{66} \end{bmatrix} \times \begin{bmatrix} \varepsilon_1 \\ \varepsilon_2 \\ \varepsilon_3 \\ \varepsilon_{23} \\ \varepsilon_{13} \\ \varepsilon_{12} \end{bmatrix} \tag{2.16}$$

This material is monoclinic material with 13 independent constants. If the material has a second plane of material symmetry, then we have two mutually orthogonal planes of symmetry, and the

stress-strain relationship can be reduced to

$$\begin{bmatrix} \sigma_1 \\ \sigma_2 \\ \sigma_3 \\ \tau_{23} \\ \tau_{13} \\ \tau_{12} \end{bmatrix} = \begin{bmatrix} C_{11} & C_{12} & C_{13} & 0 & 0 & 0 \\ & C_{22} & C_{23} & 0 & 0 & 0 \\ & & C_{33} & 0 & 0 & 0 \\ & & & C_{44} & 0 & 0 \\ & & & & C_{55} & 0 \\ \textit{sym} & & & & & C_{66} \end{bmatrix} \times \begin{bmatrix} \varepsilon_1 \\ \varepsilon_2 \\ \varepsilon_3 \\ \varepsilon_{23} \\ \varepsilon_{13} \\ \varepsilon_{12} \end{bmatrix} \tag{2.17}$$

In the stiffness matrix in Eq. (2.17) , 12 coefficients vanish and nine independent coefficients remain, which indicates an orthotropic material. Detailed composite failure theory accounts for this resolution of fidelity for calculating the failure analysis. Many composite failure theories, which we will discuss later, allow us to find the nine independent coefficients.

The nine independent coefficients cannot be directly obtained from experiments, but they can be converted from engineering constants, which are values that we measure from experiments for a specific material. For example, if we assume an orthotropic material for a unidirectional fibrous composite with axes aligned parallel and perpendicular to the fiber direction, then the nine independent coefficients can be expressed in terms of the related engineering constants obtained from experiments. In the case of an orthotropic material subjected to a three-dimensional state of stress, the equations for strains with corresponding stress are expressed as the following engineering constants.

$$\varepsilon_1 = \frac{\sigma_1}{E_1} - \frac{\nu_{21}}{E_2}\sigma_2 - \frac{\nu_{31}}{E_3}\sigma_3 \tag{2.18}$$

$$\varepsilon_2 = -\frac{\nu_{12}}{E_1}\sigma_1 + \frac{\sigma_2}{E_2} - \frac{\nu_3 2}{E_3}\sigma_3 \tag{2.19}$$

$$\varepsilon_3 = -\frac{\nu_{13}}{E_1}\sigma_1 - \frac{\nu_{23}}{E_2}\sigma_2 + \frac{\sigma_3}{E_3} \tag{2.20}$$

$$\gamma_{23} = \frac{\tau_{23}}{G_{23}} \tag{2.21}$$

$$\gamma_{13} = \frac{\tau_{13}}{G_{13}} \tag{2.22}$$

$$\gamma_{12} = \frac{\tau_{12}}{G_{12}} \tag{2.23}$$

The engineering constants in the previous equations are expressed as, $E_1, E_2,$ and E_3, and they represent the modulus of elasticity in the three coordinate directions. The definition of the modulus of elasticity is discussed in the 2.6 with Figure 2.5. The E_1 is the axial or fiber direction of the modulus, and E_2 and E_3 are the transverse moduli, respectively. ν is a Poisson's ratio, a dimensionless ratio of axial strain to lateral strain. The lateral strain is proportional to the axial strain at the same point if the material is linearly elastic. Since the material is linearly elastic only for the corresponding coordinate, in the preceding equations, ν_{ij} is expressed for each coordinate with i referring to the direction of the applied stress and j referring to the direction of the associated lateral strain.

$$\nu_{ij} = \frac{\varepsilon_j}{\varepsilon_i} \tag{2.24}$$

Lastly, the G is the shear modulus of elasticity, or the modulus of rigidity, which can be ob-

tained from the following equation for Hooke's law in shear.

$$\tau = G\gamma, \tag{2.25}$$

where γ represents the engineering shear strain. In Eqs. Eq. (2.21) to Eq. (2.23), shear strain is denoted by $\gamma_{ij} = 2\varepsilon_{ij}$ and shear stress by τ_{ij}. The shear modulus has the same units as the tension modulus of elasticity, E, and they correlate with the following equation.

$$G = \frac{E}{2(1+\nu)} \tag{2.26}$$

The shear moduli, G_{ij}, in the equations of engineering constants, from Eqs. Eq. (2.18) to Eq. (2.23), are defined for shear stress loading in the i, j plane.

Generally, laminated composite materials are regarded as materials presenting two orthogonal planes of symmetry and one plane of isotropy. Then, G_{12} and G_{13} are axial shear moduli in two orthogonal planes that include fibers, and G_{23} is the transverse shear modulus. For example, in Figure 2.6, planes (x_1, x_2) and (x_2, x_3) are the mutually orthogonal planes of symmetry and the plane of (x_2, x_3) shows the characteristics of an isotropic material. The stress-strain relationship, the stiffness matrix, for a transversely isotropic material then has the form of Eq. (2.27)

$$\begin{bmatrix} \sigma_1 \\ \sigma_2 \\ \sigma_3 \\ \tau_{23} \\ \tau_{13} \\ \tau_{12} \end{bmatrix} = \begin{bmatrix} C_{11} & C_{12} & C_{12} & 0 & 0 & 0 \\ & C_{22} & C_{23} & 0 & 0 & 0 \\ & & C_{22} & 0 & 0 & 0 \\ & & & \frac{C_{22}-C_{23}}{2} & 0 & 0 \\ & & & & C_{55} & 0 \\ \textit{sym} & & & & & C_{55} \end{bmatrix} \times \begin{bmatrix} \varepsilon_1 \\ \varepsilon_2 \\ \varepsilon_3 \\ \varepsilon_{23} \\ \varepsilon_{13} \\ \varepsilon_{12} \end{bmatrix} \tag{2.27}$$

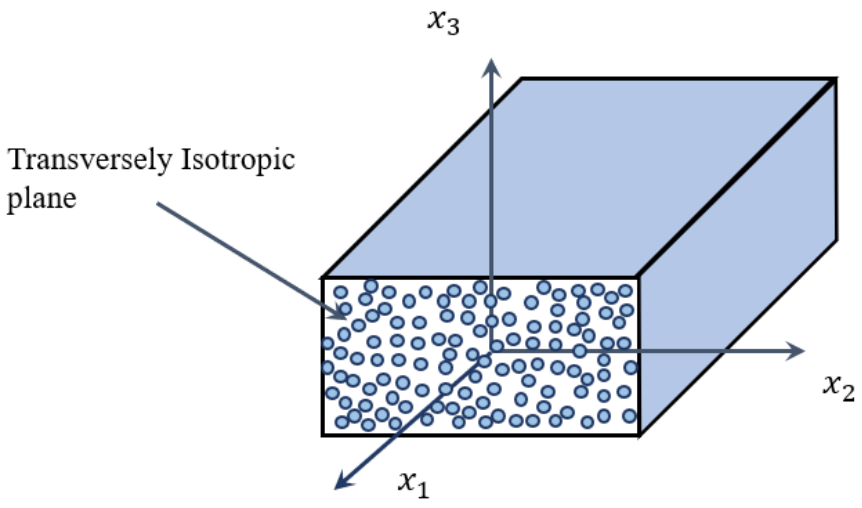

Figure 2.6: Transversely isotropic material [27]

Conversely, we need to know the constitutive equation for the compliance matrix with compliance coefficients, S_{ij}, defined in Eq. (2.12).

$$\begin{bmatrix} \sigma_1 \\ \sigma_2 \\ \sigma_3 \\ \tau_{23} \\ \tau_{13} \\ \tau_{12} \end{bmatrix} = \begin{bmatrix} S_{11} & S_{12} & S_{12} & 0 & 0 & 0 \\ & S_{22} & S_{23} & 0 & 0 & 0 \\ & & S_{22} & 0 & 0 & 0 \\ & & & \frac{S_{22}-S_{23}}{2} & 0 & 0 \\ & & & & S_{55} & 0 \\ sym & & & & & S_{55} \end{bmatrix} \times \begin{bmatrix} \varepsilon_1 \\ \varepsilon_2 \\ \varepsilon_3 \\ \varepsilon_{23} \\ \varepsilon_{13} \\ \varepsilon_{12} \end{bmatrix} \tag{2.28}$$

Only five constraints remain for the transversely isotropic material. Then, the engineering constants, that is, the modulus of elasticity of tension and shear, and the Poisson's ratio require only five independent elastic constants. For the relationship between the engineering constants and applied stress states, Figure 2.7 shows the five independent engineering constants for transversely isotropic material.

Figure 2.7 represents the relationship among $E_2 = E_3$, $\nu_{12} = \nu_{13}$, $G_{12} = G_{13}$, and $G_{23} =$

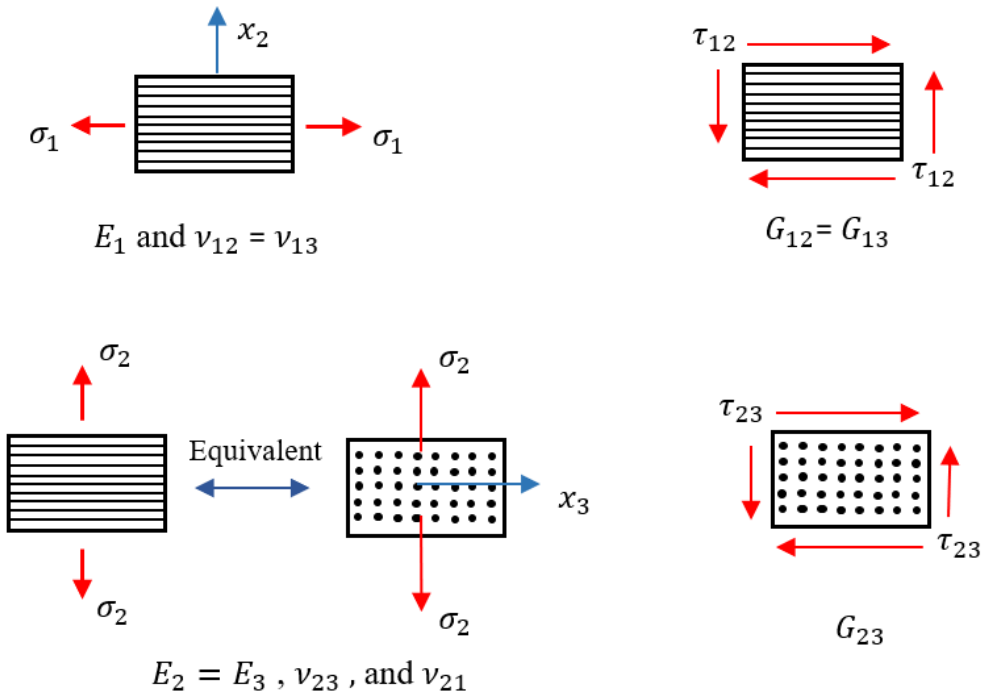

Figure 2.7: Engineering constants for transversely isotropic material [27]

$E_2/2(1+\nu_{23})$. Thus, to observe the behavior of the material, we must know only E_{11}, the fiber direction of elasticity; E_{22}, the transverse elasticity of fiber; G_{12}, the shear modulus of fiber and the transverse plane; ν_{12} , the Poisson's ratio of the same plane; and G_{23}, the shear modulus of the plane that contains the two transverse directions. The relationship of stiffness constants and engineering constants for transverse isotropic material is expressed in the following equations:

$$S_{11} = \frac{1}{E_1} \tag{2.29}$$

$$S_{12} = S_{13} = -\frac{\nu_{21}}{E_2} = -\frac{\nu_{12}}{E_2} \tag{2.30}$$

$$S_{22} = S_{33} = \frac{1}{E_2} = \frac{1}{E_3} \tag{2.31}$$

$$S_{23} = -\frac{\nu_{32}}{E_3} \tag{2.32}$$

$$S_{44} = \frac{1}{G_{23}} \tag{2.33}$$

$$S_{55} = S_{66} = \frac{1}{G_{12}} = \frac{1}{G_{13}} \tag{2.34}$$

Then, Eq. (2.28) can be expressed by the following engineering constants:

$$\begin{bmatrix} \varepsilon_1 \\ \varepsilon_2 \\ \varepsilon_3 \\ \gamma_{23} \\ \gamma_{13} \\ \gamma_{12} \end{bmatrix} = \begin{bmatrix} \frac{1}{E_1} & -\frac{\nu_{21}}{E_2} & -\frac{\nu_{21}}{E_2} & 0 & 0 & 0 \\ & \frac{1}{E_2} & -\frac{\nu_{32}}{E_3} & 0 & 0 & 0 \\ & & \frac{1}{E_2} & 0 & 0 & 0 \\ & & & \frac{2(1+\nu_{23})}{E_2} & 0 & 0 \\ & & & & \frac{1}{G_{12}} & 0 \\ \textit{sym} & & & & & \frac{1}{G_{12}} \end{bmatrix} \times \begin{bmatrix} \sigma_1 \\ \sigma_2 \\ \sigma_3 \\ \tau_{23} \\ \tau_{13} \\ \tau_{12} \end{bmatrix} \tag{2.35}$$

In the case of a thin sheet of material such as composite laminate, we can assume a plane stress state of $\sigma_3 \approx \tau_{13} \approx \tau_{23} \approx 0$. The constitutive laws expressed in compliance matrix form are reduced as follows:

$$\begin{bmatrix} \varepsilon_1 \\ \varepsilon_2 \\ \gamma_{12} \end{bmatrix} = \begin{bmatrix} \frac{1}{E_1} & -\frac{\nu_{21}}{E_2} & 0 \\ -\frac{\nu_{12}}{E_1} & \frac{1}{E_2} & 0 \\ 0 & 0 & \frac{1}{G_{12}} \end{bmatrix} \times \begin{bmatrix} \sigma_1 \\ \sigma_2 \\ \tau_{12} \end{bmatrix} \tag{2.36}$$

In the reduced compliance matrix, we see five engineering constraints, $E_1, E_2, \nu_{12}, \nu_{21}$ and G_{12},

the same as those in Figure 2.7. However, we note that the compliance matrix must be symmetric, so $\nu_{21}/E_2 = \nu_{12}/E_1$. One can be calculated by the other, so the independent constraints are actually four, indicating that we need to obtain four engineering constraints to analyze thin laminate composite material.

Lastly, isotropic material is characterized by all symmetric planes showing an identical response in all directions. In this case, the stiffness matrix, Eq. (2.27) for the transversely isotropic material can be reduced to the following:

$$\begin{bmatrix} \sigma_1 \\ \sigma_2 \\ \sigma_3 \\ \tau_{23} \\ \tau_{13} \\ \tau_{12} \end{bmatrix} = \begin{bmatrix} C_{11} & C_{12} & C_{12} & 0 & 0 & 0 \\ & C_{11} & C_{12} & 0 & 0 & 0 \\ & & C_{11} & 0 & 0 & 0 \\ & & & \frac{C_{11}-C_{12}}{2} & 0 & 0 \\ & & & & \frac{C_{11}-C_{12}}{2} & 0 \\ \textit{sym} & & & & & \frac{C_{11}-C_{12}}{2} \end{bmatrix} \times \begin{bmatrix} \varepsilon_1 \\ \varepsilon_2 \\ \varepsilon_3 \\ \gamma_{23} \\ \gamma_{13} \\ \gamma_{12} \end{bmatrix} \tag{2.37}$$

Thus, an isotropic material has only two independent elastic constraints, E and ν, for the expression of engineering constraints.

Consequently, in the proposed new digital twin method, HFEM needs to share four material properties for a laminate composite material and two material properties for an isotropic material. Then the output of each level of the hierarchical model should contain at least three degrees of freedom of stress arrays to calculate the failure of a structure. In the following chapter, we will discuss failure theories for both composite and isotropic materials.

2.6 Failure Theories for Static Loading

The general procedure for static failure analysis is to survey the margin of safety under an ultimate load condition, which is $1.5\times$ a limit load. The structure must be able to support both ultimate

loads without failing and limit loads without detrimental permanent deformation, implying that the margin of safety equals zero or greater, but it is never negative. For aluminum alloys, Niu [28] describes the margin of safety in Figure 2.8.

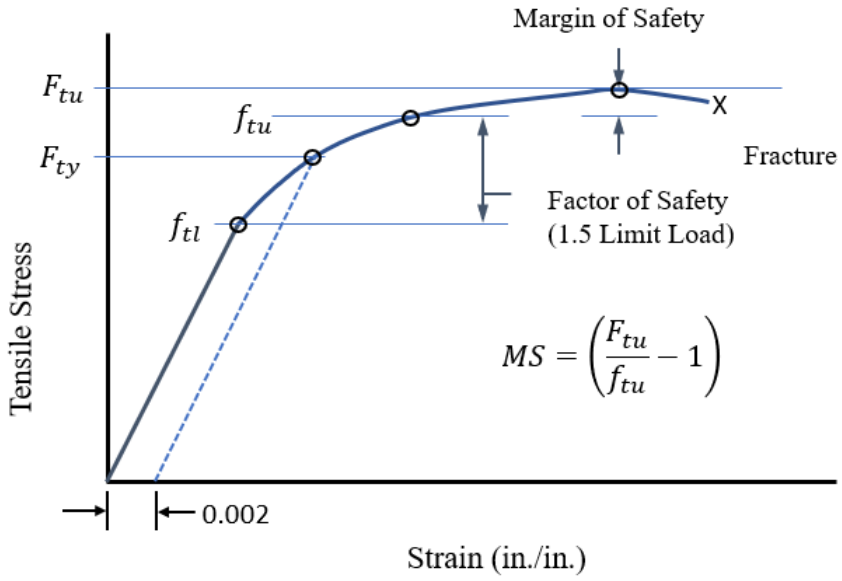

Figure 2.8: Stress and strain curves for aluminum alloy [28]

In the figure, f_{tl} is the actual stress that we obtain from the finite element model subjected by a limit load. Thus, in Eq. (2.38), f_{tl} is multiplied by 1.5, which obtains f_{tu}.

$$MS = (\frac{F_{tu}}{f_{tu}} - 1) \tag{2.38}$$

Sometimes, finite element analysis is subjected to an ultimate load. In this case, we obtain the f_{tu} directly from the results of FEM without multiplying it by 1.5 because the ultimate load is already multiplied by 1.5 in the loading. In the following sections, we will assume the former that analysis is conducted under ultimate loading cases.

In the previous chapter, Chapter 2.5, we discussed six components of stress and their relationships. For the margin of safety in Eq. (2.38), however, we need only one representative stress, f_{tl}.

The representative stress or equivalent stress can be determined by various failure theories. We will begin by discussing the isotropic application in Chapter 2.6.1, and then follow with the failure theories of a composite in Chapter 2.6.2

2.6.1 Failure theories for isotropic materials

No universal theory can be applied to a general case of material properties or stress state. Thus, the choice of a failure theory is an engineering decision made by the examiner. However, from a historical hypothesis that has been formulated and tested, we determine failure theories from representative candidates. Figure 2.9 describes a summary flowchart for the selection of failure theories for a static loading case. Failure theories for an isotropic, or homogeneous, material should be selected according to the properties of a material, specifically its ductility, and the purpose of analysis. Ductile materials are normally regarded as those with a fracture strain ε_f greater than 0.05. ε_f is the engineering strain at which a specimen fractures for a uniaxial tensile test. Ductile material has an identifiable yield strength that is often identical for both compression and tension ($S_y = S_{yt} = S_{yc}$). Brittle materials, however, do not have identifiable yield strength, so they are often characterized by their ultimate strength.

This section will examine mainly ductile material and its applications in aerospace engineering with one failure criterion, which follows the maximum shear stress theory that utilizes maximum principal stress. The maximum principal stress criterion is a conservative way to analyze a structure. In aerospace field, we normally select a conservative way when we have several options to analyze an airframe or part of an aircraft. In addition, both fatigue and damage tolerance analyses, both of which relate to cyclic loading, are assumed to occur under unidirectional loading that has mainly the portion of principal direction of stress. To calculate the margin of safety, we need to find the stresses in terms of the global coordinate system. A material could cause a failure at some angles rather than on the global coordinate. In Eq. (2.36), we analyze stress components, σ_1, σ_2, and τ_{12} for a case of plane stress. In this particular example, we use the x, y coordinate system to

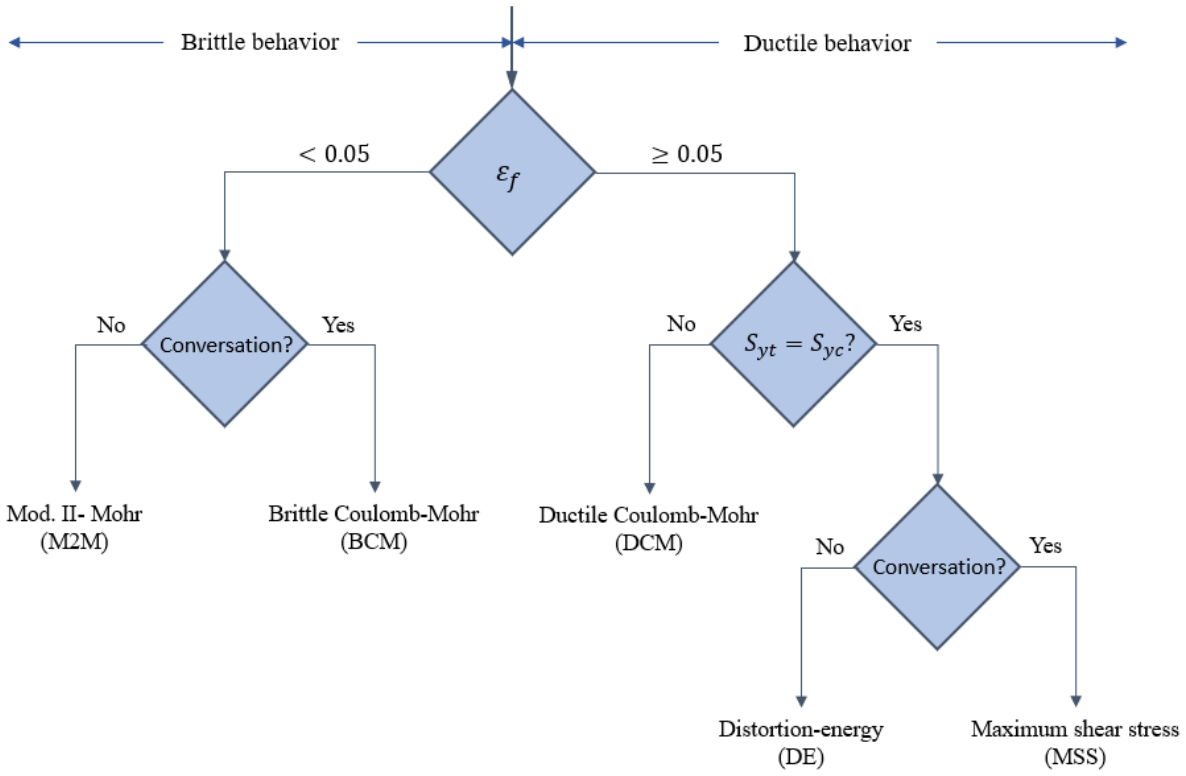

Figure 2.9: Failure theory selection flowchart [23]

describe the geometry. For plane stress, which is two-dimensional stress, free body diagrams for elements are represented in Figure 2.10.

The three components, σ_x, σ_y, and τ_{xy}, are represented in Figure 2.10(a) for the global coordinate system x and y. When we assume that the element rotates from x to x' at angle θ, an infinitesimal face is shown in Figure 2.10(b). Face AB is normal to the x' axis, and stress $\sigma_{x'}$ and shear stress $\tau_{x'y'}$ are indicated with positive signs. For the equilibrium of the forces for all the stress components, the transformation equations for stress are given in the following equations.

$$\sigma_{x'} = \sigma_x \cos^2\theta + \sigma_y \sin^2\theta + 2\tau_{xy} \sin\theta \cos\theta \tag{2.39}$$

$$\tau_{x'y'} = \tau_{xy}(\cos^2\theta - \sin^2\theta) + (\sigma_y - \sigma_x) \sin\theta \cos\theta \tag{2.40}$$

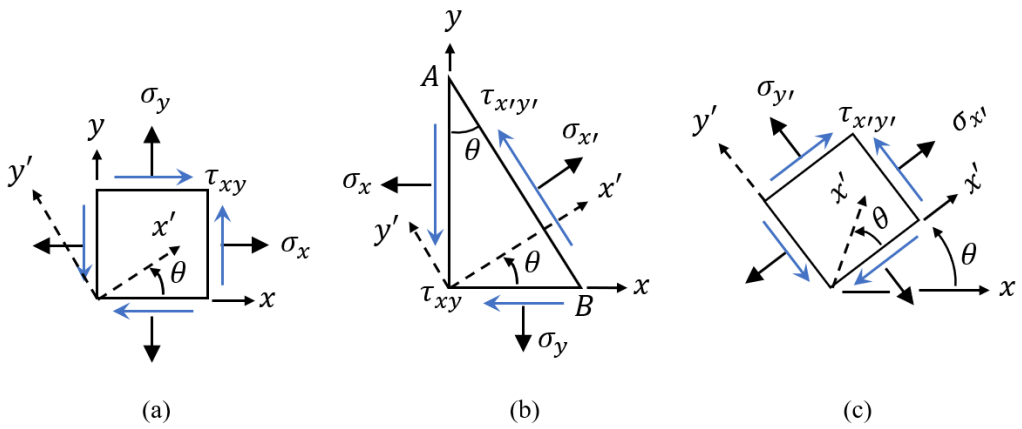

Figure 2.10: Elements in plane stress

We can find stress $\sigma_{y'}$ by substituting $\theta + \pi/2$ for θ in Eq. (2.39).

$$\sigma_{y'} = \sigma_x \sin^2\theta + \sigma_y \cos^2\theta - 2\tau_{xy} \sin\theta \cos\theta \tag{2.41}$$

The following trigonometric identities,

$$\cos^2\theta = \frac{1+\cos 2\theta}{2} \qquad \sin^2\theta = \frac{1-\cos 2\theta}{2} \qquad \sin\theta\cos\theta = \frac{\sin 2\theta}{2} \tag{2.42}$$

yield the following convenient forms,

$$\sigma_{x'} = \frac{1}{2}(\sigma_x + \sigma_y) + \frac{1}{2}(\sigma_x - \sigma_y)\cos 2\theta + \tau_{xy} \sin 2\theta \tag{2.43}$$

$$\tau_{x'y'} = -\frac{1}{2}(\sigma_x - \sigma_y)\sin 2\theta + \tau_{xy} \cos 2\theta \tag{2.44}$$

$$\sigma_{y'} = \frac{1}{2}(\sigma_x + \sigma_y) - \frac{1}{2}(\sigma_x - \sigma_y)\cos 2\theta - \tau_{xy} \sin 2\theta \tag{2.45}$$

To find the principal stresses, the maximum and minimum normal stresses, σ_x and σ_y, we first need to find θ_p , in which the shearing stress vanishes and the normal stress reaches extreme values. Angle θ_p, the orientation of principal planes, can be obtained by differentiating the transform equations.

$$\sigma_{x'} = \frac{1}{2}(\sigma_x + \sigma_y) + \frac{1}{2}(\sigma_x - \sigma_y)\cos 2\theta + \tau_{xy}\sin 2\theta$$

$$\frac{\mathrm{d}\sigma x'}{\mathrm{d}\theta} = \frac{1}{2}(\sigma_x - \sigma_y)(-2\sin 2\theta) + \tau_{xy}(2\cos 2\theta) = 0 \tag{2.46}$$

$$\frac{\mathrm{d}\sigma x'}{\mathrm{d}\theta} = -(\sigma_x - \sigma_y)\sin 2\theta + 2\tau_{xy}\cos 2\theta = 0$$

Then, we obtain the equation of principal angles,

$$\tan 2\theta_p = \frac{2\tau_{xy}}{\sigma_x - \sigma_y} \tag{2.47}$$

Eq. (2.47) carries two values of θ_p in the range of $0 - 180^\circ$, with 90° difference. We note that the planes on which the principal stresses act are perpendicular. Introducing the values of the sine and the cosine corresponding to the two principal angles obtained from Eq. (2.47) yields the following equation.

$$\sigma_{max,min} = \sigma_{1,2} = \frac{\sigma_x + \sigma_y}{2} \pm \sqrt{\left(\frac{\sigma_x - \sigma_y}{2}\right)^2 + \tau_{xy}^2} \tag{2.48}$$

The maximum principal stress is among the algebraically larger stress values in Eq. (2.48) [29]. In most of the fatigue failure analysis, we will mainly use the maximum principal stress. Thus, in

the fatigue analysis chapters, stress will indicate the maximum principal stress obtained from the FE analysis.

2.6.2 Failure theories for composite materials

Failure theories for composite material, based on comparisons between the state of stress or strain in a material and a set of defined failure criteria, predict when material failure will occur. When dealing with composite material (but not with isotropic material), we must account for the orientation effects resulting from the complex orthotropic nature of their loading properties. Therefore, we have created a reduced form of the compliance matrix under consideration of the plane and orthotropic material in Eq. (2.36). In this equation, we find stresses σ_1, σ_2, and τ_{12}. In this chapter, we refer to composite failure theories based on ply-by-ply failure to calculate loads that cause the failure of individual layers. For each layer, we will calculate failure based on a theory that yields a method that combines the three stresses and mechanical strengths. We describe this method or equation, which entails a function form as a general failure criterion, as follows:

$$F(\sigma_1, \sigma_2, \tau_{12}) = 1 \tag{2.49}$$

When the layer reaches 1, then we assume the layer is fractured.

This chapter will briefly discuss several composite failure theories for the function of f in the above equation. These theories are categorized into classic failure theories, which deal with laminated properties, and advanced failure theories, which account for the effect of fiber and the matrix itself and its interference. The former includes the maximum stress criterion, the maximum strain criterion, and the Tsai-Hill, Tsai-Wu, and Tsai-Hahn failure theories. The latter indicates the Hashin and Sun theories, and the strain invariant failure theory (SIFT). The among of many possible composite failure theories, we will mainly discuss with SIFT because the HFEM utilizes a scale factor concept which has been used in SIFT for a concept of transferring factor from micro

to macro-mechanics.

In current theories, the strength properties of a laminate are derived from the strength of individual lamina determined by an analysis of angled unidirectional lamina and related to the normal and shear strengths of the material. Principle and maximum shear stresses are transformed into a set of local axes based on fiber orientations. In unidirectional laminates, the two axes analyzed are those parallel to the fibers and a transverse axis perpendicular to the fibers, shown in Figure 2.11 below.

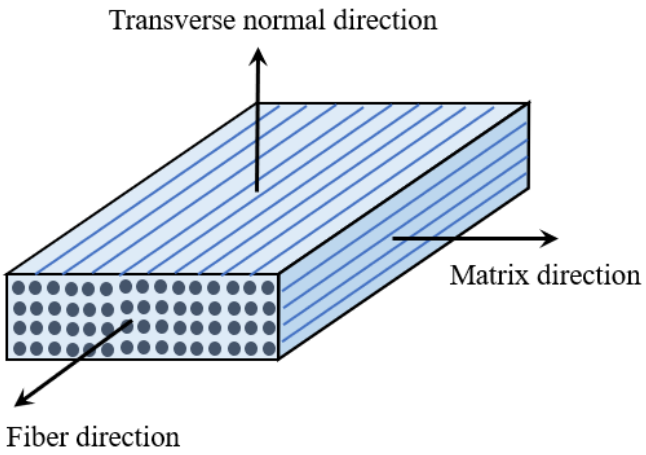

Figure 2.11: Diagram of the directions of a composite laminate

A comparison of the state of stress and strain necessitates engineering strength values. The following is a list of five strength parameters commonly used in composite analysis:

- X_t: Ultimate longitudinal tensile strength in the fiber direction
- X_c: Ultimate longitudinal compressive strength in the fiber direction (negative value)
- Y_t: Ultimate transverse tensile strength in the matrix direction
- Y_c: Ultimate transverse compressive strength in the matrix direction (negative value)
- S_{12}: Ultimate in-plane shear strength

Maximum stress theory

The traditional approach to composite analysis is ply-based failure analysis, in which the failure of a laminate is determined whenever any ply reaches its material strength limit. A representative theory is maximum stress theory, which indicates a failure when any stress component exceeds its uniaxial strength, without considering the interaction of the components. The theory is simply expressed as the following boundaries,

$$\begin{aligned} \sigma_1 &\geq X_t \\ \sigma_2 &\geq Y_t \\ |\tau_{12}| &\geq S \\ \sigma_1 &\leq X_c \\ \sigma_2 &\leq Y_c \end{aligned} \tag{2.50}$$

The margin of safety, based on the maximum stress criterion, is written in following equations,

$$MOS_{max\ \sigma_1} = \begin{cases} \dfrac{X_t}{\sigma_1} - 1 & \sigma_1 > 0 \\ \dfrac{X_c}{\sigma_1} - 1 & \sigma_1 < 0 \end{cases} \tag{2.51}$$

$$MOS_{max\ \sigma_2} = \begin{cases} \dfrac{Y_t}{\sigma_2} - 1 & \sigma_2 > 0 \\ \dfrac{Y_c}{\sigma_2} - 1 & \sigma_2 < 0 \end{cases} \tag{2.52}$$

$$MOS_{max\ \tau_{12}} = \frac{S}{|\tau_{12}|} - 1 \tag{2.53}$$

Then, the final margin of safety is

$$MOS = \min\left\{MOS_{max\ \sigma_1}, MOS_{max\ \sigma_2}, MOS_{max\ \tau_{12}}\right\} \tag{2.54}$$

Any given ply can easily be characterized by maximum stress theory, which is based solely on uniaxial ply data. However, the theory does not account for the interaction among the stress components. As discussed in the stress and strain chapters, stress does not exist independently, but it combines with other stresses or rotates to other coordinates. Thus, the application of maximum stress theory is highly likely to result in failure caused by equivalent stress.

Maximum strain theory

Maximum strain theory strongly resembles maximum stress theory. Failure can occur by the following strain-associated equations.

$$\begin{aligned} \varepsilon_1 &\geq X_{\varepsilon t} \\ \varepsilon_2 &\geq Y_{\varepsilon t} \\ |\gamma_{12}| &\geq S_{\varepsilon} \\ \varepsilon_1 &\leq X_{\varepsilon c} \\ \varepsilon_2 &\leq Y_{\varepsilon c} \end{aligned} \tag{2.55}$$

The margin of safety for maximum strain theory can be expressed in a similar way by the

following equations.

$$MOS_{max\ \varepsilon_1} = \begin{cases} \dfrac{X_t}{\varepsilon_1} - 1 & \varepsilon_1 > 0 \\ \dfrac{X_c}{\varepsilon_1} - 1 & \varepsilon_1 < 0 \end{cases} \tag{2.56}$$

$$MOS_{max\ \varepsilon_{22}} = \begin{cases} \dfrac{Y_t}{\varepsilon_2} - 1 & \varepsilon_2 > 0 \\ \dfrac{Y_c}{\varepsilon_2} - 1 & \varepsilon_2 < 0 \end{cases} \tag{2.57}$$

$$MOS_{max\ \gamma 12} = \frac{S_\varepsilon}{|\gamma_{12}|} - 1 \tag{2.58}$$

Despite these similarities, their failure envelopes differ slightly, as shown in Figure 2.12.

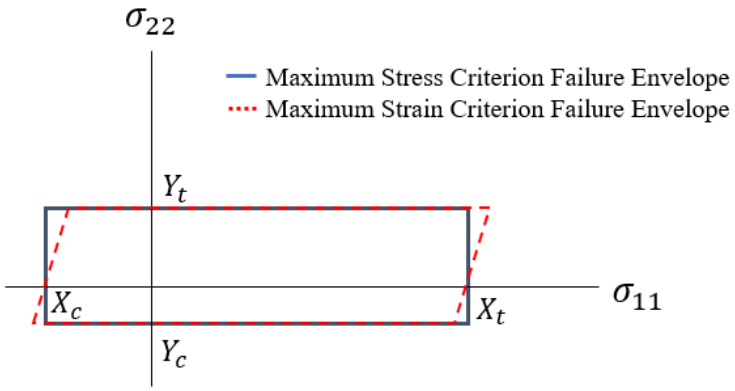

Figure 2.12: Failure envelopes for maximum stress and strain theories [26]

The selection of either the maximum stress or maximum strain theory depends on the ductility of a material. Highly ductile or nonlinear composite materials are best served by the maximum strain theory [26].

2.6.3 Strain invariant failure theory

Background

According to recent studies, damage to a composite structure under a constant load results from deformation caused by the expansion or twisting of the fiber and the matrix [30]. For example, Schilling et al. [31] studied X-ray microtomography, which facilitates the characterization of the internal configuration of flaws, including delamination, matrix cracking, and microcracking, in composite laminates. In another study, Beyerl et al. [32] surveyed the mechanical characteristics of a unidirectional composite related to the individual properties of the matrix, the fibers, and the interfaces. Sun [33] also shows the importance of analyzing a matrix, a fiber, and their interface in calculations of the failure of composite laminate.

In micro-mechanics, the fracture reference equation for the fiber and the matrix of a composite structure is defined by SIFT. This theory also assumes the strain invariant failure criterion through the first strain and equivalent strain for volume and shape changes. Each strain invariant is defined as follows.

$$J_1 = \varepsilon_{xx} + \varepsilon_{yy} + \varepsilon_{zz} \tag{2.59}$$

$$J_2 = \varepsilon_{xx}\varepsilon_{yy} + \varepsilon_{yy}\varepsilon_{zz} + \varepsilon_{zz}\varepsilon_{xx} - \frac{1}{4}(\varepsilon_{xy}^2 + \varepsilon_{yz}^2 + \varepsilon_{zx}^2) \tag{2.60}$$

$$J_3 = \varepsilon_{xx}\varepsilon_{yy}\varepsilon_{zz} + \frac{1}{4}(\varepsilon_{xy}\varepsilon_{yz}\varepsilon_{zx} - \varepsilon_{xx}\varepsilon_{yz}^2 - \varepsilon_{yy}\varepsilon_{zz}^2 - \varepsilon_{zz}\varepsilon_{xy}^2) \tag{2.61}$$

J_1 implies the most suitable condition for expressing interlaminar fracture resulting from a volume increase during the matrix phase. If we look at the equation, we see no consideration of damage under a compressive load through the above conditions. However, in general, it is

not possible to reach the yield value under a compressive load, so J_1 can be adopted as a failure equation of a structure under increasing volume [34].

SIFT is based on the first invariant and estimated changes in volume through Von-Mises strain. When the first invariant reaches a critical strain invariant, the theory defines a failure. With respect to a unidirectional laminate composite, we define the critical strain invariants that imply damage initiation by the following two equations.

$$J_1 \geq J_1^{critical} \tag{2.62}$$

$$\varepsilon_{equivalent} \geq \varepsilon_{equivalent}^{critical} \tag{2.63}$$

where, J_1 can be obtained by Eq. (2.59) and $\varepsilon_{equivalent}$ is calculated by the following Eq. (2.64),

$$\varepsilon_{equivalent} = \sqrt{0.5\left[(\varepsilon_1 - \varepsilon_2)^2 + (\varepsilon_1 - \varepsilon_3)^2 + (\varepsilon_2 - \varepsilon_3)^2\right]} \tag{2.64}$$

Critical strain invariant

Critical strain invariant values can be obtained by two methods. The first is a method used by Gosse [35] to obtain the critical value through the global-to-micro FE model of a specimen under actual failure loads. The second method entails obtaining J_1 or $\varepsilon_{equivalent}$ through a known database or experimental material strength data. For example, yield strain ε_{yield} is measured by a uniaxial tensile test or a compression test and used to obtain the critical strain invariant value, $J_1^{critical}$. The relationship is as follows.

$$J_1^{critical} = \varepsilon_{xx} + \varepsilon_{yy} + \varepsilon_{zz} = \varepsilon_{yield} + (-2\nu)\varepsilon_{yield} = (1 - 2\nu)\varepsilon_{yield} \tag{2.65}$$

The critical equivalent strain value is also obtained and shown in Eq. (2.66).

$$\varepsilon_{equivalent}^{critical} = \sqrt{0.5\left[(\varepsilon_{yield} + \nu_{12}\varepsilon_{yield})^2 + (\varepsilon_{yield} + \nu\varepsilon_{yield})^2 + (\varepsilon_{yield} + \nu\varepsilon_{yield})^2\right]} \tag{2.66}$$

For the analysis of fiber, Eq. (2.66) can be abbreviated as follows.

$$\varepsilon_{equivalent}^{critical} = (1 + \nu_{12})\varepsilon_{yield} \tag{2.67}$$

Redefined critical strain invariant

The process of obtaining the critical strain invariant value for the SIFT analysis is imperative, as it is the factor that determines the boundary of the failure state equation. To calculate the critical strain invariant, Chapter 2.6.3 provides two methods. One is the method of obtaining the threshold value through the global-to-micro FE model. However, this method has several drawbacks. First, as it is a stacking type model, its implementation is complex and increases the likelihood of errors. In addition, the threshold value obtained by testing a material cannot be acquired by physical strength. To overcome these shortcomings, we adopt a method of obtaining the critical strain invariant value from the physical strength used in conventional classical composite theory. The strength properties of most composites are already known for the analysis of conventional laminate theory. The following presents the method of using this strength property for acquiring the critical strain invariant value.

The strength properties are divided into fiber and matrix directions, as previously shown in Figure 2.11. To convert the physical properties of the composite strength into the strength in the

strain concept, it is reasonable to adopt Y_t and the modulus of elasticity, E_{22}, because the load type is the tensile in the transverse direction at $J_1 \geq 0$ on the matrix. Therefore, if the strength is defined as yield strain, ε_{yield}, and substituted into Eq. (2.65), the following equation can be obtained.

$$J_1^{critical} = (1 - 2\nu)\frac{Y_t}{E_{22}} \tag{2.68}$$

If the fiber is $J_1 < 0$, longitudinal strength X_t and longitudinal elastic modulus E_{11} are adopted. Therefore, by redefining the strain strength against the yield strain, ε_{yield}, we can rewrite Eq. (2.68) as follows.

$$\varepsilon_{equivalent}^{critical} = (1 + \nu_{12})\frac{X_t}{E_{11}} \tag{2.69}$$

CHAPTER 3

HIERARCHICAL FINITE ELEMENT METHOD

3.1 The Need for a New Digital Twin Method

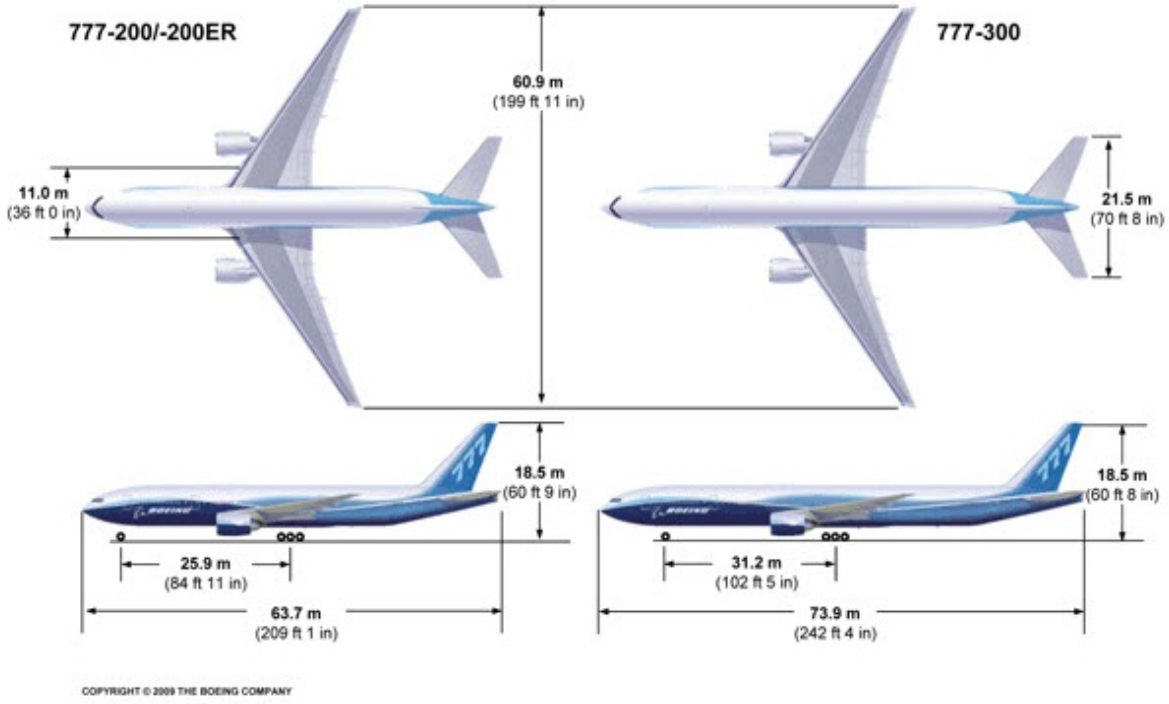

Figure 3.1: Boeing 777 wing span [36]

Structural health monitoring (SHM) is a process of assessing the current health and analyzing predictions for the remaining life of a structure. Thus, SHM requires an examination of the current state of an individual aircraft and simulation of the propagation of cracks under various conditions through a computational model. Under the presumption that such a model plays a vital role in SHM, this study applies the finite element (FE) method for both diagnosis and prognosis as a digital twin that represents an actual aircraft. However, because the sizes of flaws or cracks are extremely small compared to the size of an aircraft, FEM in SHM consumes an exorbitant amount

of computation time. For example, the wing span of a conventional aircraft, shown in Figure 3.1, is 60 m but the typical size of an identifiable surface flaw is 6.35 mm long and 3.175 mm deep [37]. Since flaws or cracks are minuscule, a FEM for the digital twin requires an extremely fine mesh, which requires enormous computation time. Therefore, a solution to the problem of mesh size requires a new method of the digital twin.

3.2 Hierarchical Finite Element Method

Using conventional FEM as a digital twin, this study entails a simple stress analysis of the system level of FEM with coarse meshes(global-level) and calculates crack propagation on the element level of FEM with fine meshes(base-level) if global-level FEM and base-level FEM are connected mutually. To solve problems related to the mesh size and computation time, this study proposes the hierarchical finite element method (HFEM) that involves the development of a flexible intrinsic FEM that adapts the size of elements, depending on the purpose. This study also proposes a method of building a stress or strain relationship between the hierarchical models that is connected by the unit load method, a virtual load analysis that uses six components of unit loads. The connection by the unit load transfers information between the higher and lower levels. For example, Figure 3.2 shows that one of the constituent elements in the higher-level of FEM with coarse mesh possesses a corresponding lower-level of FEM with extremely fine mesh.

For the case of two level hierarchy HFEM, higher-level and lower-level FEM are mutually connected and they conduct appropriate analyses for their purposes while shearing necessary data. At this time, the higher-level of FEM refers to a global level of FEM, the highest level of HFEM. The global-level model, an entire system under investigation, can apply external loads, aerodynamic forces that are pressure forces acting perpendicular to the surface of a wing. These forces, external forces, however, are generally transformed into six components of loads for structural analysis: F_x, F_y, F_z, M_x, M_y, and M_z. The primary role of the global-level model is to transfer the external forces to the internal forces and then transform the internal forces to normalized stress. Thus, each

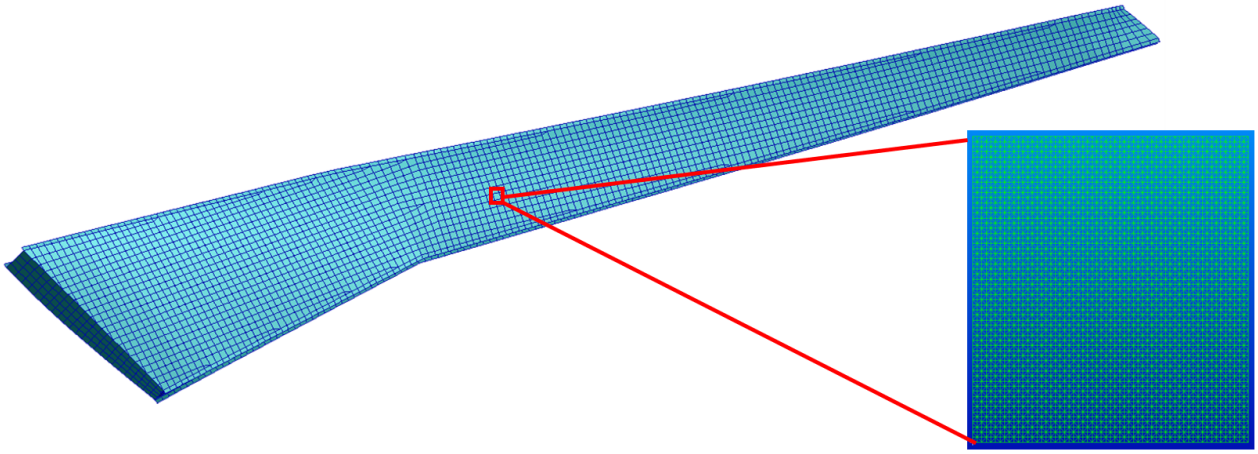

Figure 3.2: The HFEM from higher to lower element level

element in the global-level model has a unique child element, a base-level model with a normalized stress map (Figure 3.3) which is analyzed under boundary conditions of the base-level, and it acts as a base model for crack propagation. This process is enabled by transferring external load from global-model to base-model and simplified by the unit load method. The detail of those methods are introduced in Section 3.3.

Each element in the global-level FEM has unique boundary conditions and dimensions. Thus, a stress map for an element is not applicable to other elements. To generate the stress map for all elements in the global FEM, we need to apply each condition of the unit load method for each unique base-level model. However, the computation is prohibitively expensive. For example, the aircraft wing in Figure 3.2 has 4,694 BAR elements, 7,650 QUAD4 elements, and 60 TRIA elements. Therefore, the number of runs for a stress analysis of 12,404 elements for six components of a unit load is 74,424, requiring about 62 days. To mitigate the problem of time consumption, this study proposes a clustering method in which elements in the global-level FEM are clustered by element size and property type. After clustering, therefore, elements are grouped by similarity. In each group, a representative model, which is commonly the cluster center, is picked from clustered elements. Then, we only need to know the stress maps for the element of each cluster. A detailed

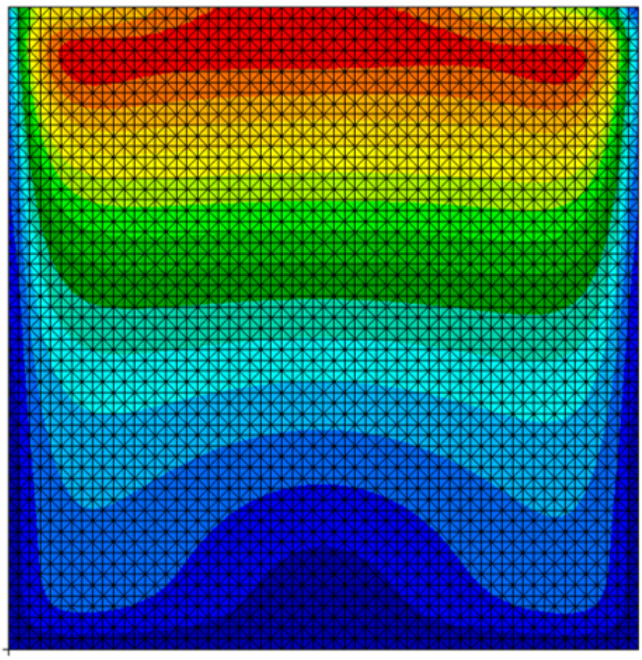

Figure 3.3: Example of a normalized stress map for the base level of HFEM

discussion of the process will be presented in Section 3.4.

3.3 Load transfer methods

3.3.1 External load transfer method

In the on-board framework, the digital twin obtains external loads from sensors that have only strain information available at the sensor locations to analyze the stress with global-level model. A common strain gauge is one option for measuring strain, but it is not suitable for this on-board framework because it requires too many wires and weighted equipment for the installation. Recently, for the structural health monitoring system, a fiber optic sensor that utilizes the fiber Bragg grating (FBG) as a strain gauge has been widely studied and adopted. One major study was published by the NASA Dryden Flight Research Center, which developed a real-time fiber optic strain and shape sensing (FOSS) technology and validated the technology with an X-33 and an F-18.

The recent development of a predator-B was validated by an experiment involving a real-time wing shape [38]. In this research, the shape estimation and strain measurement are not the subject of study. We assume that reasonable loads can be calculated from the FBG and apply it to the global level of the digital twin, or HFEM.

Since we have assumed that HFEM is receiving proper load information from the gauge, let us discuss how to transfer the point loads as a pressure load. Most preliminary design stage of aircraft FE models or even global FE models in the detail design stage use a special element called MPC (Multi-point Constraint) transfer aerodynamic loads to the FE. MPC constructs geometric relationships that are required to match the displacements of certain nodes of the FE model. This is very useful method for the FE modeling, without the numeric difficulties that would imply to model them as truly flexible bodies of high stiffness. Thus, the main function of MPC is to generate internal relationships between nodes from geometric data defined by the user.

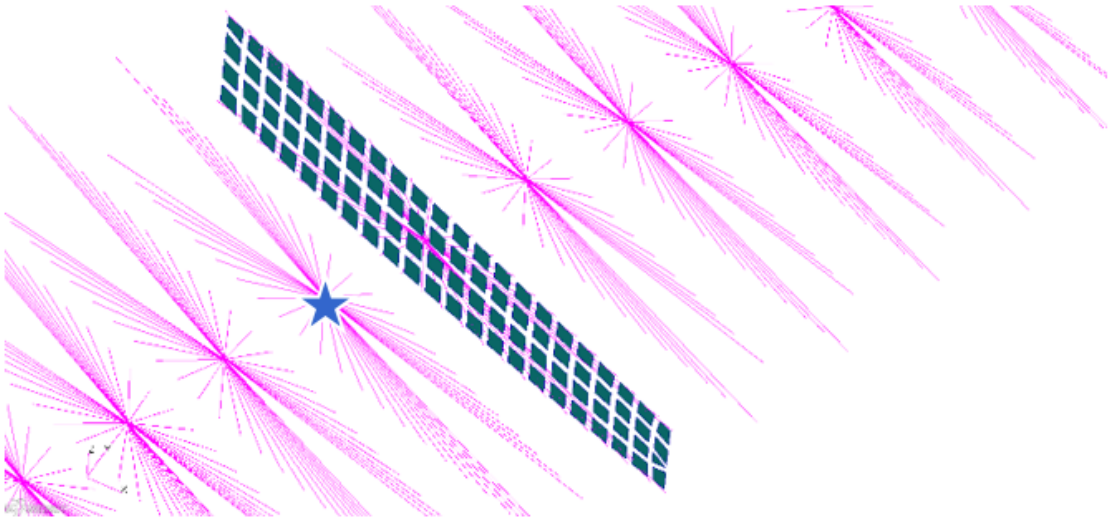

Figure 3.4: MPC example

With the functionality of MPC, we can define that a group of dependent nodes follows the movement of one independent node with predefined factors such as allowed degree of freedom and intensity of stiffness. An example for the MPC from Patran is shown in Figure 3.4 with RBE2

types, which defines that six degrees of freedom, three translations and three rotations, is allowed to transmit to the dependent nodes from the independent nodes. In Figure 3.4, the blue star is an independent node, and the ends of all lines are the positions of the dependent nodes. Then, when point loads are subjected to the independent node, the movement of dependent node acts as distributed forces in the FEM.

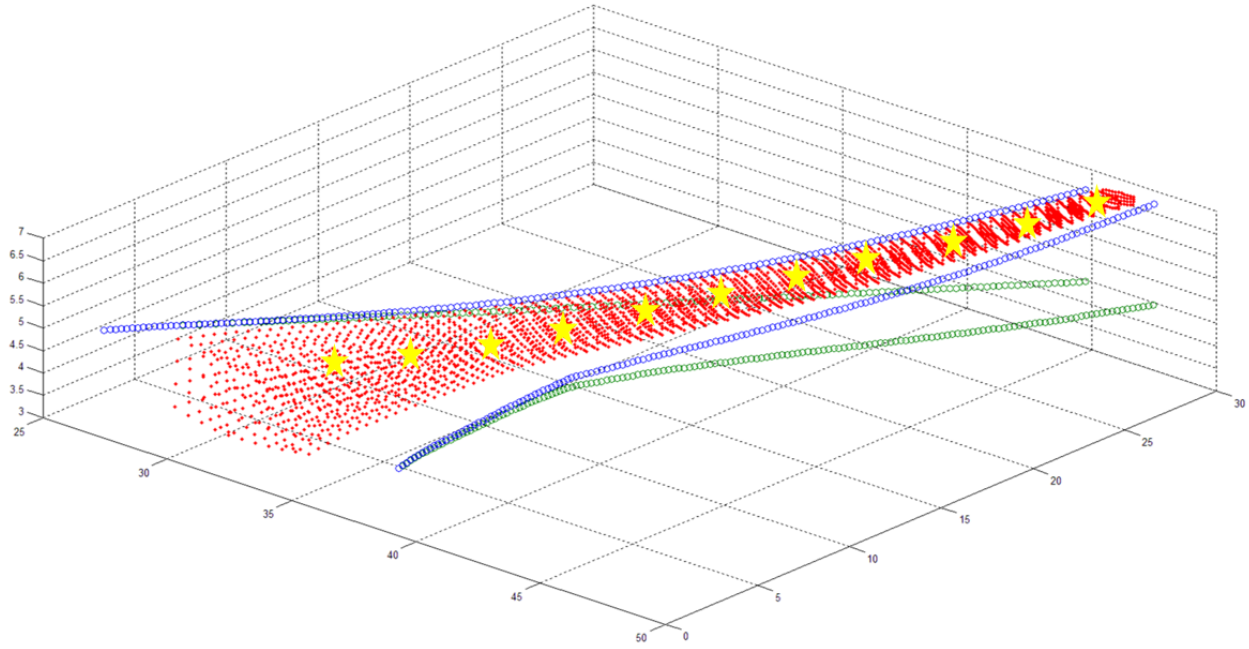

Figure 3.5: Load transferring method from FBG

Thus, in the global-level HFEM, external aerodynamic loads are transferred from the FBG point to the FEM by the MPC connection method. In Figure 3.5, the yellow star indicates the location of the FBG which are the independent nodes, the red dots are candidate dependent nodes. All free surface elements in the FE model requires to be corresponded with one independent node to transmit the load. In addition, when we have the functionality of the grouping, we can move FE model or change shape like adaptable mesh without changing geometry itself that is a big advantage in FE modeling. For example, in Figure 3.5 the green circles represent the initial shapes which is 0 g condition(ground condition), and the blue circles are shapes deformed by the loads which is 1

g condition(a cruise condition). This wing example is initially modeled for 1 g condition, but we can move it to 0 g condition or even 2 g condition as shown in Figure 3.6. The green is the initial position for 1G condition, blue is 2 g condition, and red is 0 g condition.

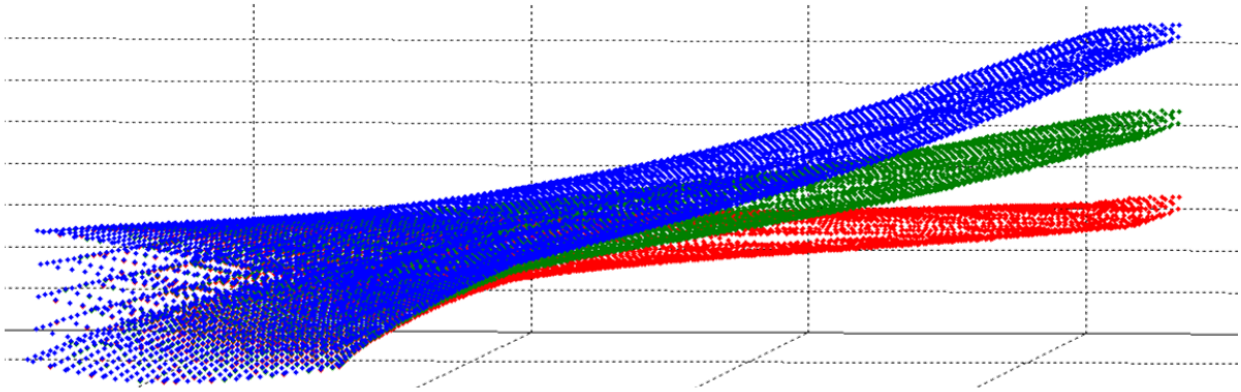

Figure 3.6: FE model shape change with elements grouping

3.3.2 Internal load transfer method

The applied external load in the global model needs to be passed on to the base-level FE model which is more detail model. The base-level can be any parts that is considered as critical parts, such as frame, skin, splices, and etc. The applied external load can be transformed to the internal forces through the analysis in global model. Then, the base-level FE will use the internal forces, which are point-grid forces, that are derived from the external forces in the global-level FE. In other words, when the global-level analysis finds a location that shows a critical remaining fatigue life, the location of element transfers the internal forces to its corresponding base-level model, thus constituent nodes in the element of global-level model are the points we need to have the internal forces. The framework developed by this study needed to find the critical location of element, its constituent nodes, and corresponding internal forces about the nodes from global-level analysis result. This series of processes should be automatic without any user interference because the new digital twin method should work as one FE model.

To help better understand the series of processes, let us assume that an initial possible crack at element 55 is detected by the result of global-level analysis, then the corresponding base-level model to the element 55 will be an FEM to progress the crack propagation. To analyze crack propagation in a base-level model, internal forces about constituent nodes in the element 55 will be extracted by an algorithm from the output file of global-level analysis. The output file which contains the internal forces for all elements in global model is often very large in ASCII format, but we only need to have the internal forces at the corner nodes of element 55. This study develops an algorithm that can search the element number, its corresponding nodes, and the internal forces of the nodes. Then, transfer the internal loads to input loads for the base-level model with a specific boundary condition, shown in Figure 3.7. The boundary condition in this figure applies only to the case in which an element is surrounded by other elements. In the case of an edge element, one degree of freedom for the free edge needs to be released.

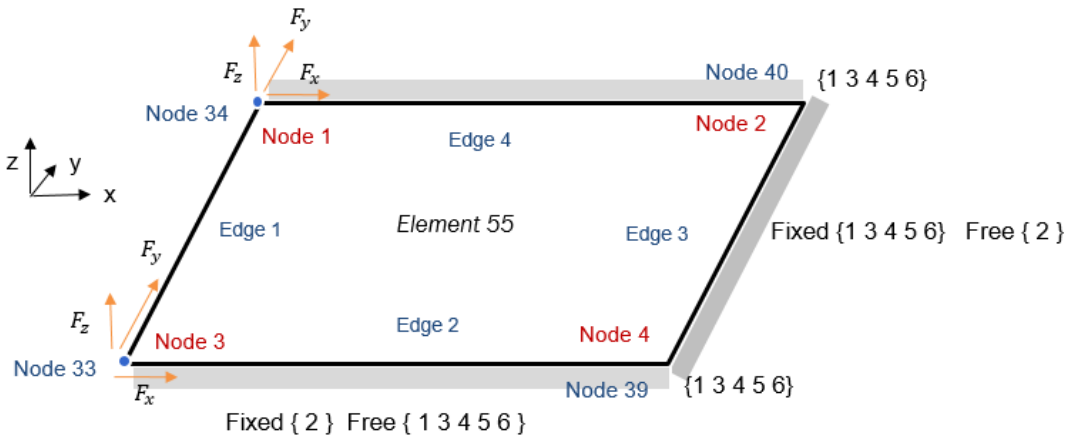

Figure 3.7: Free body diagram of grid forces

With the internal forces, the base-level model can calculate stress dependently in the area of an element. We can create the base-level model after initiating an analysis, but since the shape and size of elements in global-level model are very similar, having some representative models is preferable. Thus, grouping elements of a similar size and shape requires the introduction of a

cluster method.

3.3.3 Unit load method

As described in the previous section, the framework uses the unit load method to reduce the time consumption for stress analysis in the base-level model. The unit load method can be regarded as a direct result of the principle of virtual work, an application of the unit load method easily demonstrated by Euler-Bernoulli beam structures [39]. If the displacement at a point of the beam can be valued as magnitude Δ , the principle of virtual work can be explained as follows:

$$\Delta\delta D + \delta W_I^{'} = 0 \tag{3.1}$$

In the case of all statically admissible virtual forces in which δD is the virtually driven force, $\delta W_I^{'}$, is the internal virtual work in the Euler-Bernoulli beam. Then, the unit load method can be summarized in the following three steps.

1. Find the actual force and moment distributions acting in a beam subjected by the externally applied loads.

2. Apply a unit load at the point and in the direction of the all displacement components.

3. Evaluate the statically admissible force and moment distributions in the beam with equilibrium of the unit load.

To validate the unit load method for this framework, this study applies a simple beam model and a real wing box model to evaluate stress. In the example, six degrees of freedom are fixed at the root and 100 N of the concentration force is imposed as shown in Figure 3.8. For the unit load method, six unit loads, one in each degree of freedom, F_x, F_y, F_z, M_x, M_y, and M_z, are applied independently to construct a stress matrix. Once the stress matrix is complete, then stresses for other loading cases can be calculated by $Force \times StressMatrix$ without finite element analysis.

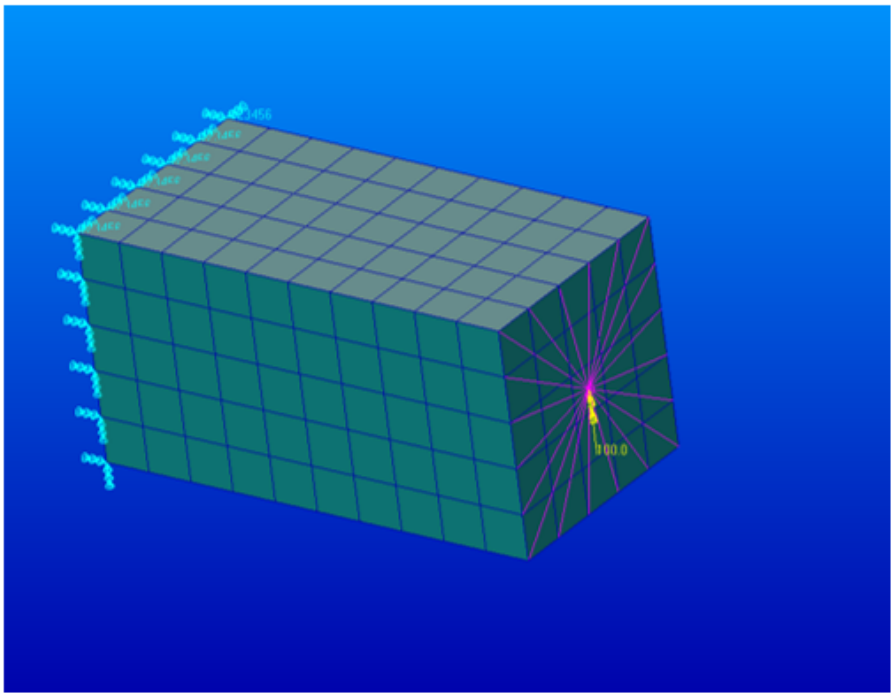

Figure 3.8: Validation model for simple beam

The results of the unit load method are compared with the results of general finite element analysis in Table 3.1. The results show almost a 0 % of error. However, we should note that this example is a very simple linear case. For further investigation, Figure 3.9 shows the error distributions of σ_x, σ_y, σ_{xy}, and Von-Mises stress (VMS) obtained by calculating the root mean square(RMS) and comparing t-distribution. As an example, the error distribution of VMS, the bottom-right distribution, illustrates accurate results of the unit load method with that a mean error of 0.00396 and a standard deviation of 0.0055

3.4 Base-model development

Representative base-level from selection of clustering results

Let us assume that the FE models of the HFEM are well integrated via previous methods. Then, the CIA informs the CPA of the possibility of an existing crack, initiating a crack propagation

	Force and Moment	Normal x	Normal y	Normal xy		von Mises
Force	0 100 0 0 0 0	-1.9245E+02	-3.4956E+00	5.8954E+01		2.1634E+02
	0 1 0 0 0 0	-1.9245E+00	-3.4956E-02	5.8954E-01		2.1634E+00
	Moment					
Moment	0 0 0 0 100 0	2.3731E+01	4.5760E-02	6.0411E-02		2.3708E+01
	0 0 0 0 1 0	2.3731E-01	4.5760E-04	6.0411E-04		2.3708E-01
Expected	0 100 0 0 100 0	-1.6871E+02	-3.4499E+00	5.9014E+01		1.9581E+02
TRUE	0 100 0 0 100 0	-1.6871E+02	-3.4499E+00	5.9014E+01		1.9581E+02
Error		0.0000%	0.0000%	0.0000%		0.00001%

Table 3.1: Results of the validation model for a simple beam

analysis. This process is part of the full framework, previously illustrated in Figure 1.9. We will focus on Figure 3.10 for this section.

When the CPA calculates the crack propagation, it must use the stress from the base-level model to calculate the stress intensity factor. In order to do this, the framework must have a finite element solver inside. However, carrying an FE solver should be avoided for the following reasons.

- FE solvers for the purpose of airworthiness are too powerful with many functions which invoke comparatively long run time.
- The purpose of this framework is to provide an on-board algorithm that can be embedded in all kinds of aircraft and a large number of drones. Thus, we prefer a simply way to get the stress distribution.
- The framework would become more complex if external software is used because of input and output file exchanging between the framework and external software.

We can solve the previous problems by simply performing a stress analysis prior to operating the framework. For the purpose of use later loading condition, the stress analysis should be conducted for unit loads. Then, the SHM will carry the performed stress information inside of the framework as a table array.

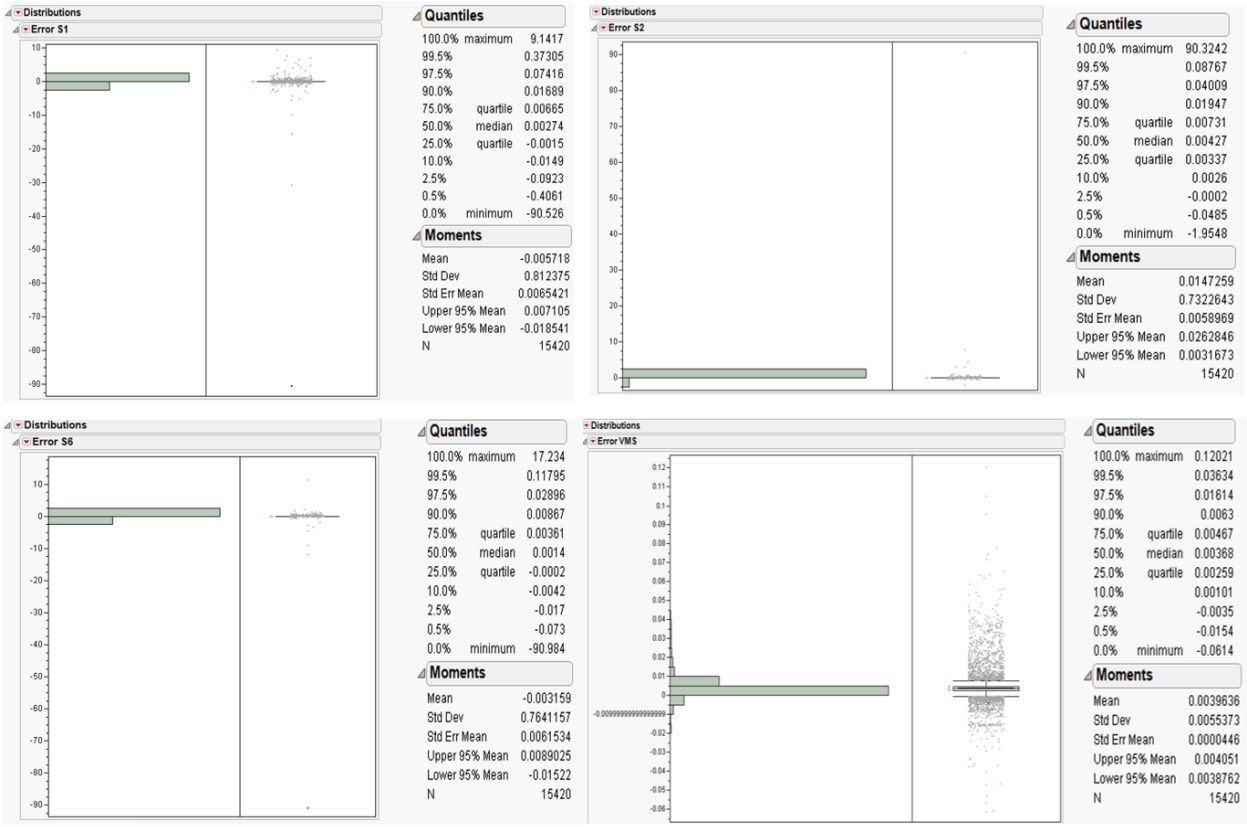

Figure 3.9: Error distributions of σ_x, σ_y, σ_{xy}, and VMS for the validation model

Since CPA cannot be informed about which elements are critical prior to the CIA result while operating, the framework needs to carry the results of unit loads for all elements, a considerable data and time-consuming task. Even though the static analysis would entail a simple calculation, solving the FE still takes some time. For example, if the FE analysis takes one second for one element, it will take 100,000 seconds, or about 28 hours, for 100,000 elements that the global-level model contains. Therefore, this study suggests an idea that carrying some representative elements only not all the elements. Actually, FEM elements are very similar for their shapes, sizes and properties. Specially, size should be similar as many to be a good FEM because it reduces singularity. Thus, we can pick some representative elements that are candidates for the base-level model. If one element is selected as a critical location, its base-level model will be that of the representative model.

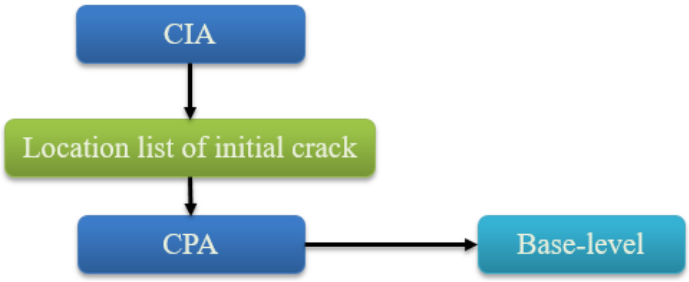

Figure 3.10: The initiation process of crack propagation

Following question is that how can we cluster the elements and pick the representative models? In Chapter 3.4.1, we will discuss the clustering method from machine-learning theories. The the clustering task, which will be carried out by the K-means algorithm, will result in ten clusters.

3.4.1 Clustering in machine learning

Machine learning is largely divided into supervised learning and unsupervised learning. Clustering is representative of unsupervised learning that finds clusters that best describe given data without adding label. To conduct classification, we need data and corresponding labels for the data; in reality, however, we already have data, but we do not know what the label or the category of the data is, so we need to explain the data in a way other than classification. The goal of clustering is to partition a dataset into some K number of clusters, with the value K normally given or assumed. Intuitively, we consider a cluster a group whose distances inside their space are shorter than those to points outside the group. Figure 3.11 illustrates a conventional clustering method, the K-means algorithm, using the re-scaled Old Faithful dataset [40].

In Figure 3.11, (a) is the initial dataset and the green points that we wish to cluster. The dataset is in a two-dimensional Euclidean space that also has initial cluster centers, $\mu_1$and μ_2, depicted by red and blue crosses, respectively. From (b) to (h), the clustering process presents an example of K-means with the application of the EM (expectation-maximization) algorithm. The EM algorithm is a general technique for finding maximum likelihood estimators in latent variable models, which

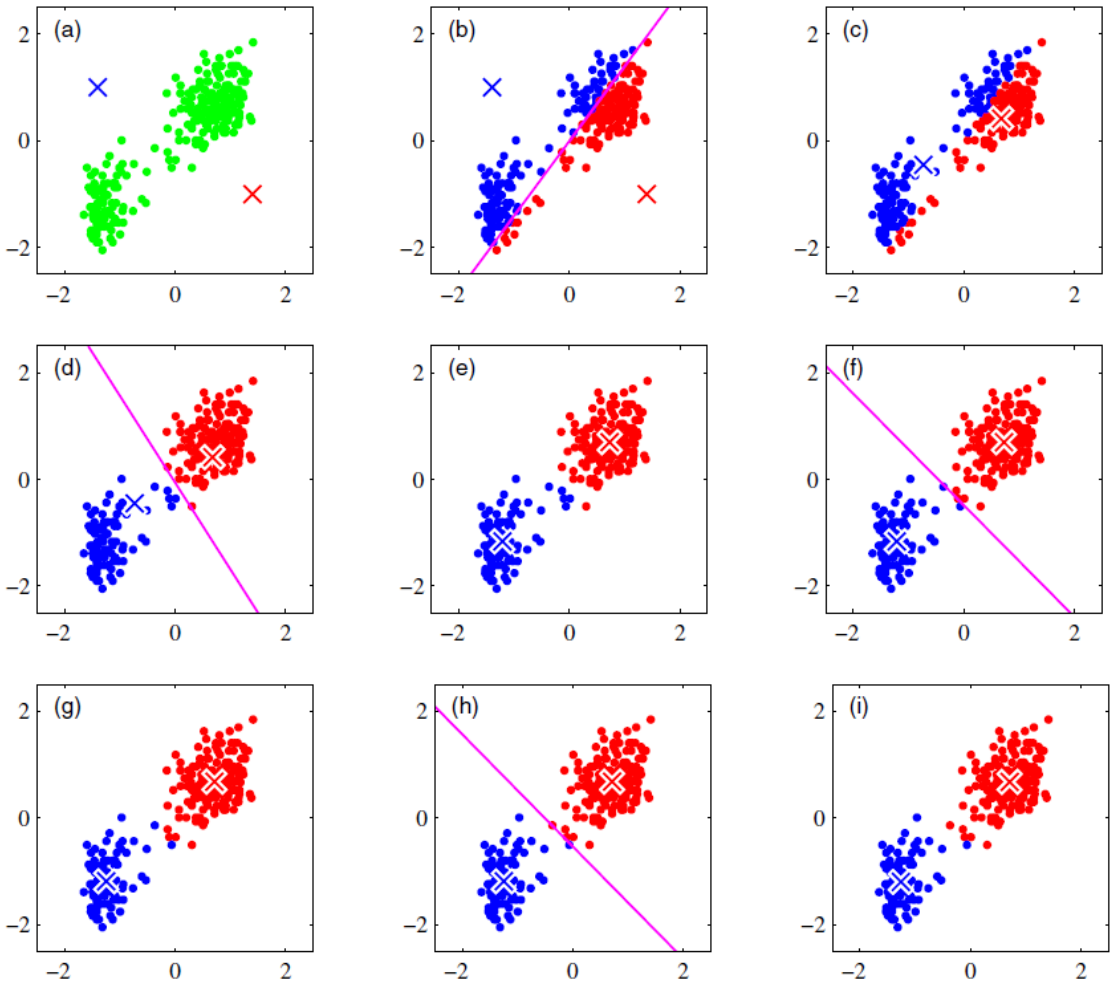

Figure 3.11: Illustration of K-means clustering algorithm [40]

we can use to determine the center of the clusters in this example. The goal of clustering is to find clusters that most accurately describe the given data in the absence of information about each piece of data. Therefore, we often use clustering to solve optimization problems as well as many other unsupervised learning problems. Although the EM algorithm is one way to solve the optimization problem, this study focuses more on the application of clustering. The figure presents the results of clustering in (i), which contains two clusters, blue and red, and the centers of these clusters are represented by their corresponding crosses.

This study uses a clustering algorithm from Python open source, Scikit-learn, an open forum of

machine-learning users. Scikit-learn defines various clustering methods in Table 3.2. For general purposes, only two dimensions are considered, and since the base-model clustering does not require many cluster centers, this study adopts the K-means algorithm for clustering with the global-level FEM.

Table 3.2: A comparison of clustering methods [41]

Method name	**Usecase**	**Geometry (metric used)**
K-Means	General-purpose, even cluster size, flat geometry, not too many clusters	Distances between points
Affinity propagation	Many clusters, uneven cluster size, non-flat geometry	Graph distance (e.g. nearest-neighbor graph)
Mean-shift	Many clusters, uneven cluster size, non-flat geometry	Distances between points
Spectral clustering	Few clusters, even cluster size, non-flat geometry	Graph distance (e.g. nearest-neighbor graph)
Ward hierarchical clustering	Many clusters, possibly connectivity constraints	Distances between points
Agglomerative clustering	Many clusters, possibly connectivity constraints, non Euclidean distances	Any pairwise distance
DBSCAN	Non-flat geometry, uneven cluster sizes	Distances between nearest points
Gaussian mixtures	Flat geometry, good for density estimation	Mahalanobis distances to centers
Birch	Large dataset, outlier removal, data reduction.	Euclidean distance between points

3.4.2 K-means clustering

A cluster can be defined in a number of ways. One of the simplest ways is as follows: data belonging to a cluster are those with the closest Euclidean distance. That is, the K-means algorithm assumes that data belonging to the same cluster are close to each other. In this case, each cluster has one "center," and the cost is defined as "how close each datum is to its center." The K-means algorithm finds clusters that minimize the defined cost, expressed in the following equation.

$$\min_{b,w} \sum_{n=1}^{N} \sum_{k=1}^{K} w_{nk} \|x_n - \mu_k\|_2^2 s.t. \sum_{j} w_{nk} = 1, \forall k \tag{3.2}$$

In Eq. (3.2), we assume an 'N' size of data and a 'K' number of clusters. To minimize the equation, we need to find and assign data points to clusters as well as a set of vectors $x_n$in which the sum of the squares of the distances of each data point to its closest vector μ_k. Each x_n corresponds to a binary variable in the vector of $w_{nk} \in \{0, 1\}$, where $k = 1, ..., K$. The set of binary variables indicates which of the K clusters the data point x_n is assigned to. If data point x_n is assigned to cluster k then $w_{nk} = 1$ and $w_{nj} = 0$, where the most case, $j \neq k$.

The goal of clustering is to find values for w_{nj} and μ_k while minimizing Eq. (3.2). This problem is difficult to solve because of the binary variable w_{nj}, which requires checking each cluster combination, one at a time, to obtain the optimal value. However, by avoiding joint optimization, we can fix either μ or w and then update the other one, then the optimization process can be a simple problem. When the remaining values are fixed, we can obtain the optimal value of μ_k by calculating the mean of the the 'mean' of the 'k'th cluster. This is why this method is referred as the K-means algorithm for finding the mean for the number of k. The optimal value of w_{nk} for all data 'k' is acquired by assigning it to the cluster with the smallest '$x_n - \mu_k$' among all clusters.Therefore, if we know exactly one of the other variables, conducting alternative optimization becomes relatively simple. We called the iterative procedure expectation (fixing a value with expectation)/maximization (optimizing the other value, the distance).

3.4.3 Clustering method for selecting representative base-level models

Using a K-means clustering algorithm for base-model clustering, we partition the various shapes and sizes of the component elements in a global-level model into k clusters. Each cluster center is a candidate for the base-level model, which conducts crack simulation with a fine mesh. Then, each candidate of the base-level model has a stress distribution map generated by six components of unit loads on the unit element. Therefore, we need results for only the cluster center elements from the FEM. An example of clustering results and the element shape of a cluster center are shown in Figure 3.12. The application of K-means clustering for base-model clustering, however, is not a simple problem because of the dimensions of the elements. In the input file of FEM, an element has four nodes when we assume it is QUAD4 element. Each node consists of three coordinate values; the location of x, y, and z. Thus, each element has $4 \times 3 = 12$ dimensions, an undesirable number for clustering. However, we can easily reduce the 12 dimensions by geometric correlation. For instance, Figure 3.13 describes a QUAD4 element and corresponding information. Node numbers begin at the top-left of the element (the arrow shows node 1). Although each of the four nodes carries three-dimensional geometry information(x,y,z coordinates), because of the symmetric shape, we need to know only the distance of either the top or the bottom lines and the distance of either the right side or left side line.

The framework developed in this study conducts dimension reduction prior to K-means clustering. For real-world applications, in the NASTRAN input file, element information is represented in Figure 3.14. Starting with the first column, each column represents the following information about each element: the type, the number, the property, node 1, node 2, node 3, and node 4. When crack propagation is initiated by the global-level FEM, we have information only about the element number, that is, the number of elements with possible cracks, and then we must conduct the propagation analysis. For example, if we analyze the crack propagation of element 55 with nodes 55, 56, 157, and 156, then we assume that each node has actual coordinate data, as shown in Figure 3.15,

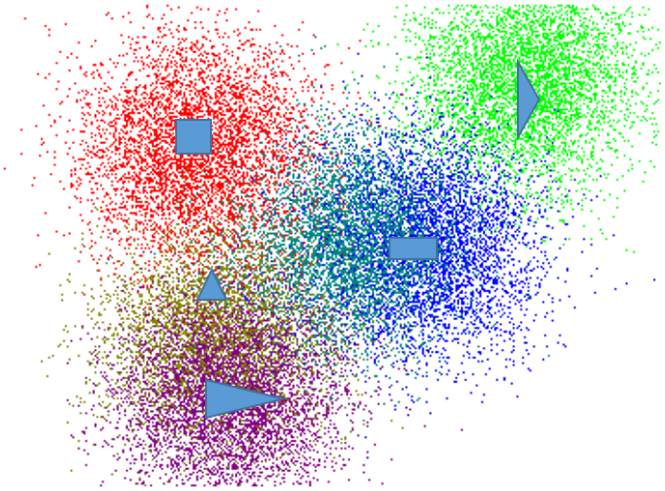

Figure 3.12: An example of clustering result

Figure 3.13: An example of QUAD4 element

with the type, the number, and the x, y, and z coordinates. From this assumption that element 55 is the base-level model, the framework obtains the coordinate data by first searching for element number 55 and then its corresponding four nodes. With the information of the coordinate data and the four nodes, we need to reduce the dimension from 12 to 2.

The reduction algorithm begins by assuming that the first node, in this example, the fixing node, is node 1, indicated by the large arrow in Figure 3.13. As we do not know the diagonal node of node 1, we find the diagonal node by calculating the maximum of the norm for the other nodes:

```
CQUAD4   50      1       50      51      152     151
CQUAD4   51      1       51      52      153     152
CQUAD4   52      1       52      53      154     153
CQUAD4   53      1       53      54      155     154
CQUAD4   54      1       54      55      156     155
CQUAD4   55      1       55      56      157     156
CQUAD4   56      1       56      57      158     157
CQUAD4   57      1       57      58      159     158
CQUAD4   58      1       58      59      160     159
CQUAD4   59      1       59      60      161     160
CQUAD4   60      1       60      61      162     161
CQUAD4   61      1       61      62      163     162
CQUAD4   62      1       62      63      164     163
CQUAD4   63      1       63      64      165     164
CQUAD4   64      1       64      65      166     165
CQUAD4   65      1       65      66      167     166
CQUAD4   66      1       66      67      168     167
CQUAD4   67      1       67      68      169     168
CQUAD4   68      1       68      69      170     169
CQUAD4   69      1       69      70      171     170
CQUAD4   70      1       70      71      172     171
```

Figure 3.14: An element section of NASTRAN input file

```
GRID     50              49.     100.    0.
GRID     51              50.     100.    0.
GRID     52              51.     100.    0.
GRID     53              52.     100.    0.
GRID     54              53.     100.    0.
GRID     55              54.     100.    0.
GRID     56              55.     100.    0.
GRID     57              56.     100.    0.
GRID     58              57.     100.    0.
GRID     59              58.     100.    0.
```

Figure 3.15: A grid section of NASTRAN input file

nodes 2, 3, and 4. Then we can determine which node is actually node 4, the diagonal node, and the other nodes 2 and 3 as well. After defining the node numbers, we can calculate the length of the edges by the following equations.

$$\Delta y_{12} = \max(|x_1 - x_2|, |y_1 - y_2|, |z_1 - z_2|) \tag{3.3}$$

$$\Delta y_{34} = \max(|x_3 - x_4|, |y_3 - y_4|, |z_3 - z_4|) \tag{3.4}$$

$$\Delta y = avg(\Delta y_{12}, \Delta y_{34}) \tag{3.5}$$

$$\Delta x_{13} = \max(|x_1 - x_3|, |y_1 - y_3|, |z_1 - z_3|) \tag{3.6}$$

$$\Delta x_{24} = \max(|x_2 - x_4|, |y_2 - y_4|, |z_2 - z_4|) \tag{3.7}$$

$$\Delta x = avg(\Delta x_{13}, \Delta x_{24}) \tag{3.8}$$

The Δx and Δy are the input metrics for the clustering method explained above. Figure 3.16 presents the clustering results for all elements in the global level. The different colored crosses indicate the cluster centers, each of which represents the base-level model for its group. These results show ten clusters, each with a number of samples, shown in Table 3.3. The results for the QUAD elements indicate that the global level has 7,650 elements. In Figure 3.16, the x-axis represents the lengths of the top or bottom edges and the y axis the side edges. The figure shows all elements labeled with their cluster centers.

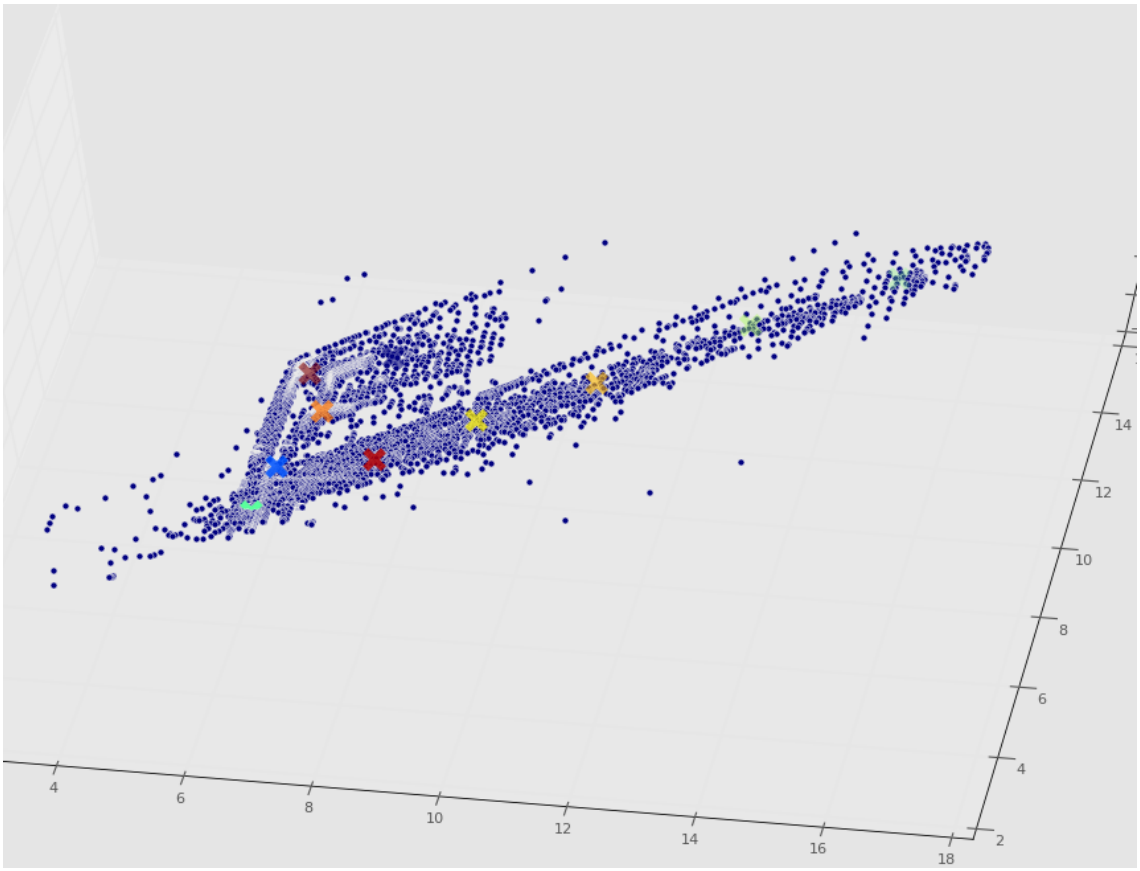

Figure 3.16: K-means clustering result for all elements in global-level

3.4.4 Additional micro-level models for composite materials

So far the HFEM has been applied to only metallic material. In a case of composite material, the stress map for the base-level model must contain additional information about laminate properties, which can be derived from a micro-level model. For the connection between the base and micro-levels, to formulate the constitutive relationship, this study proposes strain amplification factors as an important parameter in strain invariant theory (SIFT) [35]. An analysis of damage by SIFT (discussed in the introduction of SIFT in Chapter 2.6.3) requires that the SIFT of the micro concept be converted to that of the macro concept, thus simplifying its application. For example, we apply the global-level FE model for the static analysis without accounting for the effects of the fiber or the matrix, which entails a huge global FE and great detail, because such an effort would consume

Table 3.3: Results of K-means clustering

Cluster center	**Sample number**
0	562
1	2426
2	582
3	166
4	367
5	1092
6	500
7	221
8	1088
9	646
Total	**7650**

too much time.

To solve the time consumption issue in the framework, this study introduces a micro-mechanical factor, the strain-amplification factor which has been used for SIFT analysis. The strain amplification factor can be obtained by an FEM analysis of virtual composite specimens and stored in a database table. We use Eq. (3.9) to calculate the amplification factors with micro-mechanical unit-block models.

$$M_{ij} = \frac{\epsilon_{ij}}{(\Delta L_{ij}/L_0)}, \tag{3.9}$$

where ϵ_{ij} is a local strain, ΔL_{ij} is the prescribed unit displacement and L_0 is the original length of representative volume elements (RVE), an explicit model of the fiber and the matrix. The amplification factor need to be calculated from 20 locations, described in Figure 3.17. The figure shows that F9 measures the fiber strain, F1 to F8 measure the interaction in the fiber, M1 to M8

measure the interaction in the matrix, and IF1, IF2, and IS measure the matrix strain [35].

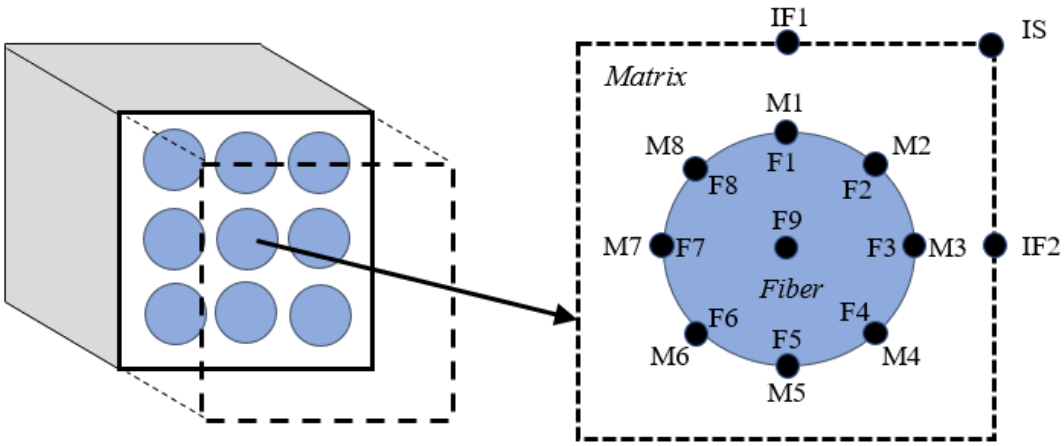

Figure 3.17: Amplification factor points[42]

To determine the appropriate amplification factors, type of fiber arrangement for a unit-block model, the representative volume elements(RVEs), are needed to identify the fiber and matrix shapes. In micro-level modeling, three shapes of fiber arrays, that are mostly used in industry are assumed to be ideal: squares, hexagons, and diamonds. From the stress analysis for the three unit of tensile loads, Figure 3.19 shows strain distributions for the square array of RVEs. The normalized strain distribution acts as a factorized ratio at specific points, shown in Figure 3.18. These points indicate F as the fiber area and M as the matrix area, which we use to distinguish independent applications of material properties and to analyze micromechanical failure, such as the breakage, delamination, or bounding of the fiber or the matrix.

Material properties of RVE model need to be defined as fiber and matrix respectively. Fiber property is determined as 3 dimensional orthotropic material , but matrix can be described as isotropic material. An example of material property of RVE is described in Table 3.4.

As the final result, amplification factors at the points described in Figure 3.17 act as a scale factor that can deliver stress magnitude in the lower level of FEM to the higher level of FEM by representing the structure format as shown in Figure 3.20. On a higher level, the ply model may

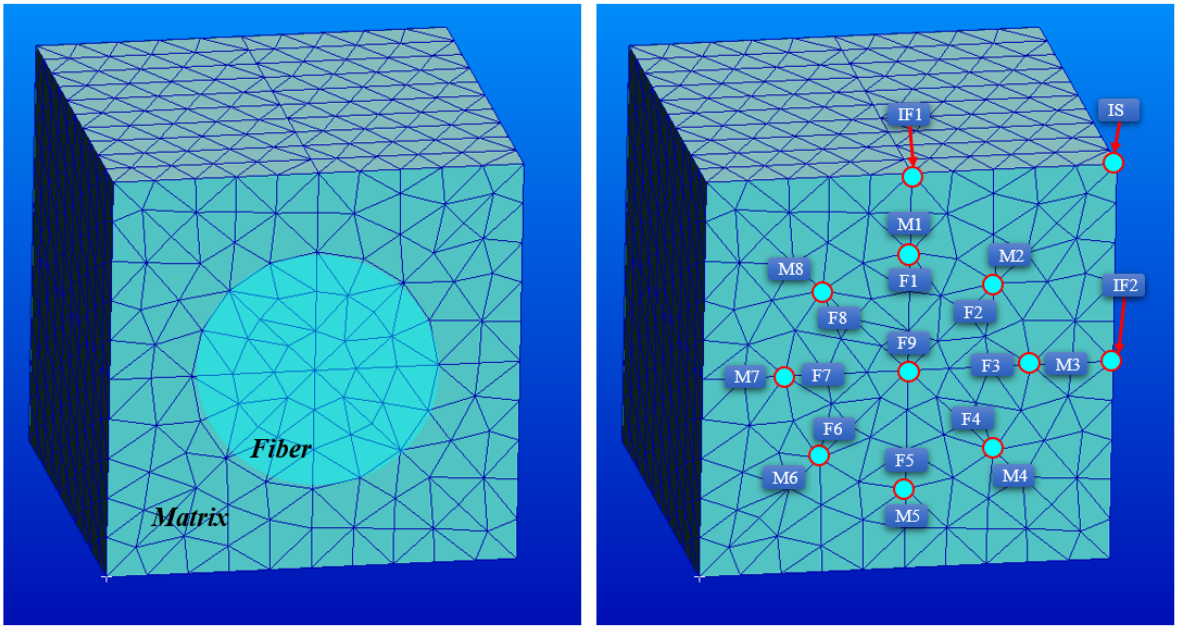

Figure 3.18: Example of RVE and amplification factor points

have a single ply or laminated plies, such as coupon-based composites. For coupon-based composite design, an examination of the mechanical and material properties of a ply from experimental coupon tests are often required to find the behavioral characteristics of a layer to laminated composites. The characteristic of coupon-based composites will be reflected on laminated composite models to be acting as a base model for the analysis of crack propagation.

3.5 Validation of Hierarchical Finite Element

By comparing the results of the FE analysis of the global model with those of the single model analysis of the corresponding element, we can validate the stress analysis functionality of HFEM. To compare these results, we first select a specific element after the FE analysis in the global model and extract the corresponding grid force (e.g., to extract the grid force in the sub-case in the Nastran input field, the input file should place the output request, GPFORCE = ALL.) The case of the Quad4 element consists of four corresponding nodes, so the four grid-forces are in the output

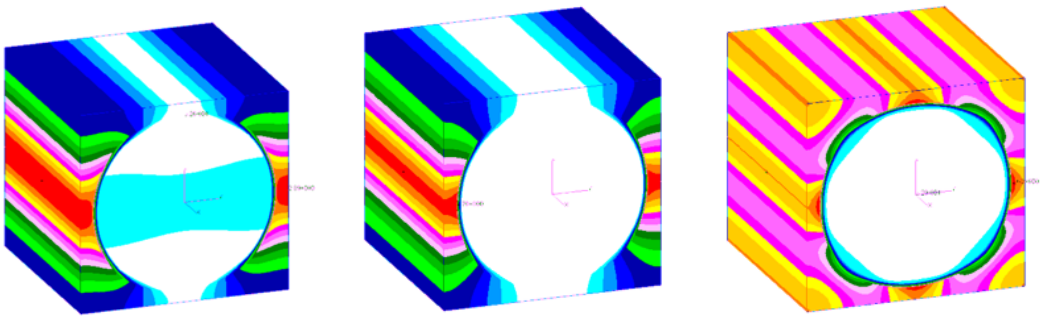

(a) Direction 22 (b) Direction 12 (c) Direction 23

Figure 3.19: Example of strain distributions for square array of RVE

	Carbon Fiber	*Epoxy*
E_{12}	6.6 GPa	2.96 GPa
E_{22}	6.6 GPa	
E_{33}	198 GPa	
ν_{12}	0.3	0.35
ν_{23}	0.01	
ν_{31}	0.2	
G_{12}	3 GPa	1.096 GPa
G_{23}	3 GPa	
G_{31}	8.5 GPa	

Table 3.4: Material properties for RVE [43]

results that need to be the input forces of the base model. With a specific element in the global model, the base model independently forms the same geometry and then conducts the FE analysis. If the stress or displacement values of the base model are similar to those of the global model, we can assume that the HFEM works correctly. Furthermore, the HFEM uses the base model as a detailed model for crack propagation, so the FE model requires only stress. Therefore, with an accurate calculation of the value of stress, we assume that no problems will arise from the model in the future with regard to the analysis of crack propagation. In other words, the verification of both stress and crack propagation or initiation analysis methods ensures verification of the entire

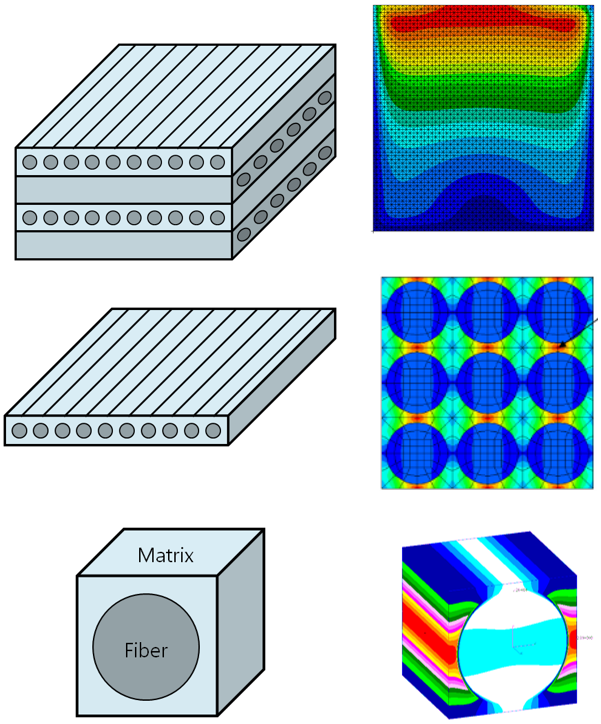

Figure 3.20: Micro-mechanical approach to base-level HFEM

framework.

3.5.1 A case study for the verification of global and base models

The following process with a simple example represents how to connect the global and base models and to verify this method through a comparison of stress. Figure 3.21 describes a thin rectangular plate 11 mm long, 5 mm wide, and 2 mm thick. The size of each element in the model is 1 mm $\times$ 1 mm.

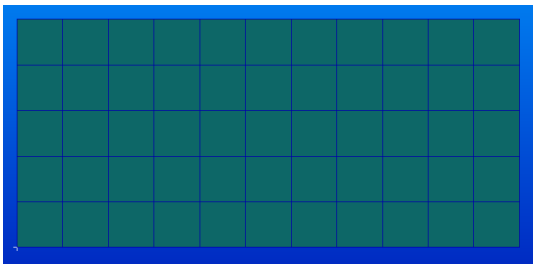

Figure 3.21: Validation example of global model

The material is Al-7050-T7451, the elastic modulus is 71,700 MPa and shear modulus is 26,900 MPa. For the boundary conditions, all directions of six degrees of freedom were constrained at the root, and 1 N and 10 N forces were applied to the ends of the material in the y and z directions, respectively. Figure 3.22 shows the combined force of two directions and the fixed boundary conditions.

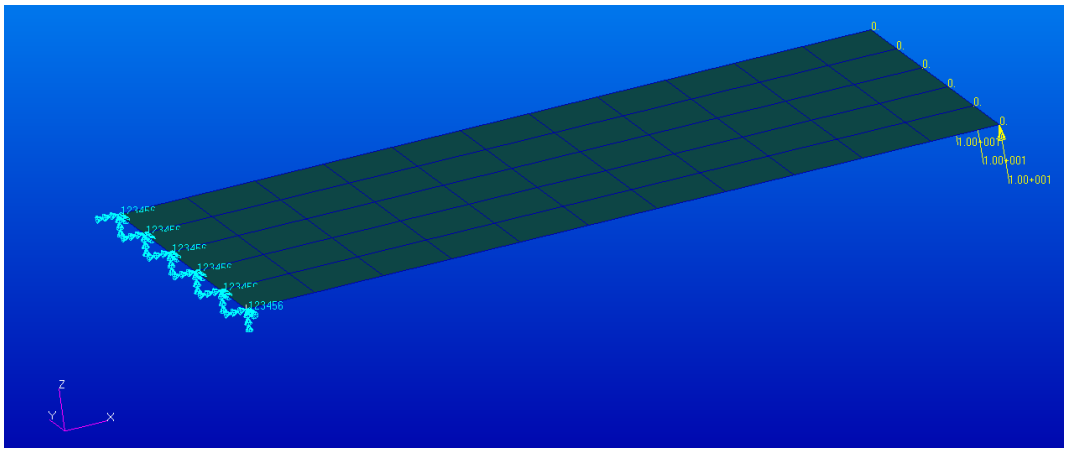

Figure 3.22: Boundary and force conditions

The results of FE analysis conducted with NASTRAN are presented in Figure 3.23 and Figure 3.24. The two figures show that maximum stress, 184 MPa, occurred near the root and translational displacement, 0.111 mm, occurred in the direction of z coordination. Now we select element 55, located in the middle of the global model; in Figure 3.24, the middle red rectangle describes the corresponding element, element 55, while showing the stress values of the four nodes.

The HFEM developed in this study reads the internal grid force of elements from the output file, such as those shown in Figure 3.25, corresponding to each component node. The HFEM extracts the grid force, the values in the red dotted boxes, to utilize it in the analysis of the base model. Figure 3.26 shows the grid forces extracted from the results of the global model by the HFEM framework. The algorithm for extracting grid forces for the base level appears in Appendix F.

Next, for the base model, the same geometry model as global Element 55 is independently generated. The base model is 1 $\times$ 1 mm and 2 mm thick, the same material and properties as that

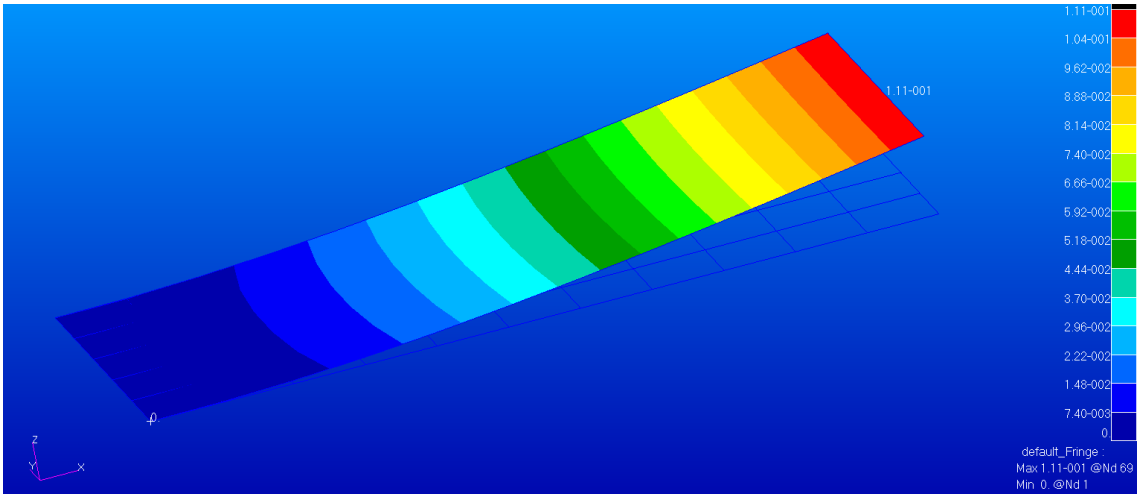

Figure 3.23: The deflection results of the global model

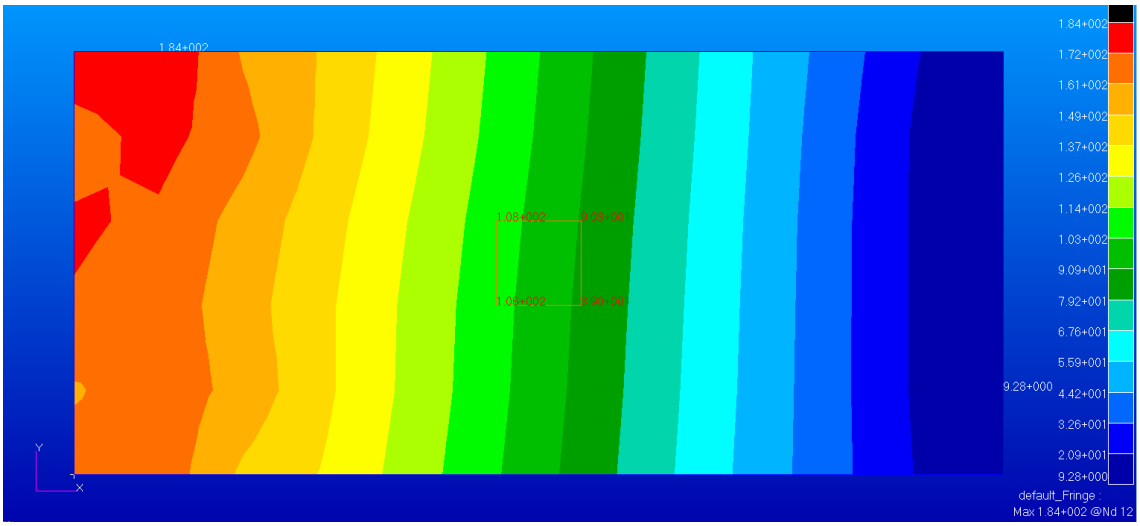

Figure 3.24: The stress results of the global model

of the global model, but fine meshes on. The stress distributions for the corresponding elements in the global model and those in the base model are compared in Table 3.5 for the stress values at each node. As evident from the tiny percentage error shown by the table, the connection method for the global and base models in HFEM works very well.

```
1475 0        33            22     QUAD4        -2.303462E+00  -7.584181E-01  -5.024008E+00  -3.968332E-01   3.557631E+01  -2.609456E-05$
1476          33            23     QUAD4         5.763095E-01  -8.887159E-01  -5.173099E+00   1.298187E+00   3.639502E+01  -3.864132E-05$
1477          33            53     QUAD4         5.759018E-01   7.598255E-01   5.264746E+00  -1.141440E+00  -3.651778E+01   3.864132E-05$
1478          33            55     QUAD4         1.151250E+00   8.873086E-01   4.932362E+00   2.400857E-01  -3.545355E+01   2.609456E-05$
1479          33                   *TOTALS*     -6.217249E-15  -5.773160E-15  -5.835332E-13  -7.105427E-14   1.705303E-13   3.252607E-19$
1480 0        34            23     QUAD4        -5.763095E-01  -8.887159E-01  -5.173099E+00  -1.298187E+00   3.639502E+01  -3.864132E-05$
1481          34            24     QUAD4         2.303462E+00  -7.584181E-01  -5.024008E+00   3.968332E-01   3.557631E+01  -2.609456E-05$
1482          34            52     QUAD4        -5.759018E-01   7.598255E-01   5.264746E+00   1.141440E+00  -3.651778E+01   3.864132E-05$
1483          34            55     QUAD4        -1.151250E+00   8.873086E-01   4.932362E+00  -2.400857E-01  -3.545355E+01   2.609456E-05$
1484          34                   *TOTALS*      1.332268E-14   3.552714E-14   7.362999E-13   1.092459E-13   3.907985E-13  -1.084202E-18$
1485 0        35            24     QUAD4         1.439673E+00  -7.284979E-01  -5.668463E+00  -1.658176E+00   3.714181E+01  -5.137268E-05$
1486          35            25     QUAD4         3.744064E+00  -3.444386E-01  -6.289787E+00  -1.544883E-01   3.490751E+01  -1.358579E-05$
1487          35            51     QUAD4        -2.591741E+00   3.446626E-01   6.807417E+00   8.587952E-01  -3.732455E+01   5.137268E-05$
1488          35            52     QUAD4        -2.591996E+00   7.282738E-01   5.150833E+00   9.538688E-01  -3.472476E+01   1.358579E-05$
1489          35                   *TOTALS*      8.881784E-16   4.973799E-14  -4.884981E-13   4.529710E-14   4.192202E-13  -1.517883E-18$
1490 0        36            25     QUAD4         3.744279E+00  -2.799363E-01  -7.844710E+00  -1.269413E+00   3.597977E+01  -3.239917E-05$
1491          36            51     QUAD4        -3.744279E+00   2.799363E-01   7.844710E+00   1.269413E+00  -3.597977E+01   3.239917E-05$
1492          36                   *TOTALS*      7.105427E-15  -1.465494E-14  -3.588241E-13   1.456613E-13   4.263256E-14   2.168404E-19$
1493 0        37            26     QUAD4         3.119729E+00   2.803816E-01   8.086546E+00  -1.378012E+00  -2.998887E+01   2.702712E-05$
1494          37            54     QUAD4        -3.119729E+00  -2.803816E-01  -8.086546E+00   1.378012E+00   2.998887E+01  -2.702712E-05$
1495          37                   *TOTALS*     -5.329071E-15   3.019807E-14   2.700062E-13  -1.776357E-14  -2.593481E-13  -1.517883E-18$
1496 0        38            26     QUAD4         2.063559E+00   3.447993E-01   6.797634E+00  -8.337413E-01  -3.144252E+01   4.587218E-05$
1497          38            27     QUAD4         2.256614E+00   7.277155E-01   5.192070E+00  -1.248933E+00  -2.858008E+01   8.084459E-06$
1498          38            53     QUAD4        -1.103882E+00  -7.282974E-01  -5.424124E+00   1.574314E+00   3.135928E+01  -4.587218E-05$
1499          38            54     QUAD4        -3.216291E+00  -3.442174E-01  -6.565581E+00   5.083603E-01   2.866331E+01  -8.084459E-06$
1500          38                   *TOTALS*      8.881784E-16   1.332268E-14   1.469047E-12   2.122746E-13  -5.684342E-13   2.168404E-19$
1501 0        39            27     QUAD4         3.370400E-01   7.596018E-01   5.098044E+00  -9.518817E-01  -3.057986E+01   3.330598E-05$
1502          39            28     QUAD4         1.103594E+00   8.875087E-01   4.825773E+00  -7.688996E-02  -2.940901E+01   2.074668E-05$
1503          39            53     QUAD4        -2.064015E+00  -7.598019E-01  -4.991455E+00   2.477035E-01   2.946768E+01  -2.074668E-05$
1504 1     MSC.NASTRAN JOB CREATED ON 13-FEB-17 AT 16:33:05                    FEBRUARY  16, 2017  MSC.NASTRAN 11/25/11   PAGE    39$
1505       DEFAULT
1506 0                                                                                                          SUBCASE 1
1507 _$
1508                                                G R I D   P O I N T   F O R C E   B A L A N C E$
1509 _$
1510     POINT-ID    ELEMENT-ID     SOURCE            T1             T2             T3             R1             R2             R3$
1511          39            55     QUAD4         6.233812E-01  -8.873086E-01  -4.932362E+00   7.810682E-01   3.052119E+01  -3.330598E-05$
1512          39                   *TOTALS*     -2.975398E-14   3.552714E-15   4.831691E-13  -5.240253E-14  -6.075140E-13   8.673617E-19$
1513 0        40            28     QUAD4        -1.103594E+00   8.875087E-01   4.825773E+00   7.688996E-02  -2.940901E+01   2.074668E-05$
1514          40            29     QUAD4        -3.370400E-01   7.596018E-01   5.098044E+00   9.518817E-01  -3.057986E+01   3.330598E-05$
1515          40            52     QUAD4         2.064015E+00  -7.598019E-01  -4.991455E+00  -2.477035E-01   2.946768E+01  -2.074668E-05$
1516          40            55     QUAD4        -6.233812E-01  -8.873086E-01  -4.932362E+00  -7.810682E-01   3.052119E+01  -3.330598E-05$
1517          40                   *TOTALS*     -2.087219E-14  -5.062617E-14   7.371881E-13   2.602363E-13  -3.801404E-13   0.0$
```

Figure 3.25: The example of output file for grid forces

Index	node	element	T1	T2	T3	R1	R2	R3
76	33	55	1.15	0.887	4.93	0.24	-35.5	2.61e-05
79	34	55	-1.15	0.887	4.93	-0.24	-35.5	2.61e-05
90	39	55	0.623	-0.887	-4.93	0.781	30.5	-3.33e-05
94	40	55	-0.623	-0.887	-4.93	-0.781	30.5	-3.33e-05

Figure 3.26: The grid forces extracted by the HFEM framework

Table 3.5: Comparison of the stress results for the global and base models

Base model		**Global model**		
Node number	***Von Mises Stress (MPa)***	***Node number***	***Von Mises Stress (MPa)***	***Error(%)***
Node 1	1.08E+02	Node 34	1.08E+02	0%
Node 2	8.81E+01	Node 40	9.03E+01	-2%
Node 3	1.07E+02	Node 33	1.06E+02	1%
Node 4	8.66E+01	Node 39	8.90E+01	-3%

CHAPTER 4
CRACK INITIATION ANALYSIS

Crack initiation, an assumption of initial cracking, can be determined by strain-life approach or stress-life approach with classical theories. One approach that is commonly used for estimating initial cracks or low cycle fatigue in not only the aerospace field but also general engineering fields is the strain life approach [44] [45]. This approach has been used on many aluminum alloys such as 2024 and 7075, the most commonly used materials in aerospace engineering [46]. However, the low cycle fatigue behavior is generally for the case of fast moving part such as engine parts in aircraft. Most primary structure and main part of aircraft which we want to construct in this study relates to high cycle fatigue behavior and that can be more suitable with stress life approach as crack initiation analysis [47] [48].

Figure 4.1 illustrates the integrated process of the CIA module with the HFEM. The load spectrum is an assumed spectrum that can be generated during the acquisition of strain information from FBG sensors.The load spectrum, a non-dimensional unit load spectrum, must be multiplied by the stress analyzed at the global-level of the HFEM. Then, the load spectrum is converted to the stress spectrum scaled by stress and load data. The stress spectrum generally consists of irregular amplitude loading that requires a counting method. For spectrum counting, this study uses rainflow counting, a standard counting method. The output of rainflow counting can be represented as a matrix with the mean stress, the intensity of stress, and the number of cycles. With either the stress- or strain-life approach, the matrix can easily be used for calculating damage while accounting for the mean stress effect, which is related to the mean of the amplitude stress. The damage results from the approach, which generates damage for a block of the spectrum matrix, is accumulated with the Miners rule. Then damage can be converted to the fatigue life with Life $= 1/$ accumulated damage. The results of CIA represent the cycles of fatigue life for ev-

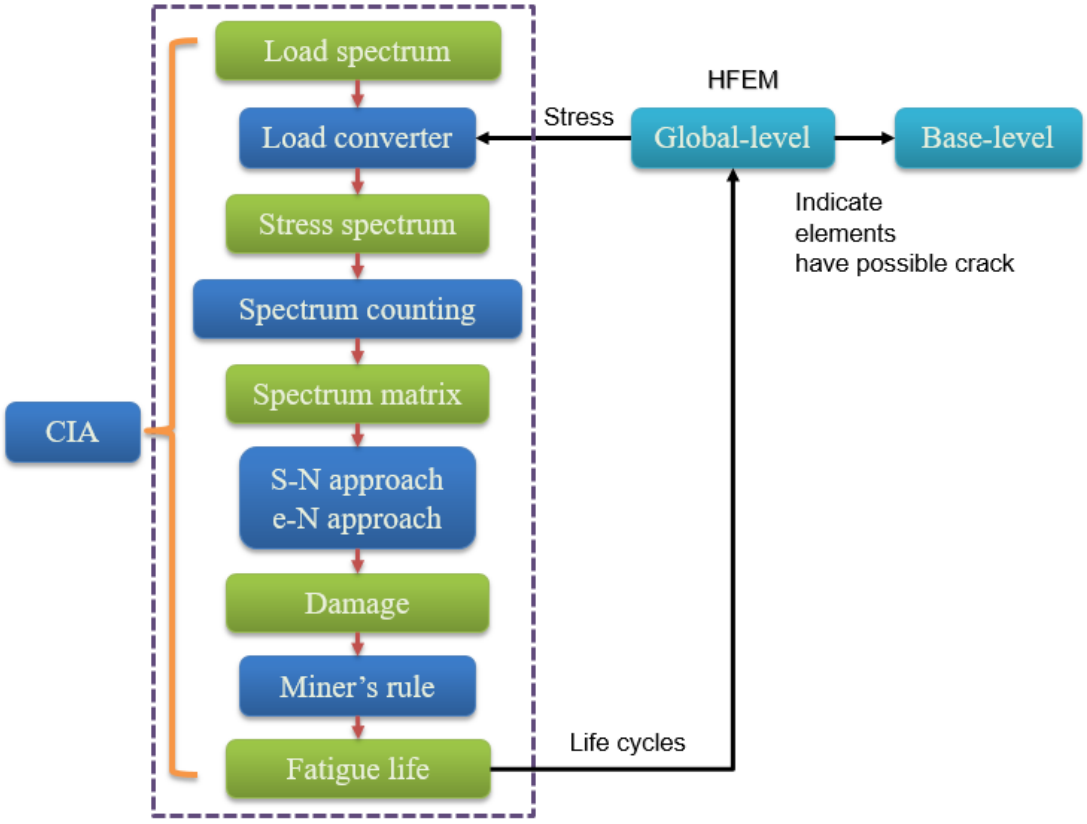

Figure 4.1: The flow diagram of CIA

ery element in the global model in the HFEM. Finally, the HFEM indicates elements that have have possible cracks based on the results of CIA to the base-level model. Thus, base-level models initiate a crack propagation analysis whenever the cycles reach a critical condition.

4.1 Fatigue Load Spectrum

Producing reliable fatigue life or crack growth analyses for aerospace structures require test dynamic loads that represent realistic loadings on a structure, which in turn, requires test loading for adequately representing common types of loading. By standardizing the test-load sequence, we can exchange and compare the variable amplitude test results of various origins while building a database containing many spectrum reference data points. Loading standards have been defined by several European aeronautical institutes: FALSTAFF for fighter aircraft wings, TWIST and Mini

TWIST for transport aircraft wings, HELIX and FELIX for helicopter rotor blades, Cold TURBISTAN for tactical aircraft cold-end engine disks, and ENSTAFF for tactical aircraft wing skin composites [49] [50].

To represent the test loading spectrum for this study, we selected the Transport Wing Standard (TWIST) to simulate loading on a transport aircraft wing. The TWIST spectrum represents the load history of the wing root of transport aircraft such as the Boeing 720, Boeing 737, and DC-10, among others [51] [52]. From historical data, the frequencies of certain levels of relative stress are determined by their intensities during flights. The intensities of flight load levels are assumed by ten different gust load conditions, which determine the amount of stress that the wing root would be under the mean flight stress value. All stress levels in the spectrum are normalized to 1 by the mean stress value. After all, the TWIST spectrum is became a normalized spectrum that can be used generally for a transport aircraft. The TWIST spectrum contains 40,000 flights and the most severe flights (each denoted as a level I flight with an amplitude of 1.6 times that of the mean flight stress value) occurred only ten times during the entire 40,000 flights. Thus, we often use a reduced spectrum that is one tenth of 40,000 flights. Figure 4.2 represents a TWIST spectrum with 4,000 flight cycles. It contains 797,330 points, and the maximum level is 2.6 with a mean of 1 for the 4,000 flights. The minimum value is -0.6, which is the ground level value that can sometimes be ignored in a tensile-to-tensile fatigue analysis.

This historically-based spectrum is recommended for performing cycle counting analysis. For analysis and testing purposes, cycle counting summarizes and simplifies the results of a complicated load spectrum. Perhaps the most widely accepted method of identifying critical fatigue events is Rainflow counting. This study used the Rainflow cycle counting program, written in Fortran, which was supplied courtesy of members of the SAE Fatigue Design and Evaluation Committee [53].

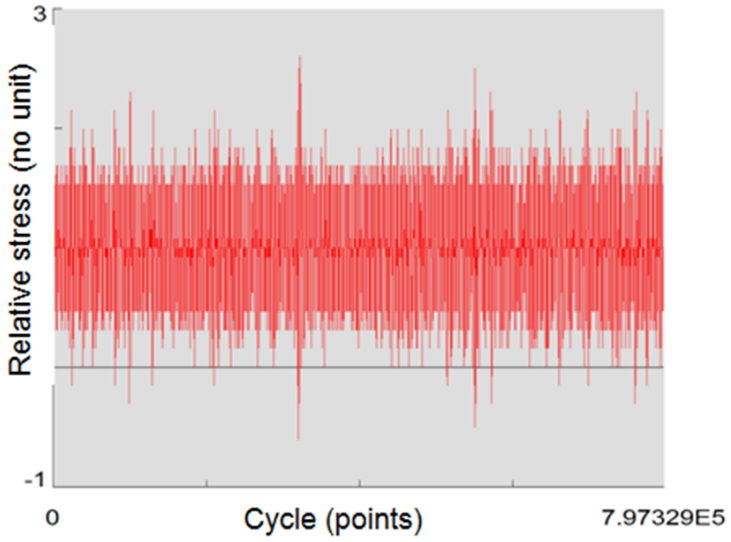

Figure 4.2: Example of load spectrum from TWIST

4.2 Strain Life Approach

Crack initiation can be estimated by the strain life approach, which is typically used in the low-cycle fatigue region where the applied strains have a dominant plastic component. In this regime, cyclic loads are relatively large and undergo a significant amount of associated plastic deformation in addition to relatively short lifetimes. This type of behavior has traditionally been referred to as "low cycle fatigue," and more recently, "strain-controlled fatigue" [54]. The strain life approach schematically represents the $\varepsilon - N$ curve on a log-log scale in Figure 4.3, where N is the number of cycles that reversals to failure. Given the total strain from the sum of the elastic and plastic strains relate to a life time by the curve that can be approximated as a curved line from the elastic and plastic curves.

The $\varepsilon - N$ curve equation can be divided into two parts, the elastic region and the plastic region, shown in Eq. (4.1). Eq. (4.2) is presented by half-amplitude strain [55] to express the equation as

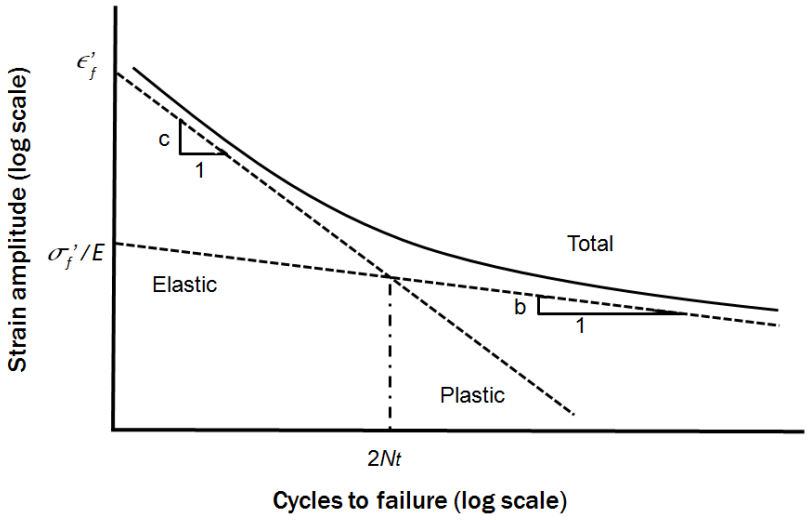

Figure 4.3: $\varepsilon - N$ curve

cyclic loading.

$$\varepsilon = \varepsilon_e + \varepsilon_p \tag{4.1}$$

$$\frac{\Delta\varepsilon}{2} = \frac{\Delta\varepsilon_e}{2} + \frac{\Delta\varepsilon_p}{2} \tag{4.2}$$

Basquin [56] identified the stress and fatigue life-cycle relationship with Eq. (4.3).

$$\frac{\Delta\varepsilon}{2} = \varepsilon_f'(2N_f)^c \tag{4.3}$$

where, ε_f' is a plastic strength defined in Figure 4.3.

After Eq. (4.3) is combined with Eq. (4.2), the final Eq. (4.4) is

$$\frac{\Delta\varepsilon}{2} = \frac{\sigma_f'}{E}(2N_f)^b + \varepsilon_f'(2N_f)^c. \tag{4.4}$$

where, b , c represent the each slope of elastic and plastic curve shown in Figure 4.3.

Eq. (4.4), which represents a constant amplitude loading case, is seldom experienced in real environments. Typically, some mean stress or strain is present, and mean stress effects predominantly follow long cycles of fatigue. Therefore, the mean stress effect must be taken into account. Two methods that account for the mean stress effect are the S.W.T (Smith Watson Topper) and Morrow. As the S.W.T. method is the more conservative, this study adopted it. Eq. (4.5) incorporates the S.W.T. method into Eq. (4.4) [57].

$$\sigma_{max}\frac{\Delta\varepsilon}{2} = \frac{(\sigma'_f)^2}{E}(2N_f)^{2b} + \sigma'_f\varepsilon'_f(2N_f)^{b+c} \tag{4.5}$$

The term σ_{max} is evaluated as Eq. (4.6) for the application.

$$\sigma_{max} = \frac{\Delta\sigma}{2} + \sigma_0 \tag{4.6}$$

The amplitude strain is accumulated by Miner's rule for adding damages. The relationship between damage and the fatigue life cycle is presented in Eq. (4.7).

$$\sum D_i = \frac{n_i}{N_i} \tag{4.7}$$

where n_i is the number of repetitions for each stress level and N_i is the lifetime of each stress level calculated from the $\varepsilon - N$ curve. When D, the fatigue damage, equals 1, we can decide that the part has an initial crack [7]. At the same time when the strain life approach returns a damage index of 1, defining the initial crack size for the following crack propagation is required. To determine the size of the initial crack, we refer to a damage tolerant design requirement for military aircraft regulation (MIL-A-83444), shown in Table 4.1 [58]. From the table, we assume that the initial crack size is 0.05 inch or 1.27 mm.

Table 4.1: Initiation crack size

Category	Critical Detail	Initial Flaw Assumption
Slow crack growth	Hole, Cutouts etc.	For $t < 0.05$ inch, 0.05 inch through thickness flaw
		For $t < 0.05$ inch, 0.05 inch radial corner flaw
	others	For $t < 0.125$ inch, 0.25 inch through thickness flaw
		For $t < 0.125$ inch, 0.25 inch radial corner flaw

4.3 Stress Life Approach

The most widely used and conventional approach for the evaluation of fatigue life is the stress-life method for a ductile material. The stress-life method is applied to high cycle fatigue while the acting stress is mainly in the elastic region of the material. Thus, it ignores the effect of plastic region which is mainly about low cycle fatigue. However, most materials used in the field of aerospace engineering have a high-cycle fatigue characteristic. In general, when evaluating the fatigue life by the stress-life method, the $S - N$ curve is typically represented by the relationship between the alternating stress (S) and the number of repetitions (N) until fracture. We obtain $S-N$ data from a fatigue test, which shows the stress-life relationship. The vertical axis represents the alternating stress, and the horizontal axis represents the number of repetitions until failure (N_f) on a log-log scale. Figure 4.4 indicates that the value of the alternating stress converges to a specific value according to the increase in lifetime (N). Under stress that is less than this specific value (S_e), referred to as the "fatigue strength" or "limit," the material has an infinite life cycle. Thus, when conducting the analysis, we truncate the small stress. If experimental data are not available, then the relationships between the general tensile strength and the fatigue limit can be introduced as shown in Eq. (4.8) [55].

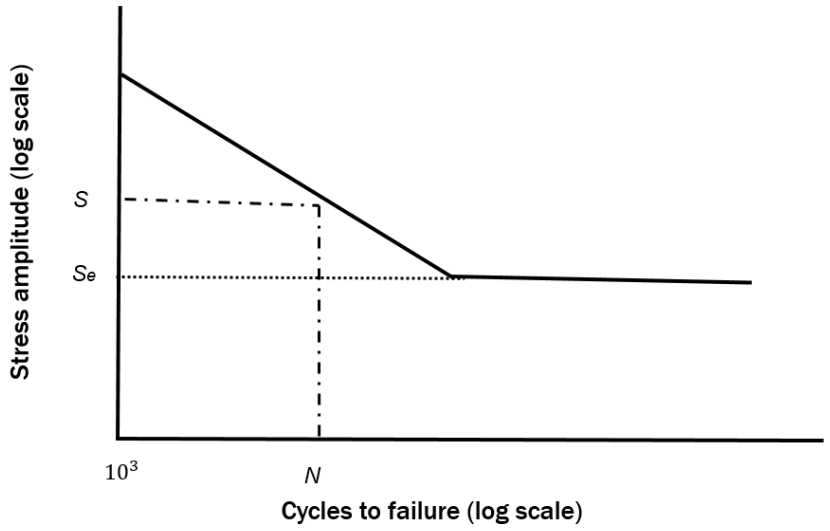

Figure 4.4: *S-N* curve

$$S_e = \begin{cases} 0.056\ S_{ut} & \text{if } S_{ut} \leq 212\ ksi\ (1460\ MPa) \\ 107\ ksi & \text{if } S_{ut} > 212\ ksi \\ 740\ Mpa & \text{if } S_{ut} > 1460\ MPa \end{cases} \tag{4.8}$$

where S_{ut} represents the ultimate strength of each material.

We estimate the magnitude of the alternating stress corresponding to the fatigue life of 10^3 cycles as 0.9 times the tensile strength and use the line connecting this point to the fatigue limit as the design line for the $S - N$ line if actual fatigue data are not available for a material. The $S - N$ diagram shown previously illustrates effect of the stress amplitude on the lifetime in the condition in which the average stress is zero. Even if the range of stress in the stress history remains consistent, the fatigue life is not always consistent. This phenomenon is due to the influence of average stress. In practice, however, the basis of many fatigue tests is a constant amplitude stress test with a mean stress of zero and a fixed maximum and minimum stress. Therefore, average stress should be used in an actual fatigue analysis.

The stress width represents the difference between the maximum stress and the minimum stress and the mean stress is the median of these stresses. The stress amplitude represents variation with respect to the mean, which is half of the stress width. The following equations Eq. (4.9), Eq. (4.10), and Eq. (4.11) mathematically represent stress width, average stress, and the stress amplitude respectively [23].

$$\Delta\sigma = \sigma_{max} - \sigma_{min} \tag{4.9}$$

$$\sigma_m = \frac{\sigma_{max} + \sigma_{min}}{2} \tag{4.10}$$

$$\sigma_a = \frac{\Delta\sigma}{2} \tag{4.11}$$

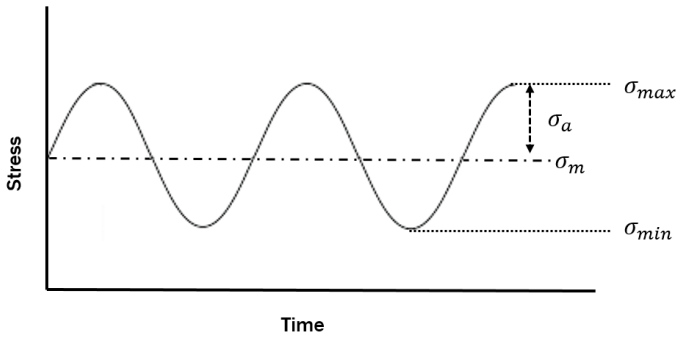

Figure 4.5: Definition of alternating stress

The stress ratio (R) and the amplitude ratio (A), used to describe the state of the applied stress, are expressed by the following Eq. (4.12). The corresponding loading situations are summarized for three cases in Eq. (4.13) and depicted in Figure 4.6 .

$$R = \frac{\sigma_{min}}{\sigma_{max}}, \quad A = \frac{\sigma_a}{\sigma_m} \tag{4.12}$$

$$\begin{cases} \text{Fully reversed case:} & R = -1 \quad A = \inf \\ \text{Tensile alternating load case:} & R = 0 \quad A = 1 \\ \text{Compressive alternating load case:} & R = \inf \quad A = -1 \end{cases} \tag{4.13}$$

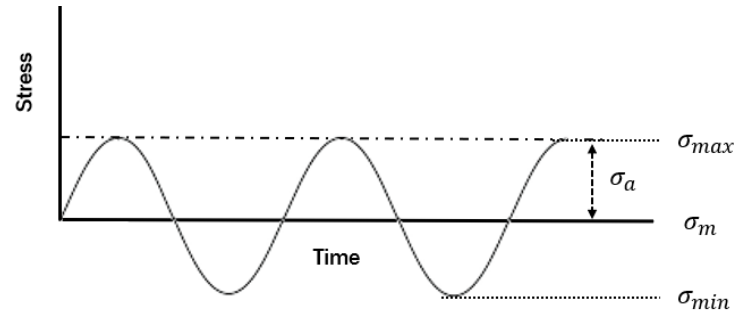

(a) Fully reversed case

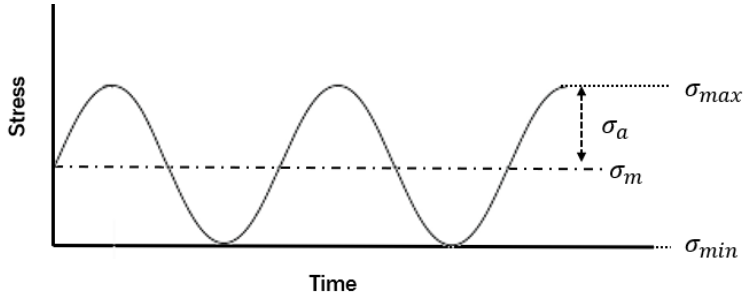

(b) Tensile alternating load case

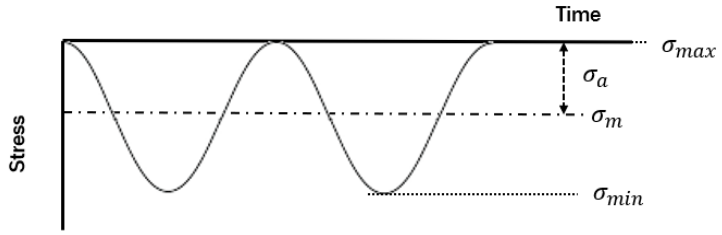

(c) Compressive alternating load case

Figure 4.6: Alternating load cases

In addition to the stress-life method, a method of calculating the fatigue life cycle that entails

average stress is the Haigh diagram, shown in Figure 4.7. The diagram depicts the stress-life relationship from several stages of experimental data using mean stress and alternate stress. The construction of the Haigh diagram, however, entails a considerable amount of time and cost, so relational expressions of fatigue life that account for the influence of mean stress need to be defined. In the case of the $S-N$ approach, the Gerber (Germany,1874) Eq. (4.15), Soderberg (USA, 1930) Eq. (4.16), Morrow (USA, 1960) Eq. (4.17), all of which account for the effects of mean stress, are used. In the following relationships, the endurance limit, the yield strength, the ultimate strength, and the true fracture stress are defined as S_e, S_y, S_{ut}, and σ_f, respectively.

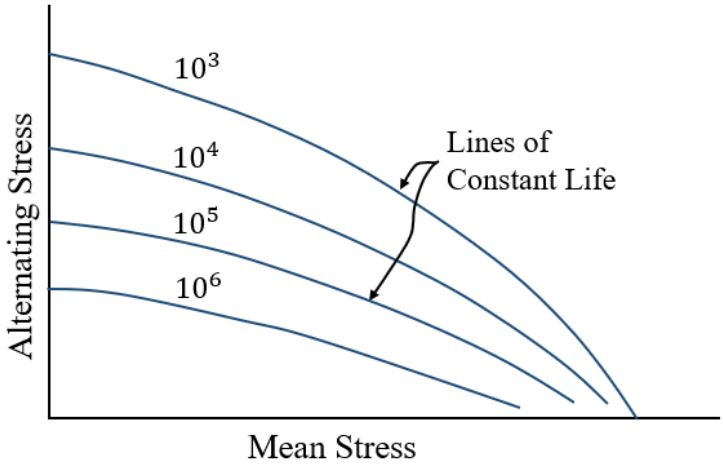

Figure 4.7: Haigh diagram [55]

$$\frac{\sigma_a}{S_e} + \left(\frac{\sigma_m}{S_{ut}}\right)^2 = 1 \tag{4.14}$$

$$\frac{\sigma_a}{S_e} + \frac{\sigma_m}{S_{ut}} = 1 \tag{4.15}$$

$$\frac{\sigma_a}{S_e} + \frac{\sigma_m}{S_y} = 1 \tag{4.16}$$

$$\frac{\sigma_a}{S_e} + \frac{\sigma_m}{\sigma_f} = 1 \tag{4.17}$$

Generally, the Goodman is the failure criterion widely used for the following reasons [23].

- It is a straight line, and the algebra is linear and simple.
- It is easily graphed for every problem.
- It reveals subtleties of insight into fatigue problems.
- Answers can be scaled from diagrams for checking the algebra.

4.4 Variable Amplitude Loading

Chapter 4.2 and 4.3 have dealt with methods of determining fatigue life under a constant amplitude load ($S - N$ or $\varepsilon - N$ method), shown in Figure 4.8, and methods that account for mean stress effects (S.W.T equation for $\varepsilon - N$ and Goodman equation for $S - N$) under constant loading with mean stresses. Figure 4.9 shows constant loading with mean stress and corresponding translations by the Goodman and Gerber equations.

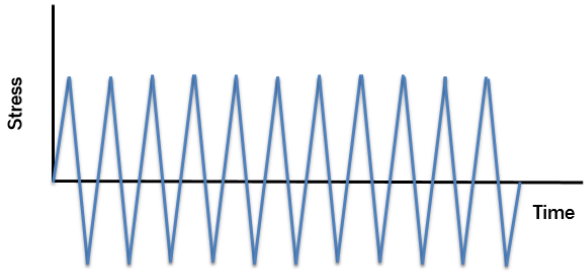

Figure 4.8: Constant loading with a fully reversed condition

The following sections will demonstrate how to apply a variable load generated from an actual aircraft or automobile to a theoretical formula, such as the damage accumulation method of load

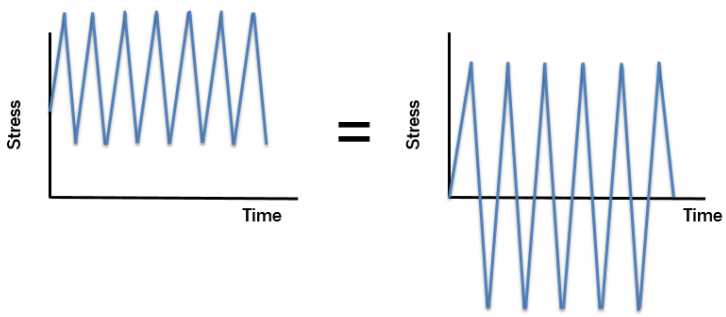

Figure 4.9: Constant loading with mean stress and corresponding fully reversed loading

blocks (Miner's rule), and the cycle counting method under a variable amplitude load (Rainflow counting).

4.4.1 Damage accumulation method

The linear damage rule, the Palmgren-Miner rule, or Miner's rule, are methods commonly used to calculate the variable amplitude loading. Miner [7] introduced the concept of the cycle ratio to express a damage fraction, which expresses the cycle ratio as the ratio of the number of repetitions (n) to the fatigue life (N) as in Eq. (4.18).

$$\text{cycle ratio} = \frac{n}{N} \tag{4.18}$$

According to Miner's rule, the damage fraction (D) in the stress magnitude (S_i) is expressed as the cycle ratio, ${}^{n_i}/_{N_i}$. In other words, the fraction of damage caused by one cycle of load (${}^{1}/_{N}$) is the application of one cycle of loading that consumes ${}^{1}/_{N}$ of fatigue life. The cumulative damage rate resulting from a series of processes is expressed in Eq. (4.19) as the sum of the damage rates at their respective stress magnitudes.

$$D = \sum_{i=1}^{n} \frac{n_i}{N_i} \tag{4.19}$$

The percentage of lifetime spent in each stress magnitude of failure at variable amplitude loading is assessed together and failure occurs when the cumulative damage rate is greater than 1, as in Eq. (4.20).

$$D \geq 1 \tag{4.20}$$

In the case of composites laminated in various directions, each ply is generally assumed to be under multiaxial stress. In this case, one way of calculating fatigue life is to perform a fatigue test on the stress values for various directions to obtain the $S - N$ curve. Because of the huge number of possible combinations for each stress element, however, this method is impractical. Therefore, a new damage guideline based on the Tsai-Wu static strength failure criterion is proposed as Eq. (4.21). This equation, proposed by Yongming Liu and Sankaran Mahadevan [59], requires only a fatigue test for the unidirectional laminate and predicts fatigue life by taking into account a typical lamination sequence and angles.

$$D = \sum_{i=1}^{K} D_i = \sum_{i=1}^{K} n_i \sqrt{\frac{1}{(N_{fl}^1)^2} + \frac{1}{(N_{fl}^2)^2} + \frac{1}{(N_{fl}^6)^2} + \frac{1}{(N_{fl}^1)^2 (N_{fl}^2)^2}}, \tag{4.21}$$

where K is ply number in laminate, and n_i and N_i are the number of repetitions and the corresponding fatigue life for the i^{th} ply.

4.4.2 Cycle counting method

To predict the life of a member subjected to variable load history or irregular sequence, shown in Figure 4.10, we have to reduce the complicated load history to several simplified load histories such as those in Figure 4.11, which correspond to useful constant amplitude experimental data

used by the damage accumulation method, Miner's rule. This process is called cycle counting, and Rainflow cycle counting is the most common [60].

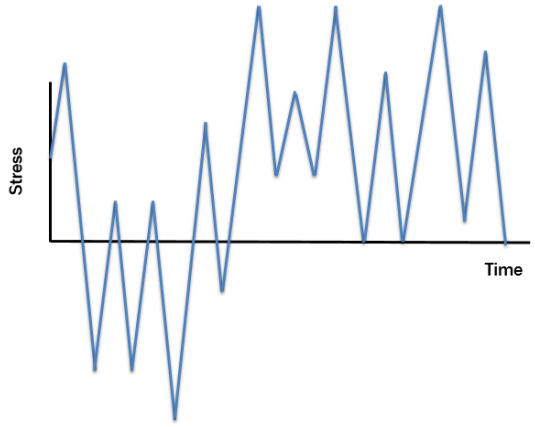

Figure 4.10: Variable loading with irregular sequences

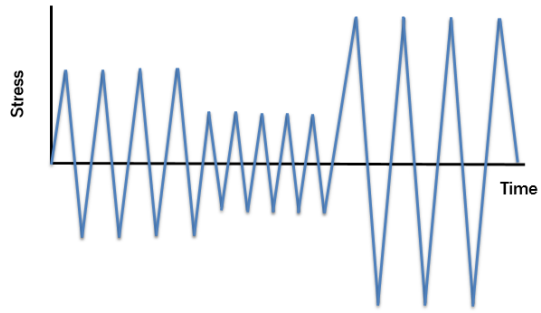

Figure 4.11: Block loading after cycle counting

Since 1967, when Endo [61] first calculated the hysteresis loop regarding stress and strain, researchers have devoted significant effort to the study of Rainflow counting, a calculation algorithm. In the 1980s, ASTM and SAE adopted the Rainflow algorithm as the official algorithm form and developed another algorithm that generated a more accurate hysteresis loop. This study upgraded Fortran code from [62] as a more applicable form for accurately calculating variable loading, but the result and the concept are identical. Figure 4.12 shows the basic concept of the rainflow counting algorithm in time domain data from a hysteresis point of view. The cycle of the hysteresis

point is described by a raindrop falling on a roof. To plot Figure 4.12, we applied several rules to represent falling rain and to identify the closed hysteresis loops.

- A. To exclude the summation of half cycles, the strain-time history is drawn to start and end at the largest strain value.
- B. The flow of rainfall begins at the reversal of each strain in the history and continues to flow, except in the following cases.
  - A raindrop flows from the local maximum point to the opposite side, a local maximum point that is greater than that which has passed.
  - A raindrop flows from the local minimum point to the opposite side, a local minimum point that is greater than the point at which it passes.
  - A raindrop meets the stream flow of a previous raindrop.

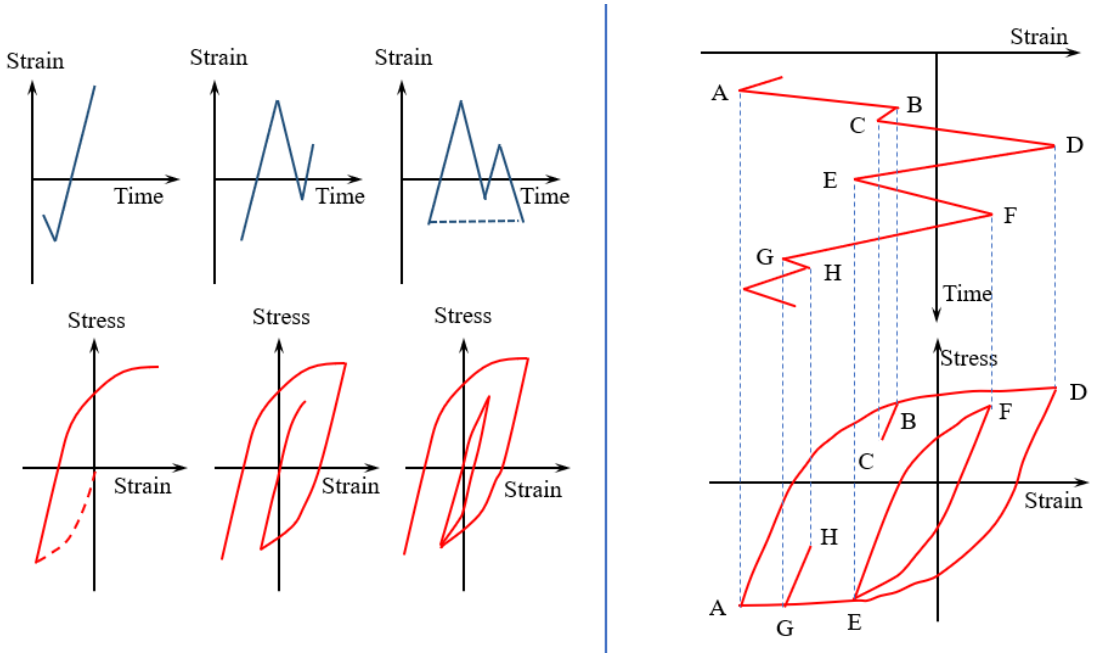

Figure 4.12: The basic concept of the Rainflow counting

As shown in Figure 4.12, the strain-time history starts at the largest strain value (Point A), and the point at which the raindrop flows down describes the change in the direction of the loading. We need the following process to complete a hysteresis loop, which is the load history that can be combined into a complete cycle.

- A. A raindrop flows from point A, passes points B and D, and there is no condition in which rain water can stop, so it continues to the end point of history.
- B. A raindrop passes from point B to point C and stops on the other side (point D) because both the local maximum point and point D are larger than point B in both points B and D.
- C. A raindrop flows from point C and stops as soon as it meets rainwater from Point A.
- D. A raindrop passes from point D to point E and point G, and there is no condition in which rainwater can stop, so it continues to the end point of history.
- E. A raindrop passes from point E past point F and stops at point G on the opposite side because both points E and G are local minimum points and point G is larger than point E.
- F. A raindrop flows from point F and stops as soon as it meets a raindrop flowing from point D.
- G. Araindrop passes from point G to point H and stops at point A on the opposite side Because both points G and A are local minimum points and the size of point A is larger than point G.
- H. A raindrop flows from point H and stops as soon as it meets a raindrop from point D.

The result of rainflow counts generally represents a load spectrum in the form of a matrix with three rows: range, mean, and cycle. Figure 4.13 illustrates a rainflow counting matrix, the Helix load spectrum.

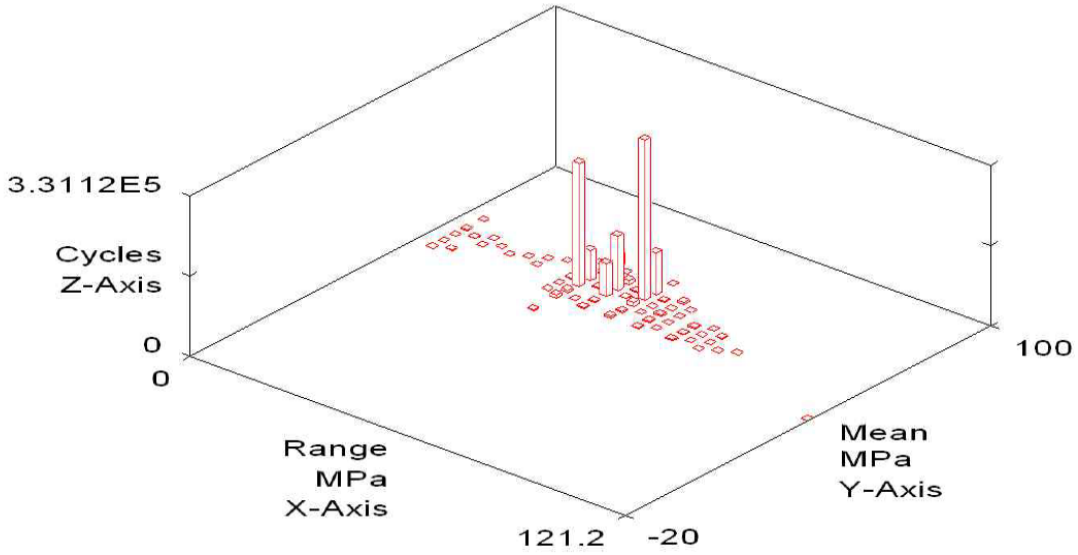

Figure 4.13: Matrix form of the Rainflow counting results

4.5 Crack Initiation Analysis Program

Based on theories and applications discussed in this chapter, this study developed a crack initiation analysis (CIA) program. Figure 4.14 presents a flowchart of the CIA for both of the $S - N$ and $\varepsilon - N$ approaches. In the beginning of the process, generation of the load spectrum produces non-dimensional variable amplitude loading from the standard load spectrum-generating program, TWIST. This load spectrum should be replaced by the actual load of a part or the structure of the system in the real application. Variable amplitude loading is converted to a Rainflow matrix consisting of mean stress, amplitude stress, and cycle numbers through the Rainflow counting technique. By contrast, a static load obtained from the aerodynamic analysis such as CFD is applied to the structure to obtain the stress of each element using the finite element method such as Nastran. The unit stress, which is the result of the previously calculated non-dimensional Rainflow matrix, is multiplied by the actual stress obtained from the finite element method. As a result, all elements of the finite element model can possess their own stress spectrum described by the

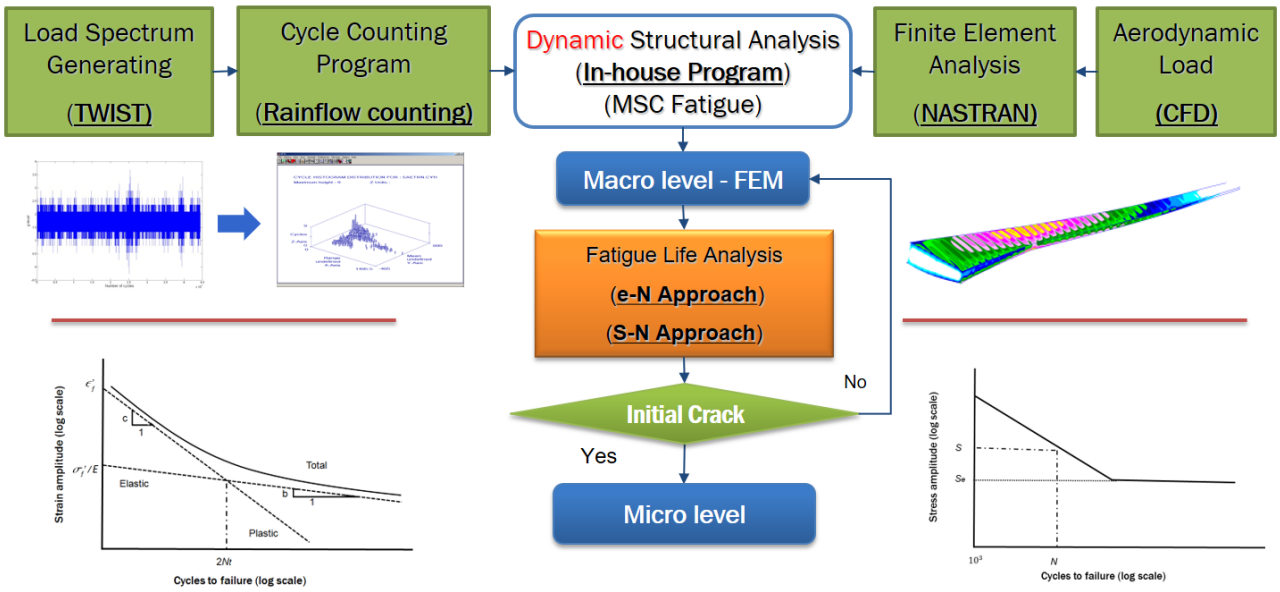

Figure 4.14: Program flow for crack initiation analysis

expression of the Rainflow matrix. For each element, the failure cycles corresponding to each stress along the loading sequence is obtained from the $S-N$ or $\varepsilon-N$curve, and then the damage is accumulated for each load block according to Miner's rule. At this time, if the damage is 1, a crack is assumed to have occurred in the element; that is, the crack initiation time is calculated based on the number of cycles that occur before a cycle in which the damage reaches 1.

4.6 Validation of the Crack Initiation Analysis Program

To validate the results of the fatigue life analysis of the CIA module, this study compares these results to those of a commercial program, MSC Fatigue. MSC Fatigue is an FE-based durability and damage tolerance solver that deals with the full range of fracture and fatigue life calculations for static and dynamic problems in both the time and frequency domains [63] [64].

4.6.1 Linear static analysis

For the purpose of validation, we suggest a keyhole model: a keyhole shaped, notched component, shown in Figure 4.15. The keyhole model is subjected to 10,000 N in the direction of the arrow, and only the top half of the keyhole is used in this validation process because of symmetry.

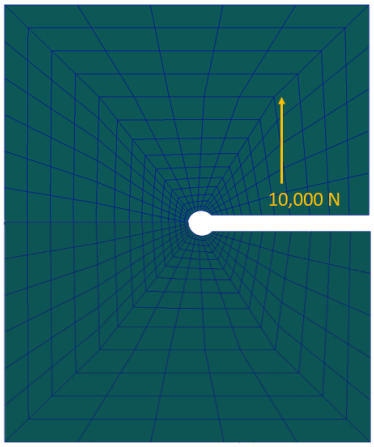

Figure 4.15: A keyhole example for the purpose of validation

This study presents a linear static finite element analysis using Nastran and performs a pre- and post-process using MSC Patran. A stress analysis was performed prior to the fatigue analysis, the results of which are shown in Figure 4.16, also including the findings from the linear static analysis for principal stress and its deformation. Maximum principal stress is about 333 MPa.

4.6.2 Loading condition

In the CIA module validation process, a unit load with a maximum of 1 and a minimum of -1 is applied, shown in Figure 4.17, has the effect of oscillating $10,000$ N from $+10,000$ to $-10,000$ in the fatigue analysis. In this unit-load condition in Figure 4.17, the mean stress is zero, and the maximum and minimum stress absolute magnitudes are identical, indicating a fully reversed loading condition, $R = -1$.

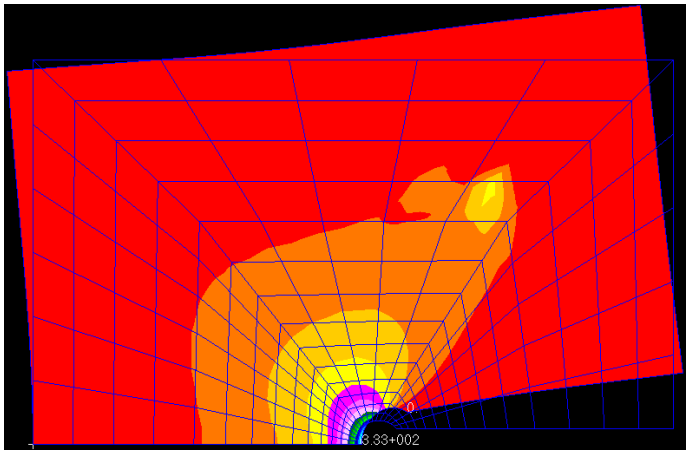

Figure 4.16: Stress and deformation for the linear static analysis

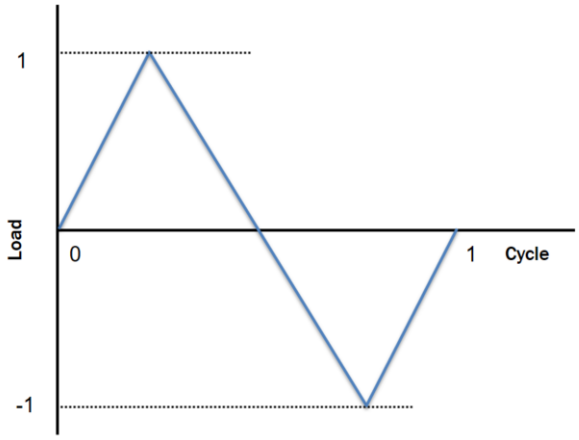

Figure 4.17: Unit load for one cycle

4.6.3 *S-N* curve

The $S - N$ curve is expressed in many equation forms. Conventionally, many companies or documentations of material databases such as MMPDS [65] use a form of Eq. (4.22).

$$\log N + m \log S = \log k \tag{4.22}$$

However, some companies include MSC software and use a different form, shown in Eq. (4.23).

$$\log N - \frac{1}{b}\log S = -\frac{1}{b}\log SRI1 \tag{4.23}$$

The two types of the equations can be exchanged using the following equations, Eq. (4.24) and Eq. (4.25).

$$m = -\frac{1}{b} \tag{4.24}$$

$$k = (SRI)^{-\frac{1}{b}} \tag{4.25}$$

Figure 4.18a, illustrating the curve of Eq. (4.23) from MSC Fatigue and Figure 4.18b, shows the curve of Eq. (4.22) from CIA developed in this study. As shown in the Figures, for the aluminum 2014-HV-T6, the $S - N$ curve of the CIA program is identical to that of MSC Fatigue.

4.6.4 Comparison of results

To evaluate the accuracy of the developed program based on the proposed methods, we analyze CIA and MSC Fatigue under the same conditions. The results of fatigue life for all elements is shown in Figure 4.19.

The minimum life cycle, or the maximum damage cycle from the result of MSC Fatigue is about 3.17×10^7, which represents a 7.50 log cycle. This number is nearly the same as 3.10×10^7 cycles or 7.49 log cycles, the results of CIA. For a more accurate comparison, we extracted 200 elements from the full model and compared the values of the fatigue results. The results of the comparison are expressed as the percentage of error in Eq. (4.26) and as a histogram in Figure 4.20.

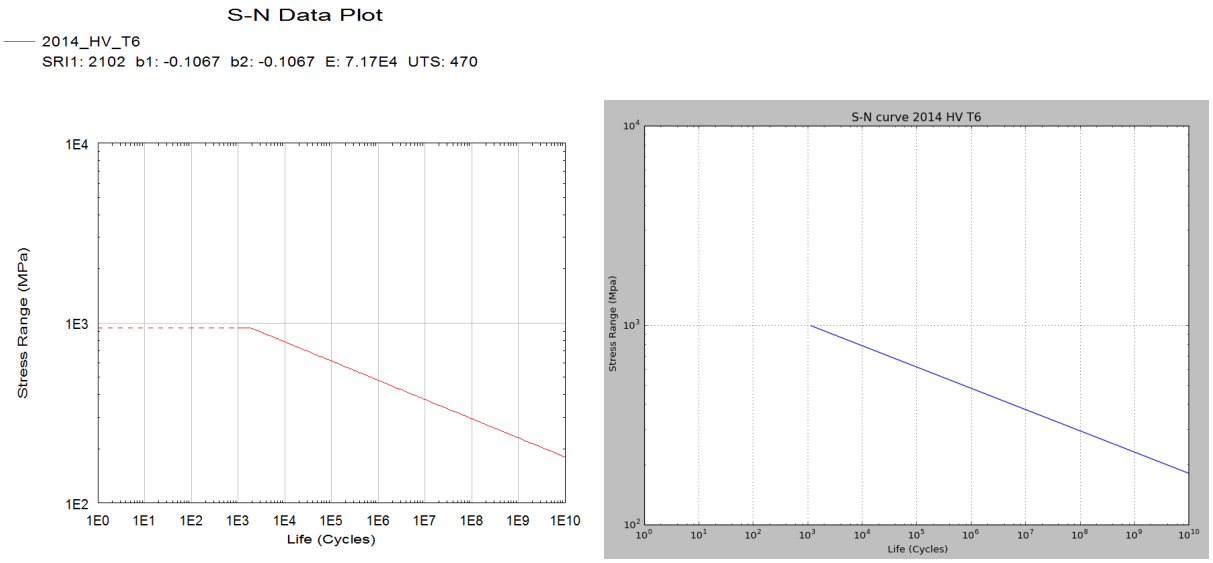

(a) *S-N* curve from MSC Fatigue

(b) *S-N* curve from CIA

Figure 4.18: *S-N* curves for aluminum 2014-HV-T6

The mean of error is 0.0494 % and the variance is 0.0122.

$$Percentage\ error = \left| \frac{Expected\ value - Obtained\ value}{Expected\ value} \right| \times 100 \tag{4.26}$$

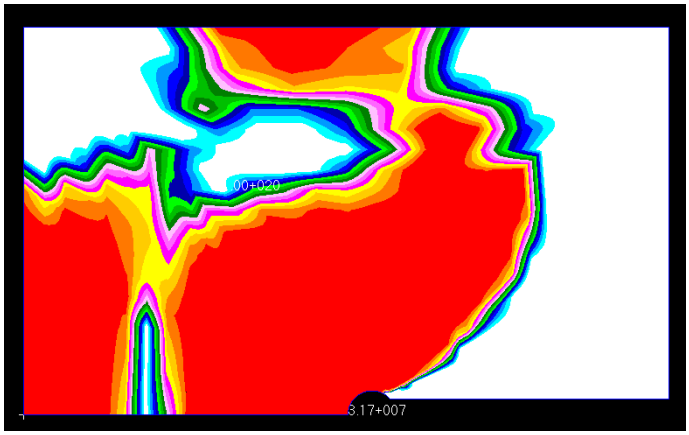

Figure 4.19: Fatigue analysis result from MSC Fatigue

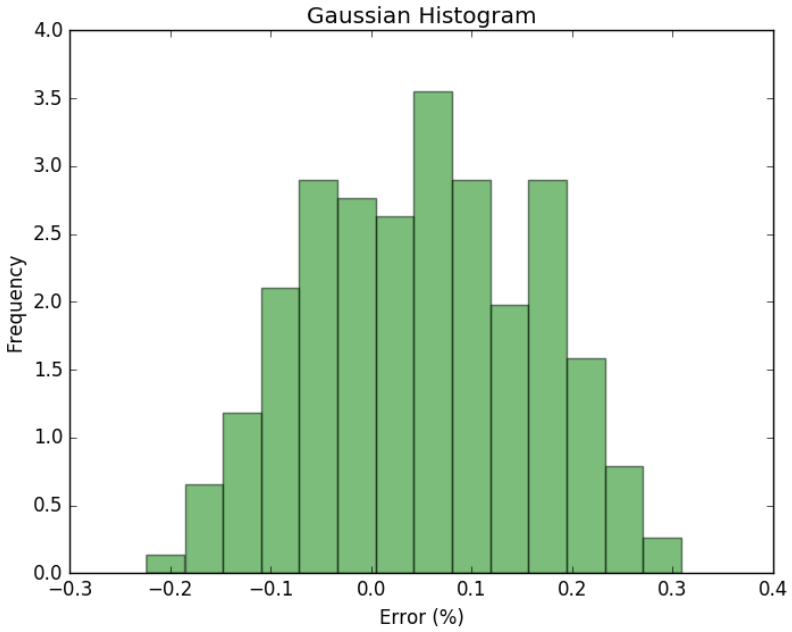

Figure 4.20: Error histogram for the program validation

CHAPTER 5

CRACK PROPAGATION ANALYSIS

Crack propagation utilizes the concept of damage tolerance design, a philosophy used to refine fail safe design by predicting structural failure, assuming that cracks exist and will grow large enough to produce failure. The global calculation of crack propagation for a structure such as a wing requires a solution of a complex system that accounts for a crack opening or a crack closure. The global level of HFEM is used as a general finite element model with coarse meshes to determine static stress, and it is analyzed as a crack initiation by the strain-life or stress-life approach. If a crack initiates in a certain element, then the element is taken into account in a base-level model to build the simulation environment of crack propagation.

For the purpose of simulation, cellular automata (CA) an effective way of solving a complex system is adopted in this study, for it functions without central control and performs according to simple local rules of operation. A CA local rule is employed such that a cell is regarded as a dead cell if the calculated residual strength based on linear elastic fracture mechanics (LEFM) approaches a critical factor. The cellular model acts automatically following a cyclic load from the history spectrum. Crack propagation at the base model was performed by independent calculations for each CA model.

Crack propagation analysis is performed by following local rules, neighboring cell rules, and CA updating rules. This simulation method raises the possibility of evaluating the safety of complex systems. The method of crack propagation on the cellular automata model with parallel computation was published in the 56th AIAA [66].

5.1 Background

Since the concept of damage tolerance design is a guideline to obtaining certification of an aircraft design, the concept of damage tolerance design can be an ideal approach to evaluating structural health. Furthermore, the use of HFEM alleviates computational burden and cellular automata provide a simple solution for a complex simulation.

Under the assumption that cracks exist and grow large enough to produce global failures, a damage tolerance design is able to predict the structural failure caused by fatigue. Defects, initial cracks, can be introduced during the manufacturing and assembly processes or from any fatigue cracks caused by accidental damage occurring in service [67]. In the aerospace industry, structural designers have applied the damage tolerance approach to verify design safety and to predict the service life of aircraft. Dale L. Ball and Scott Norwood applied the strain life approach for crack initiation and fracture mechanics for crack propagation to present airworthiness certification [68].

In the case of crack propagation, LEFM is widely used to predict the growth of fatigue cracks in a structure [69].Crack propagation with LEFM considers the geometry configuration, the load history, the static stress intensity, and the material property. From a global perspective, the calculation of crack propagation for a structural component such as a wing requires the solution of a complex system by taking micro-level crack openings or crack closures into account. It is especially difficult to predict the phenomenon of a crack closure, which is a crucial factor in the analysis of the behavior of multiple cracks. However, studies of multiple crack behaviors have examined only microscopic aspects of failure analysis. For example, several studies have examined multiple cracks to more thoroughly understand the interaction effect of cracks. Nakamura [70] has proposed investigating the failure propagation behavior of many random pores. In an analysis of porous material, Nakamura simulated crack propagation to characterize its unique failure process and found that a crack tends to propagate along the shortest path between neighboring pores. In a simulation using finite element analysis, his study showed the interaction effects of neighboring

cracks. The simulation, however, was performed from a micro-mechanical viewpoint under certain conditions, so any conclusion from the results could not be generalized to the macro level.

Choppa and Sukumar [71] proposed a numerical technique for modeling the fatigue crack propagation of multiple coplanar cracks. They applied the fast marching method to handle the merging of distinct cracks naturally with no collision detection or mesh reconstruction and then used the method in conjunction with the Paris crack growth law to propagate the crack tip. Their study showed crack propagation in the global structure of the finite element model using the Paris law, an approach suited to aircraft wing design. The authors, however, did not apply the interaction effects of neighboring cracks during the simulation.

In a previous chapter, this study suggested employing the hierarchical finite element modeling method, both at a global and base level, for the simulation of crack growth. This hierarchical modeling method enables joint solutions to both global and local problems. To reduce the complexity and computational cost of the hierarchical scheme, this study proposed CA (cellular automata). The CA method is an effective solution for solving complex systems with complicated calculationssystems in which large networks of components with no central control and simple rules of operation give rise to complex collective behavior, sophisticated information processing, and adaptation via learning or evolution [72]. This method was introduced by Von Neumann and Stephen Wolfram, who invented the cellular automation lattice [73].

Several studies have applied CA to structural engineering. Abdalla [74] used CA in the application of two-dimensional continuum topology optimization problems. Using the methods of CA, Zafer Grdal [75] implemented an integrated analysis and design approach to achieve an optimal structural configuration. His paper shows the basic features of the CA and demonstrates a formulation for the design of two-dimensional truss structures that exhibit linear and geometrically nonlinear response characteristics. Another paper by Tatting [76] takes basic elements of the CA and specific formulation used for isotropic plates. He presents analysis and design rules that satisfy static constraints and fulfill material failure conditions of maximum stress. The update rules are

based on the deformation of an equivalent structure and the relationship between the thicknesses of the isotropic plate.

5.2 Overview of Crack Propagation Analysis Module

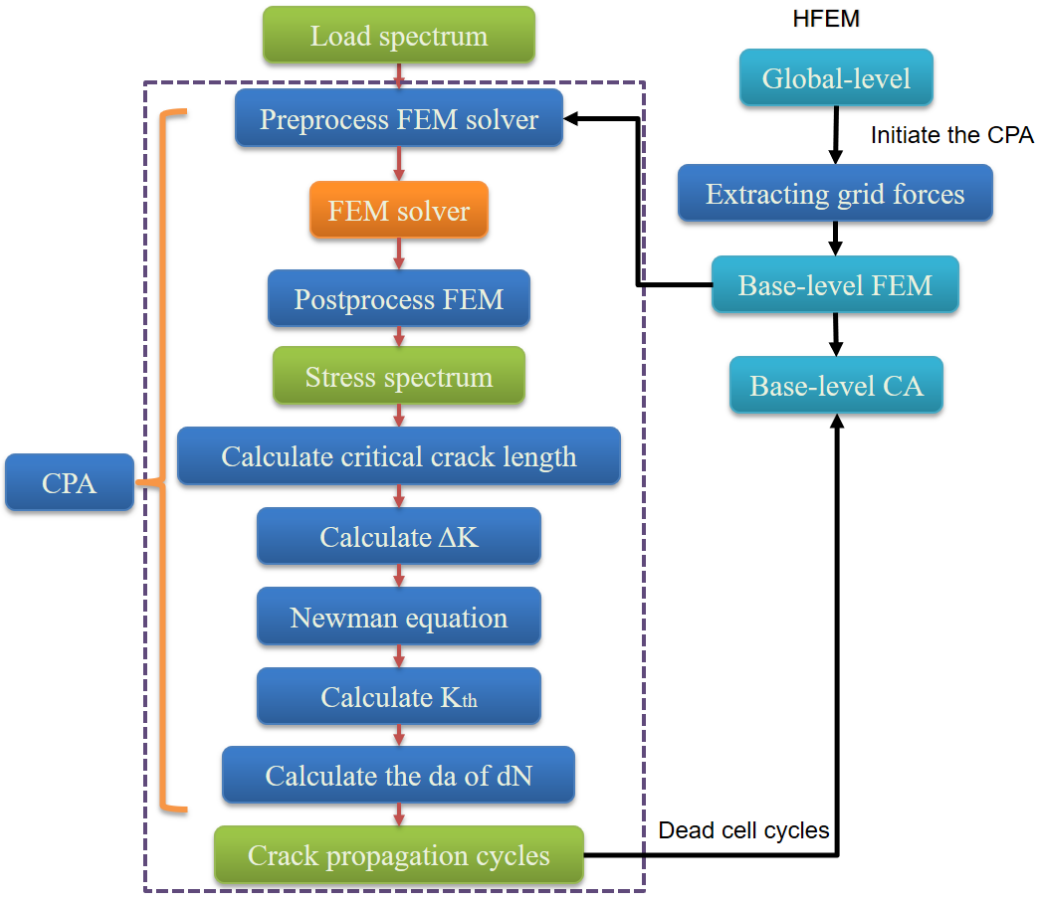

Figure 5.1: The flow diagram of CPA

The flow chart for the CPA(Crack Propagation Analysis) is described in Figure 5.1. The global-level of HFEM initiates the CPA based on the results of the crack initiation analysis and indicates elements with possible cracks. From the indicated elements, we select a representative element, which is the cluster center for the base-level FE model in the HFEM. Then the CPA is started on the base-level FE model with the internal loads formed by external loads from the global-level.

From the element number of the base-level FE that is selected, an algorithm in the framework finds the internal, or grid forces, which are nodal forces corresponding to the target element. Then, with the internal forces, it writes the FE input file, which marks the beginning of the crack propagation analysis.

The processes of finding internal forces and writing the input file with the forces and boundary conditions are conducted in the preprocessing step in the framework. Then the CPA executes an external FE solver such as NASTRAN to conduct the stress analysis. This step can be replaced by a unit load method that was introduced in Chapter 3. Results of the analysis are combined with those of the load spectrum to generate a stress spectrum. The main CPA starts by calculating the critical crack length that accounts for the critical stress intensity factor and information about the shape and the size of a crack. From the stress spectrum, the amplitude stress level is used to calculate the ΔK, which is the difference between the maximum and minimum stress intensity factors. To examine the crack closure and opening modes for the plastic region at the crack tip, this study adopts the Newman equation and factors to calculate the threshold of the stress intensity factor, which is K_{th}. With ΔK and K_{th}, we calculate the crack growth cycles from a da of the dN curve, which is closely related to the material property [77]. The final result of CPA visualized in the base-level CA model shows the effect of crack propagation based on the cycles of propagation. Detailed theories and applications will be discussed in following Chapters.

5.3 Theoretical Approach of Crack Propagation Analysis

5.3.1 Load spectrum for LEFM

For the following crack initialization procedure, the load sequence was not relevant because a cumulative method using Miners rule was simply a summation of the damage. Now, however, the sequence is important for LEFM to analyze crack propagation since LEFM uses the integration of each cycle. Thus, the load sequence effect becomes an important consideration. The load

sequence can be arranged into five sequences: low-high, high-low, low-high-low, high-low-high, and random block sequence (Figure 5.2). One study shows that the low-high combination has the shortest fatigue life [78]. The load spectrum directly from Rainflow counting, which can be considered a random sequence, is the fifth load sequence [79].

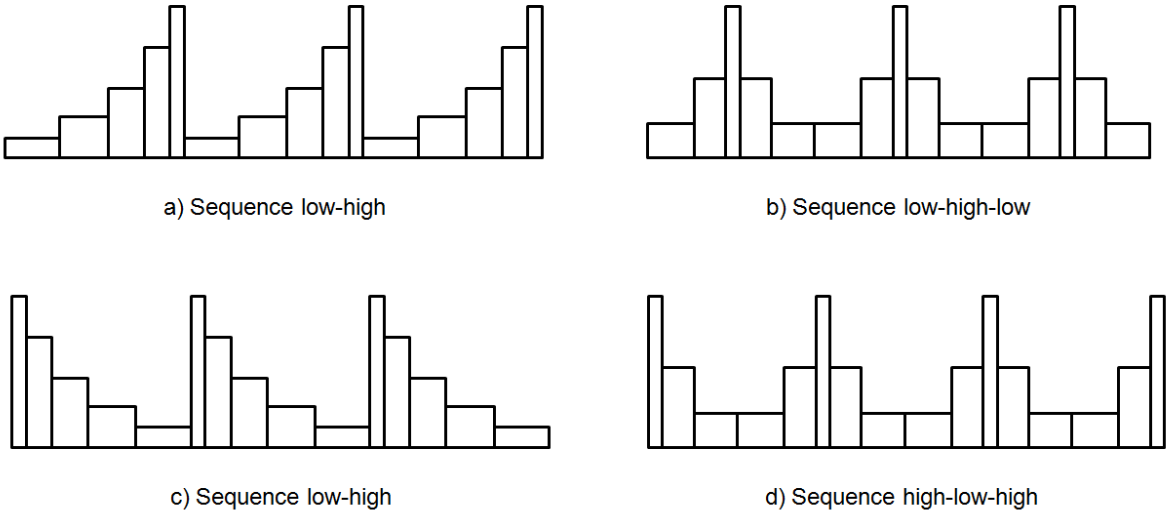

Figure 5.2: Combination of load sequences

5.3.2 Crack growth

In damage tolerance design, particularly in the aerospace field, crack propagation is calculated using the LEFM method. Under the basic assumption that material conditions are predominantly linear elastic during the propagating process, designers use this method to analyze crack growth in materials. The analysis of crack growth is important because propagation is part of the longest cycle in fatigue life. For example, if we assume that the panel in Figure 5.3 contains a crack of a half length a with a finite width and subjected to constant amplitude loading, then if the applied stress increases from zero to value σ , the crack will extend an amount δa. At this time, the stress is not high enough to cause any failure in the panel. This kind of growth is referred to here as stable growth or sub-critical crack growth. If the panel is subjected by cyclic loading from zero to

a maximum value of stress, then the crack will continue to propagate to an amount, δa, on each cycle. As the length of the crack increases, the rate of crack growth $\delta a/\delta N$ increases, shown in Figure 5.4. In this study, we will assume that this crack growth, the most typical crack growth pattern, is also steady.

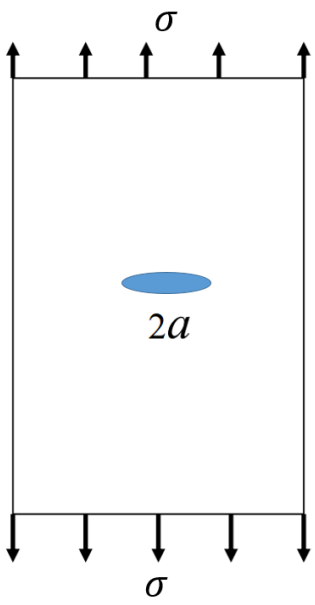

Figure 5.3: Cracked panel under constant amplitude loading

Crack propagation can be distinguished as three modes, shown in Figure 5.5, in the following load direction and crack geometry shapes: Mode I (opening mode), Mode II (sliding mode) and Mode III (tearing mode).

Typically, Mode I type crack propagation is the most common, primarily because cracks tend to grow on the plane of maximum tensile stress. This study examines Mode I crack propagation because of its high rate of occurrence. In addition, the other two modes in combination with Mode I cracks often turn into Mode I cracks. The stress intensity factor for Mode I is simply represented

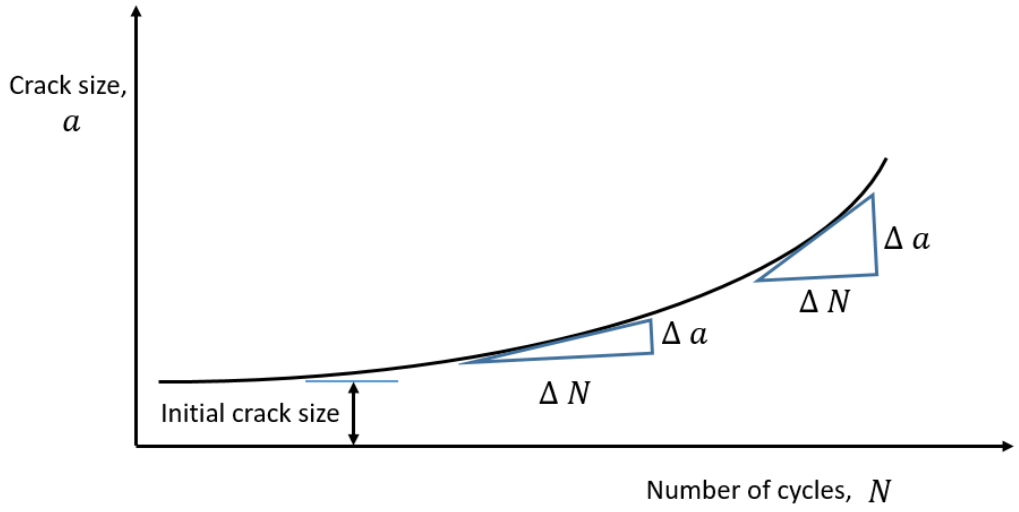

Figure 5.4: Typical crack growth curve

in Eq. (5.1) [81].

$$K_I = f(g)\sigma\sqrt{\pi a} \tag{5.1}$$

where, a is crack length and $f(g)$ is the shape correction factor, which depends on the geometric shape by the model or the crack. This simple equation is not easily solved numerically because of the shape correction factor, which depends on the geometry of the shape of the crack. An important

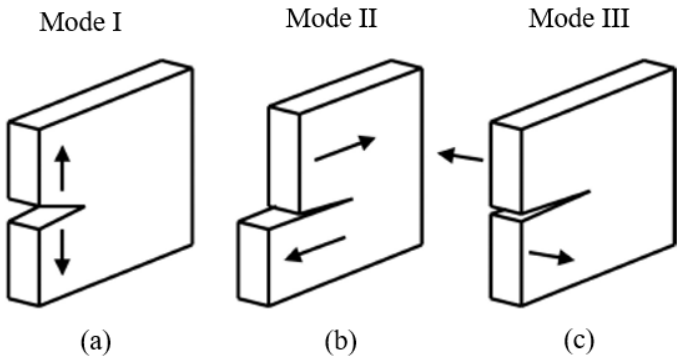

Figure 5.5: Crack propagation modes [80]

property for crack propagation is shown in Figure 5.6 by da/dN (the fatigue crack growth rate per cycle), a function of ΔK (the stress intensity factor range). ΔK is represented in Eq. (5.2) for Mode I crack propagation.

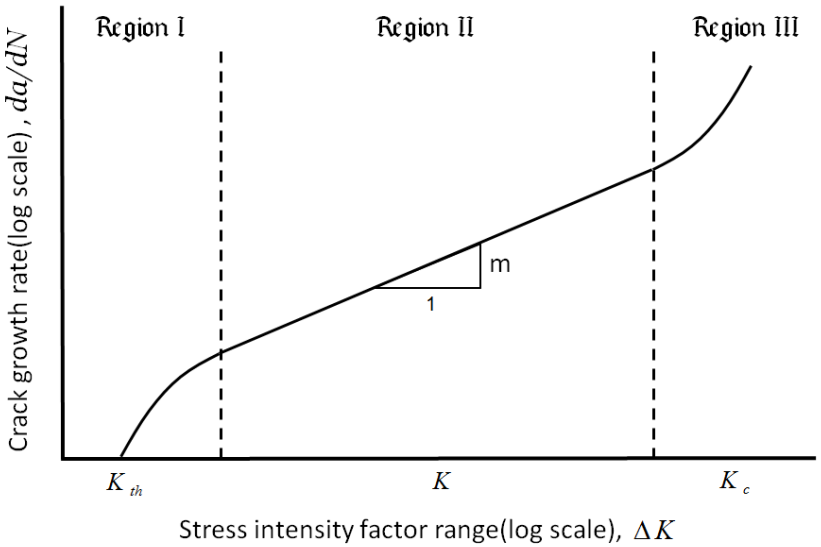

Figure 5.6: da of dN vs ΔK curve

$$\Delta K = K_{max} - K_{min} = f(g)\sigma\sqrt{\pi a} \tag{5.2}$$

As shown in Figure 5.6, crack propagation can be divided into three regions, respectively. At low stress intensities, Region I, cracking behavior is associated with threshold. In the Region II, the curve is linear and is the most commonly operated region. This region is associated with most of the current applications of LEFM approach. The Paris law, presented in Eq. (5.3), is the most widely accepted methods of approximating Region II [82].

$$da/dN = C(\Delta K)^m, \tag{5.3}$$

where C is the constant value of the Paris law and m is the material parameter value. In Region III, crack propagation is high, so Forman's law, a modified version of the Paris law, is applied [83].

As Region III shows a nonlinear tendency, the Paris saw would overestimate the crack propagation life. Therefore, it is approximated by Eq. (5.4), the Forman equation:

$$da/dN = \frac{C(\Delta K)^n}{(1-R)K_c - \Delta K}, \tag{5.4}$$

where R is the load ratio and K_c is the material resistance to fracture, referred to as "fracture toughness."

This chapter has discussed only the Paris and Forman equations, initially proposed in the early 1960s and the most common methods of estimating crack propagation to date. However, the da of dN curve can be approximated by various equations. Shantz [84] surveyed the approximation models of crack growth, and his findings are listed in Table 5.1. The following chapter will discuss the most advanced model in his list, the NASGRO model, which accounts for the crack closure effect.

5.3.3 Crack closure

Crack closure theories are imperative to the accurate prediction of amplitude fatigue crack growth. A crack closure is caused by residual plastic deformation remaining in the wake of an advancing crack. According to crack closure theory, the surfaces of fatigue cracks close when a remotely applied load is still tensile and do not open again until a sufficiently high tensile load is obtained at the next loading cycle. The applied stress level at which crack surfaces are fully open was denoted as crack opening stress, σ_{op}, by Elber [62]. Crack opening stress can be applied in fracture mechanics by using the effective stress intensity factor range, ΔK_{eff}. The effective stress intensity factor range is given in Eq. (5.5) [85].

$$\Delta K_{eff} = F_{max} - K_{op} = f(g)(\sigma_{max} - \sigma_{op})\sqrt{\pi a} \tag{5.5}$$

Table 5.1: Fatigue crack growth models [84]

Theory	Equation
Paris	$\frac{da}{dN} = C(\Delta K)^n$
Mod. Paris	$\frac{da}{dN} = C(\Delta K)^n \left(1 - \frac{\Delta K_{th}}{\Delta K}\right)^p$
Walker	$\frac{da}{dN} = C\left(\frac{\Delta K}{(1-R)^{1-p}}\right)^m$
Forman	$\frac{da}{dN} = C\left(\frac{\Delta K^m}{(1-R)K_c - \Delta K}\right)$
FNK/NASGRO	$\frac{da}{dN} = C\left(\left(\frac{1-f}{1-R}\right)\Delta K\right)^n \left[\left(1 - \frac{\Delta K_{th}}{\Delta K}\right)^p / \left(1 - \frac{K_{max}}{K_c}\right)^q\right]$
Saxena	$\frac{da}{dN} = \frac{C_1}{\Delta K^{n1}} + \frac{C_2}{\Delta K^{n2}} - \frac{C_2}{[K_c(1-R)]^{n2}}$
McEvily	$\frac{da}{dN} = C(\Delta K - K_{th})^2 \left(1 + \frac{\Delta K}{K_c - K_{max}}\right)$
Roberts/Klesnil	$\frac{da}{dN} = C\left(\Delta K^p - \Delta K_{max}^q\right)$
Arad	$\frac{da}{dN} = C\left(K_{max}^2 - K_{min}^2\right)^m$
Mostovoy	$\frac{da}{dN} = C(\Delta G)^m$

Crack opening stress is calculated by Newmans crack closure model. The model defines crack opening stress by Eq. (5.6) and Eq. (5.7), which were developed by fitting them to the results calculated by the closure model for a center crack tension specimen.

$$\frac{\sigma_{op}}{\sigma_{max}} = A_0 + A_1 R + A_2 R^2 + A_3 R^3 \qquad for \qquad R \geq 0 \tag{5.6}$$

$$\frac{\sigma_{op}}{\sigma_{max}} = A_0 + A_1 R \qquad for \qquad R < 0, \tag{5.7}$$

where,

$$A_0 = (0.852 - 0.34\alpha + 0.05\alpha^2)[\cos(\pi\sigma_{max}F/2\sigma_0)]^{1/\alpha}$$
$$A_1 = (0.415 - 0.071\alpha)(\sigma_{max}F/\sigma_0)$$
$$A_2 = 1 - A_0 - A_1 - A_3$$
$$A_3 = 2A_0 + A_1 - 1,$$

where α is a constraint factor, σ_0 is the average of the yield stress and the ultimate stress of the material, and R is the stress ratio.

5.3.4 Cellular automata model

This study examines micromechanical crack propagation by adopting CA (cellular automata). In a number of scientific fields, CA are discrete, abstract computational systems considered useful as both general models of complex systems and more specific representations of non-linear dynamics. For one, CA are spatially and temporally discrete and composed of a finite or denumerable set of homogeneous simple units, normally cells or sometimes atoms. At each time interval, the cells update and instantiate one of a finite set of states. They evolve in parallel at discrete time stepsthe load spectrum cycle in this studyfollowing state update functions, or dynamical transition rules,

which are the stress intensity factor and material strength information. The update of a cell state with a stress intensity factor is obtained by taking the states of cells in the strength of plasticity of local neighborhood cells into account.

Another reason CA are useful is that they are abstract. That is, they can be specified in purely mathematical terms and implemented in physical structures without complicated constraints. Thus, crack closure, one of most costly calculations in structural design, could be achieved under the condition of multiple-crack propagation while accounting for neighboring crack effects. In addition, since CA can compute functions and solve algorithmic problems, they are computational systems, so fundamental LEFM theory can be infused into each cell. Despite functioning differently from traditional methods, CA, with suitable rules, can emulate a universal result. For example, in this study, a crack closure is not applied to the crack itself, as is traditionally done. The crack itself is typically the object of the computational results and other elements, even if neighboring elements were not considered. In CA, however, all cells can become one crack. The model calculates their material strength from their communication with neighboring cells and updates the results at each time step. Then it enables the cells to communicate with neighboring cells or elements.

1. *CA local rules*

   The strength of a cell is calculated by the stress intensity factor, based on the LEFM method. If the damage calculated by Eq. (5.8) reaches a critical value of 1, a crack is regarded as a dead cell. Each N can be estimated from Eq. (5.9), which is the integrated form of Eq. (5.4). Dead cells become cavities in the model and induce a reduction in the strength of neighboring cells. Using the cells own information, the cellular model acts automatically while updating cyclic load from the history spectrum.

$$D_i = \frac{1}{N_i} \tag{5.8}$$

$$N = \int_{N_i}^{N_{cr}} dN = \int_{a_i}^{a_{cr}} \frac{(1-R)K_c - \Delta K}{C(\Delta K)^n} da \tag{5.9}$$

2. *CA neighborhood*

If a neighboring cell of cell "A" is dead, the residual strength of cell "A" will be declined. When a load condition reaches a certain value, however, the dead cell may form a plastic region, causing an increase in strength. This crack closure of neighboring cells is represented by updating ΔK_{eff} and K_c. When dead cells reach the edge of the micro-level model base, CA neighborhood rules are updated to other local processes. To find the effect of a neighborhood that can be applied as a CA neighborhood rule, we conducted an experiment on an isotropic material with deductibility for general aluminum alloy. In the experiment, neighboring cracks are infused in one rectangular plate, shown in Figure 5.7, and exhibit the following four stages of status.

- Distance 47.62 mm: two cracks are not affected by each other
- Distance 22.22 mm: two cracks begin to interact
- Distance 9.52 mm: two cracks have further interaction, but not neighboring elements of cracks
- Distance 5.71 mm: two cracks have a significant effect and their stress distributions have completely changed

The distance from the center of a crack to the first affected point is 3.17 mm, when the stress increased by the range of 1.4 - 1.6 times more. Thus, we can define the neighboring effect as 1.5 times more stress when a neighboring crack is in the boundary of 3.17 mm. Since the element size for the base level is 3.65 mm, we can assume that the boundary is the adjacent neighboring cells of a crack.

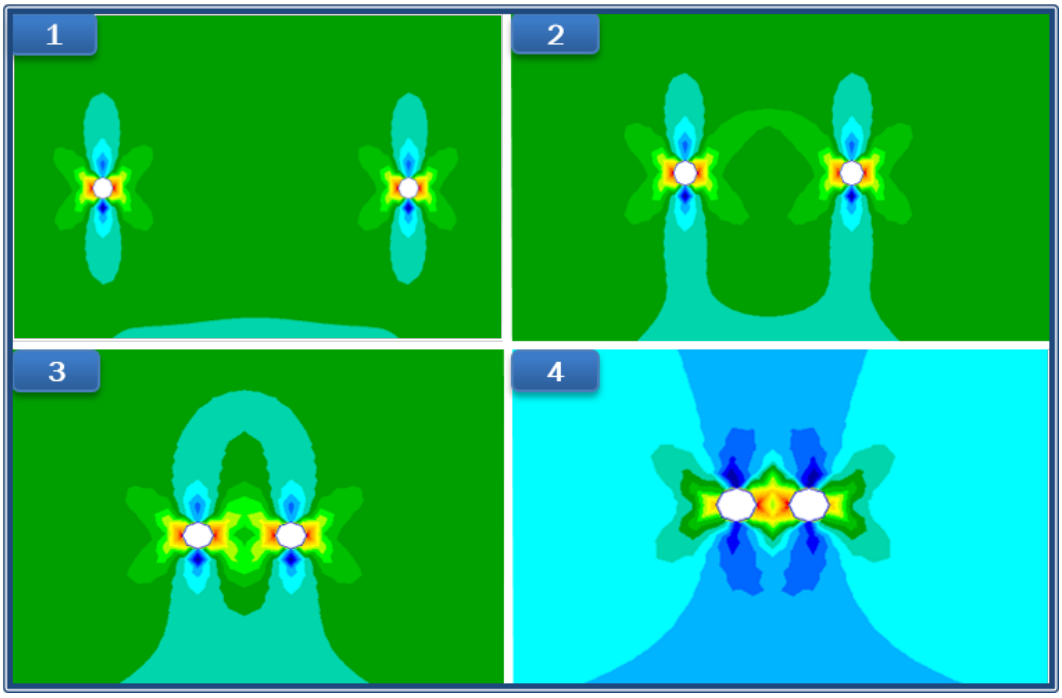

Figure 5.7: Experiment for the neighboring effect on CA

We must also acknowledge the local neighborhood effect as important in the global-level FEM. The effect can simply be accounted for by recognizing the adjacent base-level element, but even in parallelized computation (very often desired), the local can be updated by applying synchronization, explained as follows. Crack propagation at the base-level has independent calculations for each element that can be run in parallel with each crack propagation process treated as a logical process. When two cracks, however, become sufficiently close at the global level, the two base levels need to interconnect their effects, requiring a synchronization algorithm that updates the crack positions and implements a function that communicates the interaction between cracks, which explains the distributed crack propagation process.

Figure 5.8 shows a simple application of the algorithm. At the global level, the possibility of a crack at the base level proceeds as follows: G, Y1, B, and Y2. The wall clock starts from 1 and increases by 1 by initiating crack propagation on the base level. At the base level, the

blue dot represents a dead cell, which indicates that a crack has reached the critical length based on the calculation of the stress intensity factor. The red circle, which represents the region of influence, appears as a neighboring effect. The simulation begins with the G base level, which has a crack that is growing independently, and then continues with the Y1, B, Y2, and so on. All are independently simulated, except for Y1 and Y2, which are adjacent elements in the global level. Thus, the neighboring effect that we found in the previous chapter must be considered. The effect can be simply triggered by rolling back to the initial status when the framework identifies a problem. In this example, at time 5, the framework identified the problem. Then, the simulation of crack propagation for the Y2 began again at 6 with the initial condition while considering the neighboring effect of Y1. This method is an application of time warp synchronization, which is generally used for the synchronization of parallel computation [86].

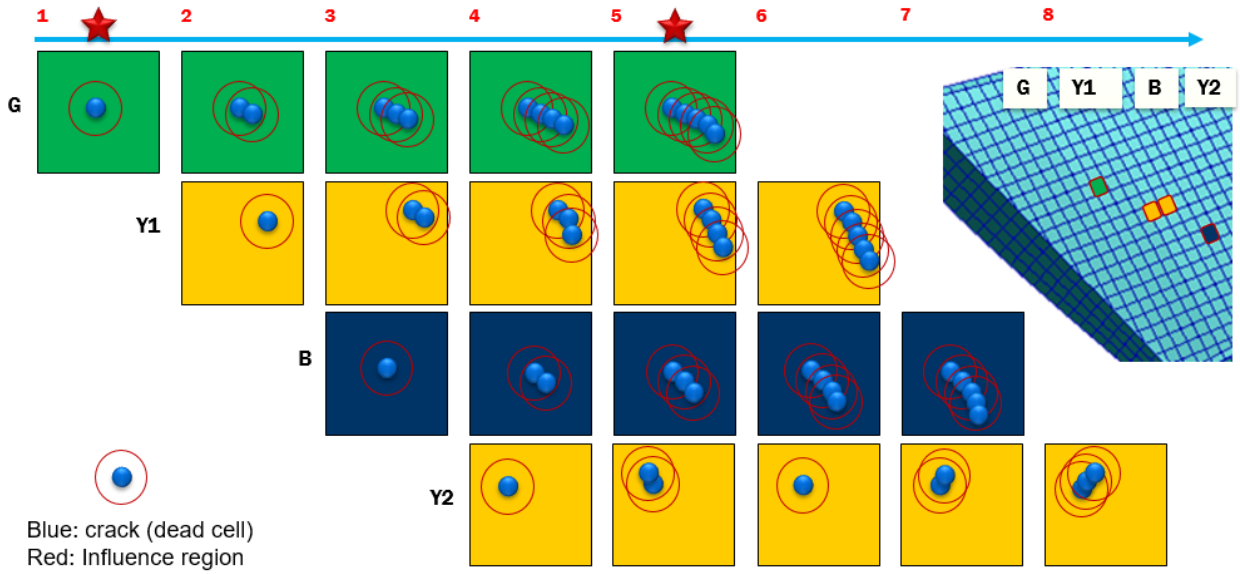

Figure 5.8: Application of the roll-back algorithm for synchronization

3. *Update rules*

Updating events follow load spectrum cycles from rainflow counting or its results. Each

cycle can be transferred to a time domain using Eq. (5.10). For example, the TWIST load spectrum contains 797,330 cycles for 4,000 flights. When we assume that one flight entails five hours of operation time, time step (1 cycle) of an updating event is equal to 0.025 hours of total operation life.

$$TimeStep(1cycle) = OperationTime\frac{TotalFlights}{TotalCycles}(hours) \tag{5.10}$$

Updating the CA status is repeated until the end of the sequence of the load spectrum, or crack size a has reached critical length a_{cr}.

5.4 Application of Crack Propagation Analysis Module

The results of the crack propagation analysis (CPA) program developed in this study are compared with the results of the analytical solution and NASGRO through a simple example. The purpose of NASGRO, which was originally developed at the NASA Johnson Space Center, was to perform fracture control analysis on NASA space systems [87]. The primary capability of NASGRO is to calculate fatigue crack growth and the crack instability of cyclically or statically loaded structures that contain initial crack-like defects [88]. With the creation of the NASA/FAA/USAF National Aging Aircraft Program, NASGRO became the preferred software package for many worldwide companies involved in the manufacturing of aircraft structures. Therefore, results generated by NASGRO will be accurate indicators of the CPA module developed in this study. The study utilizes the demo version of the NASGRO package, which allows for only the case of TC01 (a through crack in the center of a plate) and SC01 (a surface crack in the center of a plate), and the material property of Al 2024-T6.

Figure 5.9: Ultrasound scan that detects a flaw in a flap [89]

5.4.1 Problem description

All aircraft in operation are examined for safety through periodic inspections. Such inspections are typically based on visual inspection and nondestructive inspection (NDI) examination; however, the determination of components that will be inspected must follow FAA regulations, which depends on the time of flight [90]. Figure 5.9 shows an ultrasound scan, a recently developed NDI test. This study assumes that a crack is found during this ultrasound examination. The size of the crack and the shape of the surrounding structures are depicted in Figure 5.10 and used as a verification model for CPA, the subprogram of HFEM.

The identified crack on the plate is 50 mm wide and 2 mm thick; the initial crack was 1.27 mm long, which is the standard minimal size that can be found from mil-spec, Table 4.1. The material properties of this component, made from Al 2024-T3, are as follows: yield stress = 365.4 MPa, $K_{1c} = 1042$. The da of dN curve for the Al 2024-T3, shown in Figure 5.11, exhibits the following fitting parameters: $C = 2.382 \times E - 12$, $m = 3.2$. The plate is subject to a cyclic load that causes stress variation from 20 MPa to 200 MPa.

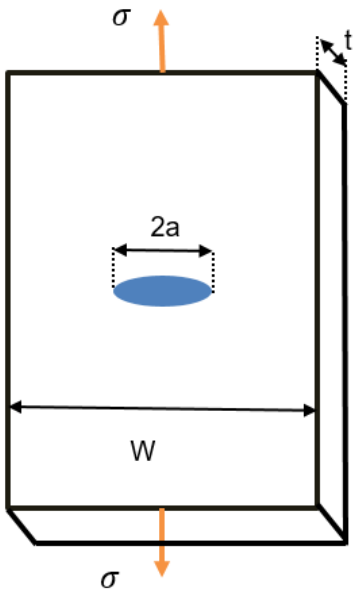

Figure 5.10: Problem description for the verification of CPA

5.4.2 Calculation of the critical crack size

The LEFM-based damage tolerance design determines the fatigue life by calculating the number of cycles from the growth of the initial crack to the growth of the critical crack. Therefore, we must first know the length of the critical crack. We can begin to determine the length of the critical crack size from Eq. (5.1), and the equation can be transformed as follows (Eq. (5.11)) with the result of substituting the actual value.

$$a_c = \left(\frac{K_{1c}}{Y \sigma_{max} \sqrt{\pi}} \right)^2 = \left(\frac{1042}{1.12 \cdot 200 \sqrt{\pi}} \right)^2 = 6.888, \tag{5.11}$$

where Y is the geometry correction factor, which we assume to be 1.12 for the following reason. Y is the value of $f(g)$, which is the shape correction function that includes the finite width effect, the front wall effect, and the crack shape. The stress intensity factor K_I is expressed as a

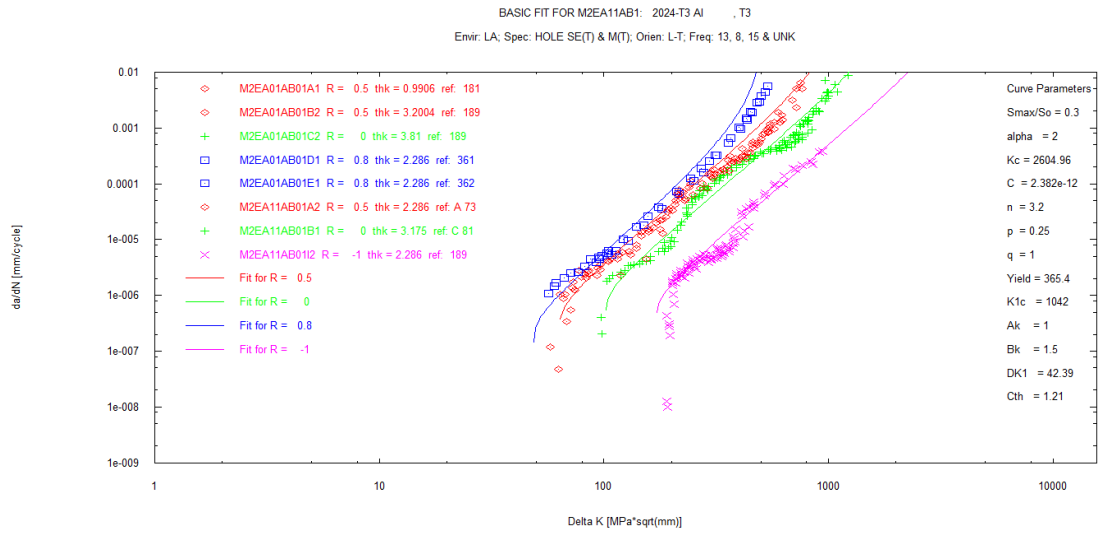

Figure 5.11: The basic fit for 2024-T3 [91]

function for $f(g)$, as in Eq. (5.12).

$$K_I = \frac{P}{B\sqrt{W}} f(\frac{a}{W}) = \frac{P}{BW} f(\frac{a}{W}) \sqrt{\frac{W}{\pi a}} \sqrt{\pi a}, \tag{5.12}$$

where B is the thickness of plate, W is the width of the plate, and the P is a force that acts on the plate. Thus, the first term of Eq. (5.12), $\frac{P}{BW}$ is actually stress; then Eq. (5.12) can be expressed by Eq. (5.13).

$$\sigma f(\frac{a}{W}) \sqrt{\frac{W}{\pi a}} \sqrt{\pi a} = Y \sigma \sqrt{\pi a} \tag{5.13}$$

Thus, Y is,

$$Y = f(\frac{a}{W}) \sqrt{\frac{W}{\pi a}} \tag{5.14}$$

when the limit a/w goes to infinity $f(a/W)$,

$$\lim_{a/W \to \infty} f(\frac{a}{W}) = \sqrt{\frac{\pi a}{W}}[0.752 + 0.37] \tag{5.15}$$

If we substitute Eq. (5.15) into Eq. (5.14) instead of $f(\frac{a}{W})$ then,

$$Y = 1.12 \tag{5.16}$$

The range of equation $f(g)$ is from 1 to 1.4, but many industrial situations show a factor of 1 to 1.2. This study uses $Y = 1.12$, derived from Eq. (5.13) to Eq. (5.16).

Let's return to Eq. (5.11), which shows the result of the critical crack size. The result of analytical solution is 6.888 mm, and the CPA module of HFEM yields the same result, 6.88794 mm, as expected. This study evaluates the critical crack size through one of the NASGRO modules, NASCCS, which calculates the critical crack size with an iteration method, Newtons method [97]. The basic concept of CPA module is very similar to the NASGRO method, but it divides the step size of a crack to calculate K_i, which originates from the stress intensity corresponding to the initial size, a_i , more precisely. In addition, the calculation of Y generates some of the difference between the CPA module and NAGRO method. However, the result of crack size, 7.0752mm, from NASGRO, shown in Figure 5.12, is almost the same as the analytical solution and the result of CPA module.

In crack propagation analysis, the next step is to calculate the crack growth from a_i , the initial crack size, and then a_c, the critical crack size from Eq. (5.11).

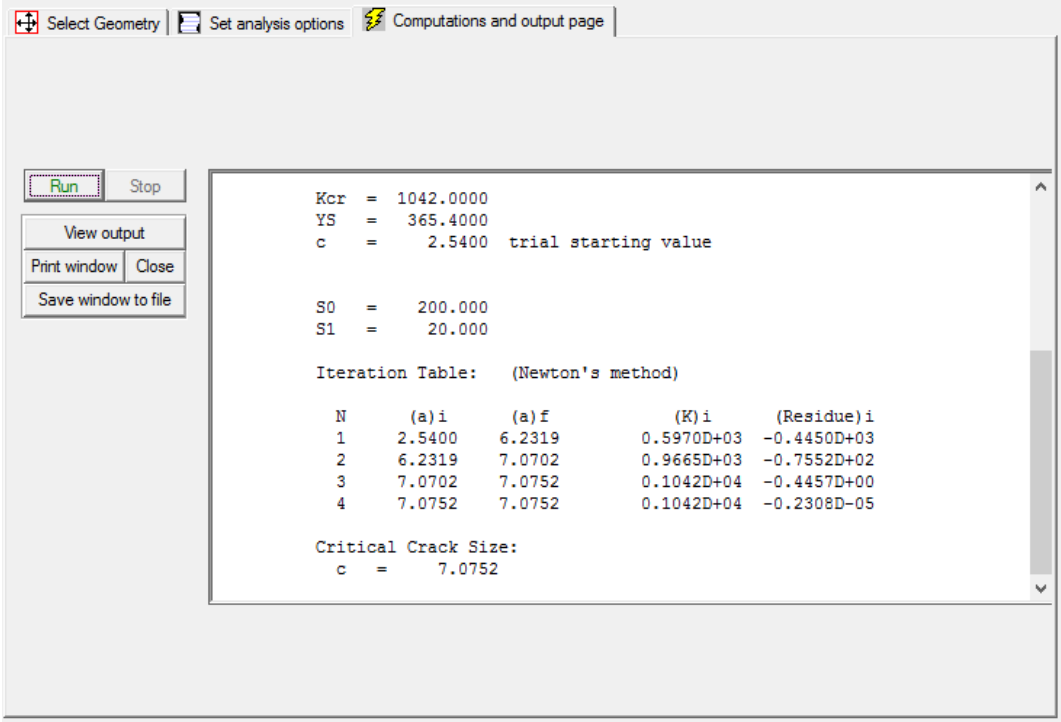

Figure 5.12: The result of critical crack size from NASGRO

5.4.3 Crack propagation

The relation between da/dN and K for the steady-state crack growth region, region II in Figure 5.6, has already been described in Paris Eq. (5.3) already. Since region II is typically seen under cyclic loading, the Paris law is generally used in many applications. The definition of Paris law was $da/dN = C(\Delta K)^m$. To calculate fatigue life, we rearrange the equation and integrate the relationship, yielding Eq. (5.17).

$$N_f = \int_0^{N_f} dN = \int_{a_0}^{a_c} \frac{da}{C(\Delta K)^m} \tag{5.17}$$

From Eq. (5.2) and Eq. (5.13), we know that $\Delta K = f(g)\sigma\sqrt{\pi a} = Y\sigma\sqrt{\pi a}$. Thus, the

Eq. (5.17) can be rewritten as Eq. (5.18).

$$N_f = \int_{a_0}^{a_c} \frac{da}{C(Y\delta\sigma\sqrt{\pi a})^m} = \frac{1}{C(Y\delta\sigma\sqrt{\pi})^m} \int_{a_0}^{a_c} a^{-\frac{m}{2}} da \tag{5.18}$$

From the integration Eq. (5.18), we obtain Eq. (5.19).

$$\begin{aligned} N_f &= \frac{1}{C(Y\delta\sigma\sqrt{\pi})^m} \left[\frac{a^{-\frac{m}{2}+1}}{-\frac{m}{2}+1} \right]_{a_0}^{a_c} \\ &= \frac{1}{C(Y\delta\sigma\sqrt{\pi})^m} \left(\frac{1}{-\frac{m}{2}+1} \right) \left[a_c^{-\frac{m}{2}+1} - a_0^{-\frac{m}{2}+1} \right] \end{aligned} \tag{5.19}$$

Then we rearrange Eq. (5.19) more conveniently,

$$N_f = \frac{1}{C(Y\delta\sigma\sqrt{\pi})^m} \left(\frac{1}{\frac{m}{2}-1} \right) \left[\frac{1}{a_0^{\frac{m}{2}-1}} - \frac{1}{a_c^{-\frac{m}{2}+1}} \right] \tag{5.20}$$

To obtain analytical solution, we substitute the actual values in Eq. (5.19).

$$N_f = \frac{1}{2.382E-12(1.12 \cdot 180\sqrt{\pi})^{3.2}} \left(\frac{1}{\frac{3.2}{2}-1} \right) \left[\frac{1}{1.27^{\frac{3.2}{2}-1}} - \frac{1}{6.888^{\frac{3.2}{2}-1}} \right] \tag{5.21}$$

The analytical solution from Eq. (5.21) shows that the initial crack size reaches the critical crack size while loading about 2,614 half-cycles because loading data have two points. Thus, we interpret 2,614 half-cycles as 1,307 cycles. However, this result differs significantly from the results we derive from NASGRO. From this conclusion, which will be discussed in the next chapter, NASGRO showed a crack propagation phenomenon of about 2.16 mm as a result of the life cycle analysis of 2,000 cycles. This finding shows a significant error from the 6.88 mm crack propagation, which is the duration of the initial crack that reached the critical crack size

during the 1,307 cycles, resulting from the analytical solution. The difference in these results is directly related to the crack closure phenomenon. Thus, because the crack tip region forms a plastic that actually blocks the propagation, the crack closure phenomenon must be considered a very important factor in the analysis of crack growth.

5.4.4 CPA module with crack closure

Forman, Newman, and other scientists from NASA, NLR, and ESA formulated well-known crack opening equation that shows the phenomenon in which cracks propagate from the plastic region of crack closure [92].

$$\frac{da}{dN} = C\left[\left(\frac{1-f}{1-R}\right)\Delta K\right]^{n} \frac{\left(1-\frac{\Delta K_{th}}{\Delta K}\right)^{p}}{\left(1-\frac{K_{max}}{K_c}\right)^{q}}, \tag{5.22}$$

where N is the number of fatigue cycles in a load spectrum, a is the crack length, R is the stress ratio, ΔK is the range of the stress intensity factor, and C, n, p, and q are empirically derived constants from the material property. For the factor of crack closure, the crack opening function is f, the threshold stress intensity factor is ΔK_{th}, and the critical stress intensity factor is K_c. In the case of a positive stress ratio, the crack growth relationship, Eq. (5.22) can be reduced to

$$\frac{da}{dN} = \frac{C\Delta K^{n}\left(1-\frac{\Delta K_{th}}{\Delta K}\right)^{p}}{\left(1-\frac{K_{max}}{K_c}\right)^{q}}. \tag{5.23}$$

Eq. (5.23) includes many types of stress intensity factors, K_{max}, K_{min}, ΔK, ΔK^{*}, and ΔK_{th}. Eq. (5.24) and Eq. (5.23) show the maximum and the minimum stress intensity factor respectively.

$$K_{max} = Y\sigma_{max}\sqrt{\pi a} \tag{5.24}$$

$$K_{min} = Y\sigma_{min}\sqrt{\pi a} \tag{5.25}$$

ΔK is the difference of $K_{max} - K_{min}$. The threshold stress intensity factor, ΔK_{th}, needs to consider two cases for $R \geq 0$ or $R < 0$ by the following approximated empirical equations:

$$\begin{aligned} \Delta K_{th} &= \Delta K_1^* \left[\frac{1-R}{1-f[R]}\right]^{1+RC_{th}^p} / \left(1-A_0\right)^{(1-R)C_{th}^p}, R \geq 0 \\ \Delta K_{th} &= \Delta K_1^* \left[\frac{1-R}{1-f[R]}\right]^{1+RC_{m}^p} / \left(1-A_0\right)^{(C_{th}^p - RC_{th}^m)}, R < 0 \end{aligned} \tag{5.26}$$

ΔK^* is related to current condition with the current crack size and initial crack size.

$$\Delta K_1^* = \Delta K_1 \left[\frac{a}{a+a_0}\right]^{\frac{1}{2}} \tag{5.27}$$

where R is the stress ratio, A_0 is a constant from Eq. (5.6) and Eq. (5.7), ΔK_1 is the threshold stress intensity factor range when R goes 1.0, C_{th} is an empirical fit constant with different values for positive(superscript p) and negative(superscript m) of R ratios, a is the crack length, and a_0 is initial crack size, and f is the Newman closure function that differs from that of Eqs. (5.6) and (5.7).

$$f = \frac{K_{op}}{K_{max}} = \begin{cases} max(R, A_0 + A_1R + A_2R^2 + A_3^3) & , R \geq 0 \\ A_0 + A_1R & , -2 \leq R < 0 \end{cases} \tag{5.28}$$

We applied the crack opening equation to develop the CPA module of HFEM, based on the phenomena of the crack closure explained in this chapter. Thus, it is through this module that we reevaluate the previously described example. According to the finding that appears in Figure 5.13,

the final crack size after 2,000 cycles is 2.431 mm; that is, the final number of life cycles from the initial crack size is about 29,340,535.

```
 ----------------------------------------
Critical crack length=  43.0483201156
Number of cycles applied = 2000.0
 ----------------------------------------
Current crack length =  2.43087625947
Estimated life cycles =  141584081.415
 ----------------------------------------
```

Figure 5.13: The result of crack propagation from CPA module of HFEM

A comparison between this result and the numerical calculation revealed a significant error. Thus, for further verification, this study conducted a crack propagation analysis for the same example using NASGRO and compared it with the CPA module. The load information input for the calculation of NASGRO was 2,000 cycles, as in the previous analysis, and a block of 1,000 cycles was repeated twice, as shown in Figure 5.14.

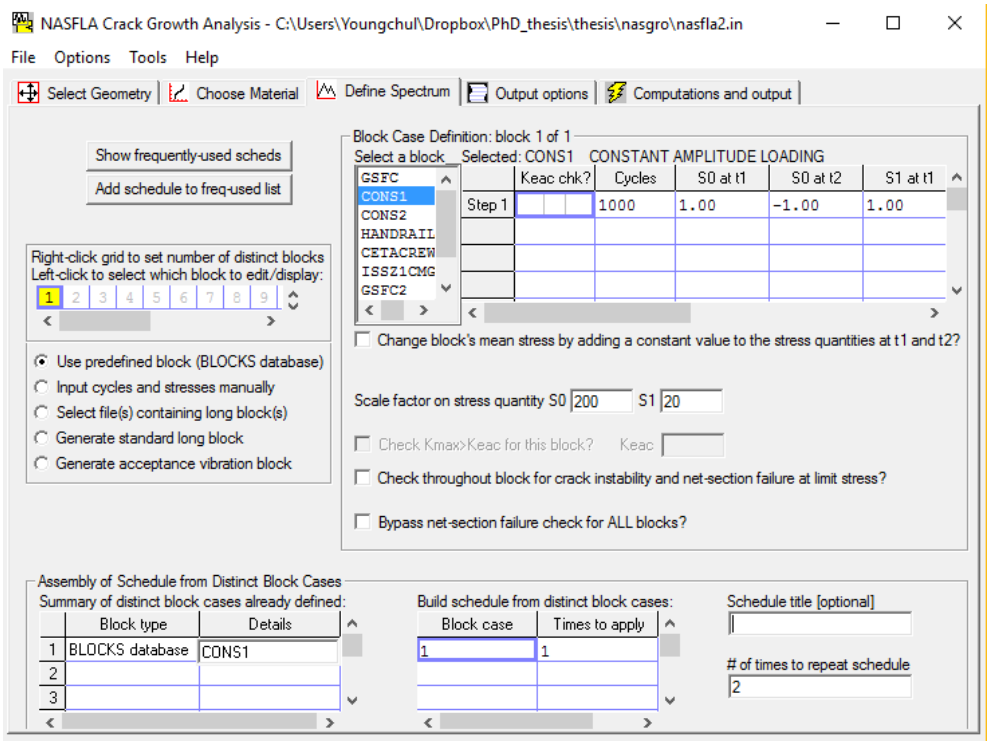

Figure 5.14: Input window of the load spectrum for the NASGRO

In the input, the stress oscillates from 200 MPa to 20 MPa along the cosine wave, which is a

simple amplitude fluctuation similar to that in the example.

The material information is already shown in Figure 5.11 through the da of dn curve, but the detail numerical data are shown in Figure 5.15. Similarly, using Al 2024-T3 material, we used the same input values in the CPA module of the HFEM analysis.

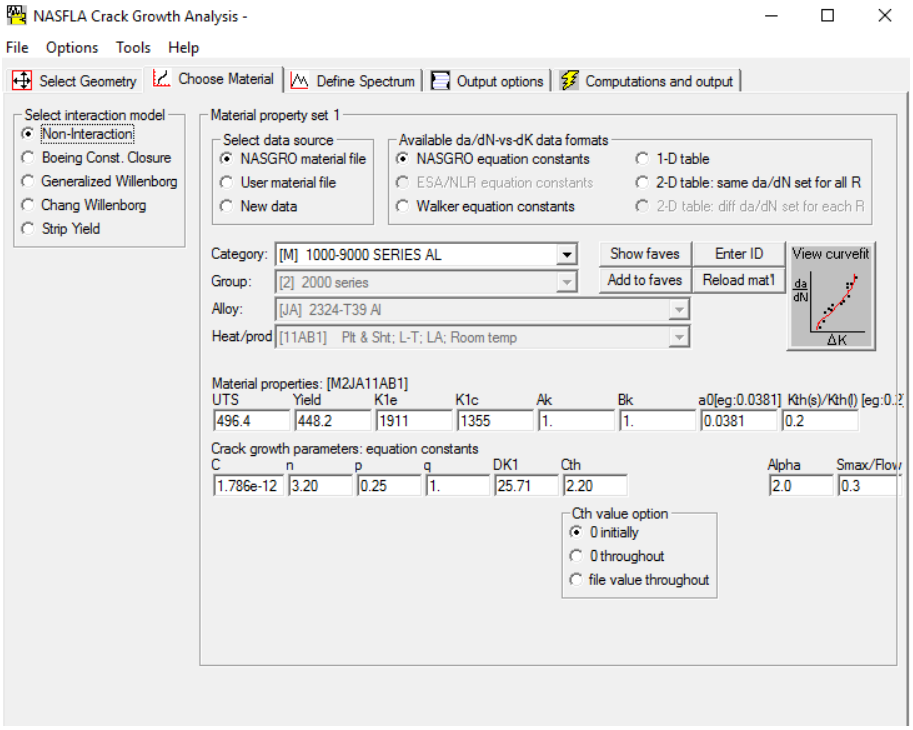

Figure 5.15: Input window of the material data for the NASGRO

Figure 5.16 represents the crack length calculated by NASGRO. As shown in the figure, the crack growth length for the 2,000 cycles is about 2.159 mm, which is close to 2.036 mm calculated by the CPA module. Because of the nature of fatigue analysis, this finding is relatively accurate and generally an adequate interpretation even if the number of digits is the same. For example, if a spectrum is generated at 60 Hz, 60 points are the duration of one second. In other words, one second has 15 cycles. If we obtain an error of 1,500 cycles, it indicates only a 100-second difference over the entire lifetime of an aircraft, which is roughly 40,000 hours.

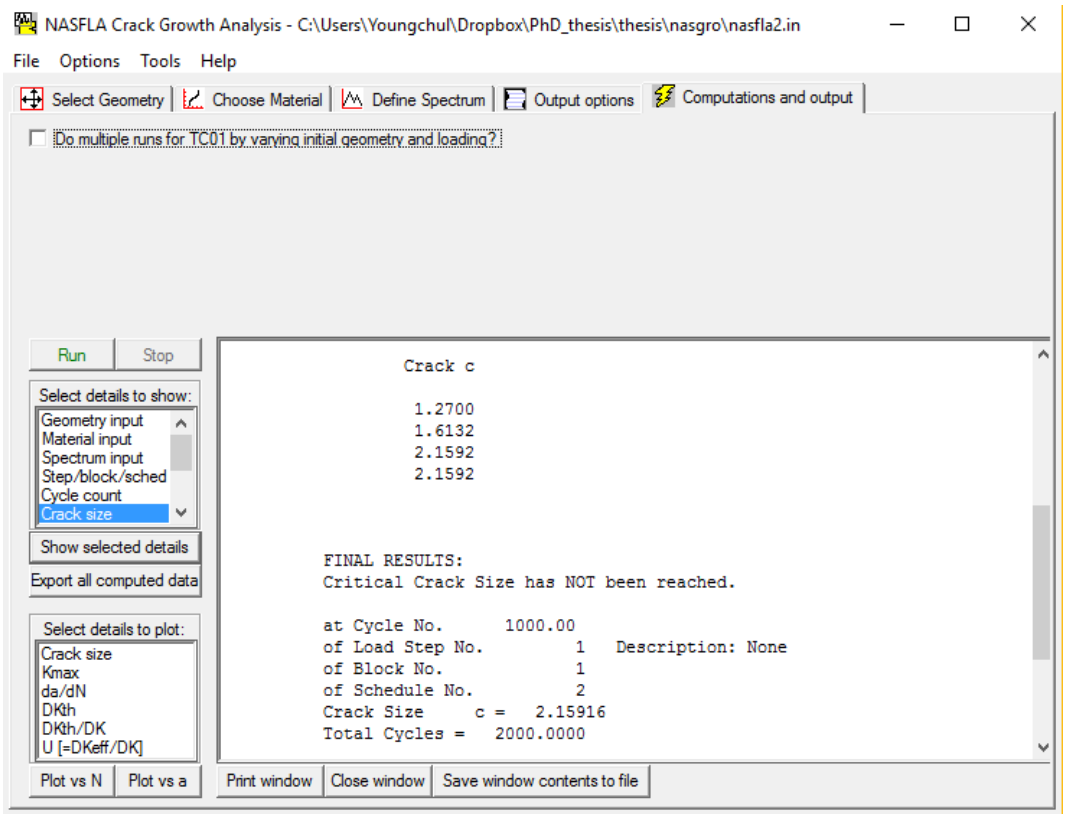

Figure 5.16: Resulting window of the NASGRO for 2,000 cycles

CHAPTER 6

FUTURE LOAD SPECTRUM

6.1 TWIST

The TWIST (Transport Wing STandard) is a program for generating the load spectrum of a fixed-wing aircraft based on the overall experimental data on historical transport aircraft such as the Boeing 720, Boeing 737, and DC-10, among others [51]. Through the experiment, the flight load spectrum related to the bending moments of the wing roots is obtained from various aircraft types to develop a standardized load spectrum. From the accumulated experimental data of the aircraft, the TWIST algorithm can generate the standardized load spectrum by considering the weight, wing load, cruise speed and design distance over a wide range.

In TWIST, all spectra were based on a 40,000 flights, which is the average value of the design life for the transport aircraft. The data obtained on load spectra for the considered aircraft are shown in Figure 6.1. As shown in the Figure 6.1, each spectrum has a similar shape, so a standardized load spectrum can be obtained based on the mean value.

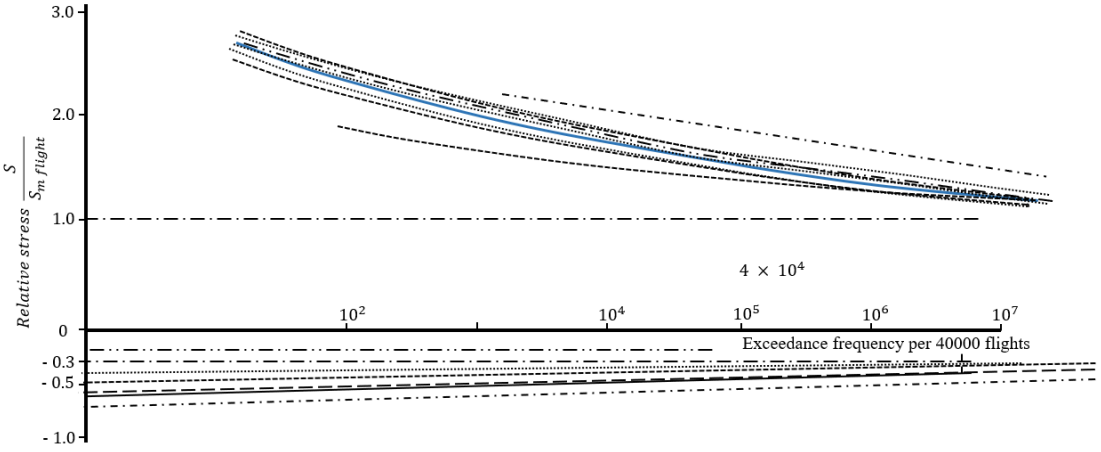

Figure 6.1: Load spectra pertaining to 40,000 flights for different aircraft [51]

In order to obtain load spectrum points for test purposes or computational analysis, it is necessary to switch data to different levels of specific strength based on the standardized spectrum. The switching process proceeds in the following order.

6.1.1 Step 1: Convert the sequenced spectrum into a "stepped" function

The continuous load spectrum is expressed as a stepped function to limit and define the number of different load amplitudes. The limitations considerably simplify the load control system and the analysis system of the fatigue machine or program. To convert a continuous spectrum into a stepped state, the size of the largest amplitude and the smallest amplitude must first be determined. From the two amplitudes, ten different types of gust load distribution are computed. This is defined as the load level, which is divided by the magnitude of the load spectrum. The strongest load is level I, and the weakest load is level X. The magnitude of each load is 1.0 ± 1.60 for level I and 1.0 ± 0.222 for level X. The magnitude of the load at this time is dimensionless and can be expressed as Eq.(6.1).

$$Load\ magnitude = \frac{S}{S_{m\,flight}}, \tag{6.1}$$

where, the S is the stress and the $S_{m\,flight}$ is the mean stress during a flight.

The flight type according to the cruise condition of the aircraft can be represented by the distribution of the load levels I to X. For example, flight type A is the strongest flight with the largest amplitude (level I), and flight type J includes only the lowest amplitude (level X). The load spectrum is obtained from a series of these flight types. The Figure 6.2 is a stepped flight load spectrum showing the frequency and magnitude of occurrence by load level constructed through the explained conditions.

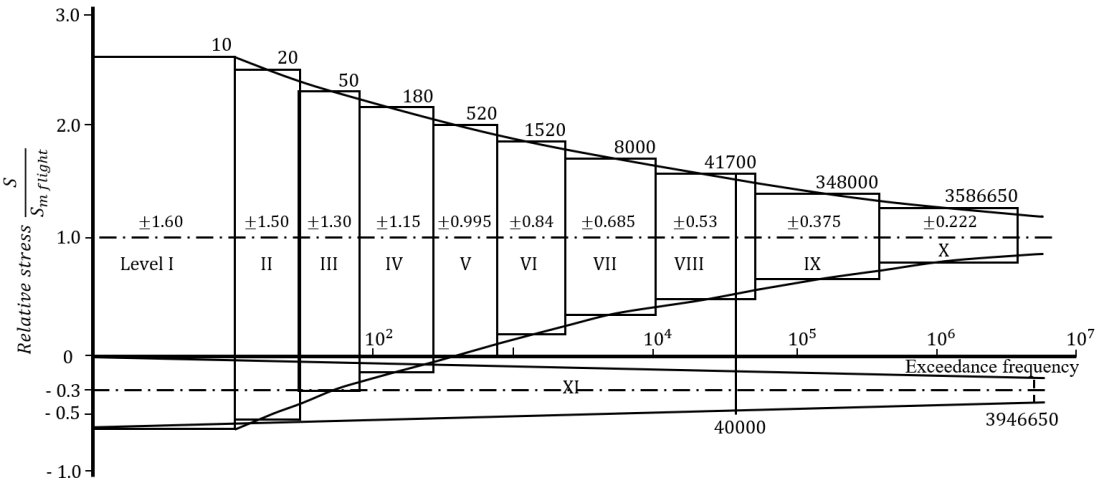

Figure 6.2: Stepped test load spectrum for 40,000 flights [51]

6.1.2 Step 2: Definition of "flight block"

A method of dividing the standardized load spectrum for a 40,000 hour flight into a constant "flight block" is required. This is considered to be the obvious choice, to divide 4,000 flights into 10 "flight blocks", since the highest load occurs 10 times in 40,000 flights. As a result, one block of 4,000 flights will be repeated periodically in the experiment or the computational analysis.

The 4,000 flight hour block contains ten different flight types, denoted from A to J, in which flight type A contains a level I flight and is hence the most severe flight type. The different flight types, as well as frequency at which each amplitude level is experienced during the flight type, is shown in Table 6.1.

6.2 Inverse TWIST Method

Based on the historical load data, TWIST divides the intensity of flight into 10 sections that are from I to X and arranges the number of load cycles corresponding to the each flight type. By combining these flight types into a single spectrum, the load spectrum for the required aircraft design is completed. For this study, inversed TWIST method is developed and it will be referred

Table 6.1: Definition of flight types and number of load cycles within one block [51]

Flight Type	Number of flights in one block of 4,000 flights	Number of gust loads (full cycles) at the 10 amplitude levels										Total number of cycles per flight
		I	II	III	IV	V	VI	VII	VIII	IX	X	
A	1	1	1	1	4	8	18	64	112	391	900	1,500
B	1		1	1	2	5	11	39	76	366	899	1,400
C	3			1	1	2	7	22	61	277	879	1,250
D	9				1	1	2	14	44	108	680	950
E	24					1	1	6	24	165	603	800
F	60						1	3	19	115	512	650
G	181							1	7	70	412	490
H	420								1	16	233	250
I	1,090									1	69	70
J	2,211										25	25
Total number of cycles per block of 4,000 flights		1	2	5	18	52	152	800	4,170	34,800	358,665	
Cumulative number of load cycles per block of 4,000 fl.		1	3	8	26	78	230	1,030	5,200	40,000	398,665	

as iTWIST. The iTWIST aims to update the load spectrum based on the data that an aircraft has experienced using the method of TWIST.

The iTWIST first identifies the intensity of the load when it receives load data from sensors, such as a fiber optic sensor, mounted on a wing or structure. The magnitude of intensity and number of intensity accumulated at the end of the flight help to determine which of the 10 flight types corresponds to current flight. This eventually corresponds to a classification method classified into 10 labels, which are flight types based on the accumulated data. The data are an array of non-dimensionalized stress values and the order is not important because of the random arrangement from TWIST itself. For example, a flight with only level X intensity of 25 cycles seems to be a J-type flight obviously. On the other hand, if there is at least one level IX of flight intensity, it becomes I-type flight. Classification is thus accomplished easily according to the greatest stresses in flight. However, the number of cycles for each lower intensity level can be determined when it completes the total number of flights occurring in one flight block has.

The iTWIST algorithm eventually replaces the values of Table 6.1 with the unique values from each aircraft based on the data obtained during the flight. Therefore, if the spectrum is generated according to the TWIST algorithm based on the updated table, the inherent fatigue spectrum of the aircraft can be obtained. As the aircraft continues to operate, the resulting load values will continue to update this table, and iTWIST will gradually learn the table values in the direction of utilizing the unique values. In other words, as data accumulates, more accurate structural health prediction becomes possible.

CHAPTER 7

FRAMEWORK DEVELOPMENT

7.1 Structural Common Research Model

The parametric structural wing model, an applied finite element analysis, is based on the CRM (common research model) of NASA. The NASA CRM, widely used in studies of the aerodynamic behavior of a wing, contains one-half of a notional aircraft cut away at the plane of symmetry. It includes one half of the fuselage and one wing and consists of surfaces necessary for aerodynamic analysis. However, it does not offer ample opportunity for structural analysis as it lacks the required internal components for stiffness and strength calculations. This chapter introduces such missing components for structural analysis of the CRM by adopting the most widely used design choices.

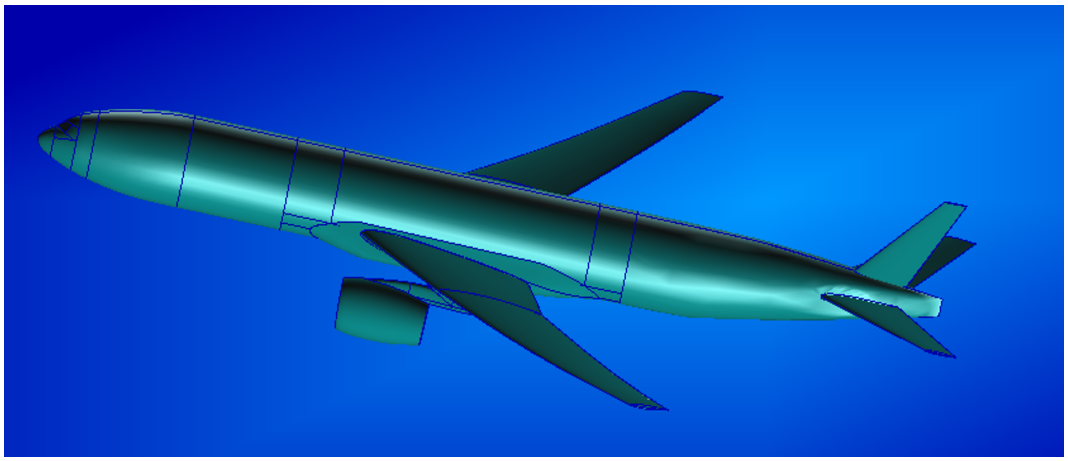

Figure 7.1: The geometry of the full CRM model

7.1.1 NASA common research model

This model is based on the CRM, a common NASA research model that focuses on the aerodynamic design of the wing. The model adopts a contemporary transonic supercritical wing de-

sign with well behaved, high-performance aerodynamic characteristics for configurations with and without the nacelle/pylon group [93].

This study first developed a full CRM model from a part of CRM distributed by NASA for an example of a digital twin. The geometry outer model is shown in Figure 7.1. For the purpose of stress and fatigue analysis, the digital twin requires the development of an FE model. Figure 7.2 and Figure 7.3 show the FE model that represents a digital twin developed in this study. Nevertheless, we examined the wing box only for the on-board framework.

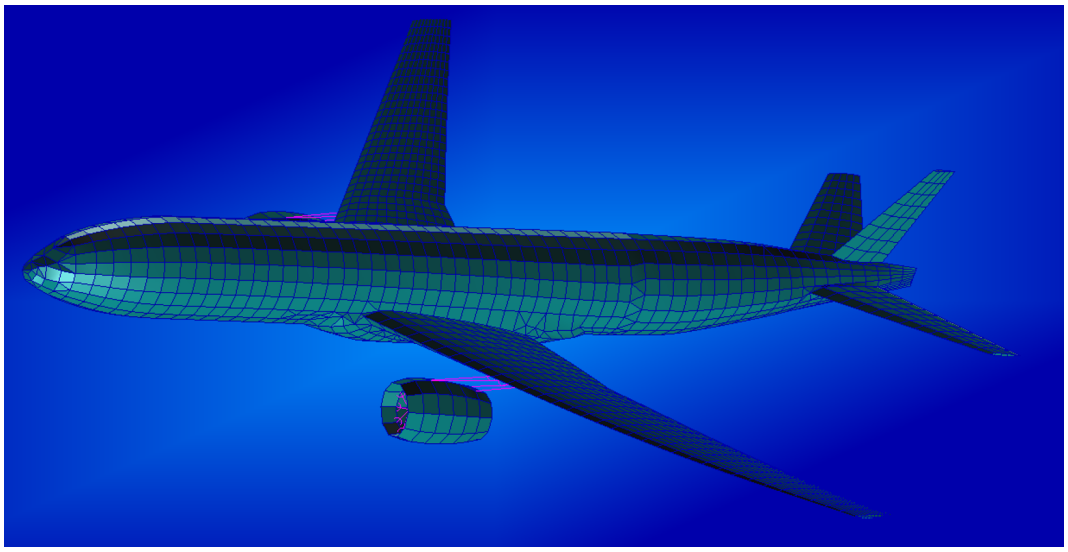

Figure 7.2: Top view of the full FEM of the CRM

7.1.2 Configuration and description of the finite element model

The development of the CRM involved the use of contemporary experimental databases for the purpose of validating specific applications of computational fluid dynamics (CFD). Therefore, the CRM wing has mainly been modeled with a skin surface because CFD analysis requires only the layout of wing geometry. Because of the absence of an internal structure, a structural analysis is virtually impossible. A valid investigation of structural analysis requires internal structures such as spars, ribs, and stringers. Therefore, to examine the internal structure, this chapter uses specific geometry that represents todays most common types of aircraft.

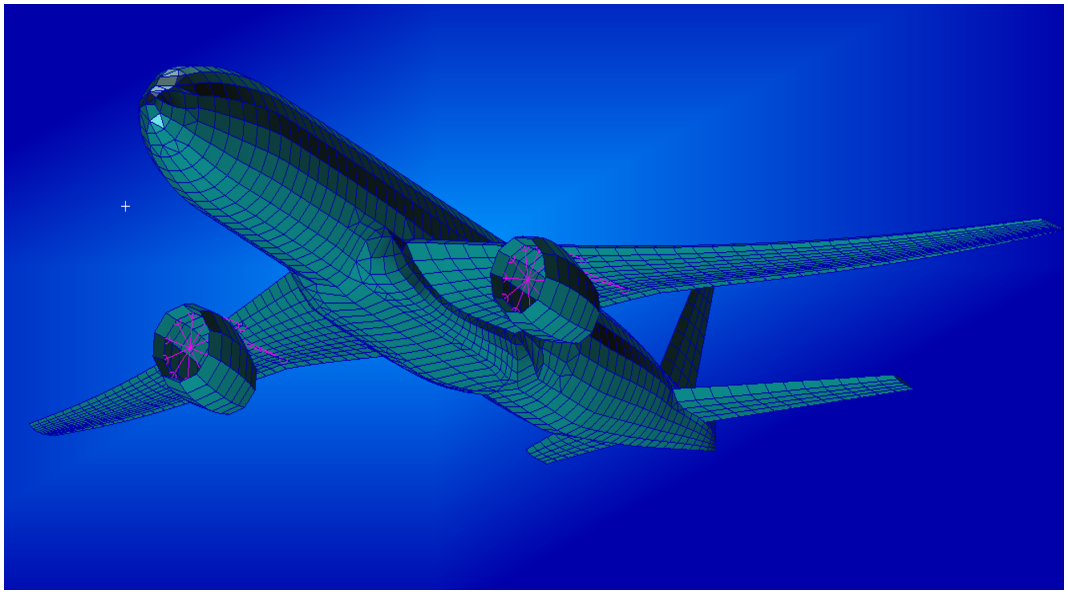

Figure 7.3: Bottom view of the full FEM of the CRM

Wing box configuration

We determine a structural model by defining the part of the CRM wing occupied by the wing box, so we select wing-box geometry by imposing its chord-wise extension, that is, the position of the front and rear spars. Although commercial transport aircraft generally have two main wing spars, some models contain a third spar in the portion of the wing closest to the fuselage. The locations of the main wingbox spars for Boeing are shown in Figure 7.4. The NASA CRM wing model closely resembles the Boeing 777 with a half span of 1,038 inches and a chord length of 624 inches. Since the sizes of aircraft wings vary, the locations are shown as a percentage of the chord (measured from the leading edge) versus the percentage of the span (measured from the fuselage) [94]. The results of this notional model show that the front spar is located at 25% of the chord and the rear spar at 70%, shown in Figure 7.5.

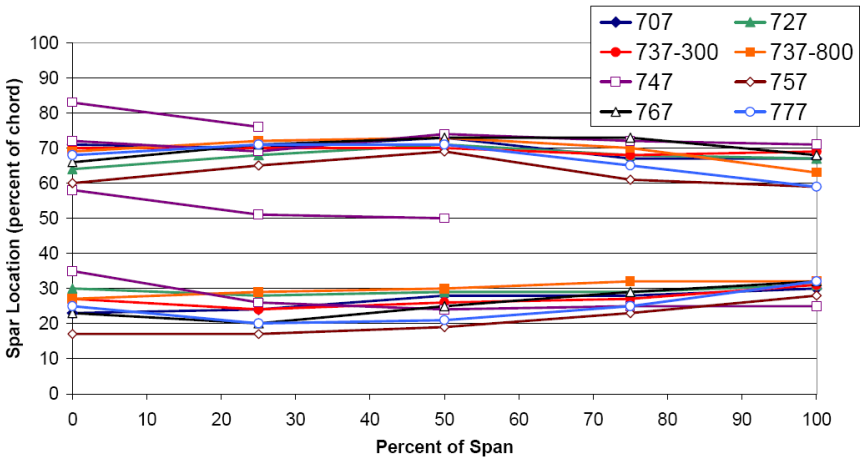

Figure 7.4: Spar location chart for the Boeing 7X7 Series [94]

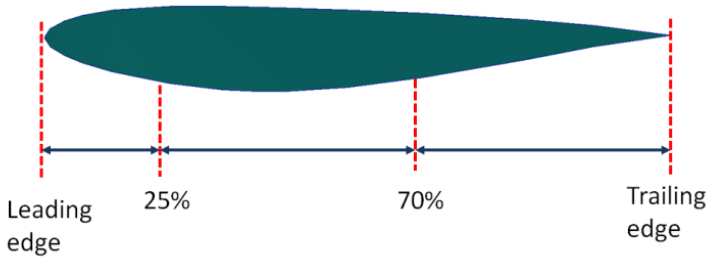

Figure 7.5: Position of the wing box

Wing rib arrangements

Wing-rib arrangements outside of the wing-root joint are critical for designing compression structural stability, especially on the wing upper surface. The root joint design and two basic arrangements are shown in Figure 7.6 [95]. Rib spacing is also important. The wing ribs for transport aircraft are typically uniformly spaced over the majority of the wing span. The average spacing between the centers of the ribs for the Boeing is 2.1 - 2.6 ft. along the wing sweep direction (i.e., along the wing) and approximately 2 ft. for the span direction (i.e., perpendicular to the fuselage axis). The uniformity of rib spacing for transport jets is most likely driven by maintenance access requirements [94]. The shape of the rib arrangement for this model is shown in Figure 7.7.

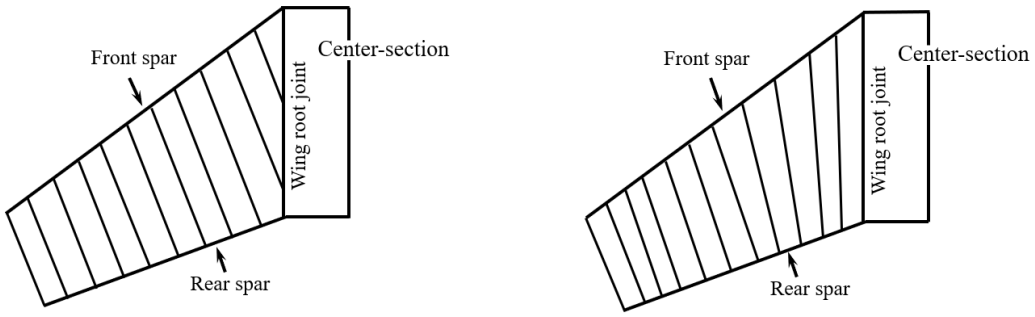

(a) Perpendicular to spar (b) Parallel to streamline

Figure 7.6: Arranged internal structure

[95]

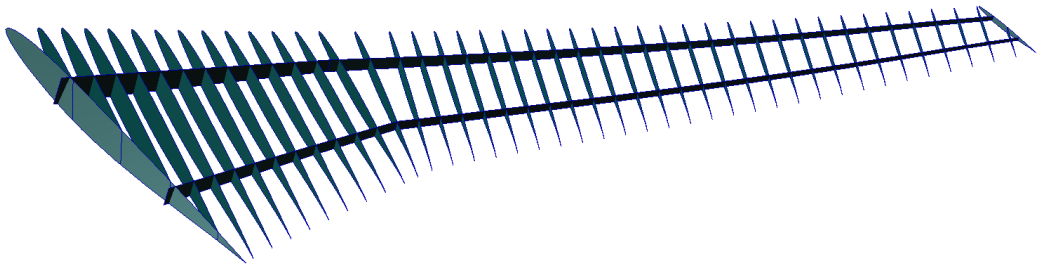

Figure 7.7: Rib arrangements

All ribs are perpendicular to the rear spar, which is parallel to the fuselage and spaced 30 inches, common in recently developed transport.

FEM model

The FEM model is based on the geometry model developed by NASA CRM for an internal structure of an aircraft. This model is meshed with shell elements for the skin and beam elements for stringers. In the case of shell elements, QUAD4 is mainly used for the upper and lower skin, flanges, spars, and ribs. Sometimes TRIA3 elements, which adapt to changes in geometry, are used. The QUAD4 element contains four nodes located on every apex and isoparametric flat-plate element. This element behaves well when irregularly shaped and good results can be obtained with

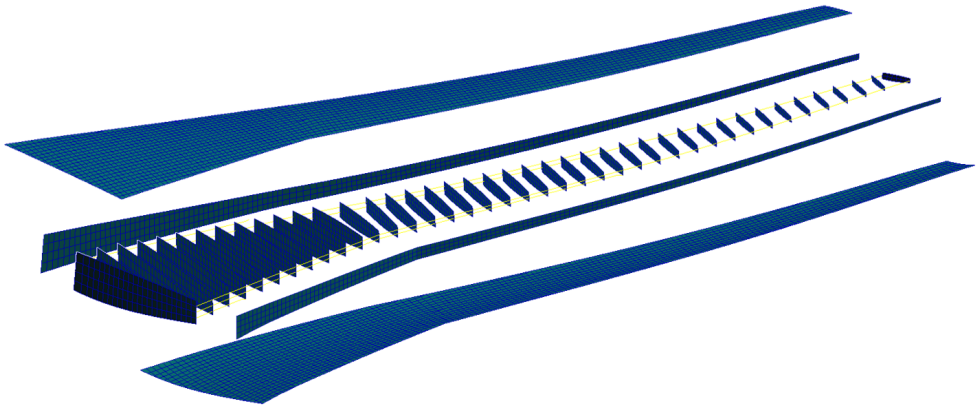

Figure 7.8: SCRM internal structure

skew angles up to 45 degrees [94].

7.1.3 Global finite element model

The reference wing model used for the purposes of a macro-mechanical approach to initial crack evaluation is the CRM (common research model) from NASA. This model was initially developed as a reference configuration model with a focus on the aerodynamic design analysis of a wing. The model adopted a contemporary transonic supercritical wing design with well-behaved aerodynamic characteristics typical of high-performance configurations. The model has associated contemporary experimental databases for the purpose of validating specific applications of computational fluid dynamics (CFD). Therefore, the CRM wing has mainly been modeled only with an outer mold line with no internal structure. The wing platform geometry follows: the wing span is 58.765 m, the aspect ratio is 9.0, and the taper ratio is 0.275 [93]. The internal structural components developed for the CRM consist of spars, robs, and stringers. The intense structure, modeled by the structural common research model (SCRM), is based the standard layout of common aircraft types [94]. Details for the SCRM components for the wing box of the finite element model are shown in Figure 7.8.

We select the wing-box geometry by imposing its chord-wise extension, that is, the position

of the front and rear spars. Although commercial transports generally have two main wing spars, some models contain a third spar in the portion of the wing closest to the fuselage. This FEM model is covered by shell elements for skin and beam elements for stringers. We assume a flight condition based on the most severe aerodynamic load condition for static stress analysis. The selected condition is a cruise with a velocity of Mach 0.75, an altitude of 5,500 m and a load factor of 2.3 g. For this flight condition, aerodynamic loading is generated through Georgia Tech - Quick Hit Loads (GT-QHL), an in-house static aeroelastic solver for aircraft wings [96]. GT-QHL is a MATLAB-based tool that calculates static, steady-state loads that act on an aircraft during simple, symmetric pull-up or push-over maneuvers or under vertical gust conditions. The tool was originally used in the Airbus uncertainty quantification and management (UQ&M) spreadsheet.

For the application of equivalent stress to the load spectrum, the fatigue and crack propagation analysis requires static stress results. Figure 7.9 shows the results of the stress analysis for a structural CRM model. Maximum stress occurs around the Yehudi break area on the lower skin, the value of which is 242.7 MPa. Margins of safety are 1.4 for the yield strength and 1.48 for the ultimate strength for an element whose material is Al 2324. The results of stress for each element are combined with a standardized load spectrum for the fatigue data to perform the fatigue analysis with the stress-life approach.

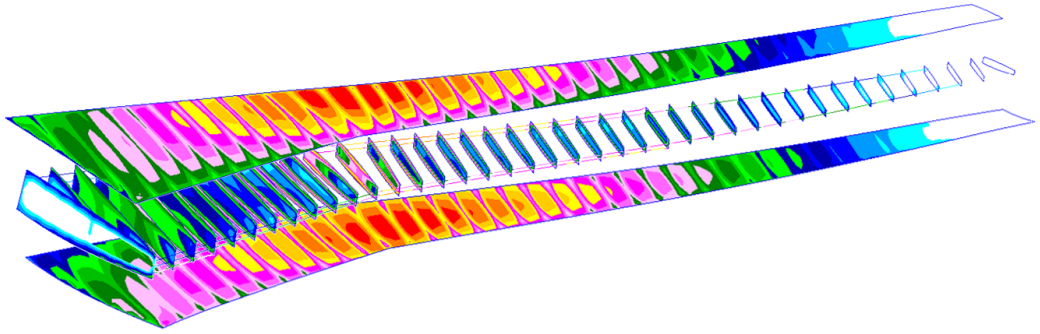

Figure 7.9: Results of the static stress analysis

7.2 Framework Overview

This simulation time step follows the history load spectrum from TWIST, the output of which is counted by the Rainflow counting method for the transfer of load blocks. The load spectrum is transferred to the stress spectrum by applying static stress results. The SCRM is analyzed though NASTRAN with one of the critical aerodynamic loads from GT-QHL. Then, the analysis of the dynamic structure begins. The simulation is performed with a two-level hierarchical finite element model, and the flowchart for the analysis is shown in Figure 7.10. At the macro level, a finite element wing model is analyzed with the $\varepsilon - N$ or the $S - N$ approach from the results of static stress. In the CIA program, if a crack is initialized in a certain element, then the element is considered a base model upon which the base-level environment will be built. To perform this base-level analysis, we use LEFM to calculate crack propagation using CA. The finite element model yields valid information about geometry, material properties, and internal loads on cells in the CA model.

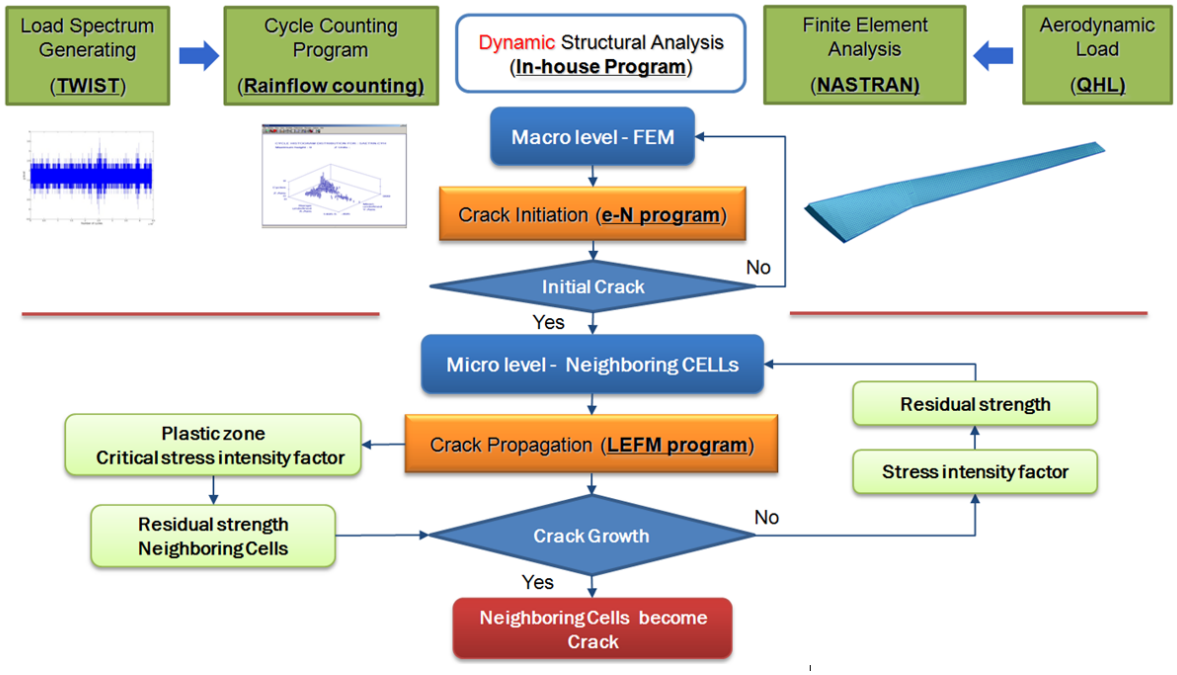

Figure 7.10: Flowchart of the framework

This study employs CA local rules for visualization, which require that a cell be regarded as dead if the residual strength calculated by LEFM approaches a critical factor. Dead cells, considered cavities in the model, induce a reduction in the strength of neighboring cells, and they may form a plastic region when the load condition meets a certain value, causing an increase in strength. To speed up calculation, we use Fortran to write the CIA program and then code the CPA module in Python for the local rule of CA. Then we follow the steps of the framework in the hierarchical two stepscrack initiation and crack propagationand conduct both analyses with a dynamic load spectrum defined by TWIST. The spectrum can be a discrete cycle- or time-based event. Crack initiation at the global level and crack propagation at the base level are independent calculations.

In the case of conventional damage tolerance analysis, a crack propagation analysis was conducted in a separated model with an assumption of the crack shape and location. To build a separate crack propagation model, we imported or calculated all material properties, geometric shapes, and corresponding internal loads from an outside source. In HFEM, however, the internal load was delivered from the global model to the local model automatically, and the local model inherently contained all of the required information for the simulation of crack behavior.

7.2.1 Composite mechanical property

This study focuses on isotropic materials, but introduces a method of dealing with anisotropic material with the third hierarchical FE model, the micro-level model, with amplification factors from SIFT (strain invariant failure theory). The theoretical background of SIFT is introduced in Chapter 2.

Strain Invariant Failure Theory (SIFT) is a composite fracture theory that can simultaneously address the difficulty of considering the interaction between fiber and matrix in the classical laminate failure theory and the difficulty of applying it to complex structures in micro-mechanics to be. SIFT theory was first proposed by Gosse [2001] as a technique for evaluating whether a strain invariant reaches a critical failure value by designating it as a variable for the volume change of fiber

and matrix [97]. Kelly [2003] reiterated that the first invariant is applicable only to interlaminar fracture due to the matrix volume change under tensile load, the distinction between tension and compressive load, and the distinction between fiber and matrix [43].In order to apply SIFT based on previous research to complex complex structures, it is necessary to apply a micro concept SIFT as a macro concept. Tay proposed an element failure method (EFM) and damage theory through SIFT [2005] [98] and further proposed a macro approach to SIFT for failure and damage of composites [2006] [99]. In the Chapter 2.6.3 , the validity of the SIFT theory was compared with the classical laminate theory. Fracture analyses were done using an in-house Fortran code and FEM analysis. Stresses, and strains were determined using MSC Nastran for FEM analysis.

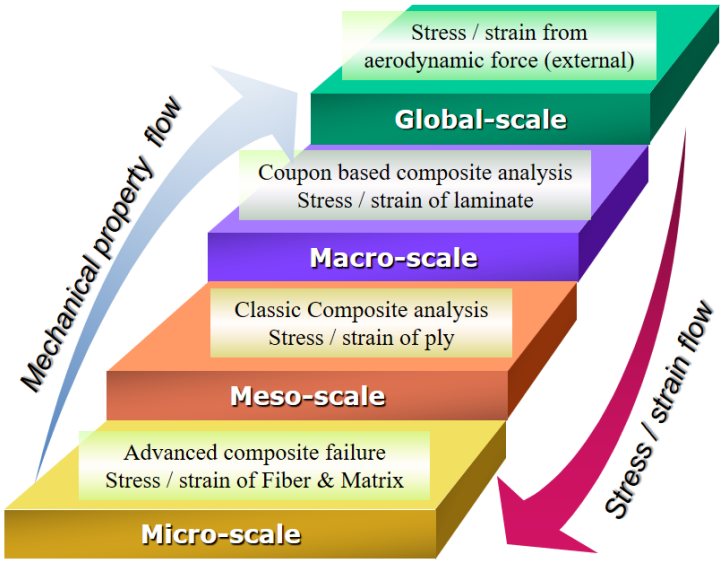

Figure 7.11: Information flow for composite failure analysis

The difficulty of interconnecting models is that the flow of data is not in one direction. Figure 7.11 shows the schematic flow of data required for each model in the analysis of the composite material. In the figure, the micro-scale, meso-scale, macro-scale, and global-scale are a modeling scheme or analysis resolution, and they are not the same as defined in HFEM. The scale in this figure refers to the fidelity of theories that indicate how much detail model or analysis is considered for the composite failure analysis. What is important, however, is that we need to have

similar functionality for the exchanging information between the macro- and micro-scales for this framework. In HFEM, the complex damage tolerance is achieved at the base level, which must receive information such as the composite stacking sequence, the angle of lamina, and the strength of fibers and the matrix. This information, used for calculating the mechanical properties, enables the crack propagation analysis. For a more accurate interpretation, information is exchanged at the global scale, which corresponds to the global level in the HFEM. In this case, we derive the results of the stress analysis that apply composite properties with a micro-mechanical aspect that can possible to observe an effect of fiber or matrix, or their correlation.

The main point in the Figure 7.11 is that the stress or strain flows from the top down, but the mechanical properties for composite laminate flows from the bottom up. That means we need to have mechanical properties to calculate stress and vice versa the detail level of analysis needs the stresses, or strains, for estimating the micro-mechanical behaviors. To solve this difficulty, a scale factor is introduced from SIFT theory. Using the scale factor, or amplification factor, we can decide the intensity of stress variation that is due to composite lamination that consists of fiber and matrix. The scale factor represents stress or strain by adding six degrees of unit loads to the composite stack, modeled with fiber and a matrix for the micro-mechanical aspect. Then, the scaling factor is superimposed onto the base-level analysis process. Details of the methodology of this application will be described in Chapter 3.

CHAPTER 8

SIMULATION

8.1 Background

Simulation is performed with a two-level HFEM in the framework described in Chapter 7. The HFEM for isotropic materials consists of a global model and a local model that is also a base model for crack propagation. While the global model is used for analyzing crack initiation based on the stress life approach, the local model performs crack propagation based on the Paris law. If the initiation of a crack occurs in a certain element of the global model, then the element is considered in a base model for crack propagation. A crack propagation analysis is performed with one of the elements in the base model while accounting for its neighboring effects. For the calculation of crack propagation, the finite element in the base model plays a role equivalent to that of the CA (cellular automata) by interacting with information about the material properties and the stress intensity factor. When the local element is played as an autonomous cell, the local rules provided in Chapter 5, which account for the neighboring crack effect, are applied.

The principal input data for deriving results is the stress spectrum discussed in Chapter 6. Although the chapter discusses standardized single spectra derived from TWIST, introducing a stochastic approach that assumes differences in gusts or maneuvers during operation rather than determining the spectra deterministically would be prudent.

In this chapter, we use the stochastic approach to determine a fatigue spectrum for the input of the simulation and then present a method of converting a single standardized spectrum into several hypothetical spectra for this approach. In addition, we evaluate whether such a hypothetical spectrum would meet the purpose of the actual simulation, how many runs are required to obtain confident representative spectrum, run the actual simulation with HFEM using the hypothetical

representative spectrum, and discuss the results.

8.2 Stochastic fatigue spectrum

A hypothetical fatigue spectrum is created for the purpose of simulation by applying randomness to the original TWIST spectrum. The original TWIST spectrum was developed based on historical operation data from ten aircraft. The historical data, which are exceedance curves, are traces of their operational history. The data are standardized as a single representative exceedance curve. Thus, we assume that the variations in the distributed trace curves can be regarded as randomness caused by differences in the aircraft size, maneuvers, gusts, and other factors.

Note that in the output analysis, the TWIST spectrum is truncated by removing load level X since the small amplitude of level X does not contribute to damage. This method, one of the methods used in MINITWIST [52], reduces the number of load cycles.

The most widely used method of statistical analysis in engineering is the normal distribution, which has been proven to successfully approximate many natural phenomena; thus, it is frequently used for probabilistic analyses in many fields. Most data samples that do not appear to be normally distributed tend to become a normal distribution when a sufficiently large amount of population data is cumulated, known as the central limit theorem. The probability density function (PDF) of a normal distribution is given by Eq. (8.1) for a random variable X that is normally distributed with mean μ and variance σ^2.

$$F(x) = \frac{1}{\sigma\sqrt{2\pi}} e^{\frac{-(x-\mu)^2}{2\sigma^2}} \tag{8.1}$$

From Figure 8.1, exceedance curves for ten aircraft are assumed to be normally distributed along with the standardized exceedance curve. The pixel points in the figure are used to estimate the variance of the distribution at 0.12, which is a normalized non-unit stress ratio. The mean of the

distribution should be 1, as it is applied to the standardized exceedance curve. Figure 8.1 depicts the concept of an applied normal distribution, a blue bell shape, to the standardized exceedance curve, a solid red line. A new spectrum is created by data points that we can obtain from the distribution that lies on the exceedance curve. To obtain data points from the distribution, this study uses a random number generator. A Python module, referred to as random, produces data points from the normal distribution, expressed as

$$X\ N[\mu, \sigma^2] = N[1, 0.12] \tag{8.2}$$

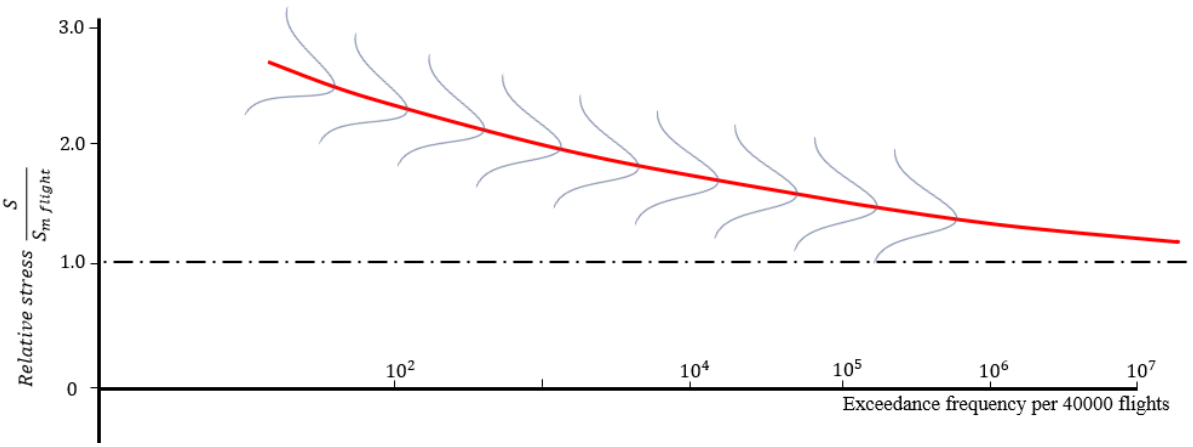

Figure 8.1: Stochastic exceedance curve

The hypothetical fatigue spectrum generated by applying random values from the normal distribution is compared to the legacy fatigue spectrum in Figure 8.2. Since the spectrum is a huge piece of information with 797,330 points, only 500 points are compared, which is an arbitrarily selected portion consisting of between 1,000 and 1,500 points. The portion fluctuates in a range not exceeding 0.8, which corresponds to the amplitude load level VII, which is 0.685 of the relative stress ratio. Note that the max value for the legacy point is 0.685, defined as level VII; 0.53, defined as level VIII; 0.375, defined as IX; and mostly 0.222, defined as level X in Figure 6.2.

In the figure, the comparison shows that the points from the hypothetical spectrum vary according to their corresponding legacy points. The random variation applied in the hypothetical fatigue spectrum is considered noise that is assumed to be caused by a number of uncertainties.

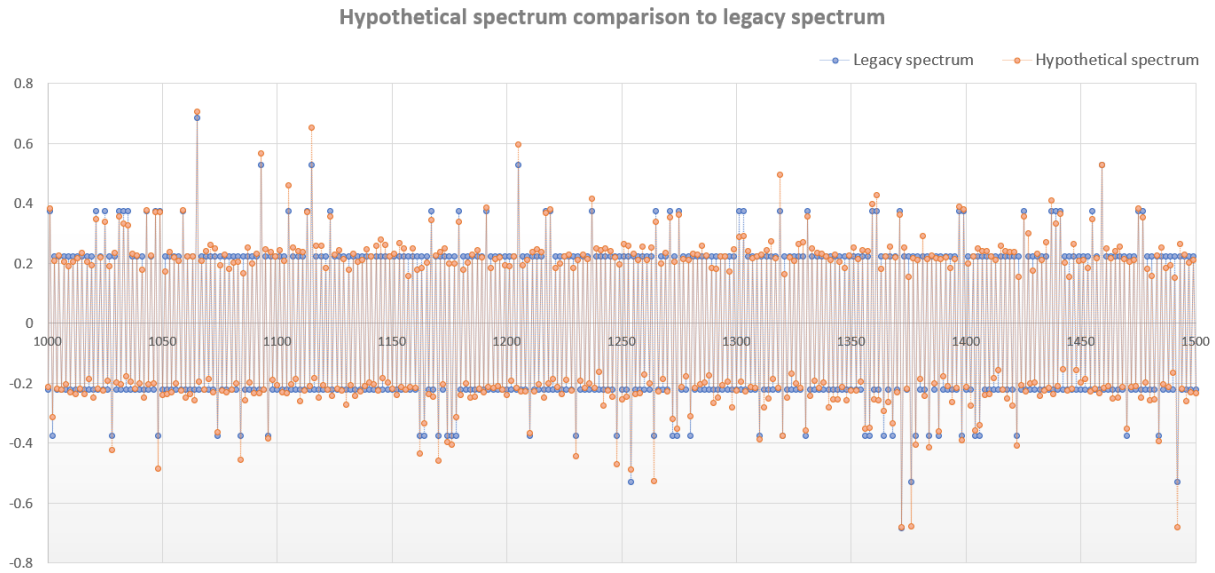

Figure 8.2: Stochastic exceedance curve

8.3 Input analysis

Determining whether the generated spectrum is suitable for the simulation requires several verifications. To be input to the simulation, the derived spectrum must be verified as an independent and identically distributed(iid) condition. In addition, it must be clearly shown that the results derived through the hypothetical spectrum have an effect similar to that of the legacy spectrum.

8.3.1 IID condition

In their book Modeling and Simulation, published in 2007 [100], Lewis and Gilbert covered the discrete event dynamic simulation (DEDS) in depth. DEDS is a collection of interacting entities that produce some form of behavior that can be observed over an interval of a discrete event or time. For example, the HFEM framework presented in this study is one of the DEDS for observing

crack initiation and propagation of 40,000 flights by the fatigue spectrum. In the book, the authors claimed that the variable in a DEDS model can be considered a set of stochastic processes that can be divided into autonomous and dependent stochastic processes. Dependent stochastic processes are usually derived from autonomous stochastic processes coupled by the behavior of a model, and generally they are an output variable. The autonomous stochastic process is generally an input variable that can be represented by a homogeneous stochastic process that is a sequence of random variables constituting an iid conditioned stochastic process.

When the HFEM is connected to a sensor that measures the actual load, obtaining insight into its autonomous stochastic processes are possible by observing the acquired data from FBG sensors or strain gauges. For the purpose of simulation at the design stage, however, a hypothetical spectrum is created as input to an HFEM with random behavior. To use the hypothetical spectrum as input to the DEDS, we must first ensure that the hypothetical spectrum is a homogeneous stochastic process, which we can prove by showing its iid condition, generally evaluated by two graphical methods: scatter plots and autocorrelation plots. As a simple verification, a scatter plot is used with Eq. (8.3) for the fatigue spectrum, which is a time series $x = (x_1, x_2, x_3, ..., x_n)$.

$$P_i = (x_i, x_{i+1}) \tag{8.3}$$

where, i is from 1 to 797,330 for the fatigue spectrum.

For comparison, Figure 8.3(a) below presents a scatter plot generated from the equation for the hypothetical spectrum and Figure 8.3(b) presents a scatter plot for the legacy spectrum.

In the case of little or no dependence, the points should be scattered in random fashion, confirmed by Figure 8.3(a). The figure displays symmetrical points in relation to the red diagonal, which is due to the nature of the fatigue spectrum from an oscillation caused by repeated loading. Therefore, it would be correct to evaluate the random fashion from only one side of the symme-

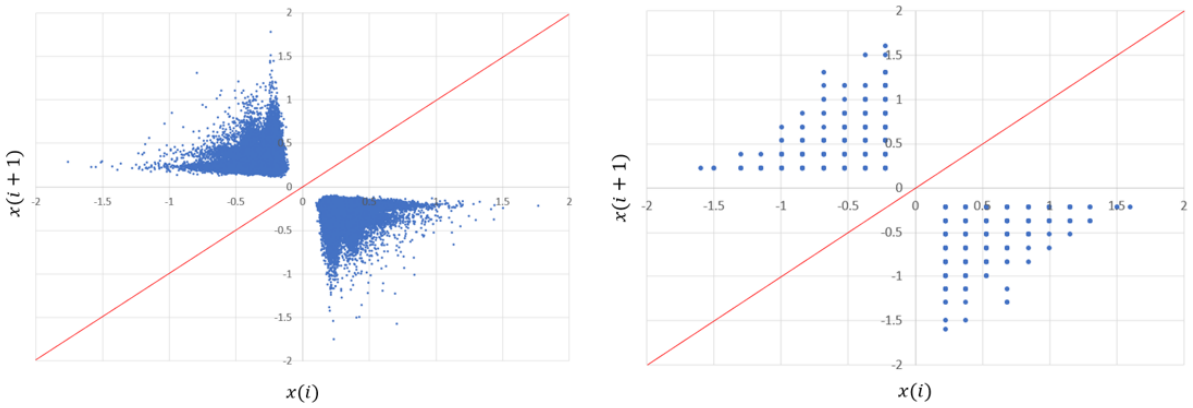

(a) Hypothetical spectrum

(b) Legacy spectrum

Figure 8.3: Scatter plots for hypothetical and legacy spectra

tries. The symmetrical tendency is more pronounced in the legacy spectrum in Figure 8.3(b), which shows almost perfect symmetry with respect to the red diagonal. Note that this spectrum also contains 797,330 points but is mostly overlaid since it uses step-wise stress values. The column near the x-axis with the largest value is made up of 10 points, which is consistent with the 10 stress levels defined in the TWIST method detailed in Chapter 6.

8.3.2 Verification of the hypothetical spectrum

For the purpose of simulation, the hypothetical spectrum has been generated by imposing uncertainties on the standardized legacy spectrum. The hypothetical spectrum is derived from the normal distribution, which lies on the standardized exceedance curve. Thus, the trend, or the intensity of the hypothetical spectrum should be similar to its standardized spectrum. To check for similarity, we use one of the modules in HFEM to compare the results derived from the hypothetical spectrum to those of the legacy spectrum.

The HFEM simulates crack initiation in the global domain and crack propagation in the local domain. In the simulation, the crack propagation analysis, which integrates the crack length, is more sensitive to the fatigue spectrum than to crack initiation, which summarizes the damage.

Therefore, comparing the results of crack propagation from the hypothetical spectrum to the results from the legacy spectrum will provide a more accurate evaluation. That is, the similarity between the effect of the hypothetical spectrum and that of the legacy spectrum can be evaluated by checking the similarity of crack growth curves.

Introduced in Chapter 5, the square plate example, which has an identified crack at its center, is used here as an example to verify the similarity of the spectrum. First, ten sample hypothetical spectra are created by the methodology described in the previous Section 8.2, and then a crack propagation analysis based on the CPA simulation is conducted on each spectrum; only one element of the base model, however, is considered.

Figure 8.4 presents a comparison between the crack growth curves analyzed from the ten sample spectra and the crack growth curve analyzed from the legacy spectrum. The x-axis is logarithmic, and the y-axis is representative of the incremental size of the crack length. The results of the ten-sample hypothetical spectra, represented by the brown curve, mostly overlap. Thus, it appears as if only one curve is plotted, but actually, ten sample curves are plotted. From this comparison, we confirm that the crack growth results from the hypothetical spectra are consistent with the targeted crack growth curve resulting from the legacy spectrum.

8.4 Simulation overview

The method for generating the spectrum and its input analysis are discussed in the previous section, and the framework and the structural common research model using HFEM are described in Chapter 7. Using the framework and the model, we simulate the wing model of the SCRM, assuming that an external load, which is the input spectrum created by the method that uses random variables, is transferred. The results of the HFEM simulation for both of crack initiation and propagation are discussed in the next sections.

Figure 8.5 illustrates the simulation. The upper left shows the distribution of the initial crack potential in the wing box, and the lower left displays the spectrum imposed on the global model.

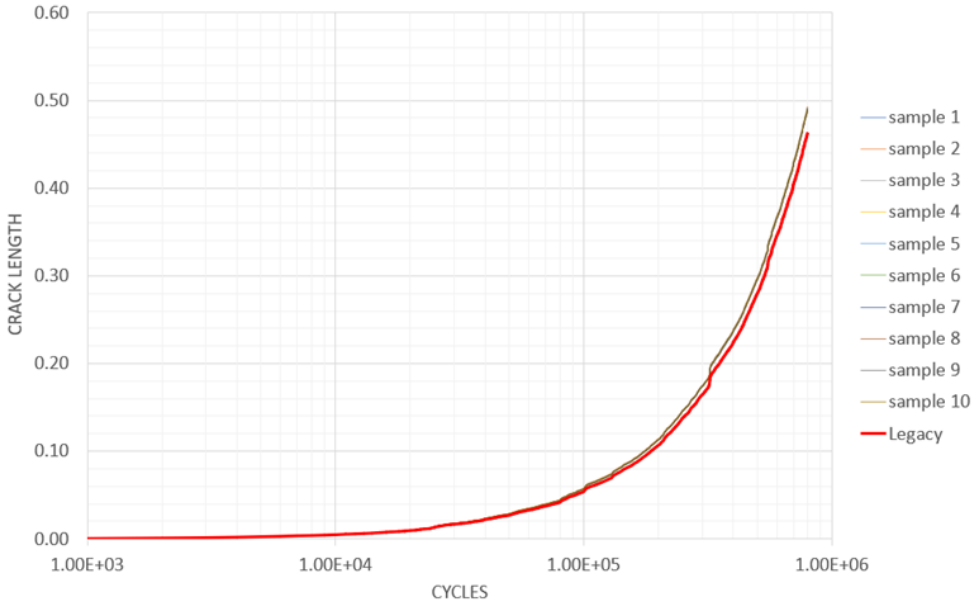

Figure 8.4: Crack growth curves for ten hypothetical spectra and the legacy spectrum

The lower right shows the spectrum imposed on the local model, and the upper right displays the CPA module, with a red dot representing an element whose cracks have grown above the critical limit in the base model.

8.5 Output analysis

The stochastic approach has been introduced in the input analysis, in which the ten hypothetical sample spectra are generated and discussed by introducing DEDS simulation into HFEM. For the output analysis of DEDS, output variables can be categorized by point-set output variables (PSOVs) and derived scalar output variables (DSOVs). PSOVs are data delivered from the execution of the simulation through the accumulation of a finite set of time indexed input. However, in most simulations, we should focus on the property derived from the accumulated PSOV rather than the individual value of PSOV. The property, which is a value computed and assigned a designated scalar value for the accumulated data, is a DSOV [100]. For example, in the HFEM simulation, the hypothetical spectrum, a random input variable, produces a set of output consisting of the crack

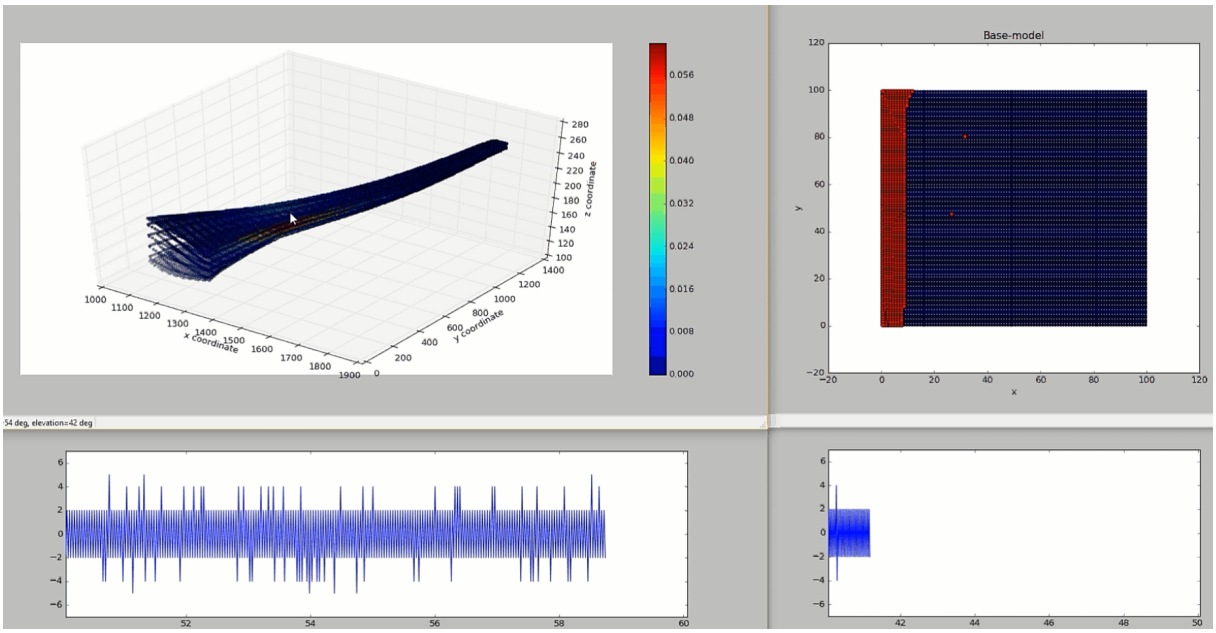

Figure 8.5: Simulation snapshot

growth results for elements. One spectrum produces one set of these output for elements in the base-level FEM. In the one set, information about the results of the crack growth for each element is PSOV output. When the simulation runs a finite number, we can calculate an output value from the collection of PSOVs. The calculated output, such as the minimum, the maximum, or the average, is the DSOV. The information that we finally seek in this simulation is the values of the parameters of the distribution from the DSOVs. We simply choose the mean value.

8.5.1 Estimation of the means and the confidence interval

Suppose that crack growth curve $Y_1, Y_2, ..., Y_n$ is obtained by the crack propagation simulation for spectrum $X_1, X_2, ..., X_n$. X is the input, with each spectrum containing 759,300 points. Y is the output, the accumulation of the crack growth size, which is analyzed from the simulation of elements in the base level. If a spectrum is not counted by a counting method, then the Y should be the shape of 759,300 x 10,000 (spectrum points x element numbers). An analysis of all elements in the base-model, however, is not required because if the crack growths exceeds the

initial crack size, which becomes twice the observable size (0.125 inch or 3.175mm, from Table 4.1), it must be discovered through close inspection and targeted for repair or replacement. In this simulation, therefore, only some of the elements that exhibit high stress are analyzed. This approach is reasonable because most of the elements do not incur any cracks during the entire operating life of an aircraft unless their stress concentration is exceedingly high. The element number 5700, the most critical element in the base level, is selected for the output analysis. In addition, with a suitable single stochastic fatigue spectrum determined to represent the number of replications in the output analysis, more elements that show high stress are observed in the simulation.

The replication sample number, n, of the fatigue spectrum is generated by the method described in the section "Stochastic fatigue spectrum." The collection of the n observed crack growth curve for one element is $Y_1, Y_2, ..., Y_n$ for the n number of the hypothetical spectrum. Each Y contains m number of crack growth sizes per loading cycle, which is $y_1, y_2, ..., y_m$. For the purpose of the output analysis, the series of y is cumulated to obtain the final crack size, that is, the crack size at the final stage of the fatigue spectrum. The sample mean of the final crack sizes for n number of replicated spectra is calculated by

$$\overline{y}(n) = \sum_{k=1}^{n} y_{f,k} \tag{8.4}$$

where, n is the number of random spectra, and y_f is the final entity of the cumulated crack growth curve. The histogram plot and expected distribution, depicted in Figure 8.6, show a mean of 1.2210 and a variance of 0.0043 for the 250 samples of spectra runs. As explained in Section 8.2, the 250 stochastic spectra are truncated at the lowest stress level which is X in Table 6.1. Therefore, the number of n is became 80,000 instead of 759,330.

The difficulty of adopting $\overline{y}(n)$ as an estimator of μ, which is a true mean without any additional

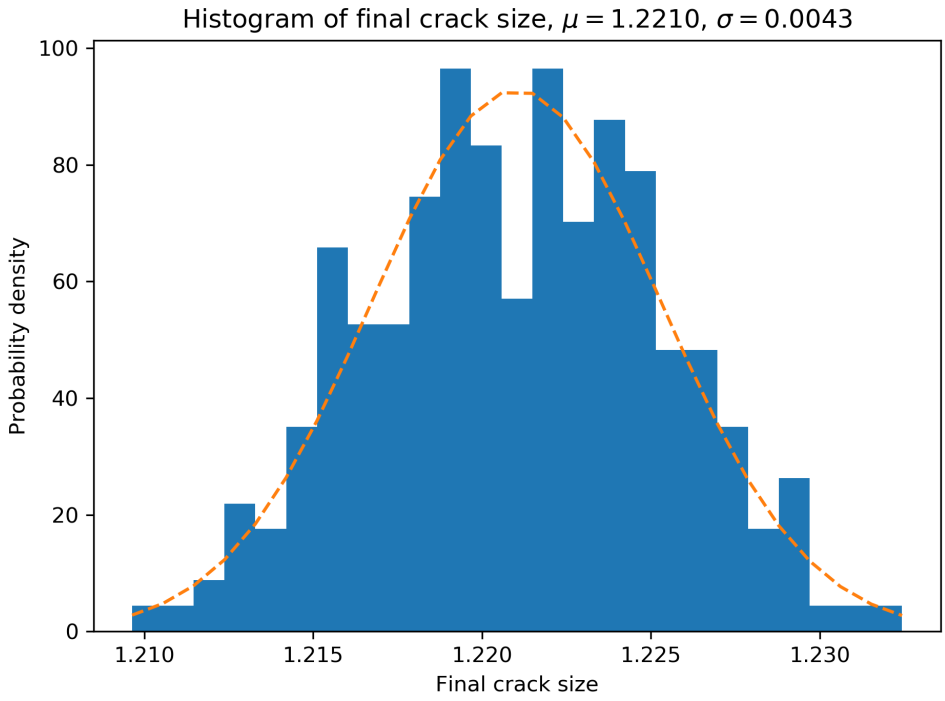

Figure 8.6: Final crack size of the histogram plot and the distribution of 250 spectra

information, is that we do not have a way of assessing how close $\overline{y}(n)$ is to μ because $\overline{y}(n)$ is a random variable with variance. Although in one simulation, $\overline{y}(n)$ may be close to μ, another $\overline{y}(n)$ may differ from μ by a considerable amount [101]. Therefore, adopting $\overline{y}(n)$ as an estimator of μ requires additional information, the confidence interval, which identifies where the known mean is likely to fall, together with the measurement of the "confidence" associated with the collected data. The half length of confidence interval is shown below

$$\zeta = \frac{t_{n-1,\alpha} s(n)}{\sqrt{n}} \tag{8.5}$$

When we collect data, we can quantify the quality of a sample by the confidence obtained from Eq. (8.5). Further, when the confidence meets a certain criterion, we can determine the number of replications required to run a simulation for the sample. The quantification can be achieved by

comparing the sample mean to the ζ in Eq. (8.5), and the required number of replications can be determined when the quantification is greater than value chosen as confidence level which is r in following equation.

$$\frac{\zeta(n)}{\overline{y}(n)} < r \tag{8.6}$$

n	μ	σ	$\zeta(n)$	CI Min	CI Max	r
10	1.22260	0.00360	0.00272	1.21988	1.22532	0.00222
20	1.22165	0.00398	0.00191	1.21974	1.22356	0.00157
30	1.22147	0.00429	0.00163	1.21984	1.22310	0.00133
40	1.22140	0.00436	0.00141	1.21999	1.22282	0.00116
50	1.22145	0.00411	0.00118	1.22027	1.22263	0.00097
60	1.22121	0.00427	0.00111	1.22010	1.22232	0.00091
70	1.22056	0.00444	0.00107	1.21949	1.22163	0.00087
80	1.22074	0.00443	0.00099	1.21975	1.22173	0.00081
90	1.22085	0.00445	0.00094	1.21991	1.22179	0.00077
100	1.22088	0.00436	0.00087	1.22001	1.22175	0.00071
110	1.22100	0.00454	0.00086	1.22014	1.22186	0.00071
120	1.22103	0.00452	0.00082	1.22021	1.22185	0.00067
130	1.22114	0.00453	0.00079	1.22035	1.22193	0.00065
140	1.22129	0.00456	0.00076	1.22052	1.22205	0.00063
150	1.22140	0.00454	0.00073	1.22067	1.22214	0.00060
160	1.22121	0.00451	0.00071	1.22050	1.22192	0.00058
170	1.22113	0.00446	0.00068	1.22046	1.22181	0.00055
180	1.22108	0.00437	0.00065	1.22044	1.22173	0.00053
190	1.22107	0.00430	0.00062	1.22045	1.22168	0.00051
200	1.22106	0.00432	0.00060	1.22046	1.22167	0.00050
210	1.22109	0.00431	0.00059	1.22050	1.22168	0.00048
220	1.22103	0.00429	0.00057	1.22046	1.22160	0.00047
230	1.22097	0.00426	0.00055	1.22042	1.22153	0.00045
240	1.22098	0.00426	0.00054	1.22044	1.22152	0.00044
250	1.22102	0.00430	0.00054	1.22049	1.22156	0.00044

Table 8.1: Results of the simulation run

As the number of sample spectra increases, the r converges to a certain confidence level; then we can determine the suitable number of required sample spectra. For example, Table 8.1 shows the calculation of r with confidence intervals, the mean, and the variance. As the number of

spectra, n, increase, r decreases monotonically. When the n is reached at 250, r converges to about 0.00044. This convergence, plotted in Figure 8.7, shows that the ratio of reduction slows down at 100 and flattens between 200 and 250. Therefore, the sample mean that is observed in this simulation for 250 replicated samples is considered a true mean and applied to determine the representative spectrum.

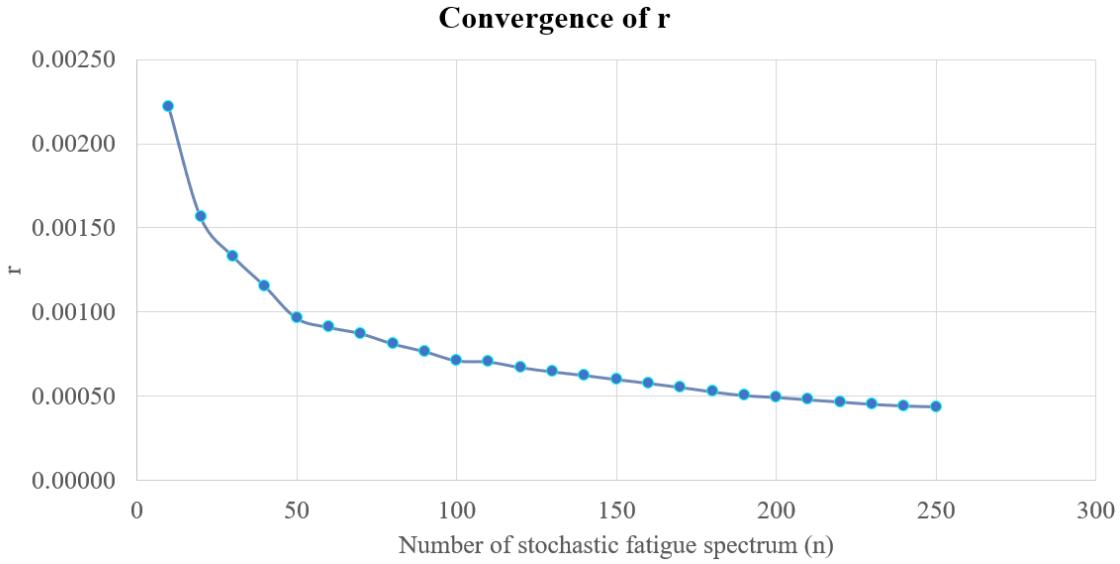

Figure 8.7: The convergence of r for 250 runs

The last step of the output analysis is the selection of a representative spectrum from among the replicated spectra. A representative spectrum can be the one that produces a final crack size that is closest to the true mean. Figure 8.8 shows the crack growth curves analyzed from the representative spectrum. The final crack size is 1.22101, which is the value among those of the samples closest to the true mean, 1.22102. For the purpose of simulation, the representative spectrum, acting as an external load, is applied to the HFEM. The results of the simulation are discussed in the following sections.

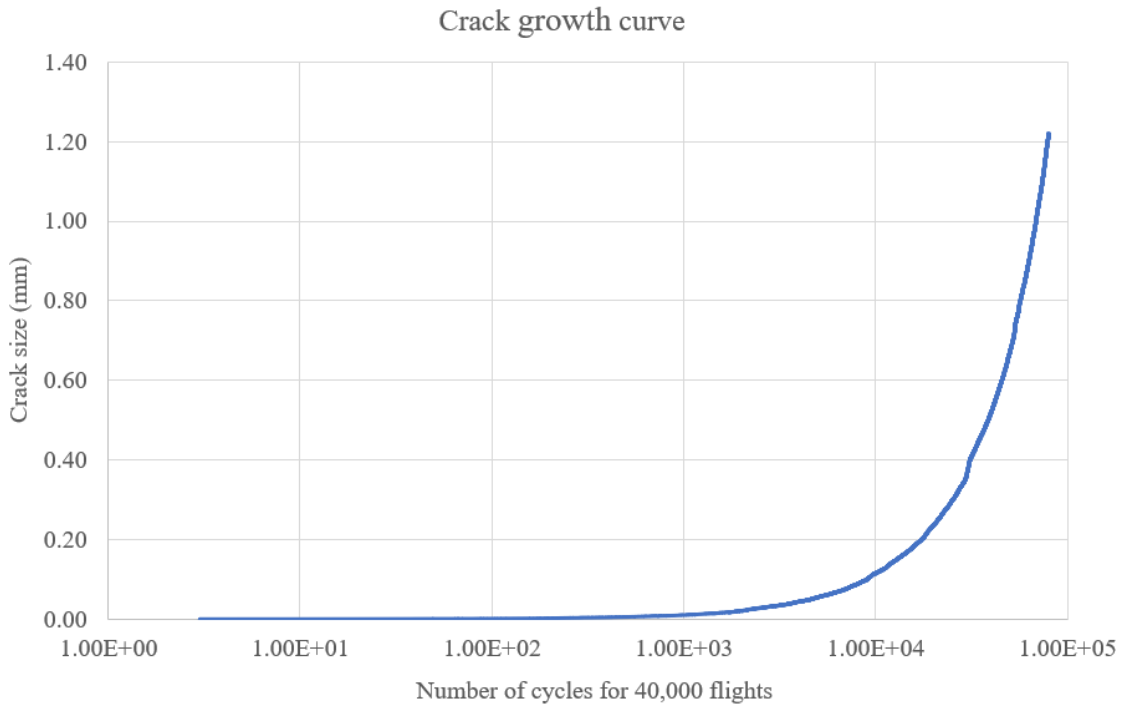

Figure 8.8: Representative crack growth curve

8.6 CIA results

Figure 8.9 shows the results of global-level analysis for crack initiation by the simple life-cycle approach. The color spectrum shows a range of values for fatigue damage. More red indicates that the element has a greater possibility of developing cracks. The figure shows that the bottom of the aircraft wing suffers the most severe damage, even though the lower skin, made of Al 2324-T39, has higher fatigue resistance. The value of static stress was similar in both the upper and lower wing from the static analysis result shown in Figure 7.9. However, the upper skin suffers mostly compressive stress, which is a minor contributor in fatigue life. In contrast, the bottom of the aircraft wing experiences greater tensile loads. Thus, unlike the static stress result, the fatigue damage distribution is more concentrated in the lower skin in Figure 8.9.

If the direction of the stress component and material property are not different, then the principal factor affecting fatigue life is obviously the magnitude of the stress. Fatigue results for five

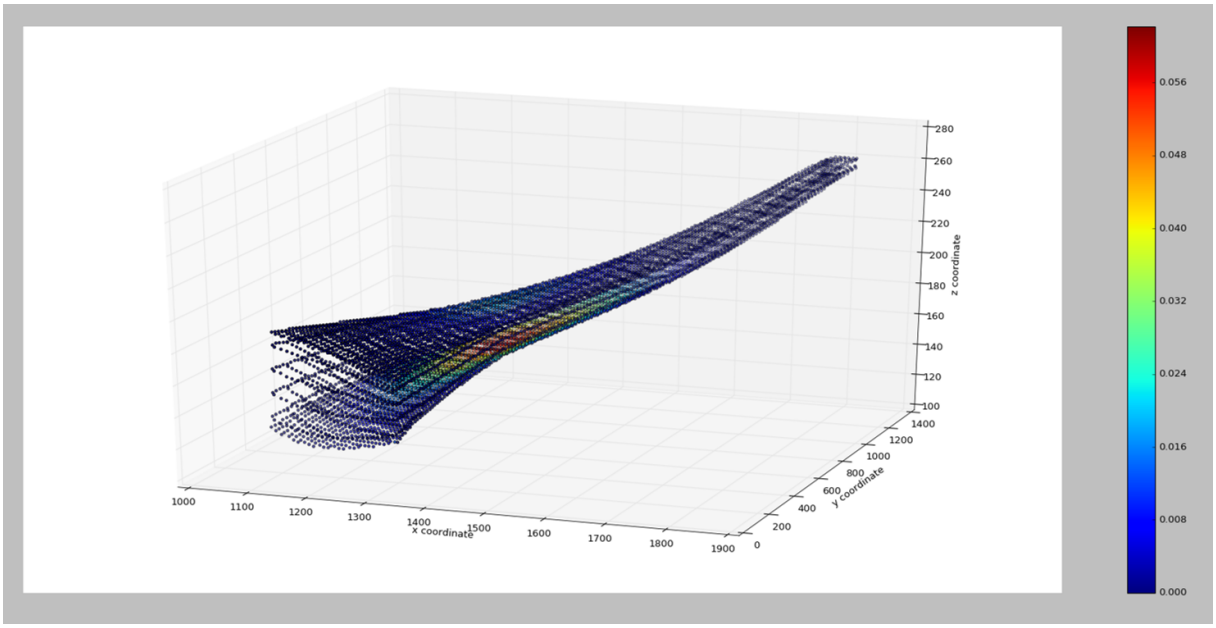

Figure 8.9: The simulation of crack initiation for global-level

critical elements in the lower skin are summarized in Table 8.2. These results are located at the Yehudi break area as mentioned in Section 7.1.3, and Figure 8.10 shows their locations in the bottom view of the global-level FEM. In the static analysis, the five elements exhibited maximum stress.

Table 8.2: Crack initiation results

Element No.	Location	Material	Damage	Crack initiation block cycles
3561	Lower skin	Al 2324-T39	0.062127	16.09608
3557	Lower skin	Al 2324-T39	0.061808	16.17901
3549	Lower skin	Al 2324-T39	0.061269	16.32147
3565	Lower skin	Al 2324-T39	0.061123	16.36057
3553	Lower skin	Al 2324-T39	0.060979	16.39902

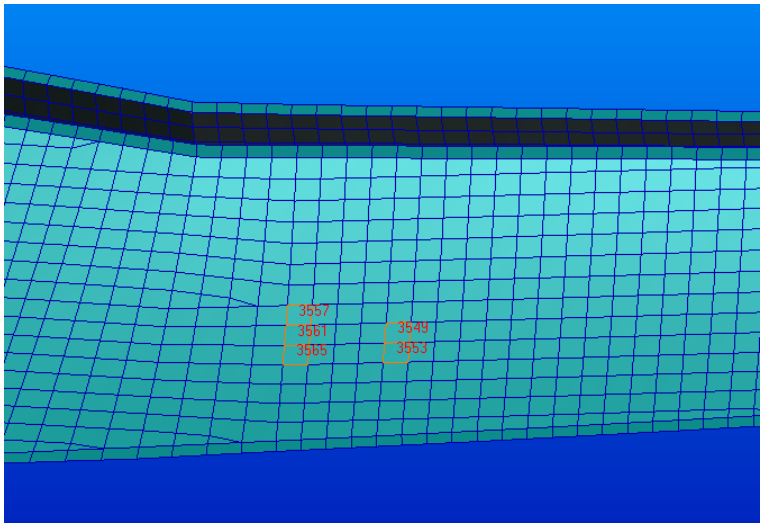

Figure 8.10: The five critical locations in global-level FEM

The fatigue damage for all elements are presented in Figure 8.11. The x-axis is the element number and y axis is the value of damage. The maximum damage, which is 0.0621, occurred at element 3561. The value of damage represents the possibility of fatigue failure, and the life cycles for the one-block cycle can be calculated by Miners rule. Based on the Miner's rule, 0.0621(damage) divided by 1 is 16.096, and it is block numbers that can be repeated a standard block. Since the standard block is 4,000 flights in TWIST, the surveyed aircraft wing is safe until 64,384 flights, which can be calculated simply by the following: $4,000 \times 16.096 = 64,384$.

We know that the correlation between fatigue damage and stress is very high because the fatigue spectrum is obtained from the load spectrum derived by multiplying the stress of the element. Figure 8.12 describes a trend for the normalized fatigue damage and the resulting stress: normalized with maximum values. This figure shows that the assumption is not always proved true. In some cases, high stress does not result in greater damage. Regions that show a different trend include element numbers from mid-4000 to about 5000, which represent elements that are located in spars, and element numbers from 7161 to 7502, which are located in the ribs. In these regions, even though the normalized stress is very high, the normalized fatigue damage is very low. In aircraft structure, spars and ribs mainly take compressive loads, and this result shows again that the

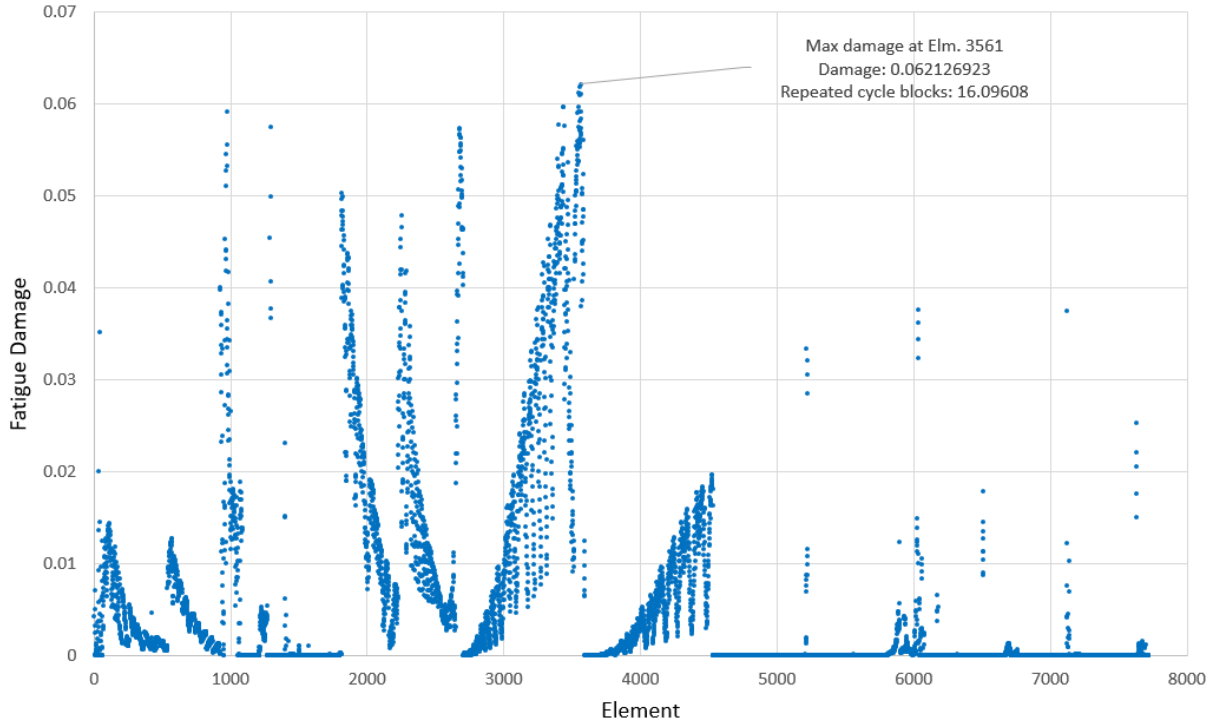

Figure 8.11: The results of crack initiation for global-level

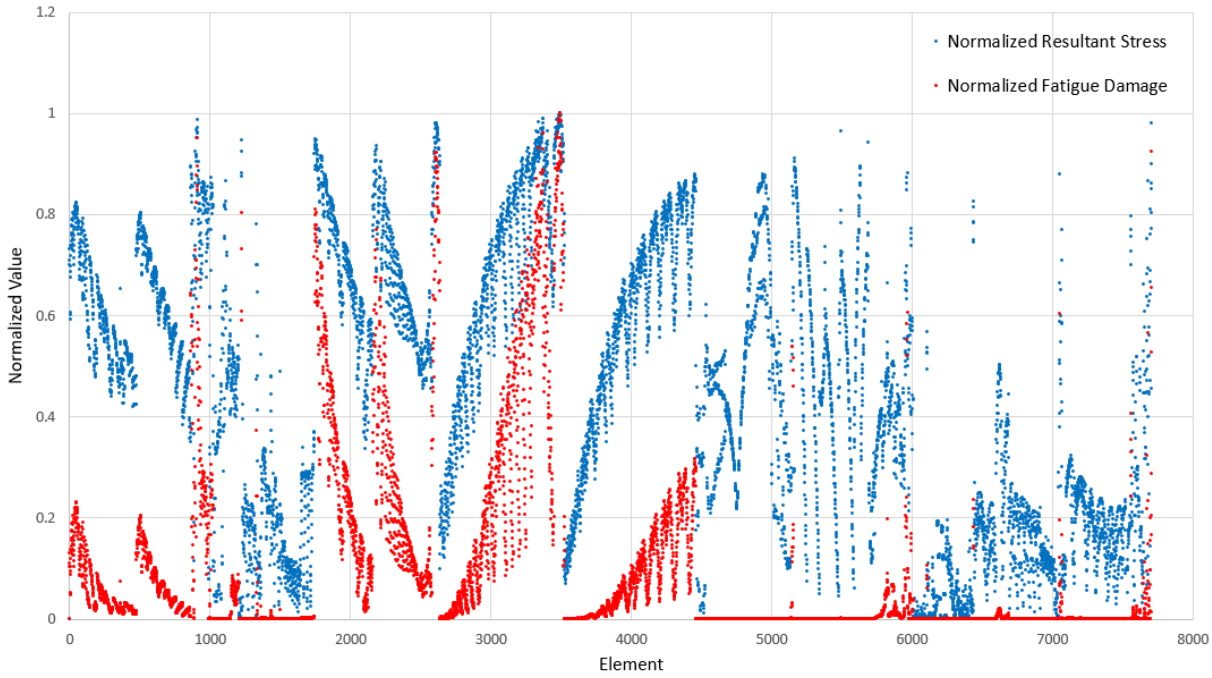

Figure 8.12: Comparison of normalized fatigue damage and resultant stress

principal factors of fatigue damage are not only the magnitude of the stress but also the component of stress or material properties related to stress- or strain-life curves.

8.7 CPA results

The crack propagation analysis performed in the CPA module and the results of the analysis are discussed in this section. HFEM begins by identifying the element with the most critical fatigue damage from the global-level FEM to analyze crack propagation on the base-level FEM, a local model. It is a representative model developed by clustering elements, a method introduced in Section 3.4. When the external load (the load spectrum for the case of simulation) is applied on the global level, internal loads are transferred to the base-level FEM by the internal forces transfer method (introduced in Section 3.3.2). Then, the actual stress can be obtained by applying the internal force to the normalized stress distribution determined in the base-level FEM by the unit-load method (introduced in Section 3.3.3).

	Parameters	***unit***
S_{max}/S_o	0.3	
$alpha$	2	
K_C	76.5326	$ksi\sqrt{in.}$
C	6.00E-09	
n	3.2	
p	0.25	
q	1	
Y_{yield}	65	ksi
$K1_C$	39	$ksi\sqrt{in.}$
A_k	1	
B_k	1	
DK1	0.74	$ksi\sqrt{in.}$
C_{th}	2.2	

Table 8.3: Curve parameters for 2324-T39 [102]

Material is applied to the wing model, as described in Appendix C. The elements in the wing

model mainly consist of four materials: 7055-T7751 for the upper wing, 2324-T39 for the lower wing, 7150-T7751 for the spar, and 7050-T7451 for the rib. The analysis of the CIA module confirms that the lower wing is a fatigue critical area. The material used for the lower wing is 2324-T39, which is a typical for the lower wing of aircraft. The material is an age-hardened, high-strength version of alloy 2024, but it has stronger fatigue resistance and fracture toughness [103]. The curve fit parameters of da/dN of Delta K curve for 2324-T39, from National Aerospace Laboratory NLR [102], are applied to the crack propagation analysis and listed in Table 8.3.

Among the elements of the global-level FEM in which crack propagation first initiated, element 3561 is shown in Figure 8.13 with its stress distribution. Note that the boundary condition and forces are applied by the method described in Section 3.3.2.

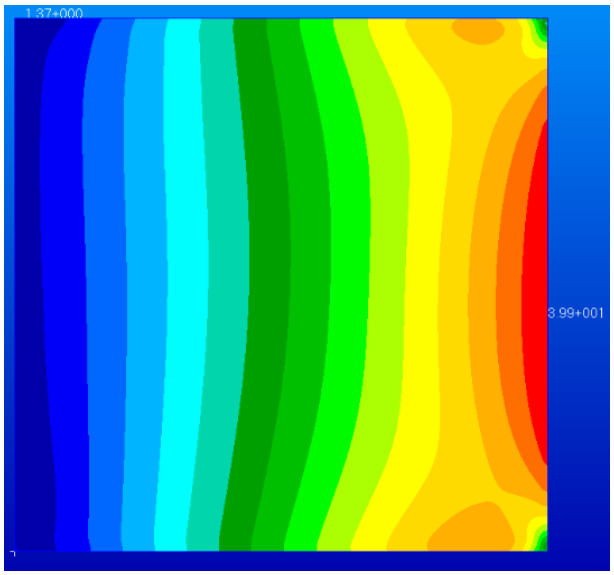

Figure 8.13: Static stress distribution for the base-level FEM

The initial occurrence of the crack obviously begins on the right central side, which is the maximum stress point. The initial cracked element, which acts as a cellular automata, described in Section 5.3.4, conducts the crack propagation analysis described in Sections 5.3.2 and 5.3.3 of itself internally. When the results of the analysis exceed the element size or a given limit size, the cracked element switches to a dead cell and stops the propagation analysis. Simultaneously, other

elements also conduct crack propagation analysis of themselves. During a self-analysis, when a neighboring cell switches to a dead cell, the neighboring effect of the dead cell is applied as a weighting factor, which is discussed in Chapter 2.

In the simulation of the CPA base-level model, the first crack is initiated in element number 5700 which is the most critical element in the base-level, when the crack size from the self-analysis of the element exceeds 1mm, the size of the element. Crack initiation of the base-level model occurs at 34,327 cycles(68,654 points), or 0.85 of the aircraft life time, and element 5700 becomes a dead cell. The dead cell broadcasts its status to its neighboring cells: elements 5600, 5599, 5699, 5799, and 5800. Figure 8.14 depicts the dead cell and neighboring cells from the simulation signals. After the 34,327 cycles, the neighboring cells conduct their self-analysis under more stress, which is 1.5 times as much as their initial stress.

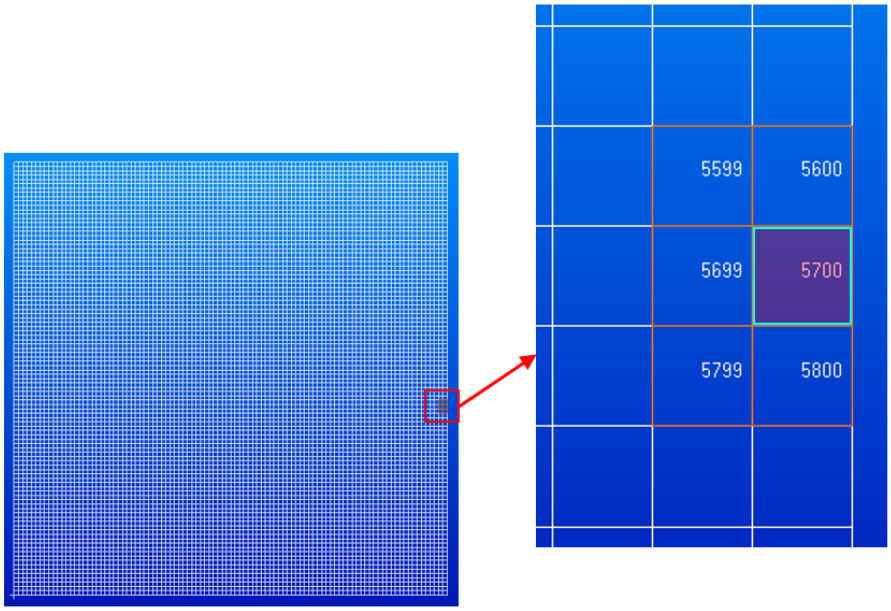

Figure 8.14: Neighboring effect from a dead cell

The CPA simulation continues throughout the life time of an aircraft, allowing for observation of the crack growth of the base-level FEM. The results of the first 100 elements of 10,000 in the base level are depicted in Figure 8.15, which display the shapes and sizes of crack propagation.

Interestingly, the shape of the crack propagation in the simulation reveals three phases for the 100 elements:

- Phase I: The first dead cell occurs at 34,327 cycles (Figure 8.15a); then, by 34,340 cycles, 10 more dead cells have propagated rapidly; and by 34,679 cycles, 40 dead cells have propagated along the edge (Figure 8.15b).
- Phase II: The crack propagation path changes. When a dead cell develops in the second column, which is element 41 at 34,684 cycles, the path widens (Figure 8.15c). The crack propagates lengthwise until 60 dead cells have propagated at 34,729 cycles (Figure 8.15d). Both columns of dead cells propagate until the 89th dead cell, which occurs at 35,141 cycles.
- Phase III: The crack propagation path changes again. The path widens again at 35,163 cycles, with 90 dead cells (Figure 8.15e), and propagates lengthwise (Figure 8.15f).

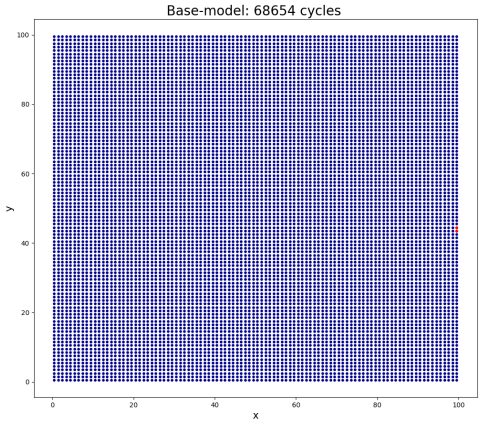

(a) Dead cells at 68,654 cycles

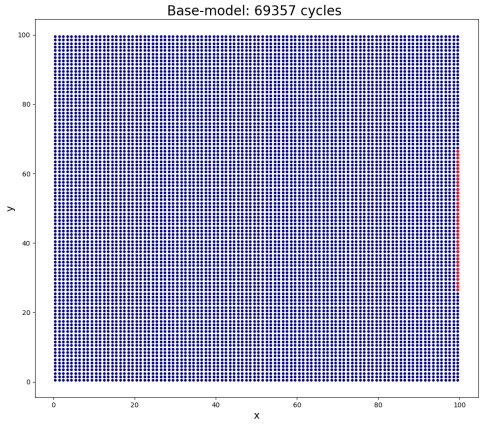

(b) Dead cells at 69,357 cycles

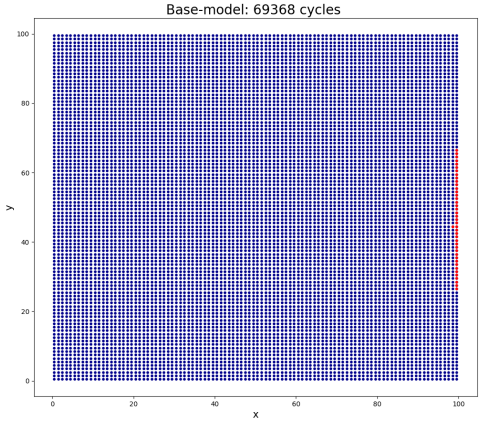

(c) Dead cells at 69,368 cycles

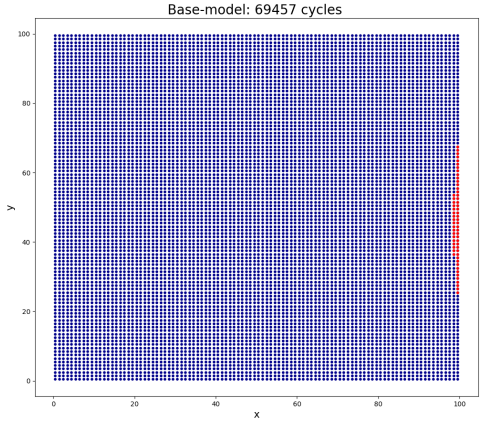

(d) Dead cells at 69,457 cycles

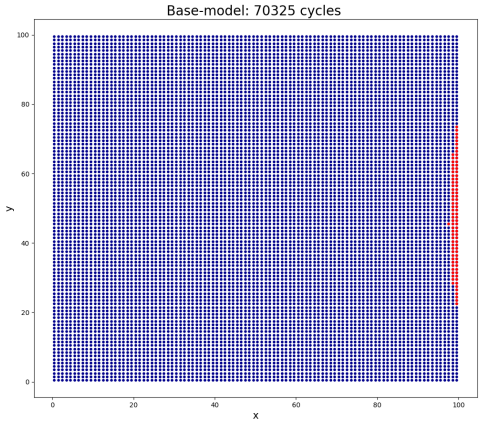

(e) Dead cells at 70,325 cycles

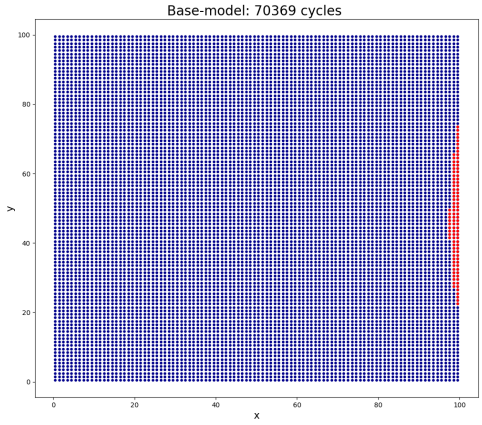

(f) Dead cells at 70,369 cycles

Figure 8.15: CPA simulation result

A summary of the sequence for the propagation of dead cells appears in Figure 8.16. The first cracked element with the highest stress and its neighboring elements becomes a dead cell within a small number of cycles (Phase I). Then, in the relatively lower stress region, the ratio of becoming dead cells per cycles is slowed down, but dead cells are monotonically increased. From 34,679 to 34,729 cycles, about 22 cells rapidly become dead cells because of both accumulated damage to them and the effect of neighboring dead cells, which have formed an elongated line (Phase II). At 35,163 cycles, when the crack widens, the number of dead cells rapidly increases again (Phase III).

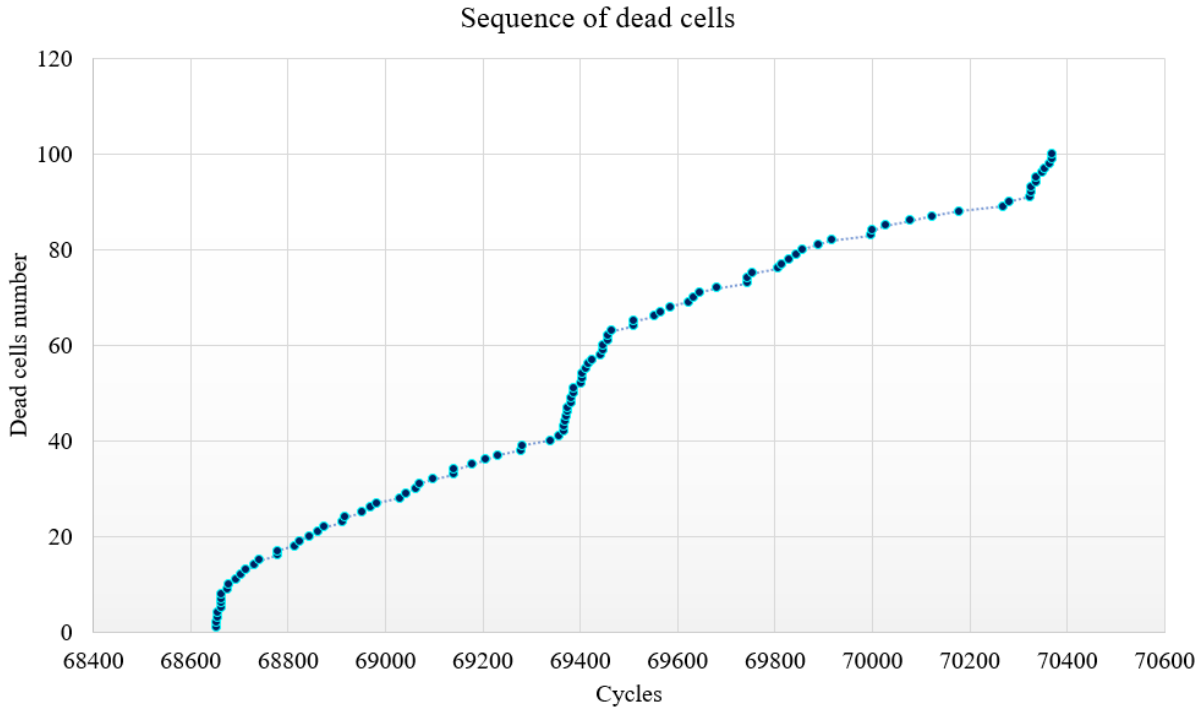

Figure 8.16: Sequence of dead cell numbers

Analyzing the results obtained from the example simulation, we can claim that the current design of SCRM wing falls short of the acceptable damage tolerance design criterion, which requires a change in the design or the release of a maintenance manual of periodic inspection to the operating airline. The manual should provide guidelines for the periodic inspection, such as the inspection interval, the critical location, and the recommended inspection method, which can be determined based on a detailed damage tolerance analysis. Unless a separate detailed FEM is

analyzed, the conventional damage tolerance analysis is typically one dimensional, involving the calculation of only the length of a crack based on an assumption of the location of the initial crack and the direction of crack propagation. HFEM framework simulation provides a two-dimensional analysis, allowing us to observe the direction of cracks and the propagation phase simultaneously. Therefore, when a design changes or when inspections are required, more information will be available to those making decisions.

8.8 Summary of simulation

The simulation progression of the operational lifetime of the aircraft has been presented during which time the wing experiences cyclic loading represented by its loading history generated by TWIST. The method to develop stochastic spectra from historical TWIST spectrum is suggested and analyzed in the input analysis.A representative single spectrum is selected in the output analysis among of the stochastic spectra, and utilized for the simulation of HFEM.

In the simulation model, cyclic loading causes a reduction in material strength that can be calculated by the stress intensity factor. The Paris law is used to calculate the residual strength with mode I, based on LEFM, by the stress intensity factors. This simulation study performed crack propagation modeling with cellular automata and observed the phenomenon of crack propagation for a wing with infused cracks over the operational lifetime of an aircraft. A crack initiation analysis generated initial crack cycle information for every element in the global-level FEM. The crack propagation analysis following local rules, neighboring cell rules, and the updating CA rules. The results enabled the estimation of damage tolerance design safety while accounting for in-service or manufacturing defects. This simulation method also introduced the possibility of evaluating the safety of complex systems for both macro- and micro-mechanical aspects.

CHAPTER 9

CONCLUSION

This study suggests the application of and development of a framework for a hierarchical FEM methodology that can be used for monitoring the current structural health condition at the operation stage and analyzing crack behavior in an aircraft design at the design stage. In the HFEM, since the framework deals with a very large subject and tiny cracks simultaneously, we divided the analysis into global-level (CIA) and base-level (CPA) FE modeling to improve the practicality of the FE analysis. As variables from the global model, such as external loads, are paramount to crack propagation analysis at the base level, mutual information exchange between the global and base levels was important. Load transfer methods, representative base-model development, and unit load methods are applied in the HFEM and enabled the interaction between CIA and CPA.

The HFEM is a systematized framework for simulating crack initiation and propagation for CIA and CPA. In the simulation section of this study, the framework was tested with a wing example from SCRM, and the results were discussed. An input analysis of the simulation, which provided a reliable input variablethe iid condition of the load spectrumwas conducted. The input variable, the load spectrum, was replicated to a stochastic spectrum by applying a random number from a probability distribution. From the results of the simulation runs, the output analysis provided information on the number of replications that affected the simulation and the number of runs required in order to ensure reliable simulation results. From the results of the input and output analysis, a representative spectrum was selected and used for the simulation of CIA and CPA in the HFEM.

The global model, the CIA module in the HFEM, was developed by the stress- or strain-life approach that determined the occurrence of cracks from a global perspective. The results of the CIA were compared to those of a commercial fatigue analysis program and the results were satisfactory.

For the local model, the CPA module in the HFEM, the LEFM approach with crack closure effect was considered for the simulation of the crack propagation. The stress intensity factor introduced in the LEFM approach was calculated for each cycle to determine the crack growth rate, which entailed the use of the Paris law, an approximation of the da of the dN curve. To overcome the crack closure phenomenon caused by the plastic region generated at the tip of the crack, this study used a crack opening equation from Newman theory and introduced a more accurate crack growth formula into the CPA module. The CPA results were compared to those of NASGRO, developed by NASA, and the effectiveness of the CPA module was verified by its insignificant number of errors.

The design of this framework enables researchers to address two issues: changes in the requirements at the design stage of an aircraft and changes in the inspection requirements at the operating stage. First, at the design stage, simulation via the HFEM can be used as a tool for determining whether or not the current design of an aircraft meets the FAA certification of requirements for damage tolerance design. Conventionally, this verification is carried out by a number of engineers who conduct detailed analyses based on load data from the global FEM for all major components and critical areas. Through the load transfer method and the automated crack growth analysis model, which link the global FEM and the local FEM, this study proposed a framework for reducing the amount of effort devoted to analysis, thus reducing the time and the cost of design development.

From the perspective of aircraft operation, this study suggested a method of generating a unique spectrum of an aircraft and a method of predicting crack behavior through simulation. These methodologies can help us determine which component should be intensively inspected during a subsequent maintenance cycle for the specific aircraft. Furthermore, if the performance of the sensor and the reliability of the algorithm improve, we expect that the HFEM can be used as a framework that can be referred to as a hierarchical digital twin of structural health monitoring (SHM).

The SHM system, based on the developed HFEM, will be conducive to ensuring the structural safety of aircraft if it is installed in the system of an aircraft in operation. It could also reduce the time and the cost of frequent, periodic maintenance. By intelligently estimating the impact of unexpected damage on a structure within a few hours after such damage occurs, we can enhance the efficacy of pilot decision making regarding the continuation of a mission. In addition, in the near future, when tens of thousands of drones become operational, we expect to be able to infuse the self-maintenance algorithm based on HFEM into drones and dramatically reduce the labor and time required for their maintenance.

Appendices

APPENDIX A

THE FUNCTION OF ELEMENT SHAPE

```
1  def GenElemShape(elem, grid):
2
3  import numpy as np
4
5  elemShape = np.zeros((len(elem),2))
6
7  for i in range(len(elem)):
8
9  node1=grid.loc[ grid['node'] == elem['node1'][i]]
10 node1=node1.drop('node', axis=1).values
11 node2=grid.loc[ grid['node'] == elem['node2'][i]]
12 node2=node2.drop('node', axis=1).values
13 node3=grid.loc[ grid['node'] == elem['node3'][i]]
14 node3=node3.drop('node', axis=1).values
15 node4=grid.loc[ grid['node'] == elem['node4'][i]]
16 node4=node4.drop('node', axis=1).values
17
18 totalNode =np.concatenate((node1, node2, node3, node4), axis=0)
19
20 # base node=1 let's finde diagnal node
21 dist12 = np.linalg.norm(node1-node2)
22 dist13 = np.linalg.norm(node1-node3)
23 dist14 = np.linalg.norm(node1-node4)
```

```
24
25 dist=[dist12, dist13, dist14]
26 diagnalNode= dist.index(max(dist))+1
27
28 diagnalNodeCoord =np.append( [totalNode[0]], [totalNode[diagnalNode]],
       axis=0 )
29
30 remainNode = np.delete( [0,1,2,3],0, 0)
31 remainNode = np.delete( [0,1,2,3],diagnalNode, 0)
32
33 subtractNodeCoord = np.append( [totalNode[remainNode[0]]], [totalNode[
       remainNode[1]]], axis=0 )
34
35 dely12 =  max(abs(diagnalNodeCoord[0]-subtractNodeCoord[0]))
36 delx13 =  max(abs(diagnalNodeCoord[0]-subtractNodeCoord[1]))
37 dely43 = max(abs(diagnalNodeCoord[1]-subtractNodeCoord[0]))
38 delx42 = max(abs(diagnalNodeCoord[1]-subtractNodeCoord[1]))
39
40 dely= max(dely12, dely43)
41 delx= max(delx13, delx42)
42
43 #elemShape[i,0]= elem['element'][i]
44 elemShape[i,0]= delx
45 elemShape[i,1]= dely
46
47 return elemShape
```

APPENDIX B

THE FUNCTION OF CRACK CALCULATION

```
1  def crackCalStep(s_max, s_min, a_0):
2  import numpy as np
3  import math
4
5  # Properties
6  K_c =  39
7  Y =1.12
8  S_max_s_0 = 0.3
9  DK1 = 0.74
10
11 # Paris curve
12 C= 6E-09
13 m= 3.2  # n in NASGRO
14 p = 0.25
15 q = 1
16 alpha =2
17
18 a_critical = (K_c/(Y*s_max))**2/ np.pi
19 print "  ----------"
20 print " Critical crack length= ", a_critical
21
22 a = a_0
23 K_max = Y*s_max*np.sqrt(np.pi*a)
```

```
24 K_min = Y*s_min*np.sqrt(np.pi*a)
25
26 R= s_min/s_max
27
28 #beta_R = 0.9+0.2*R**2 - 0.1*R**4
29 # R>=0
30 delK= (K_max-K_min)
31 delK_star = DK1*(a/(a+a_0))**(1/2.0)
32
33 # Newman equation
34 aA_0 = (0.825 - 0.34*alpha + 0.05*alpha**2)*( np.cos( (np.pi/2)*
       S_max_s_0))**(1.0/alpha)
35 aA_1 = (0.415 - 0.071*alpha )*S_max_s_0
36 aA_3 = 2*aA_0 +aA_1 - 1
37 aA_2 = 1 - aA_0 - aA_1 - aA_3
38
39 if R >= 0:
40 f_newman = max(R,aA_0 + aA_1*R +aA_2*R**2 + aA_3*R**3 )
41 else:
42 f_newman = aA_0 + aA_1*R
43
44 if R < 0:
45 delK_th = (delK_star*( (1-R)/(1-f_newman)**(1+R*C**m))) / (1-aA_0)**((C
       **p -R*C**m))
46 else:
47 delK_th = (delK_star*( (1-R)/(1-f_newman)**(1+R*C**p))) / ((1-aA_0)
       **((1-R)*C**p))
```

```
48
49 # Main equation
50 if delK > delK_th:
51 da_dN = (C*(delK**m)*(1- delK_th/delK)**p ) / ( ( 1 - K_max/K_c )**q)
52 else:
53 da_dN =0
54
55 a_current = a_0 + da_dN*cycle_number
56
57 print " Number of cycles applied =" , cycle_number
58 print "  ----------"
59 print " Current crack length = " , a_current
60
61 del_a = a_critical-a_0
62 Total_cycles = del_a* (cycle_number/da_dN)
63
64 print " Estimated life cycles = " , Total_cycles
65 print "  ----------"
66
67 #if math.isnan(da_dN):
68 #     da_dN=  0
69
70 return da_dN
```

APPENDIX C

MECHANICAL PROPERTIES FOR EVERY SECTIONS

Region	Upper skin	Lower skin	Forward Spar web	Fwd. Upper Spar flange	Fwd. Lower Spar flange	Rear Spar web	Rear Upper Spar flange	Rear Lower Spar flange	Rib
Material	7055-T7751	2324-T39	7150-T7751	7150-T7751	7150-T7751	7150-T7751	7150-T7751	7150-T7751	7050-T7451
Section									
0	1.15	1.05	0.5	1.65	1.55	0.4	1.55	1.45	0.12
1	1.13	1.03	0.49	1.62	1.52	0.39	1.52	1.42	0.12
2	1.11	1.01	0.49	1.60	1.50	0.38	1.49	1.39	0.12
3	1.09	0.99	0.48	1.57	1.47	0.38	1.47	1.37	0.12
4	1.07	0.97	0.47	1.54	1.44	0.37	1.44	1.34	0.12
5	1.05	0.95	0.47	1.52	1.42	0.36	1.41	1.31	0.12
6	1.03	0.93	0.46	1.49	1.39	0.35	1.38	1.28	0.12
7	1.01	0.91	0.46	1.46	1.36	0.35	1.35	1.25	0.12
8	0.99	0.89	0.45	1.43	1.33	0.34	1.32	1.22	0.12
9	0.97	0.87	0.44	1.41	1.31	0.33	1.30	1.20	0.12
10	0.94	0.84	0.44	1.38	1.28	0.32	1.27	1.17	0.12
11	0.92	0.82	0.43	1.35	1.25	0.32	1.24	1.14	0.12
12	0.90	0.80	0.42	1.33	1.23	0.31	1.21	1.11	0.12
13	0.88	0.78	0.42	1.30	1.20	0.30	1.18	1.08	0.12
14	0.86	0.76	0.41	1.27	1.17	0.29	1.16	1.06	0.12
15	0.84	0.74	0.40	1.25	1.15	0.28	1.13	1.03	0.12
16	0.82	0.72	0.40	1.22	1.12	0.28	1.10	1.00	0.12
17	0.80	0.70	0.39	1.19	1.09	0.27	1.07	0.97	0.12
18	0.78	0.68	0.38	1.17	1.07	0.26	1.04	0.94	0.12
19	0.76	0.66	0.38	1.14	1.04	0.25	1.01	0.91	0.12
20	0.74	0.64	0.37	1.11	1.01	0.25	0.99	0.89	0.12
21	0.72	0.62	0.37	1.08	0.98	0.24	0.96	0.86	0.12
22	0.70	0.60	0.36	1.06	0.96	0.23	0.93	0.83	0.12
23	0.68	0.58	0.35	1.03	0.93	0.22	0.90	0.80	0.12
24	0.66	0.56	0.35	1.00	0.90	0.22	0.87	0.77	0.12
25	0.64	0.54	0.34	0.98	0.88	0.21	0.84	0.74	0.12
26	0.62	0.52	0.33	0.95	0.85	0.20	0.82	0.72	0.12
27	0.60	0.50	0.33	0.92	0.82	0.19	0.79	0.69	0.12
28	0.58	0.48	0.32	0.90	0.80	0.18	0.76	0.66	0.12
29	0.56	0.46	0.31	0.87	0.77	0.18	0.73	0.63	0.12
30	0.53	0.43	0.31	0.84	0.74	0.17	0.70	0.60	0.12
31	0.51	0.41	0.30	0.82	0.72	0.16	0.68	0.58	0.12
32	0.49	0.39	0.29	0.79	0.69	0.15	0.65	0.55	0.12
33	0.47	0.37	0.29	0.76	0.66	0.15	0.62	0.52	0.12
34	0.45	0.35	0.28	0.73	0.63	0.14	0.59	0.49	0.12
35	0.43	0.33	0.28	0.71	0.61	0.13	0.56	0.46	0.12
36	0.41	0.31	0.27	0.68	0.58	0.12	0.53	0.43	0.12
37	0.39	0.29	0.26	0.65	0.55	0.12	0.51	0.41	0.12
38	0.37	0.27	0.26	0.63	0.53	0.11	0.48	0.38	0.12
39	0.35	0.25	0.25	0.6	0.50	0.10	0.45	0.35	0.12
40	0.33	0.23	0.24	0.57	0.47	0.09	0.42	0.32	0.12

APPENDIX D

NASTRAN BDF FILE READER

```
1  def readBDF(fileName):
2  import numpy as np
3  import os
4  import pandas as pd
5
6  #############  grid read ############3
7  f = open(fileName,'r')
8  searchlines = f.readlines()
9  f.close()
10 fw = open( "grid.dat","w")
11
12 for i, line in enumerate(searchlines):
13 if "GRID" in line:
14 for l in searchlines[i]: fw.write(l)
15 # print ("GRID data created !!! ")
16 fw.close()
17
18 grid= np.genfromtxt("grid.dat",usecols = (1,2,3,4))
19 #print gridInt
20
21 #############  mesh read ############3
22 f = open(fileName,'r')
23 searchlines = f.readlines()
```

```
24 f.close()
25
26 fw = open( "element.dat","w")
27 for i, line in enumerate(searchlines):
28 if "CQUAD4" in line:
29 for l in searchlines[i]: fw.write(l)
30 #print ("Element data created !!! ")
31 fw.close()
32
33 elem= np.genfromtxt("element.dat",usecols = (1,2,3,4,5,6))
34
35 ############  mesh read for tri ##########3
36 f = open(fileName,'r')
37 searchlines = f.readlines()
38 f.close()
39
40 fw = open( "elementTri.dat","w")
41 for i, line in enumerate(searchlines):
42 if "CTRIA3" in line:
43 for l in searchlines[i]: fw.write(l)
44 #print ("Element data created !!! ")
45 fw.close()
46
47 elemTri= np.genfromtxt("elementTri.dat",usecols = (1,2,3,4,5))
48
49 ############  pshell read ##########3
50 f = open(fileName,'r')
```

```
searchlines = f.readlines()
f.close()

fw = open( "pshell.dat","w")
for i, line in enumerate(searchlines):
if "PSHELL" in line:
for l in searchlines[i]: fw.write(l)
#print ("Pro data created !!! ")
fw.close()

pshell= np.genfromtxt("pshell.dat",usecols = (1,2,3,4,5))

os.remove("grid.dat")
os.remove("element.dat")
os.remove("pshell.dat")
os.remove("elementTri.dat")

grid = pd.DataFrame(grid, columns=['node', 'x','y','z' ])
elem = pd.DataFrame(elem, columns=['element', 'property','node1','node2
    ', 'node3' , 'node4' ])
elemTri = pd.DataFrame(elemTri, columns=['element', 'property','node1',
    'node2', 'node3'])
pshell = pd.DataFrame(pshell, columns=['property', 'material','
    thickness','mat2', 'mat3' ])

elemProp =elem.drop('node1', axis=1)
elemProp =elemProp.drop('node2', axis=1)
```

```
75 elemProp =elemProp.drop('node3', axis=1)
76 elemProp =elemProp.drop('node4', axis=1)
77
78 elemPropTri =elemTri.drop('node1', axis=1)
79 elemPropTri =elemPropTri.drop('node2', axis=1)
80 elemPropTri =elemPropTri.drop('node3', axis=1)
81
82 # Quad element
83 elemProp['material']=0
84
85 for i in range(len(elemProp)):
86 rowProperty=pshell.loc[ pshell['property'] == elemProp['property'][i]]
87 elemProp.set_value(i,'material',rowProperty['material'])
88
89 # Tri element
90 elemPropTri['material']=0
91
92 for i in range(len(elemPropTri)):
93 rowPropertyTri=pshell.loc[ pshell['property'] == elemPropTri['property'
    ][i]]
94 elemPropTri.set_value(i,'material',rowPropertyTri['material'])
95
96 print ("Reading BDF file is completed.. ")
97 return grid, elemProp, elemPropTri, pshell, elem, elemTri
```

APPENDIX E

THE FUNCTION OF CHECKING NASTRAN RUN

```
1  def nastranRunCheck():
2  import os
3  # check ststus of nastran
4  status=0
5  while (status >= 0):
6  taskList =os.popen('tasklist').read()
7  status = taskList.find('nastran.exe')
8
9  # Delete useless files
10 directory = os.getcwd()
11 test = os.listdir( directory )
12
13 for item in test:
14 if item.endswith(".DBALL"):
15 os.remove( os.path.join( directory, item ) )
16 if item.endswith(".f04"):
17 os.remove( os.path.join( directory, item ) )
18 if item.endswith(".log"):
19 os.remove( os.path.join( directory, item ) )
20 if item.endswith(".MASTER"):
21 os.remove( os.path.join( directory, item ) )
22 if item.endswith(".xdb"):
23 os.remove( os.path.join( directory, item ) )
```

```
24 if item.endswith(".IFPDAT"):
25 os.remove( os.path.join( directory, item ) )
26 if item.endswith(".1"):
27 os.remove( os.path.join( directory, item ) )  # delte previous f06 file
28
29 print (" Run Global model is completed ... ")
```

APPENDIX F

THE FUNCTION OF EXTRACTING GRID FORCE FROM GLOBAL-LEVEL FOR BASE-LEVEL

```
1
2  def gridForceSearch(fileName, targetElm):
3
4  import pandas as pd
5  import numpy as np
6  import os
7
8  f = open(fileName,'r')
9  searchlines = f.readlines()
10 f.close()
11
12 fw = open( "gridForces.dat","w")
13 for i, line in enumerate(searchlines):
14 if "POINT-ID    ELEMENT-ID" in line:
15 for j in range(1,51):
16 for l in searchlines[i+j]: fw.write(l)
17 fw.close()
18
19 f = open('gridForces.dat','r')
20 searchlines = f.readlines()
21 f.close()
22 fw = open( "gridForces2.dat","w")
```

```
23
24 for i, line in enumerate(searchlines):
25 if not "1    MSC.NASTRAN" in line and \
26 not "     DEFAULT" in line and not" \n" in line and \
27 not "                                        G R I D" in line and \
28 not"   POINT-ID" in line and \
29 not " * * * *   " in line and \
30 not "0 SEID" in line and \
31 not " ---" in line and \
32 not "=" in line and\
33 not "F-OF-SPC" in line and\
34 not "F-OF-MPC" in line and\
35 not "MSC.NASTRAN" in line and\
36 not "END OF JOB" in line and\
37 not "'" in line and\
38 not " No" in line and\
39 not "APP-LOAD" in line and\
40 not "*TOTALS*" in line :
41 for l in searchlines[i]: fw.write(l)
42
43 fw.close()
44
45 f = open('gridForces2.dat','r')
46 searchlines = f.readlines()
47 f.close()
48
49 fw = open( "gridForces3.dat","w")
```

```
50 for i, line in enumerate(searchlines):
51 li = line.lstrip()
52 if not li.startswith("0"):
53 for l in searchlines[i]: fw.write(l)
54 fw.close()
55
56 gridForces= np.genfromtxt("gridForces3.dat")
57
58 df=pd.DataFrame(gridForces, columns=['node', 'element', 'source', 'T1',
       'T2','T3','R1','R2','R3'])
59 df =df.drop('source', axis=1)
60
61 #  with 0
62 f = open('gridForces2.dat','r')
63 searchlines = f.readlines()
64 f.close()
65
66 fw = open( "gridForces4.dat","w")
67 for i, line in enumerate(searchlines):
68 li = line.lstrip()
69 if li.startswith("0"):
70 for l in searchlines[i]: fw.write(l)
71 fw.close()
72
73 gridForces= np.genfromtxt("gridForces4.dat")
74 df2=pd.DataFrame(gridForces, columns=['0','node', 'element', 'source',
       'T1','T2','T3','R1','R2','R3'])
```

```
75 df3 =df2.drop('0', axis=1)
76 df4 =df3.drop('source', axis=1)
77
78 frames = [df, df4]
79 dfx = pd.concat(frames)
80
81 if targetElm in dfx['element'].values:
82
83 keyForces=dfx[dfx['element']==targetElm]
84 keyForces=keyForces.drop_duplicates(subset=['node'], keep='first')
85
86 print (" Found grid forces !!! ")
87 else:
88 keyForces = 0.0
89 print (" No grid forces for the target Element !!! ")
90
91 os.remove("gridForces.dat")
92 os.remove("gridForces2.dat")
93 os.remove("gridForces3.dat")
94 os.remove("gridForces4.dat")
95
96 return keyForces
```

APPENDIX G

THE FUNCTION OF STRESS FINDER IN GLOBAL-LEVEL

```
1  def stressFinder(fileName):
2  import numpy as np
3  import pandas as pd
4  import os
5
6  f = open(fileName,'r')
7  searchlines = f.readlines()
8  f.close()
9
10 fw = open( "stress.dat","w")
11 for i, line in enumerate(searchlines):
12 if "CEN/4" in line:
13 for l in searchlines[i]: fw.write(l)
14 fw.close()
15
16 stress= np.genfromtxt("stress.dat")
17 stressQuad=pd.DataFrame(stress , columns=['0','element', 'source', '
       Distance ', 'NORMAL-X', 'NORMAL-Y', 'SHEAR-XY', 'ANGLE', 'MAJOR', '
       MINOR','VON MISES'])
18 stressQuad=stressQuad.drop('source', axis=1)
19
20 #### Finding Tri element ###################
21 fw = open( "stressTri.dat","w")
```

```
22 for i, line in enumerate(searchlines):
23 if "    ID.        DISTANCE" in line:
24 for j in range(1,33):
25 for l in searchlines[i+j]: fw.write(l)
26 fw.close()
27
28 f = open('stressTri.dat','r')
29 searchlines = f.readlines()
30 f.close()
31
32 fw = open( "stressTri1.dat","w")
33 for i, line in enumerate(searchlines):
34 li = line.lstrip()
35 if not "SUBCASE" in line and\
36 li.startswith("0"):
37 for l in searchlines[i]: fw.write(l)
38 fw.close()
39 stress= np.genfromtxt("stressTri1.dat")
40 stressTri=pd.DataFrame(stress, columns=['0','element', 'Distance ', '
    NORMAL-X', 'NORMAL-Y', 'SHEAR-XY', 'ANGLE', 'MAJOR', 'MINOR','VON
    MISES'])
41
42 os.remove("stressTri.dat")
43 os.remove("stressTri1.dat")
44 os.remove("stress.dat")
45 return stressQuad, stressTri
46
```

```
47 print ( " Extracting stress data from f06 file is completed .... ")
```

REFERENCES

[1] "Metal fatigue caused comet crashes," BBC News, 1954.

[2] W HTench, "Danair b707 accident report," FAA, 1979.

[3] T Swift, "Application of damage tolerance technology to type certification," SAE Technical Paper, Tech. Rep., 1981.

[4] FAA U.S department of Transportation, "Establishing and implementing limit of validity to prevent widespread fatigue damage," AC No: 120-104, 2011.

[5] F. U. department of Transportation, "Fatigue, fail-safe, and damage tolerance evaluation of metallic structure for normal, utility, acrobatic, and commuter category airplanes," AC 23-13A, 2005.

[6] P. R. Edwards and J Darts, "Standardized fatigue loading sequences for helicopter rotors," 1984.

[7] M. A. Miner, "Cumulative damage in fatigue," *J. Appl. Mech.*, vol. 12, pp. 159–164, 1945.

[8] E. H. Glaessgen and D. Stargel, "The digital twin paradigm for future nasa and u.s. air force vehicles," *AIAA, Structures, Structural Dynamics, and Materials Conference*, 2012.

[9] "The federal aviation administrations oversight of on-demand aircraft operators," FAA, Mar. 2010.

[10] L. Cartz, *Nondestructive Testing*. ASM International, 1995, ISBN: 9780871705174.

[11] R. A. Pyles, *Aging Aircraft: USAF Workload and Material Consumption Life Cycle Patterns*. CA: RAND Corporation, 2003.

[12] IATAs Maintenance Cost Task Force, "Airline maintenance cost executive commentary an exclusive benchmark analysis," MCTF, 2015.

[13] D. Stewart, "MRO market forecast and trends," Aviation week, 2015.

[14] P. Seidenman and D. J. Spanovich, "Aircraft health monitoring sensors cutting MRO costs," Aviation week, 2016.

[15] C. Bockenheimer and H. Speckmann, "Validation, verification and implementation of shm at airbus," IWSHM 2013, 2013.

[16] W. Staszewski, C. Boller, and G. R. Tomlinson, *Health Monitoring of Aerospace Structures: Smart Sensor Technologies and Signal Processing*. Wiley, 2004, ISBN: 978-0-470-84340-6.

[17] "The future for industrial services: the digital twin," *infosys tech talk*, 2016.

[18] S. C. Forth1 and A. Staroselsky, "A hybrid numerical analysis method for structural health monitoring," NASA Technical report, Aug. 2004.

[19] S. Gopalakrishnan, A. Chakraborty, and D. R. Mahapatra, *Spectral Finite Element Method*. Springer, 2008.

[20] E. J. Tuegel, A. R. Ingraffea, T. G. Eason, and S. Spottswood1, "Reengineering aircraft structural life prediction using a digital twin," *International Journal of Aerospace Engineering*, vol. 2011, no. Article ID 154798, p. 14, 2011.

[21] D. Rancourt, S. Ghosh, N. R. Weston, and D. N. Mavris, "Inference of aerodynamic loads under uncertainty using strain measurements and bayesian networks," *NASA Dryden Flight Research Center, In-Space Non-Destructive Inspection Technology Workshop*, 2012.

[22] J. D. Anderson, *Aircraft performance and design*. Tata Mcgraw-Hill, 2010, ISBN: 978-0-07-070245-5.

[23] J. E. Shigley, C. R. Mischke, and R. G. Budynas, *Mechanical Engineering Design*. Mc Graw Hill, 2003, ISBN: 007-252036-1.

[24] W. C. Young, *Roark's formulas for stress and strain*. McGraw-Hill, 1989, ISBN: 0-07-072541-1.

[25] O. Bauchau and J. Craig, *Structural Analysis with Applications to Aerospace Structures*. Springer, 2009, ISBN: 978-90-481-2515-9.

[26] J. M. Gere and B. J. Goodno, *Mechanics of Materials*. Cengage Learning, 2009, ISBN: 978-0-534-55397-5.

[27] C. T. Herakovich, *Mechanics of Fibrous Composites*. John Wiley and Sons Inc., 1998, ISBN: 0-471-10636-4.

[28] M. Chun and Y. Niu, *AIRFRAME - stress analysis and sizing*. Hong Kong Conmilit Press Ltd., 2007, ISBN: 962-7128-08-2.

[29] A. C. Ugural, *Stresses in Plates and Shells*. McGraw-Hill, 1999, ISBN: 0-07-116793-5.

[30] R. M. Jones, *Mechanics of Composite Materials*. Taylor and Francis cop., 1999.

[31] P. J. Schilling and et al., "X-ray computed microtomography of internal damage in fiber reinforced polymer matrix composites," *Composites Science and Technology*, vol. Volume 65, Pages 2071–2078, 14 2005.

[32] D. S. Beyerle, S. M. Spearing, F. W. Zok, and A. G. Evans, "Damage and failure in unidirectional ceramicmatrix composites," *Journal of the American Ceramic Society*, vol. Volume 75, Pages 2719–2725, 10 1992.

[33] C. Sun and J Tao, "Prediction of failure envelopes and stress strain behaviors of composite laminates," *Composite Science Technology*, vol. Vol.58, p.1125–1136, 1998.

[34] H. Z., "Failure criterion for unidirectional fiber composites," *Journal of Applied Mechanics*, vol. Vol.47, p.329–334, 1980.

[35] J. H. Gosse and S. Christensen, "Strain invariant failure criteria for polymers in composite materials," *AIAA paper*, vol. 1184, p. 2001, 2001.

[36] *Boeing 777*, Cielotech Online, 2015.

[37] "Military specification: airplane damage tolerance requirements," MIL-A-83444, Mar. 1987.

[38] P. H. M. Chan, A. R. Parker, A. Piazza, J. A. Bakalyar, and W. L. Richards, "Real-time fiber optic strain and shape sensing (foss) technology," *AIAA SciTech Forum*, 2014.

[39] E. P. Popov, *Engineering mechanics of solids*. Prentice Hall, 1990.

[40] C. M. Bishop, *Pattern Recognition and Machine Learning*. Springer, 2009.

[41] *Machine-learning in python*, Scikit-learn.

[42] T. Tay, V. Tan, and G. Liu, "A new integrated micro-macro approach to damage and fracture of composites," Materials Science and Engineering, 2006, pp. 138–142.

[43] R. Li, D. Kelly, and R. Ness, "Application of a first invariant strain criterion for matrix failure in composite materials," *Journal of Composite Materials*, vol. 37, no. 22, pp. 1977–2000, 2003.

[44] Y. Liu and et al., "Fatigue crack initiation life prediction of railroad wheels," *Int. Journal of Fatigue*, vol. 28, no. 7, pp. 747–756, 2006.

[45] K. Ni, "Strain-based probabilistic fatigue life prediction of spot-welded joints," *Int. Journal of Fatigue*, vol. 26, no. 7, pp. 763–772, 2004.

[46] E. U. Lee and et al., "Environmental effects on low cycle fatigue of 2024-t351 and 7075-t651 aluminum alloys," *International Journal of Fatigue*, vol. 31, no. 11, 2009.

[47] A. Fatemi and L. Yang, "Cumulative fatigue damage and life prediction theories: a survey of the state of the art for homogeneous materials," *International Journal of Fatigue*, vol. 20, no. 1, pp. 9 –34, 1998.

[48] Z. Xiulin, "A further study on fatigue crack initiation life mechanical model for fatigue crack initiation," *International Journal of Fatigue*, vol. 8, no. 1, pp. 17 –21, 1986.

[49] J. M. Potter and R. T. Wantanabe, "Development of fatigue loading spectra," ASTM, STP1006, 1916.

[50] J. Schijve, "Crack growth in aluminum alloy sheet material under flight simulation loading," Delft University of Technology, 1984.

[51] J. Jonge, "A standardized load sequence for flight simulation tests on transport aircraft wing structures, twist," Tech. Rep., 1973.

[52] H. Lowak, "Mini twist, a shorted version of twist," Tech. Rep., 1979.

[53] C. R. Richard, *SAE Fatigue Design Handbook*. SAE, 1997.

[54] R. I. Stephens, A. Fatemi, R. R. Stephens, and H. O. Fuchs, *Metal Fatigue in Engineering*. John Willey and Sons, 2001.

[55] J. A. Bannantine, J. J. Comer, and J. L. Handrock, *Fundamentals of Metal Fatigue Analysis*. Prentice Hall, 1989.

[56] O. Basquin, "The exponential law of endurance tests," *Am. So. Test. Mater. Proc.*, vol. 10, pp. 625–630, 1910.

[57] K. N. Smith, P. Watson, and T. H. Topper, "A stress-strain function for the fatigue of metals," *Jounal of Material*, vol. 5, no. 4, pp. 767–778, 1970.

[58] "Handbook for damage tolerant design," Tech. Rep.

[59] Y. Liu and S. Mahadevan, "Probabilistic fatigue life prediction of multidirectional composite laminates," *Composite Structures*, vol. 69, pp. 11–19, 2005.

[60] C Amzallag, J. Gerey, J. Robert, and J Bahuaud, "Standardization of the rainflow counting method for fatigue analysis," *International journal of fatigue*, vol. 16, no. 4, pp. 287–293, 1994.

[61] T. Endo, K. Mitsunaga, and et. al., "Damage evaluation of metals for random or varying loads," *Behaviour of Materials*, 1974.

[62] W. Elber, "The significance of fatigue crack closure in damage tolerance in aircraft structures," ASTM STP, 1971.

[63] *Msc fatigue*, MSC software, 2017.

[64] P. J. Heyes, "Finite element based fagigue design and analysis system-msc/fatigue [j]," *China Mechanical Engineering*, vol. 11, 1998.

[65] "Mmpds 06 aluminum," Tech. Rep., 2011.

[66] Y. Park, N. R. Weston, and D. N. Mavris, "Simulation of distributed co-crack propagation in cellular automata by time warp synchronization," *56th AIAA/ASCE/AHS/ASC Structures*, 2015.

[67] U. G. Goranson, *Damage tolerance facts and fiction*, in *Damage Tolerance of Aircraft Structures*, ISBN: 978-90-9022230-1. 2007.

[68] D. L. Ball and et al., "Joint strike fighter airframe durability and damage tolerance certification," *47th AIAA/ASME/ASCE/AHS/ASC Structures*, 2006.

[69] J. Newman and et al., "Fatigue life and crack growth prediction methodology," NASA Langley Research Center, 1993.

[70] T. Nakamura and Z. Wang, "Simulations of crack propagation in porous materials," *Applied Mechanics*, vol. 68, no. 2, p. 242, 2001.

[71] D. Choppa and N. Sukumar, "Fatigue crack propagation of multiple coplanar cracks with the coupled extended nite element fast marching method," Elsevier Science, 2002.

[72] M. Mitchell, *Complexity: A Guided Tour*. Oxford University Press, 2009.

[73] S. Wolfram, *Cellular Automata and Complexity: Collected Papers1*. Addison-Wesley, 1994.

[74] M. Abdalla and Z. Gurdal, "Structural design using optimality based cellular automata," AIAA, 2002.

[75] Z. Grdal, "Cellular automata for design of truss structures with linear and nonlinear response," AIAA, 2002.

[76] B. Tatting and Z. Gurdal, "Cellular automata for design of two-dimensional continuum structures," AIAA, 2002.

[77] F. McClintock and G. Irwin, "Plasticity aspects of fracture mechanics," in *Fracture toughness testing and its applications*, ASTM International, 1965.

[78] T. Swift, "Application of damage tolerance technology to type certification," SAE Technical Paper, 1981.

[79] A. De Koning, "A simple crack closure model for prediction of fatigue crack growth rates under variable-amplitude loading," in *Fracture Mechanics*, ASTM International, 1981.

[80] K. J. Mach, D. V. Nelson, and M. W. Denny, "Techniques for predicting the lifetimes of wave-swept macroalgae: a primer on fracture mechanics and crack growth," *Journal of experimental biology*, 2007.

[81] T. L. Anderson, *Fracture mechanics fundamentals and application*. CRC press Taylor and Francis, 2005.

[82] P. C. Paris and F. Erdogan, "A critical analysis of crack propagation laws," *Trans. ASME, J. Basic Eng.*, vol. D85, no. A, pp. 528–530, 1963.

[83] R. G. Forman, V. Kearney, and R. Engle, "Numerical analysis of crack propagation in cyclic-loaded structures," *Journal of basic Engineering*, vol. 89, no. 3, pp. 459–463, 1967.

[84] C. R. Shantz, "Uncertainty quantification in crack growth modeling under multi-axial variable amplitude loading," Ph.D. Dissertation, Graduate School of Vanderbilt University, 2010.

[85] J. J. Newman, "A crack opening stress equation for fatigue crack growth," *International Journal of fracture*, vol. 24, no. 4, R131–R135, 1984.

[86] R. M. Fujimoto, *Parallel and Distributed Simulation Systems*. Wiley, 2000.

[87] N. Consortium *et al.*, "Fatigue crack growth computer program nasgro® version 3.0. user manual, jsc-22267b," *NASA Technical report*, 2001.

[88] *Fracture mechanics and fatigue crack growth analysis software, reference manual*, NASA and SwRI, 2002.

[89] D. Roach, "Assessing conventional and advanced ndi for composite aircraft," *Composites World*, 2008.

[90] C.-S. Chen, P. A. Wawrzynek, and A. R. Ingraffea, "Crack growth simulation and residual strength prediction in airplane fuselages," 1999.

[91] L. Schra and et. al., "Engineering property comparisons for 2324-t39 and 2024-t351 aluminium alloy plate," NLR TR 84021 U, 1984.

[92] R. G. Forman and S. R. Mettu, "Behavior of surface and corner cracks subjected to tensile and bending loads in ti-6al-4v alloy," *Fracture Mechanics: Twentysecond Symposium*, vol. 1, no. ASTM STP 1131, pp. 519–546, 1992.

[93] J. C. Vassberg and M. A. DeHaan, "Development of a common research model for applied cfd validation studies," AIAA journal.

[94] M. D. Sensmeier and J. A. Samarehl, "A study of vehicle structural layouts in post-WWII, aircraft," AIAA.

[95] M. Chun and Y. Niu, "Airframe structural design practical design information and data on aircraft structures," Conmilit press Ltd., Jan. 1989.

[96] J. A. Corman, D. Rancourt, C. Lee, D. N. Mavris, and T. Wilson, "Preliminary wing weight estimation under probabilistic loads for a transport aircraft," in *55th AIAA/ASME/ASCE/AHS/SC Structures, Structural Dynamics, and Materials Conference*, 2014, p. 1205.

[97] J. Gosse and S. Christensen, "Strain invariant failure criterion for polymer in composite materials," *Collection of Technical papers-AIAA/ASME/ASCE/AHS/ASC Structures*, vol. Vol. 1, p.45–55, 2011.

[98] T.-E. Tay, S. Tan, V. Tan, and J. Gosse, "Damage progression by the element-failure method (efm) and strain invariant failure theory (sift)," *Composites Science and Technology*, vol. 65, no. 6, pp. 935–944, 2005.

[99] T. Tay, V. B. Tan, and L. Guangyan, "A new integrated micro-macro approach to damage and fracture of composites," *Materials Science and Engineering*, vol. Vol. 132, p. 138–142, 2006.

[100] G. A. Louis G. Birta, *Modeling and Simulation -Exploring Dynamic System Behaviour*. Springer, 2007.

[101] Averill M. Law, W. David Kelton, *Simulation Modeling and ANALYSIS*, Third. McGraw Hill, 2000.

[102] Schra, L., et. al, "Engineering property comparisons for 2324-t39 and 2024-t351 aluminium alloy plate," Tech. Rep., 1984.

[103] Alloy Digest, "Alcoa 2324-t39 plate," Tech. Rep., October 2000.

VITA

Youngchul Park was born in 1979 in Jindo, South Korea. He graduated from Korea Aerospace University, where he received two masters degrees in mechanical engineering (2009). He earned another masters degree in aerospace engineering at Georgia Tech (2014) . He graduated with his Doctor of Philosophy degree in a joint program in aerospace engineering and computational science engineering at Georgia Tech in May 2017. Park has expertise in finite element methods for linear and nonlinear stress analyses and fatigue analysis for metallic and composite structures. He worked at KARI (the Korea Aerospace Research Institute) as a member of a team that developed a light four-passenger aircraft, KC-100, or Naraon, a certification model designed for the Bilateral Aviation Safety Agreement (BASA). He also participated on projects that led to the design of the SMART-UAV, a tilt rotor unmanned aircraft developed by KARI and KUH, and a Korean utility helicopter developed by the Korean government. His research experience also includes the development of a wing analysis tool for a high aspect ratio wing from NASA and a system that integrates aerodynamics and structures with an uncertainty certification from Airbus. To solve this complex design challenge, he utilized machine-learning theories from computational science and engineering such as principal component analysis, K-means clustering, the support vector machine, and the random forester.